University of Bath

PHD

Numerical method for calculating electromagnetic fields in three dimensions.

Davidson, John A. M.

Award date:
1982

Awarding institution:
University of Bath

Link to publication

Alternative formats
If you require this document in an alternative format, please contact:
openaccess@bath.ac.uk

Copyright of this thesis rests with the author. Access is subject to the above licence, if given. If no licence is specified above, original content in this thesis is licensed under the terms of the Creative Commons Attribution-NonCommercial 4.0 International (CC BY-NC-ND 4.0) Licence (https://creativecommons.org/licenses/by-nc-nd/4.0/). Any third-party copyright material present remains the property of its respective owner(s) and is licensed under its existing terms.

Take down policy
If you consider content within Bath's Research Portal to be in breach of UK law, please contact: openaccess@bath.ac.uk with the details. Your claim will be investigated and, where appropriate, the item will be removed from public view as soon as possible.

Download date: 05. May. 2023

NUMERICAL METHOD FOR CALCULATING ELECTROMAGNETIC FIELDS IN THREE DIMENSIONS

submitted by

JOHN A.M. DAVIDSON

for the degree of Ph.D.

of the University of Bath

1982

COPYRIGHT

"Attention is drawn to the fact that copyright of this thesis rests with the author. This copy of the thesis has been supplied on the condition that anyone who consults it is understood to recognise that its copyright rests with the author and that no quotation from the thesis and no information derived from it may be published without the prior written consent of the author".

"This thesis may be made available for consultation within the University Library and may be photocopied or lent to other libraries for the purposes of consultation".

John A.M. Davidson

ProQuest Number: U333006

All rights reserved

INFORMATION TO ALL USERS
The quality of this reproduction is dependent upon the quality of the copy submitted.

In the unlikely event that the author did not send a complete manuscript
and there are missing pages, these will be noted. Also, if material had to be removed,
a note will indicate the deletion.

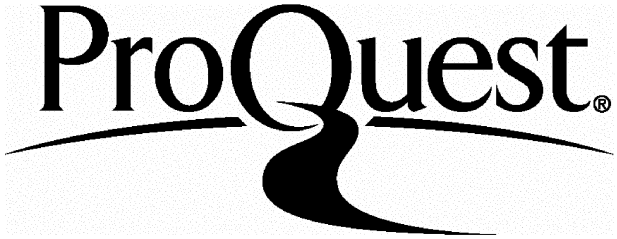

ProQuest U333006

Published by ProQuest LLC(2015). Copyright of the Dissertation is held by the Author.

All rights reserved.
This work is protected against unauthorized copying under Title 17, United States Code.
Microform Edition © ProQuest LLC.

ProQuest LLC
789 East Eisenhower Parkway
P.O. Box 1346
Ann Arbor, MI 48106-1346

UNIVERSITY OF BATH
LIBRARY
33 -6 SEP 1982 FRD
PHD

ABSTRACT

A network method is presented for the numerical solution of general three-dimensional electromagnetic field problems. Two physically separate circuit models are derived to represent the electric and magnetic parts of the field. Linkage between the two parts of the network model is through mesh variables. Conventional network techniques are used to define a minimum independent set of mesh variables, for which the linked network is solved.

The solution of the simultaneous equations from the network field model, by a preconditioned conjugate gradient algorithm, is described. The main problems that have been found to occur in the use of this algorithm are demonstrated. It is shown how these problems are related to the form of the network model used. Recommendations are made as to how the preconditioned conjugate gradient algorithm can be used most efficiently for the solution of the linked network mesh field equations.

The validity and accuracy of the linked network method, for solution of the general three-dimensional electromagnetic field, is demonstrated by a comprehensive comparison of calculated and experimental results for power frequency eddy current problems. Good agreement is shown to be obtained between calculation and experiment.

A form of the full three-dimensional linked network model is developed for problems that are periodic along one cartesian coordinate direction (quasi-3D). The validity of this model is confirmed by a comparison of flux density, thrust and normal force calculations with experiment for an axial flux linear motor. Where applicable,

the quasi-3D model greatly reduces the cost, in terms of both computer time and storage, of a full three-dimensional field solution.

ACKNOWLEDGEMENTS

The Author wishes to express his sincere gratitude to his supervisor Dr. M.J. Balchin for providing the inspiration behind the work presented in this thesis, and for his encouragement and guidance throughout the course of the work. Thanks are also due to Professor J.F. Eastham for his continued interest in the project and to Mr. G. Carter for constructing the experimental apparatus.

The Author also wishes to thank Mrs. A. Balchin for her careful and efficient typing of the thesis.

Finally the provision of financial support and computing facilities, by the Science and Engineering Research Council, is gratefully acknowledged.

CONTENTS

LIST OF PRINCIPAL SYMBOLS

b	=	magnetic flux density
C	=	capacitance
C_M, C_E, N	=	connection matrices
E,e	=	lamellar and solenoidal components of voltage
F,f	=	lamellar and solenoidal components of electric field strength
G	=	conductance
H,h	=	lamellar and solenoidal components of electric field strength
I,i	=	lamellar and solenoidal components of current
j	=	$\sqrt{(-1)}$
K,k	=	lamellar and solenoidal components of current density
M,m	=	magnetomotive force (mmf)
n	=	unit outward normal vector
P	=	permeance
p	=	time derivative, d/dt
R	=	resistance
$\mathcal{R}$	=	reluctance
s	=	slip
V	=	electric scalar potential
v_s	=	synchronous speed
ε	=	permittivity
μ	=	permeability
σ	=	conductivity
τ_p	=	pole pitch of p^{th} harmonic
ϕ	=	magnetic flux
Ω	=	magnetic scalar potential
ω	=	angular frequency

CHAPTER 1

GENERAL INTRODUCTION

A significant proportion of the development cost of an item of electrical apparatus is associated with the construction of prototypes. It is possible to avoid some of this expense if the performance of trial designs can be reliably predicted. The operation of many electrical devices is dependent on, or is influenced by, spatial distributions of magnetic flux and electrical current. Performance predictions for these devices will therefore involve the calculation of electromagnetic field quantities.

Recent activity in the field of advanced ground transport has revealed a need for accurate performance predictions for linear induction machines, vehicle lift magnets and new types of linear synchronous machines[1]. Examples of other problems currently receiving attention are waveguide junctions, turbogenerator end regions, solid iron rotors and transformer leakage. The configuration of all these devices is such that their geometry is complex and as a result both the electric and magnetic fields may be truly three-dimensional in nature.

The complete electromagnetic field is described by the familiar Maxwell's equations[2]. These indicate that electric and magnetic parts of the field are tightly coupled, one providing a source to the other and vice versa. It is this tight interlinkage which makes the solution of the full three-dimensional electromagnetic field such a difficult problem.

A common method used to tackle the problem is to eliminate using Maxwell's equations to obtain a differential or integral equation which uniquely describes the electromagnetic field in terms of one or more field variables. The problem is then to solve the resulting equation.

The form of the equation will depend on the variable(s) chosen to represent the field and also on the simplifying assumptions made, if any, when the equation was derived. If the equation is to be solved analytically some simplifying assumptions will invariably have to be made regarding the region which the equation represents. In the case of a differential equation this is normally that the medium is continuous so that boundary conditions are simple.

Analytical solutions have been performed[3] for three-dimensional electromagnetic field problems but their application is usually limited to problems where the geometry is simple.

If analytical solution of the equations describing the field is not possible, the alternative is to solve them numerically. The numerical solution of differential or integral equations invariably reduces to the solution of a large system of linear simultaneous equations. An important practical requirement of any formulation of the field problem which is to be solved numerically is that it is expressed economically in terms of a minimum number of functions. If this is not so a numerical solution to the equations, which is theoretically possible, may be impractical because of the large number of simultaneous equations to be solved. Even with a minimum number of variables it may still be impractical to solve the simultaneous equations because of the form of the coefficient matrix. For example,

integral formulations lead to a very dense coefficient matrix[4]. In this case the computer storage requirement and computation time for the solution of the equations may be excessive. It is therefore very important to consider whether a numerical solution is viable in practice when formulating the equations to represent the field.

Numerical solution procedures are now well established for full three-dimensional magnetostatic and electrostatic field problems[5,6,7,8]. Both differential and integral methods have been developed, the most successful of which are in terms of a scalar potential solution. In electrodynamic eddy current problems adequate solution procedures have only been developed, as yet, for two-dimensional problems[9] and for cases in which the magnetic field is three-dimensional but the eddy currents are limited to planar flow[10,11]. The two-dimensional problem can be solved for a vector function, for example the magnetic vector potential A, that has only one component at each node point. This effectively reduces the problem to a scalar solution. When the eddy currents are planar these can be described by a vector function, for example the electric vector potential T with only one component. Again the problem is limited to a scalar solution over the magnetic region but now an extra "scalar potential" is required at each node in conducting regions.

When the eddy current problem is truly three-dimensional the field equations become much more complex. All the vector field quantities have three components in space and the surface charge and polarity effects of electric and magnetic boundary conditions become apparent. The fact that all vector field quantities are likely to have three components makes the solution of the field in terms of a vector very costly, because in general all three components

have to be calculated at each node point. To satisfy boundary conditions at material interfaces a scalar potential function has also to be introduced. In certain formulations[12] it is necessary to solve directly for this scalar in addition to the vector function. The boundary conditions further complicate the solution process because they interrelate all three vector components at the interface thereby requiring a simultaneous solution for all components and a possible scalar.

A recent publication[12] has given a comparison of the alternative formulations of the three-dimensional electromagnetic field and discussed their application. This confirms the idea that extension of the magnetic vector potential formulation to three dimensions is a difficult problem. In practice it leads to a solution process which is uneconomical due to the complexity of the equations and the number of variables required per mesh point.

Despite its analogy with the A formulation, a method which does seem to show favourable prospects is the electric vector potential or so-called T-Ω method[11,13]. This is at present being investigated by Preston and Reece and some preliminary results have just been published for the full three-dimensional electromagnetic field[14]. In the T-Ω method the electric vector potential is a current describing function equivalent to the solenoidal component of the magnetic field strength. As such, T only need exist inside the conductor and can be limited to a vector with two components only. This is computed simultaneously with the magnetic scalar potential Ω, with all boundary conditions imposed directly in the numerical equations.

One of the main problems with the methods just described in which Maxwell's equations are manipulated to get an equation to describe

the field in terms of one, or if necessary two, field quantities is that the elimination process obscures the physical relationships in the field. It is also necessary to satisfy all boundary conditions explicitly in the numerical formulation in terms of the remaining field quantities and this is not always straightforward. Alternatively if the field problem is expressed in network terms these problems can be avoided.

The network analogy for magnetic fields is well known. In some formulations[15,16] a single network is found, by analogy, to model the differential form of Maxwell's equations. An approach used by Carpenter and Djurović[10], however, produces a network model that gives more direct insight into the physical interactions in the electromagnetic field. This model consists of one complete network to represent the magnetic part of the field throughout the region of interest and a separate network in conducting regions only, to represent the electric field effect. The two networks are physically separate but they interlink so that the surfaces of one network are intersected normally by branches of the other and vice versa. In this way the linked network satisfies Ampere's and Faraday's Laws and the interaction between the magnetic and electric field variables is clearly defined. Boundary conditions are also satisfied automatically by choosing the appropriate values for the circuit elements on the boundary. The field problem is transformed using this model to the solution of a linked network in which the linkage is formed through mesh variables.

When the field is solely magnetostatic or electrostatic the linked network model reduces to a single network with known sources and the solution is straightforward in terms of node potentials[17]. In reference (10) the interaction between a two-dimensional electric

and a three-dimensional magnetic field is considered. The electric field quantities are restricted to two dimensions, therefore the corresponding electric field network model is planar. In a planar network each of the basic rectangular meshes can be considered to support an independent circulating current[18]. The circulating electric current is driven by an emf that is equal to the time rate of change of flux in the intersecting magnetic branch. In this two-dimensional case it is possible to construct a dual network with nodes centred on each of the basic meshes in the original electric network. The node potentials in the dual network are associated with the original independent circulating currents and the dual network is node fed with the time rate of change of flux in the coinciding magnetic branch. Taking the dual of the electric network enables all mesh sources in the linked network model to be replaced by branch or node sources. Simultaneous solution of the magnetic and dual electric network, in terms of the scalar node potential in both networks, is then straightforward. This method of solution of the linked network model is indeed successful for laminar eddy current problems but unfortunately it cannot as yet be extended to the full three-dimensional case. In a three-dimensional linked circuit field model it is not possible to associate circulating currents with each of the basic rectangular meshes, because these are not all independent. No simple dual can therefore be found for either part of the equivalent circuit. The complete network model must therefore be solved as a linked circuit problem.

It is possible to solve the linked equivalent circuit of the three-dimensional electromagnetic field very simply using one of the readily available circuit analysis programs[19]. Although this may

be a very straightforward method of solving the field problem it is unlikely to be the most economical in many cases. This is because most of the commercial circuit analysis programs have been written for the general network problem with a view to obtaining a wide application. For example, the program ASTAP[19] uses a form of the tableau approach in which the network is solved directly for the potential across and the flow through all branches. This does not take advantage of any special features that may simplify the solution of a particular type of network problem. For economy of solution the linked network problem is far better expressed in terms of an independent set of variables that are the minimum number required to uniquely define the problem. In the linked network field model the form of the network linkage suggests the use of mesh variables. This is the approach adopted in the work to be described. Conventional network techniques are used to define a minimum number of independent closed paths in both networks. The network is then solved by the mesh method[18], thereby giving a solution directly in terms of loop fluxes and currents. This provides an accurate and economical solution to the three-dimensional linked circuit problem.

The following chapter gives a derivation and detailed description of the linked network field model for full three-dimensional electromagnetic field problems. The field equations for the solution of the linked network by the mesh method are derived and the formation of these equations in a practical problem is described. Chapter 3 deals with the solution of the resulting set of linear simultaneous equations. A brief review of the most common methods is given and one suitable for the solution of the mesh equations is chosen. The main problems encountered in the application of this method to a practical network

solution are described. It is shown how these problems are related to the form of the network and recommendations are made as to how they can be avoided.

It was found that although many problems have truly three-dimensional field distributions, there was a dearth of actual measurements against which the calculation method could be checked. A test model was therefore designed and built. A comprehensive set of measurements were performed and these are compared with corresponding computed results in Chapter 4. The linked network method is shown to be a valid technique for the solution of practical three-dimensional electromagnetic field problems.

A comparison is made, in Chapter 5, of the number of variables required by the linked network method presented and that required by the T-Ω method, to solve the same test problems.

The main work presented concludes with a discussion of some of the advantages and drawbacks of the linked network field solution method. One disadvantage of all numerical field solutions in three dimensions is the large number of variables required.

A form of the general linked network for problems that are periodic in one coordinate direction is also derived and applied to the analysis of an axial flux linear motor in Annex 1. This quasi-three-dimensional form, where applicable, results in a great reduction in the number of variables required for the three-dimensional field solution.

The work presented regarding the full three-dimensional linked network model has already been published[20,21] under joint authorship through the Institution of Electrical Engineers.

CHAPTER 2

THE LINKED NETWORK MODEL FOR THREE-DIMENSIONAL ELECTROMAGNETIC FIELDS

2.1 Introduction

The general eddy current problem can always be described by Maxwell's equations[2], 2.1, together with the constitutive relations, 2.2,

$$\begin{aligned} &\text{curl } h = k \qquad \text{curl } H = 0 \\ &\text{curl } f = -\frac{\partial b}{\partial t} \qquad \text{curl } F = 0 \\ &\text{div } b = 0 \\ &\text{div } k = 0 \qquad \text{div } K = -\frac{\partial \rho}{\partial t} \end{aligned} \tag{2.1}$$

$$\begin{aligned} &(K + k) = (\sigma + \varepsilon p)(F + f) \\ &b = \mu(H + h) \end{aligned} \tag{2.2}$$

all of which are satisfied simultaneously by the actual field. The simultaneous solution of these equations is therefore a basic requirement for any model used to represent the electromagnetic field.

In the network method, to be described, the electric and magnetic constitutive relations are used to derive separate network models to represent the respective parts of the field. Maxwell's curl equations are used to define the linkage between the two networks and the divergence conditions are shown to be satisfied by definition in both networks.

2.2 Derivation of one network element for the electric field

The derivation of the network model is based on a subdivision of the continuum into two separate sets of rectangular brick elements, one to represent the electric and the other to represent the magnetic properties of the region. The subdivisions are arranged so that the surfaces of one set are intersected normally by the edges of the other and vice versa.

A typical brick element 1-8 representing the electrical properties is shown in Fig. 2.1. The region, which is assumed to be formed of an isotropic material, supports a current flow. This includes displacement current. It is proposed that a component of current density should be associated with each of the region edges. In order to assign the current densities it is first necessary to consider the geometric properties of the magnetic subdivision, a node O of which is contained within the volume shown in Fig. 2.1. The edge O-a intersects the surface 1-2-3-4 normally and likewise the edge O-b intersects the surface 1-2-5-6 normally. The area A is therefore part of a rectangular surface in the magnetic subdivision that is intersected normally by the edge 1-2.

Within an isotropic electrically conducting medium the constitutive relation is:

$$K + k = (\sigma + \varepsilon p)(F + f) \qquad 2.3$$

In this expression the vector quantities are represented as the sum of solenoidal and lamellar components. The solenoidal parts are represented by lower-case symbols and the lamellar parts by upper case.

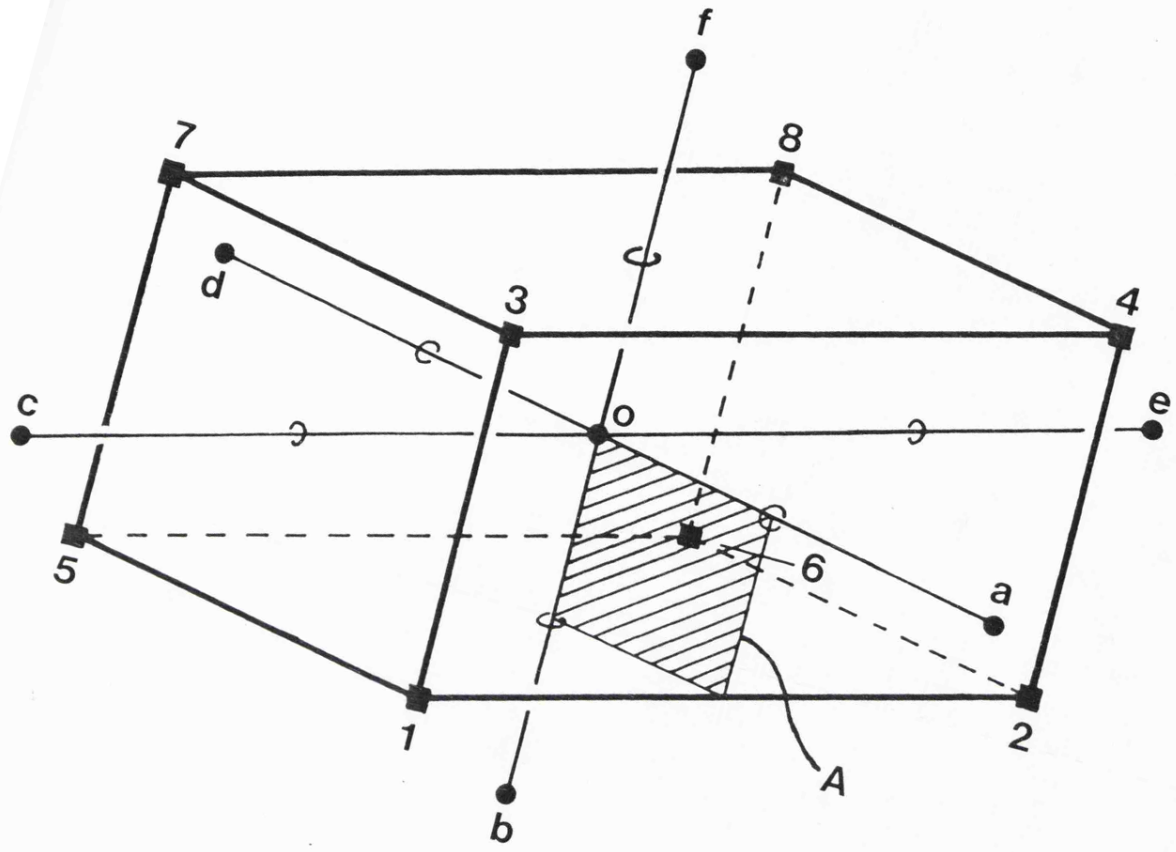

Fig. 2.1 Region of the subdivided field.

Resolving the current density and electric field strength in a direction parallel to edge 1-2 gives

$$(K + k)\cos\alpha = (\sigma + \varepsilon p)(F + f)\cos\alpha \qquad 2.4$$

where α is the angle between the vectors and line 1-2. It is assumed that the components of the vectors parallel to edge 1-2 are constant over area A and constant between points 1 and 2. The components of current within the region that are associated with edge 1-2 are those flowing through area A, i.e.:

$$\begin{aligned} I_{12} &= AK\cos\alpha \\ i_{12} &= Ak\cos\alpha \end{aligned} \qquad 2.5$$

The potential differences existing between points 1 and 2 are given by

$$\begin{aligned} \int_1^2 F\cos\alpha\, d\ell &= E_{12} \\ \int_1^2 f\cos\alpha\, d\ell &= e_{12} \end{aligned} \qquad 2.6$$

where $d\ell$ is parallel to line 1-2.

Evaluating these integrals with the components of field strength parallel to line 1-2 constant gives

$$\begin{aligned} F\ell_{12}\cos\alpha &= E_{12} \\ f\ell_{12}\cos\alpha &= e_{12} \end{aligned} \qquad 2.7$$

Substituting equations 2.7 and 2.5 into equation 2.4 gives

$$(I_{12} + i_{12}) = (\sigma + \varepsilon p)\frac{A}{\ell_{12}}(E_{12} + e_{12}) \qquad 2.8$$

In equation 2.8 the quantities $\sigma A/\ell_{12}$ and $\varepsilon A/\ell_{12}$ represent the conductance and capacitance that admit the flow of current through area A in Fig. 2.1. It is therefore convenient to represent the equation by means of an equivalent circuit, one possible combination of elements being shown in Fig. 2.2. The fact that certain of the variables are represented by means of sources and others by means of branch quantities is explained in the following section. The procedure described in this section is repeated at each of the element edges. This results in a circuit similar to that of Fig. 2.2 replacing each edge.

2.3 Complete electric field model

In order to model the complete electric field the whole space in which it exists is subdivided into rectangular brick elements, such as that shown in Fig. 2.1. As volumes associated with the edges of each brick element are replaced by equivalent circuits there will be a number of these circuit branches connected in parallel along each element edge. This means that the conductivity and permittivity of the material contained within each volume need not necessarily be the same. Interface and boundary conditions can therefore be imposed at the surface of any brick element by arranging that the element surface coincides with the interface.

The distribution of current density in an electric field is described by means of a surface integral relationship. In the complete discretisation for the electric field each vertex or node is surrounded by a closed surface S. The surface is formed of a number of areas such as A (Fig. 2.1), across which a uniform and normal current density exists. The surface integral, over the complete closed surface S, of the normal component of solenoidal current density is zero by definition.

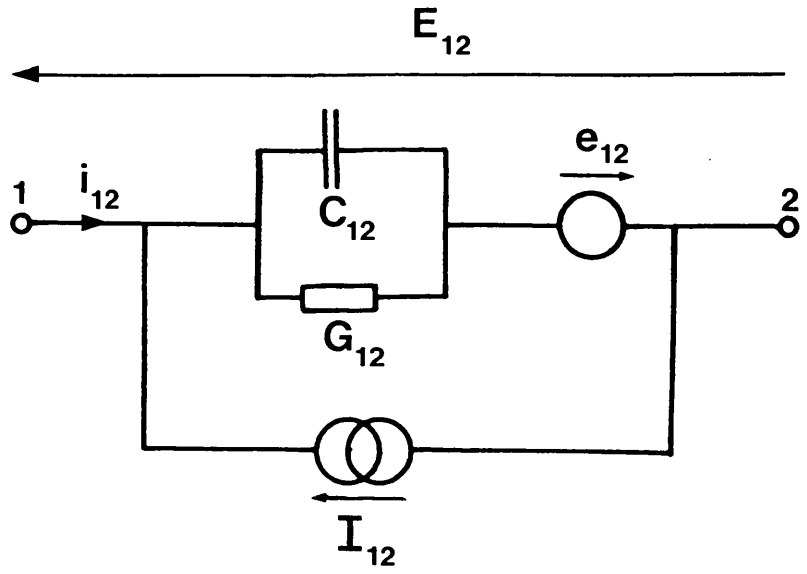

Fig. 2.2 Element of the electric field model.

i.e. $\int_S k.n \, ds = 0$ 2.9

The symbol n represents a unit outward normal vector. The way in which the total current has been subdivided in the derivation of the circuit model means that expression 2.9 can be written

$$\sum_S i = 0 \qquad 2.10$$

where the summation is over all the areas such as A which form the closed surface S. Thus the interconnection, at a vertex, of circuits like that in Fig. 2.2 is justified if current i_{12} is chosen to be the branch current as shown. The corresponding surface integral for the lamellar current density K is equal to the negative time rate of change of charge contained within S. This accumulation of charge can be obtained by specifying that currents like I_{12} be represented by means of independent source quantities.

The distribution of field strength in an electric field is described by means of a line-integral relationship. Within the complete discretisation for the electric field a closed path L can be traced by following region edges. Along each region edge the field strength is uniform, so that the expression for the line integral of the lamellar electric field strength,

$$\int_L F.d\ell = 0 \qquad 2.11$$

can be interpreted as

$$\sum_L E = 0 \qquad 2.12$$

where the summation is over all edges which form the closed path. Thus the interconnection, in a closed path, of equivalent circuits like that of Fig. 2.2 is justified if voltage E_{12} is chosen to be the branch voltage. The corresponding line integral for the solenoidal field strength

f will in general not be zero. This effect can obviously be represented by specifying voltages like e_{12} as source quantities.

2.4 Magnetic field model

The development of an equivalent circuit for the magnetic field follows lines similar to those adopted for the discretisation of the electric field. The flow quantity associated with the edges of a brick element in the magnetic discretisation is now the magnetic flux. The network analogy follows from consideration of the magnetic constitutive relation for the region. The edges of each volume of the discretisation are represented by a magnetic branch of the type shown in Fig. 2.3. In the complete magnetic equivalent circuit common edges are replaced by a parallel combination of branches. There is no requirement for the material properties to be the same in adjacent regions of the discretisation, so as before boundary conditions can be imposed directly.

Branch variables are chosen following a consideration of the line and surface integrals of field strength and flux density. In this case, however, the integral of the lamellar component of flux density does not exist because there are no free magnetic poles. This means that sources of magnetic flux, analogous to I_{12} in Fig.2.2, do not appear in the equivalent circuit.

2.5 Complete electromagnetic field model

Both the electric and the magnetic field regions are subdivided into rectangular brick elements and the subdivisions are replaced by their circuit analogs as described in sections 2.2 to 2.4. The

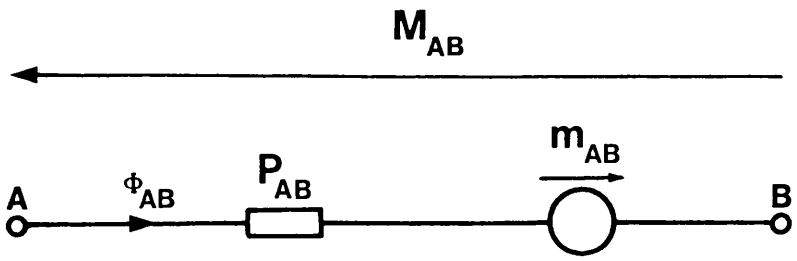

Fig. 2.3 Element of the magnetic field model.

subdivision is arranged so that, in regions where both types of field exist, each basic rectangular circuit in the magnetic equivalent circuit is intersected normally by a branch of the electric equivalent circuit and vice-versa. The reason for this will become apparent when the interaction between the electric and magnetic equivalent circuits is considered in the following section.

The electric and magnetic parts of the complete electromagnetic field are represented by two circuit models that are physically separate but have electromagnetic coupling between them. The way in which the field model has been derived has led to there being only one type of independent source quantity. This source is the current generator I_{12} shown in Fig. 2.2. It is often found, however, that excitation of the field system can be considered to be due to applied potentials. In order to represent this, independent potential sources e_{s12} and m_{sAB} are introduced into the branch elements as shown in Fig.2.4. The solution of the electromagnetically linked circuit problem with branch elements such as these is now described.

2.6 Method for solution of the network model and derivation of the field equations

To solve the linked circuit problem it is necessary to formally define the linkage between the two parts of the equivalent circuit. This is done using the discrete forms of Faraday's and Ampere's Laws. For one closed path L in the electric model surrounding a surface S

$$\int_L (F + f).d\ell = - p \int_S b.n \, ds \qquad 2.13$$

A similar expression holds for the magnetic model, i.e.

$$\int_L (H + h).d\ell = \int_S k.n \, ds \qquad 2.14$$

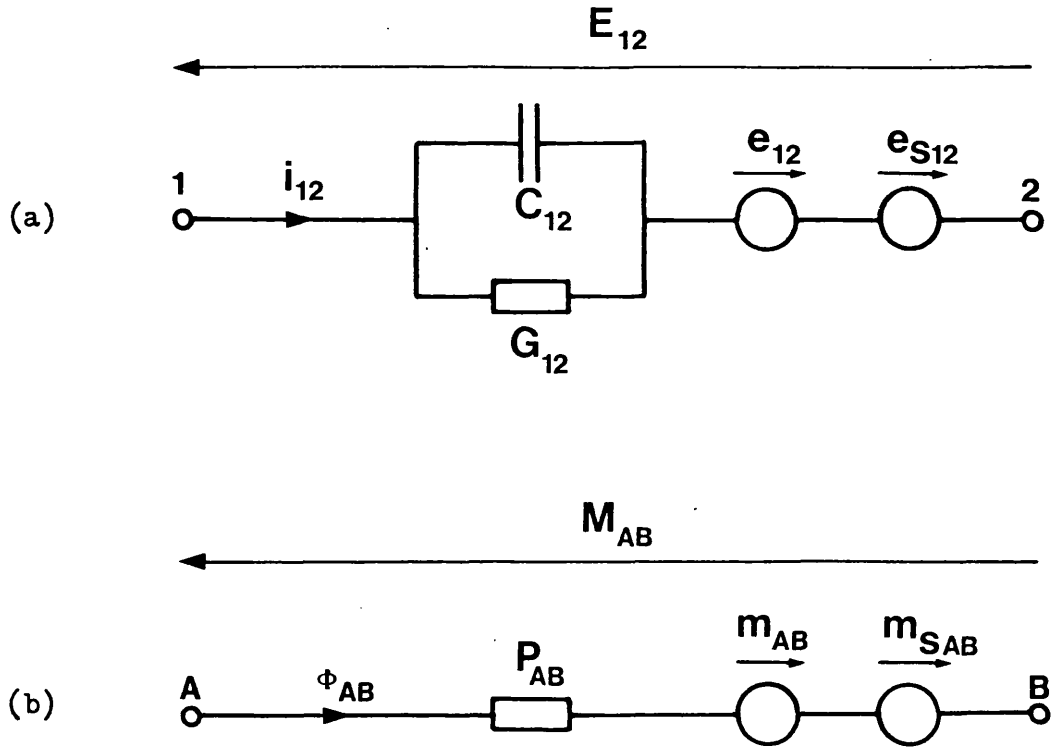

Fig. 2.4 Elements of the network field model with potential sources.
(a) electric (b) magnetic

The manner in which the fields are subdivided is such that each closed path is formed with segments of uniform field strength parallel to the path. Furthermore each closed path surrounds a surface through which flux or current passes normally. Thus equations 2.13 and 2.14 can be written,

$$\sum_{L} (E + e) = - p \sum_{S} \phi \qquad 2.15$$

$$\sum_{L} (M + m) = \sum_{S} i \qquad 2.16$$

The complete linked circuit model is solved using the "mesh current" technique[18]. This is a convenient method of solution in view of the interlinkage between the two parts of the network through the circuital laws. It gives all branch fluxes and currents in terms of an independent set of fluxes and currents that flow in closed paths. The minimum number of such closed paths required to solve the networks by the mesh method is equal to the total number of "link" or "co-tree" branches in both networks. This is represented formally by the expressions[18],

$$i = C_E \, i_I \qquad 2.17$$

$$\phi = C_M \, \phi_I \qquad 2.18$$

where i and ϕ are the vectors of all fluxes and currents, C_E and C_M are connection matrices for the electric and magnetic circuits respectively and i_I and ϕ_I are vectors of closed path currents and fluxes. When equations 2.15 and 2.16 are applied to the closed paths defined in equations 2.17 and 2.18 and all closed paths are considered then the following matrix equations are obtained.

$$C_E^T (E + e) = - pN^T \phi_I \qquad 2.19$$

$$C_M^T (M + m) = Ni_I \qquad 2.20$$

In these equations the superscript T denotes the transpose and N is a further connection matrix that indicates which of the closed path fluxes links a closed path in the electric model and vice versa. The connection matrices C_E, C_M and N are described more fully in section 2.7.

The branch relations for all branches of the type shown in Fig. 2.4 from both networks can be represented by the following matrix equations.

$$E + e + e_s = (G + pC)^{-1} i \qquad 2.21$$

$$M + m + m_s = P^{-1} \phi \qquad 2.22$$

The set of equations 2.17-2.22 reduce to the following set of simultaneous equations in the variables ϕ_I and i_I. These are the general set of equations for the mesh method solution of the linked network field model.

$$\begin{array}{|c|c|} \hline C_M^T P^{-1} C_M & -N \\ \hline -N^T & -C_E^T \left(\frac{G}{p} + C\right)^{-1} C_E \\ \hline \end{array} \begin{array}{|c|} \hline \phi_I \\ \hline i_I \\ \hline \end{array} = \begin{array}{|c|} \hline C_M^T m_s \\ \hline -\frac{C_E^T e_s}{p} \\ \hline \end{array} \qquad 2.23$$

Following a solution of 2.23 it is possible to obtain all fluxes and currents in the equivalent circuit by using equations 2.17 and 2.18.

Under steady state sinusoidal excitation conditions the time derivative term p in equation 2.23 can be replaced by $j\omega$. In power frequency problems where the displacement current is negligible in

comparison to the conduction current, the field equations simplify further to that given below, by omitting the capacitance term C.

$$\begin{bmatrix} C_M^T R C_M & -N \\ -N^T & -C_E^T \frac{R}{j\omega} C_E \end{bmatrix} \begin{bmatrix} \phi_I \\ i_I \end{bmatrix} = \begin{bmatrix} C_M^T m_s \\ \frac{C_E^T e_s}{j\omega} \end{bmatrix} \qquad 2.24$$

The matrices R and R are the reluctance and resistance matrices for the two parts of the linked network. These are equivalent to P^{-1} and G^{-1} respectively in equation 2.23. Equation 2.24 gives the general form of the discrete field equations obtained from the linked network model of all full three-dimensional electromagnetic field problems solved in the work presented. Furthermore, throughout the work all field problems are assumed to be linear. The field equations 2.24 are therefore a set of linear simultaneous equations.

2.7 Procedure for setting up the network model and field equations in a practical problem

2.7.1 Subdivision of region to be modelled

The first step in the use of the linked network method is to subdivide both the magnetic and electric regions of the field and hence obtain the equivalent circuit models as described in sections 2.2-2.5. The disposition of the two subdivisions is chosen, thus defining branch reluctance and resistance values, such that all boundary conditions for the field quantities are satisfied within the regions. There is no requirement for the mesh to be regular so the coarseness of the subdivision throughout a region is chosen with due regard to the rate of change of the field expected at each point.

In practice the magnetic field extends to infinity, so to limit the extent of the magnetic subdivision it is common to set an exterior boundary round the region of interest. This normally takes the form of a flux plane or equipotential surface and is acceptable if it is far enough away so as not to be significant in the solution. Both flux plane and equipotential boundaries are simple to represent in the network model as open circuits and short circuits respectively. The exterior boundaries for the electric part of the field are also straightforward to represent. These are normally defined by conductor surfaces, that appear as open circuits in the network model. When planes of symmetry exist these should be exploited by treating them as external boundaries, thereby reducing the region to be subdivided. Both positive and negative planes of symmetry can be represented in the network model as 'flow' plane and equipotential surfaces respectively in the manner described above using open and short circuits.

All branches and nodes are numbered separately in both parts of the network model using an arbitrary numbering scheme. An arbitrary datum node is specified in both parts of the network. The flow in all branches is also given an arbitrary positive direction. This defines a start and finish node for each branch with the positive flow from the start node to the finish node. All known sources to the field, such as winding currents, must be transformed into known branch sources or equivalent. For known current distributions this is normally performed by the method of "tearing"[10]. That is all known currents are "torn" from the network. In each magnetic circuit branch cut by a current an mmf generator, equal in magnitude to that of the current, is inserted. The sign of the mmf generator is positive if the current tends to induce positive flux in the magnetic branch it cuts and negative if it tends to give negative flux.

2.7.2 Choice of the set of independent closed path variables

Once the equivalent circuit models have been set up and numbered, the next step is to choose the independent set of closed path flows for which the network is to be solved. This is done by defining a separate tree graph[18] in the network graphs for both parts of the equivalent circuit. The remaining branches in the magnetic and electric networks are link branches. These, inserted individually into the corresponding tree, define the paths for the independent set of fluxes and currents. The link branch flows are then equal to the closed path flows. The choice of the tree and resulting link branches has been performed by a computer program TSORT, based on the procedure described in Ref. 22. TSORT defines a set of tree and link branches on input of a datum node and a list of all branches in the network, together with their corresponding start and finish nodes. TSORT also defines an order for the tree and link branches. This order is maintained throughout the calculations.

2.7.3 Construction of the resistance and reluctance matrices

The resistance matrix (R) is simply a square diagonal matrix of dimension equal to the total number of branches in the electric circuit. The diagonal elements are equal to the resistance values of the electric circuit branches. The order of the elements is that chosen for the branches by TSORT with all tree branches preceding the links. To conserve storage the resistance matrix is stored in 'linked list' form as follows. A 'real' list vector holds the diagonal elements in column order, a 'half length integer' list vector holds the row number and a 'full length integer' pointer vector is used to define the columns in the list. This is a more complicated storage scheme than is necessarily

required for a diagonal matrix. It is used, however, so that the stored matrix is compatible with sparse matrix multiplication routines used in the course of setting up the field equations.

The reluctance matrix (R) similarly holds the reluctance values for all branches in the magnetic circuit and is constructed and stored in exactly the same way as the resistance matrix.

2.7.4 The formation of the connection matrices C_M and C_E

This is the next step in the procedure to set up the field equations. In network terms C_M and C_E are the branch-mesh or circuit matrices[22] for the magnetic and electric networks respectively. They are so called because each column defines all the branches included in a closed path or mesh. As a consequence these matrices have the same number of columns as there are independent closed paths and rows equal in number to the total branches in the network. The only non-zero elements in these matrices are either +1 or -1, the sign indicating whether a mesh flow through a branch is in the positive or negative sense respectively.

Standard network techniques exist for setting up branch-mesh matrices (C-matrices). The program SETC was written to produce the C matrix of a network on input of the datum node and a list of all tree and link branches of the network, together with the corresponding start and finish node for each branch. SETC first uses a procedure described in Ref. 22 to set up the node-to-datum-path matrix B_T. A column of this matrix defines all branches included in a path in the network tree from a specified node to the datum node. A column of the C-matrix corresponding to a given link is found by subtracting the columns of B_T which give the node to datum paths for the start and

finish nodes of the link[23]. This gives the part of the required column of C corresponding to all tree branches in the closed path. The column of C is completed by adding a single entry to account for the link in the closed path. The branch order is chosen such that all the tree branches precede the links. The C-matrix therefore has the form shown in Fig. 2.5, where C_T is the part for the tree branches and C_L is the part for the link branches. C_L is in fact an identity matrix.

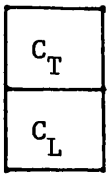

Fig. 2.5 The C-matrix partitioned into tree and link parts.

The C-matrices are normally very sparse and all the non-zero elements are either +1 or -1. To reduce the storage requirement the C-matrices are produced in linked list form as follows. A half length integer list vector is used to store the row number and sign of the non-zero elements only. Element values are stored by columns and a full length integer pointer vector defines the columns.

2.7.5 Formation of the connection matrix N

The matrix N is a connection matrix that describes the inter-linkage between the two sets of independent closed paths in the magnetic and electric parts of the field equivalent circuit. N has been defined so that it has NOLM rows and NOLE columns, where NOLM and NOLE are the number of closed paths (link branches) in the magnetic and electric parts of the model respectively.

Each column of N is associated with an individual closed path in the electric circuit. It defines all the closed paths in the magnetic model which link the specified closed path in the electric circuit. Columns of N are arranged in the chosen electric link order. The rows of N similarly define the electric circuit closed paths which link a specified closed path in the magnetic model. The rows are arranged in the chosen magnetic link order. The magnetic and electric closed paths are defined in such a way that the interlinkage between any two closed paths may only be either, once in the positive sense, once in the negative sense or zero. This is denoted in the matrix N by the values +1, -1 and 0 respectively.

The N matrix is formed by a computer program SETN that requires the following data;

a) A list of all branches in the magnetic circuit in the chosen order.

b) The branch-mesh matrix C_M for the magnetic circuit.

c) A list of links in the electric circuit, in the chosen order, together with a list, for each link, of all branches in the magnetic circuit that intersect the surface formed by the closed path, in the electric circuit, associated with the link. The sign of the magnetic branch is used to denote whether the flux it carries interacts in a positive sense with the electric link current. That is, the sign is positive if positive flux tends to induce positive current and negative if the induced current is negative.

The column of N associated with a particular closed path (link) in the electric circuit is found in SETN by summing the rows of C_M corresponding to the magnetic branches which intersect the surface formed by the closed path. If the magnetic branch and the electric link interact in the positive sense then the row of C_M is added. If they interact in the negative sense then the row of C_M is subtracted. A row of C_M gives all the closed paths in the magnetic circuit in which a particular magnetic branch occurs. Summing the rows of C_M in this way for each branch intersecting the electric link closed path surface gives all the magnetic circuit closed paths linking that closed path in the electric circuit.

The N matrix is normally very sparse and non-zero elements can only take the value +1 or -1. N is therefore produced in linked list form, the same as that used for C_M and C_E.

The method described for setting up N requires the input, as data, of the electric link numbers and the corresponding magnetic branches intersecting the electric link closed path surface. At present this data is set up by hand. When a mesh generation program is used to set up the magnetic and electric subdivision it should be possible to produce this data automatically, thereby removing the need for any major manual data writing.

2.7.6 Formation of the coefficient matrix and right hand side of the field equations

The coefficient matrix of the field equations 2.24 is produced from the individual matrices R, R, C_M, C_E and N using sparse matrix routines to perform the matrix multiplication and transposing. The coefficient matrix is normally very sparse, thus allowing computer storage to be reduced by using a linked list storage scheme similar

to that used for the resistance and reluctance matrices. The coefficient matrix is symmetric, so only the non-zero elements on the diagonal and in the lower triangle are stored. A single precision complex list vector holds the non-zero elements by column, a half length integer vector stores the corresponding row number and a full length integer pointer vector defines the columns in the lists. The numerical precision used for the computer storage of the element values in the coefficient matrix is discussed more fully in the following chapter.

The right hand side vector is produced in a similar manner using sparse routines but is stored finally as a normal single precision complex vector.

The problem remaining is the solution of the resulting set of linear simultaneous field equations. This forms the subject of the next chapter.

CHAPTER 3

SOLUTION OF THE FIELD EQUATIONS FROM THE LINKED NETWORK MODEL

3.1 Introduction

There are many methods available for the solution of sets of linear simultaneous equations[24]. These are divided broadly into two classes, namely direct and iterative methods. The direct methods calculate the solution of the equations in a finite number of arithmetic operations. Iterative methods proceed to a solution by calculating a sequence of approximations that eventually converge to the required solution.

The applicability of either method depends on the set of equations to be solved and is determined mainly by the form of the coefficient matrix. The coefficient matrix for the mesh equations 2.24 is complex and in general it is large and very sparse. It is symmetric but does not have any of the recognisable structures that limit the number of elements that can become non-zero ("fill-in") during a direct solution procedure. An attempt was made to band the matrix using the technique proposed by Gibbs, Poole and Stockmeyer[25], but the minimum half bandwidth obtainable was found to be N/2, where N is the order of the matrix. In this case the many direct solution algorithms[26,27,28] for large systems of linear equations are not suitable because the possibility of excessive "fill-in" within the large bandwidth can lead to prohibitive storage requirements and computation times.

Iterative methods have also had widespread use in the solution of linear simultaneous equations[29,17,30,31], particularly those resulting

from finite difference problems. The main advantage of iterative methods is that they do not in general suffer from "fill-in". Hence storage is normally only required for the non-zero elements of the coefficient matrix plus at least two vectors for the right hand side and the solution.

The problem of convergence is of course inherent in the iterative method and it is this which can lead to its downfall. The success of iterative methods in the solution of equations from the finite difference problem is due to the form of the coefficient matrix. For example, in static Laplacian and Poissonian field problems[17] the coefficient matrix of the standard finite difference equations is real, symmetric and positive definite[24]. In this case it is a simple matter to theoretically guarantee the convergence of successive over-relaxation (SOR) and its related methods[24]. The finite difference equations for eddy current field problems, in which the coefficient matrix is complex and is not necessarily positive definite, have also been solved by SOR techniques[31]. In this case, however, a general theoretical guarantee of the convergence of SOR methods is not straightforward.

A further reason for the success of iterative methods with finite difference problems is that by consistent ordering of the nodes in a finite difference mesh, the coefficient matrix of the difference equations can be made narrowly banded, with all non-zero elements on a number of diagonal rows. Iterative solution of the simultaneous equations by the alternating direction implicit (ADI) method[29] and by the strongly implicit procedure (SIP)[30] is then practicable.

The coefficient matrix of the mesh equations from the linked network field model is complex and is not positive definite. The solution of these mesh field equations by SOR could not be made to

converge in a typical test problem. In view of this fact and the uncertainty regarding the convergence of SOR with complex sets of equations[31] it was felt that SOR was not a suitable method for the solution of the mesh field equations. Furthermore, the coefficient matrix of the mesh field equations is not banded and hence solution by ADI and SIP is not feasible. Most of the common iterative methods are not therefore suitable for solving the mesh field equations.

There does exist one class of "iterative" method, or semi-iterative method for which, in theory, a guarantee of convergence can be given for solution of the mesh field equations. This is the method of conjugate gradients, introduced in basic form by Hestenes and Stiefel[32]. Meijerink and van der Vorst[33] developed the method for real M-matrices [33] by the introduction of incomplete Choleski pre-conditioning. Kershaw[34] further investigated the performance of the preconditioned algorithm with real, symmetric, positive definite coefficient matrices. He also presented a preconditioned algorithm for the non-symmetric, non-positive definite real matrix.

In this chapter the following section briefly describes the operation of the basic conjugate gradient method, the idea of preconditioning and then describes the preconditioned algorithm given by Kershaw for non-positive definite, real matrices. This algorithm is adapted to operate with a complex, symmetric coefficient matrix. The programing of such an algorithm, in practice, is described in section 3.3. Finally, the latter sections of the chapter describe some practical experience obtained using the complex, preconditioned conjugate gradient algorithm for the solution of the mesh field equations.

3.2 Description of the conjugate gradient algorithm for solution of the mesh field equations

3.2.1 The basic conjugate gradient method

The operation of the basic conjugate gradient method is described for the solution of a system of n linear simultaneous equations,

$$A\bar{x} = b \qquad (3.1)$$

where $\bar{x}$ is the exact solution vector. Let the approximate solution at the i^{th} iteration be denoted by the vector x_i. The corresponding residual vector is then

$$r_i = b - Ax_i \qquad (3.2)$$

The conjugate gradient method is based on the properties of quadratic functions such as,

$$x^T Ax - 2b^T x = \text{constant} \qquad (3.3)$$

If the matrix A is symmetric and positive definite then the quadratic Q(x) has an absolute minimum for $x = \bar{x}$[24]. The conjugate gradient method exploits this feature and can be regarded as a minimisation procedure. The absolute minimum $\bar{x}$ is sought by finding the local minima $x_0, x_1, x_2, \ldots$ along a series of search lines in n-dimensional space. The directions of these search lines, given by the vectors, $p_0, p_1, p_2, \ldots$ are chosen to be A-orthogonal. That is, the inner product relation 3.4 is enforced.

$$(p_i, Ap_j) = 0 \qquad (i \neq j) \qquad (3.4)$$

This is performed recursively by a dual orthogonalisation process in which the residual and direction vectors are formed in the order $r_0, p_0, r_1, p_1, \ldots, r_i, p_i, \ldots$. The r_i are formed by applying an orthogonalisation procedure to the linearly independent vectors r_0,

Ap_0, Ap_1, Ap_2,..., Ap_i,... . The A-orthogonal p vectors are produced by a similar procedure using the residual vectors as the base. This process is implemented by the basic algorithm of Hestenes and Stiefel[32] as given below in equation 3.5.

$$
\begin{aligned}
p_0 &= r_0 = b - Ax_0 \qquad (x_0 \text{ arbitrary}) \\
\alpha_i &= \frac{|r_i|^2}{(p_i, Ap_i)} \\
x_{i+1} &= x_i + \alpha_i p_i \\
r_{i+1} &= r_i - \alpha_i Ap_i \\
\beta_i &= \frac{|r_{i+1}|^2}{|r_i|^2} \\
p_{i+1} &= r_{i+1} + \beta_i p_i
\end{aligned}
\qquad (3.5)
$$

The finite termination property of the conjugate gradient algorithm is due to the fact that all residual vectors, generated during the course of the algorithm, are orthogonal, i.e.

$$(r_i, r_j) = 0 \qquad (i \neq j) \qquad (3.6)$$

This means that at the n^{th} iteration, the residual vector r_n is expressible as a linear combination of the previous n linearly independent residual vectors. It is orthogonal to all of them, so it must be zero. It can be shown (Appendix 1) that $r_n = b - Ax_n$, so that if $r_n = 0$, x_n is the exact solution.

The guarantee of convergence of the conjugate gradient method in at most n iterations relies on the use of exact arithmetic throughout. With computer solutions finite termination cannot be guaranteed because round-off error in the computer disturbs the orthogonality relations, such as (3.6) and r_n is not zero. This does not prevent the method from being useful in practice provided that the residual can be made

sufficiently small to give the required accuracy in the solution. In some solutions this condition may be satisfied in less than n iterations, whereas in others it may take more than n iterations or even fail completely due to an excessive build-up of round-off errors.

Meijerink and van der Vorst[33] applied a form of preconditioning to the basic algorithm when the coefficient matrix was a symmetric M-matrix ($A = (a_{ij})$ is an M-matrix if $a_{ij} \leq 0$ for $i \neq j$, A non-singular and all non-zero elements of A^{-1} are greater than zero). This preconditioning technique is now described.

3.2.2 Preconditioning technique for conjugate gradients

The convergence of a conjugate gradient algorithm is fast for a coefficient matrix, the eigenvalues of which are[35]

a) clustered in a small number of groups. That is the eigenvalues in each group are approximately the same magnitude but there may be considerable difference in the magnitude of the eigenvalues between any of the individual groups.

b) all of approximately the same magnitude.

In the latter case the matrix has a small condition number, defined as the ratio of the largest to the smallest eigenvalue.

The idea of preconditioning for conjugate gradients is to multiply the coefficient matrix by some conditioning matrix so as to give it a more degenerate spectrum of eigenvalues and hence reduce the condition number. To be of practical value the conditioning matrix must satisfy the further constraints that it is easily and quickly constructed and that its inclusion in the algorithm does not increase computer time or storage excessively.

The preconditioning method proposed by Meijerink and van der Vorst[33] for a symmetric M-matrix A is based on a partial Choleski decomposition (LL^T) of A. The decomposition is partial in the sense that "fill-in" is controlled. That is, an element which becomes non-zero during the process may be ignored. A full decomposition of A is obviously not feasible as a conditioning matrix, both from a time and storage viewpoint. If the partial decomposition LL^T is such that $(LL^T)^{-1}$ is a good approximate inverse of A, then it can be used to precondition the system $A\bar{x} = b$ so that it becomes,

$$\left[L^{-1}AL^{-T}\right] L^T\bar{x} = L^{-1}b \tag{3.7}$$

The new coefficient matrix $L^{-1}AL^{-T}$ now approximates an identity matrix. All its eigenvalues should be close to unity and conjugate gradients applied to this system will converge quickly. This was implemented by Meijerink and van der Vorst[33] using the following algorithm in which it is not necessary to form the preconditioned coefficient matrix explicitly.

$$\begin{aligned}
&x_0 \text{ arbitrary} \\
&r_0 = b - Ax_0 \qquad p_0 = (LL^T)^{-1}r_0 \\
&\alpha_i = \frac{(r_i, (LL^T)^{-1}r_i)}{(p_i, Ap_i)} \\
&x_{i+1} = x_i + \alpha_i p_i \\
&r_{i+1} = r_i - \alpha_i Ap_i \\
&\beta_i = \frac{(r_{i+1}, (LL^T)^{-1}r_{i+1})}{(r_i, (LL^T)^{-1}r_i)} \\
&p_{i+1} = (LL^T)^{-1}r_{i+1} + \beta_i p_i
\end{aligned} \tag{3.8}$$

Meijerink and van der Vorst[33] showed that this type of preconditioned conjugate gradients applied to real symmetric M-matrices could give fast rates of convergence, even for the case where the sparsity pattern of the original matrix was forced on the decomposition and no fill-in allowed. Kershaw[34] removed the restriction that A be an M-matrix and showed that the preconditioned algorithm 3.8 with no fill-in could be used successfully for an arbitrary real, positive definite, symmetric matrix.

3.2.3 Preconditioned conjugate gradient algorithm for the general complex, non-singular, non-positive definite, symmetric matrix

A conjugate gradient algorithm for the general non-positive definite case was first proposed by Hestenes and Stiefel[32]. This simply applied the basic algorithm 3.5 to the normalised system 3.9, without having to form the matrix A^TA explicitly

$$A^TA\bar{x} = A^Tb \qquad (3.9)$$

This corresponds to a minimisation of the quadratic given by equation 3.10 in inner product notation,

$$((x_i - \bar{x}), A^TA(x_i - \bar{x})) \qquad (3.10)$$

where $(x_i - \bar{x})$ is the error vector at the i^{th} iteration.

Reid[36] states that the "ideal" choice of quadratic is the minimisation of the Euclidian norm of error 3.11, since this is a direct measure of the accuracy of the solution.

$$((x_i - \bar{x}), (x_i - \bar{x})) \qquad (3.11)$$

This is not possible when solving the original system $A\bar{x} = b$ since it would require the solution $\bar{x}$ to be known, but it can be used when solving the normalised system.

Kershaw[34] presented an algorithm of this type for arbitrary, non-singular, real matrices using an incomplete LU decomposition for preconditioning. This algorithm can be extended to operate with complex matrices if the complex conjugate transpose (Hermitian transpose) is used in place of the simple transpose in the evaluation of inner products. The mesh equations are symmetric so the incomplete LU decomposition becomes LL^T, where T denotes the ordinary transpose. With some re-arranging and including these changes, the algorithm is then as in 3.12, where the superscript H denotes the Hermitian transpose.

$$
\begin{aligned}
x_0 &= (LL^T)^{-1}b \\
r_0 &= L^{-1}(b - Ax_0) \\
p_0 &= (L^{-1}AL^{-T})^H r_0 \\
\alpha_i &= \frac{r_i^H r_i}{p_i^H p_i} \qquad (3.12) \\
x_{i+1} &= x_i + \alpha_i L^{-T} p_i \\
r_{i+1} &= r_i - \alpha_i (L^{-1}AL^{-T}) p_i \\
\beta_i &= \frac{r_{i+1}^H r_{i+1}}{r_i^H r_i} \\
p_{i+1} &= (L^{-1}AL^{-T})^H r_{i+1} + \beta_i p_i
\end{aligned}
$$

This is the form of conjugate gradient algorithm adopted for the solution of the mesh field equations. No fill-in is allowed in the incomplete Choleski decomposition and the sparsity pattern of A is forced on L.

3.3 Computer implementation of the conjugate gradient algorithm for solution of the mesh field equations

The algorithm 3.12 was programed to operate totally in core. The coefficient matrix A for the mesh field equations is symmetric and very sparse. A sparse storage scheme was therefore adopted for A. This uses one single precision complex vector to store the non-zero elements in the lower triangle in column order, one half length integer vector to store the corresponding row numbers and an integer pointer vector to mark the columns. The lower triangular partial decomposition L is stored in a similar manner. This only requires one additional single precision complex vector to store the non-zero element values. The row and pointer vectors are the same as that for A since its sparsity pattern is maintained with no fill-in. The algorithm also requires storage for five double precision complex work vectors of length n, where n is the dimension of the set of simultaneous equations. The precision of these complex work vectors greatly affects the operation of the algorithm. The precision used for all storage has been chosen from experience with solutions of the mesh equations. This is discussed in section 3.4.

When the electromagnetic field problem is represented by a set of simultaneous equations, the quantities involved such as the fluxes and currents may differ by an order of magnitude which is close to the computer accuracy. This can lead to the accumulation of large rounding errors in the computer arithmetic. In order to minimise the rounding error in the solution, the equations are scaled so that the diagonal elements of the coefficient matrix are 1 + j0. To preserve symmetry the rows and columns are scaled symmetrically. The right hand side is also scaled so that the magnitude of its largest

element is unity. This type of scaling should help to bring the quantities involved in the computer arithmetic, during the solution of the equations, into a common range around unity, in which computer rounding error is a minimum.

Throughout the computer program written to implement the algorithm 3.12 all matrix/vector products in the algorithm are formed from right to left, so that no matrix by matrix products have to be evaluated explicitly. Forward and backward substitution routines are used to perform products involving L^{-1} and L^{-T} respectively. All Hermitian transpose operations are limited to vectors.

The performance of the conjugate gradient algorithm in practice is very dependent on the degree of numerical error, so care was taken to minimise this when programing. In particular, products such as a vector and its complex conjugate transpose, that in theory is a real number, are explicitly formed as real numbers. This avoids the occurrence of a non-zero imaginary part to the product due to round-off error. It was also found that the use of double precision is most important when forming the residuals, especially the initial value r_0. The expression for r_0 includes the difference $b - Ax_0$. This is the only place where the right hand side b occurs, so any error in this expression will lead to the solution of a different system. This situation occurs frequently in practice, particularly if x_0 is a good estimate of the solution and hence Ax_0 and b are approximately the same value. Numerical error in performing the approximate decomposition is reduced by using double precision for all accumulating variables.

In theory the starting value x_0 for a conjugate gradient routine is arbitrary, but in practice the use of a better estimate will usually give convergence in fewer iterations. A good starting value can normally be obtained by using the partial decomposition LL^T to solve the sytem approximately, i.e.

$$x_0 = L^{-T}L^{-1}b \qquad (3.13)$$

This is the default method used to generate x_0 in the algorithm, but it may be supplied externally if desired. It has been found that in most cases a good starting value is obtained by using the magneto-static field results, if these are known.

The stopping criterion for the main iteration is,

$$\frac{|r_i|}{|r_0|} \leq \text{TOL} \qquad (3.14)$$

where r_0 is the initial residual and TOL sets the accuracy required. A suitable value for TOL was found to be TOL = 1.0×10^{-5}. This value has been used in all solutions.

3.4 Practical experience in using the preconditioned conjugate gradient algorithm for solution of the mesh field equations

3.4.1 Introduction

The performance of the preconditioned conjugate gradient algorithm depends greatly on the form of the equations being solved. This section examines its behaviour when solving some typical sets of mesh field equations. The main problems which have been found to occur are demonstrated and recommendations are made as to how the algorithm can be used most efficiently for the solution of the mesh field equations.

3.4.2 Effect of round-off error in relation to the arithmetic precision

It was stated in section 3.2.1 that, in practice, the conjugate gradient solution of n simultaneous equations cannot be guaranteed to converge in n iterations, due to the presence of round-off error. It is now shown how the degree of round-off error affects the performance of the conjugate gradient algorithm 3.12 when solving a typical set of mesh field equations.

The test equations used result from a linked network method solution of the three-dimensional eddy current problem shown in Fig.3.1. The magnetic region of this problem is cubic in shape. The external boundary conditions for this cubic region are,

a) a flux plane on two sides

b) an equipotential surface on three sides

c) a mixed flux plane and equipotential surface on the remaining side.

The electric region for the problem consists of a conductor of conductivity 2.7×10^7 S/m, completely filling the lower half of the cubic magnetic region. The problem is excited by a 50 Hz sinusoidal mmf applied between the two equipotential surfaces as shown in Fig.3.1. The test problem is similar to a practical problem solved in Chapter 4. However the physical origin of the problem does not have to be considered for the present application. It is sufficient that the mesh field equations obtained from the problem are typical of those which have to be solved in three-dimensional, power frequency eddy current problems.

The solution of the test problem for the present analysis was performed using a regular linked network model. The magnetic network was of dimension 4 x 4 x 4. This gave rise to a set of linear simultaneous equations of order 158. The effect of round-off error in

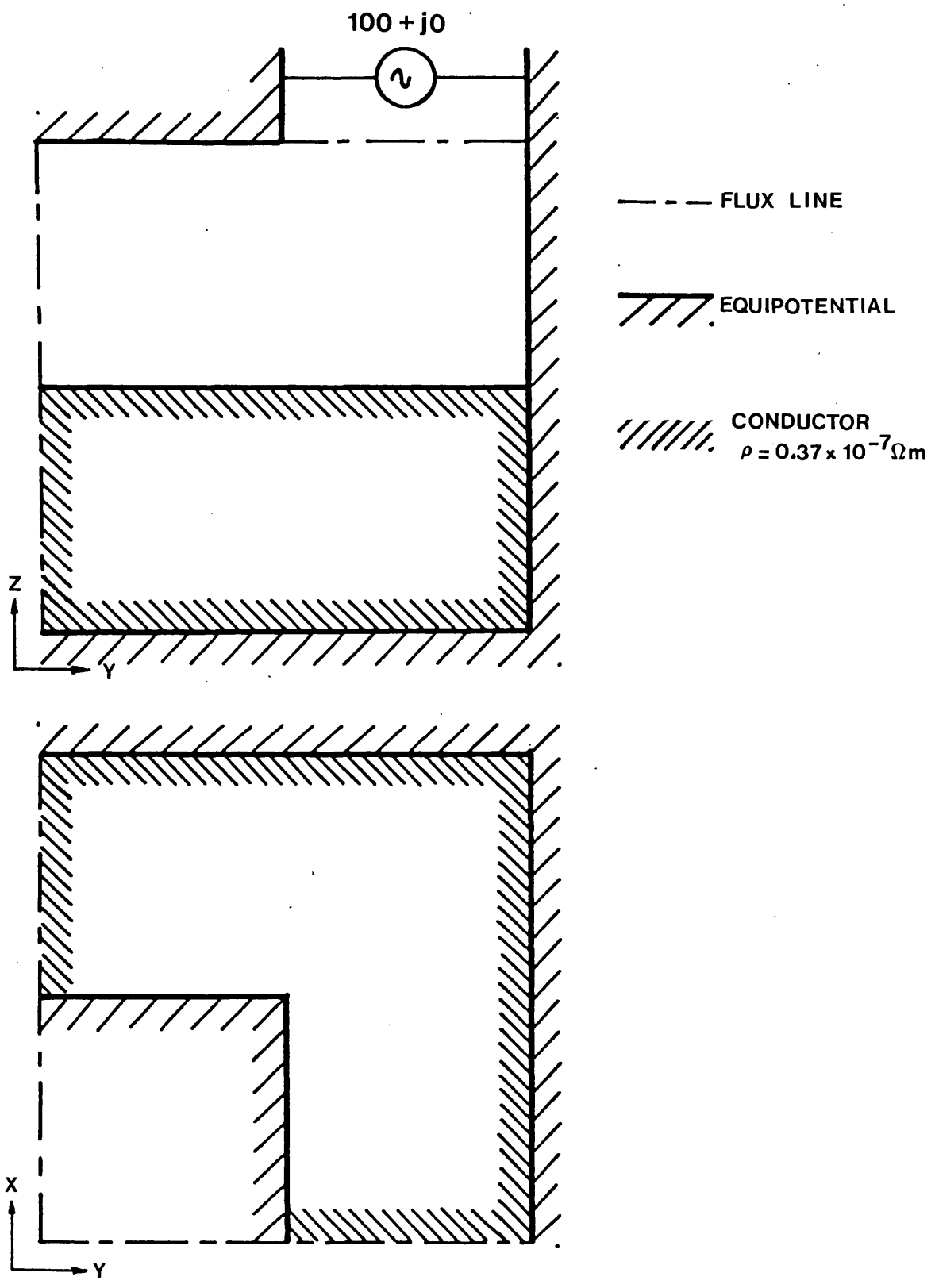

Fig. 3.1 Details of a three-dimensional eddy current test problem.

the preconditioned conjugate gradient solution of these equations is now described.

The amount of round-off that occurs in the computer depends on the precision used for storage of all real and complex variables involved in arithmetic operations. On the IBM 195 single, double and quadruple precision is available. These correspond to storage of approximately 7, 16 and 35 decimal places respectively per real variable.

In the conjugate gradient algorithm a major part of the storage is for the non-zero elements of the complex coefficient matrix and those of its approximate inverse. To accommodate the large storage requirement of three-dimensional problems it was decided that storage of these matrices must be limited to single precision. It is not believed that this will affect the accumulation of rounding error in the course of the algorithm because, once formed, these matrices are simply constant multiplying factors for the work vectors. All work vectors r_i, p_i, x_i accumulate as the algorithm proceeds. This is the main source of rounding error.

The test problem has been solved using single double and quadruple precision for all the work vectors and factors α and β. The function $e = \log_{10} \frac{|r_i|}{|r_0|}$, where r_0 is the initial residual, is plotted against the iteration number i for each solution in Fig.3.2. This gives a direct comparison of how the degree of rounding error affects the convergence properties of the algorithm when solving the typical mesh field equations. Table 3.1 gives the corresponding storage requirements and run times for a tolerance of TOL = 1.0×10^{-5} in each case.

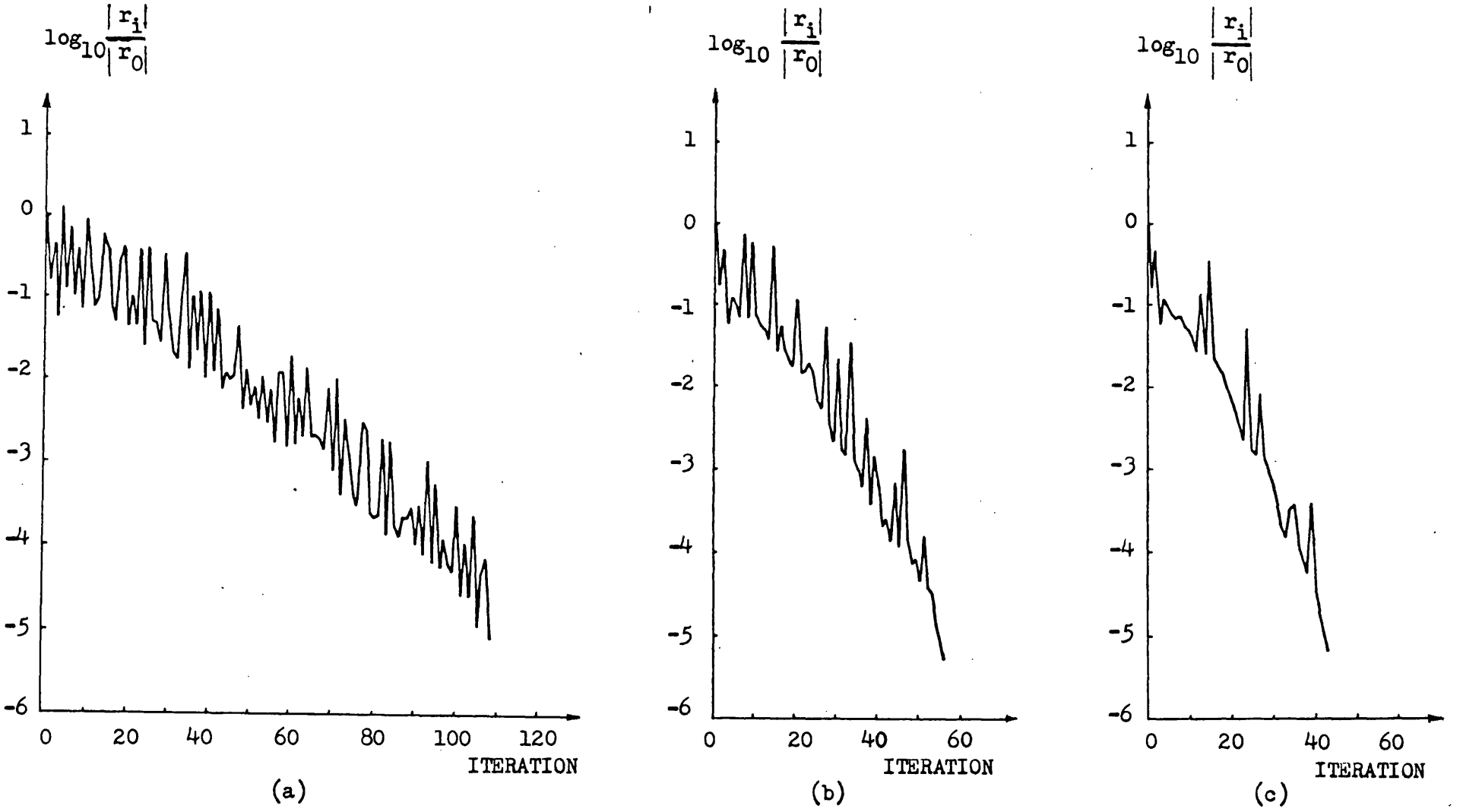

Fig. 3.2 Convergence rates for solution of the regular 158 equation test problem, using algorithm 3.12 with work vectors of,
(a) single precision (b) double precision (c) quadruple precision

	single	double	quadruple
CPU time (sec)	19	11	39
work vector storage K-bytes	6.3	12.6	25.3
Total storage K-bytes	45.3	51.6	64.3

Table 3.1 Computation times and storage requirements for solution of test problem using algorithm 3.12, with single, double and quadruple precision work vectors.

It is seen from Fig. 3.2 that for this problem the use of double precision gives convergence in many fewer iterations than single precision and that further improvement is small when quadruple precision is used. The residual is also seen to be less oscillatory when greater precision is used. This indicates that severe oscillation of the residual is a characteristic associated with the presence of large round-off errors.

Table 3.1 shows that even though quadruple precision converges in the fewest number of iterations, double precision requires by far the shortest computation time. This occurs because the decrease in the number of iterations with quadruple precision is not great enough to compensate for the slower arithmetic with increased precision. With regard to storage, a very large increase in the work vector storage requirement (Table 3.1) makes the use of quadruple precision even less attractive.

The "best" choice of precision for the algorithm vectors in the test example is seen to be double precision. This does not increase the total storage by a large proportion, but reduces the solution time significantly. In general double precision has been found to be

preferable for the solution of most sets of equations that have arisen from the mesh method solution of the linked network field model. In a few cases, however, when the coefficient matrix was particularly well conditioned, single precision was adequate and when very poorly conditioned, quadruple precision was necessary.

3.4.3 Effectiveness of the incomplete Choleski preconditioning

The effectiveness of the incomplete Choleski type of preconditioning for the mesh equations is illustrated using the test problem introduced in the previous section. The same mesh field equations as used before for this problem have been re-solved with the preconditioned conjugate gradient algorithm 3.12, using double precision work vectors and with a version of this algorithm in which the preconditioning has been omitted. The same starting value $x_0 = L^{-1}L^{-T}b$, where L is the approximate decomposition, was used in both cases. The quantity $e = \log_{10} \frac{|r_i|}{|r_0|}$, where r_0 in the initial residual, is plotted in Fig. 3.3 for both solutions as a function of the iteration number i.

The corresponding computation times and storage requirements are given in Table 3.2.

	with preconditioning	without preconditioning
CPU time (sec)	11	15
Storage (K-bytes)	51.6	34.5

Table 3.2 Computation times and storage requirements, with double precision work vectors, for solution of the test problem with and without preconditioning.

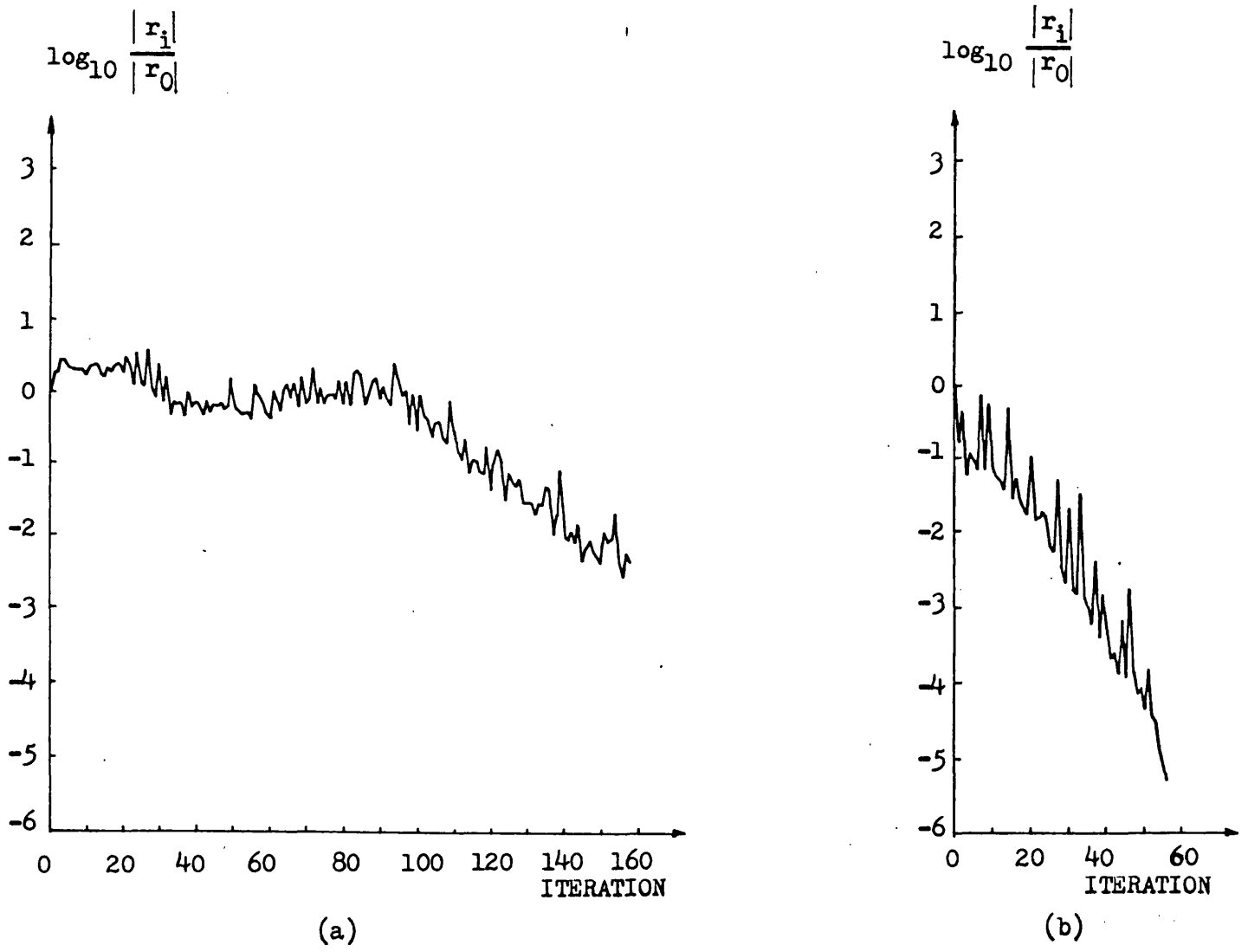

Fig. 3.3 Convergence rates, using double precision work vectors, for solution of the regular 158 equation test problem, (a) without preconditioning (b) with preconditioning

It can be seen from Fig. 3.3 that in the case without preconditioning the tolerance of TOL = 1.0×10^{-5}, for convergence of the solution, has not been reached even after the theoretical maximum number of iterations of n = 158. The preconditioned algorithm, however, converges to a tolerance of TOL = 1.0×10^{-5} in many fewer iterations than the theoretical maximum. Furthermore, even if the solution without preconditioning could be made to converge by performing some extra iterations, it can be seen from Table 3.2 that the preconditioned algorithm would still be superior in terms of computation time. The preconditioned algorithm does of course require more storage.

The success of the incomplete Choleski type of preconditioning depends on obtaining a partial decomposition that is a good approximation to the full decomposition. If this is achieved then the preconditioned system matrix approximates an identity matrix (I) and convergence of the subsequent conjugate gradient solution is fast. The accuracy of the partial Choleski decomposition in the preconditioning of the test mesh field equations is shown by a comparison of the eigenvalue spectrum of the coefficient matrix before and after preconditioning. The algorithm 3.12 solves the normalized system of equations. The coefficient matrix for these equations is A^TA, although it is not formed explicitly, and hence the preconditioned coefficient matrix is $(L^{-1}AL^{-T})^T(L^{-1}AL^{-T})$. The eigenvalues of these matrices were calculated using the Numerical Algorithms Group (NAG), mark 6 routine FO2AJF[37] and are shown in Fig. 3.4. This comparison confirms that the incomplete decomposition, in this case, is sufficiently accurate for the preconditioning to modify the eigenvalue spectrum of the coefficient matrix to that approximating the spectrum of the identity matrix, apart from a few extreme eigenvalues. The overall condition number of the matrix has also been

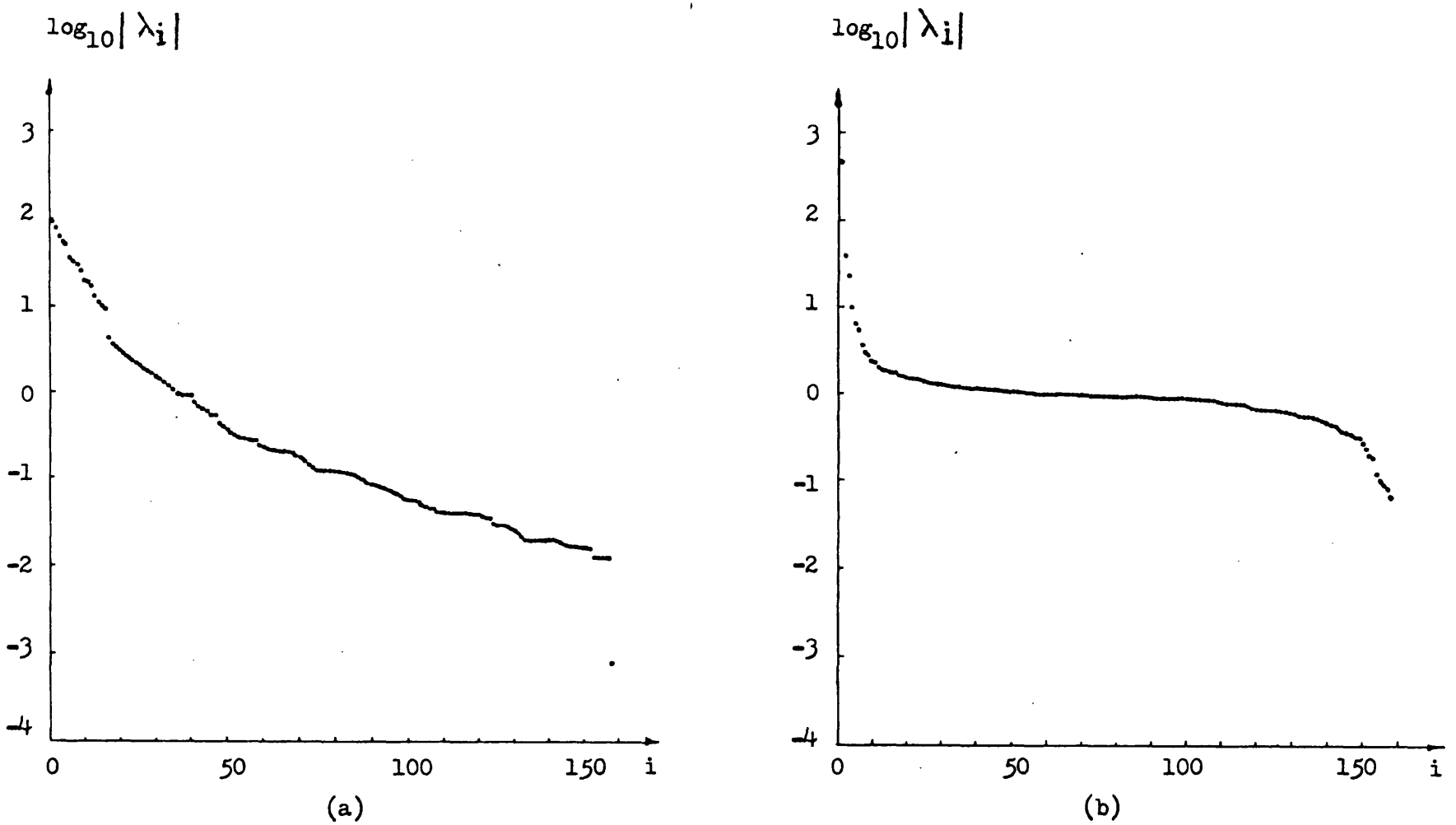

Fig. 3.4 Eigenvalue spectra of the normalized coefficient matrix for the regular 158 equation problem,
(a) without preconditioning (b) with preconditioning

reduced from 1.22×10^5 to 7.15×10^3. In this case the coefficient matrix is better conditioned with respect to rounding error when preconditioned. This is very important in view of the squaring of the condition number that occurs in the normalized equations.

In general, it has been found that the efficiency of the Choleski type of preconditioning for the mesh field equations depends greatly on the form and dimension of the actual equations. To identify the main problems that can occur in solving any general set of mesh field equations, two important cases are now described.

3.4.4 Solution of equations from an irregular network

The coefficient matrix for the mesh field equations was given in Chapter 2, equation 2.24 as,

$$\begin{array}{|c|c|} \hline C_M^T R C_M & -N \\ \hline -N^T & \frac{-1}{j\omega} C_E^T R C_E \\ \hline \end{array} \qquad (3.15)$$

The square submatrices $C_M^T R C_M$ and $\frac{-1}{j\omega} C_E^T R C_E$ on the diagonal can be expressed alternatively as

$$C_M^T R C_M = C_{MT}^T R_T C_{MT} + R_L \qquad (3.16)$$

$$-\frac{1}{j\omega} C_E^T R C_E = -\frac{1}{j\omega}\left[C_{ET}^T R_T C_{ET} + R_L\right] \qquad (3.17)$$

where C_{MT} and C_{ET} are the parts of the branch-mesh matrices which deal only with tree branches in the magnetic and electric circuits respectively (see Chapter 2, section 2.7.4). R_T and R_L are the diagonal reluctance matrices for the tree and link branches respectively in the magnetic circuit. Similarly, R_T and R_L are the resistance matrices for the tree and link branches in the electric circuit.

In expressions 3.16 and 3.17 the submatrices have been split into a tree part and a link part. All reluctance and resistance values are positive, so the tree parts are square matrices with positive diagonal elements, the magnitude of which cannot be less than any of the off-diagonal elements[38]. The link parts are seen to be diagonal matrices with positive elements. The effect of the link parts of the submatrices, defined in 3.16 and 3.17, on the complete matrix 3.15 is therefore to strengthen the main diagonal. This means that for any row, the magnitude of the diagonal element a_{ii} is increased relative to the sum of the moduli of the off-diagonal elements, a_{ij}, $j \neq i$. It should be noted that in the following discussion the term "strong diagonal" does not require the usual definition of diagonal dominance[24] ($a_{ii} > \sum_{j \neq i} |a_{ij}|$, $i = 1,n$) to be satisfied rigorously. It is sufficient for this condition to be approached for the diagonal to be termed strong. The term "weak diagonal" is also used when the conditions for diagonal dominance are far from being satisfied.

If the linked network field model is irregular, in such a way that the tree branches generally have smaller reluctances and resistances than the link branches, then from the splitting of the submatrices 3.16 and 3.17, it can be seen that this type of irregularity in the network model strengthens the diagonal of the coefficient matrix. When this is the case, the equations are better conditioned for solution by conjugate gradients. In particular the partial decomposition used for preconditioning is more accurate because the effect of neglecting fill-in, which only occurs in off-diagonal positions, is reduced. This is demonstrated with the test linked network model used in the previous sections.

The equations from a regular network model have already been solved and the results presented. The network model is made irregular, with "small trees", by halving the reluctance and resistance of the tree branches in the magnetic and electric circuits respectively. The eigenvalue spectra of the resultant coefficient matrix without and with preconditioning are given in Fig.3.5. Comparing these with the corresponding spectra for the regular network (Fig. 3.4) shows that the equations without preconditioning are slightly better conditioned for the small tree network. The overall condition number has been reduced from 1.22×10^5 to 3.16×10^4. With preconditioning, the majority of the eigenvalues of the small tree coefficient matrix are only slightly closer to unity than those of the regular case (Fig.3.4(b)). Most important, however, the extreme eigenvalues are much closer to unity. As a result the overall condition of the preconditioned matrix is reduced from 7.15×10^3 for the regular network to 24.54 for the irregular network. The preconditioning for the small tree mesh field equations is thus shown to reduce the condition number of the coefficient matrix by a factor of approximately 1300. For the regular network the corresponding reduction in condition number is only a factor of 17. This confirms that the preconditioning is more effective when the coefficient matrix has a stronger diagonal, as is the case with the small tree network.

The effect of the more accurate preconditioning on the convergence properties of the conjugate gradient algorithm are now demonstrated. The convergence graphs of $\log_{10} \frac{|r_i|}{|r_0|}$ for the solution of the small tree network model, using a double precision algorithm without and with preconditioning, are given in Fig. 3.6. This shows that the preconditioned algorithm converges very fast with no oscillation of the residual.

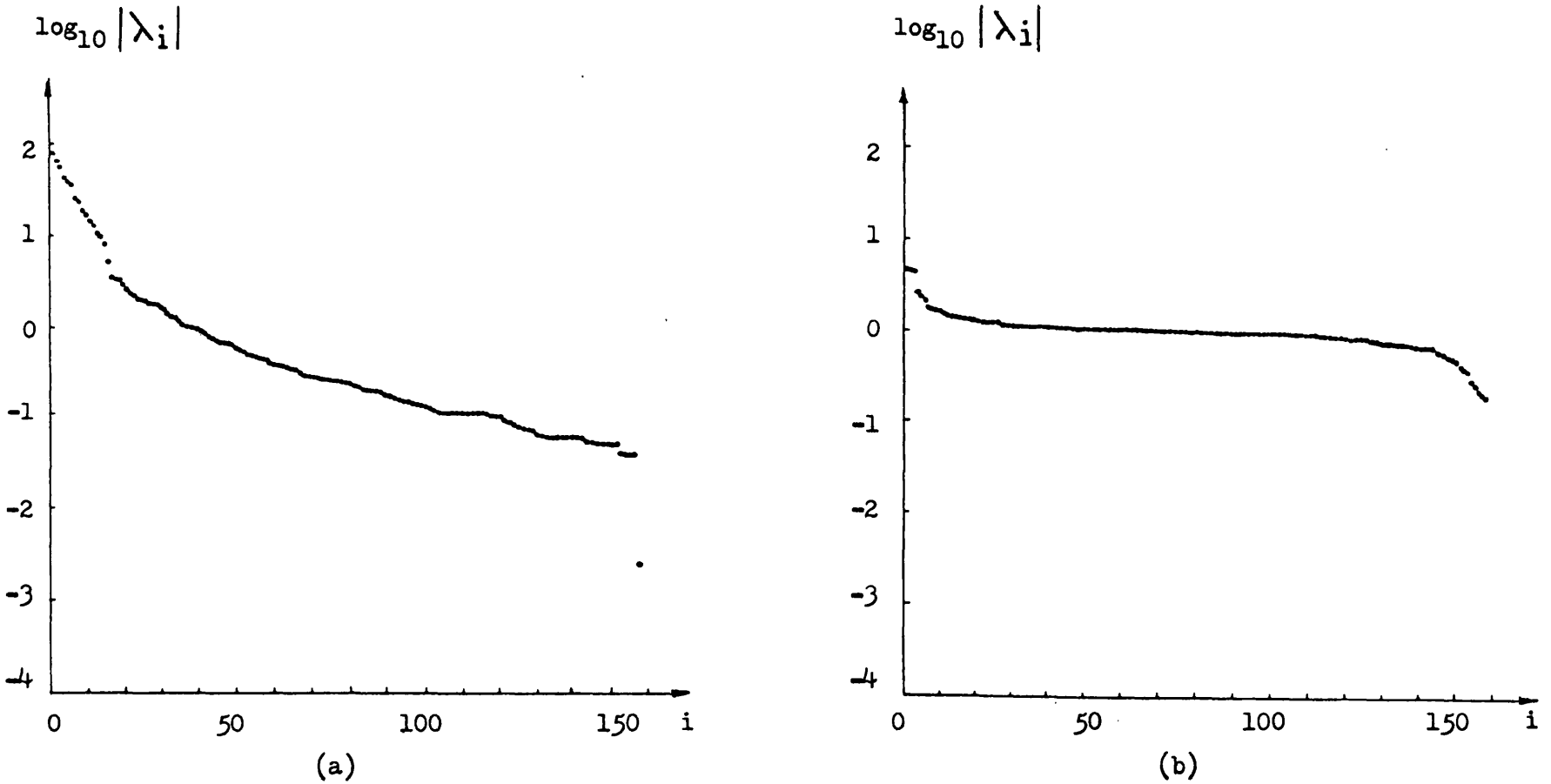

Fig. 3.5 Eigenvalue spectra of the normalized coefficient matrix for the "small tree" 158 equation problem, (a) without preconditioning (b) with preconditioning

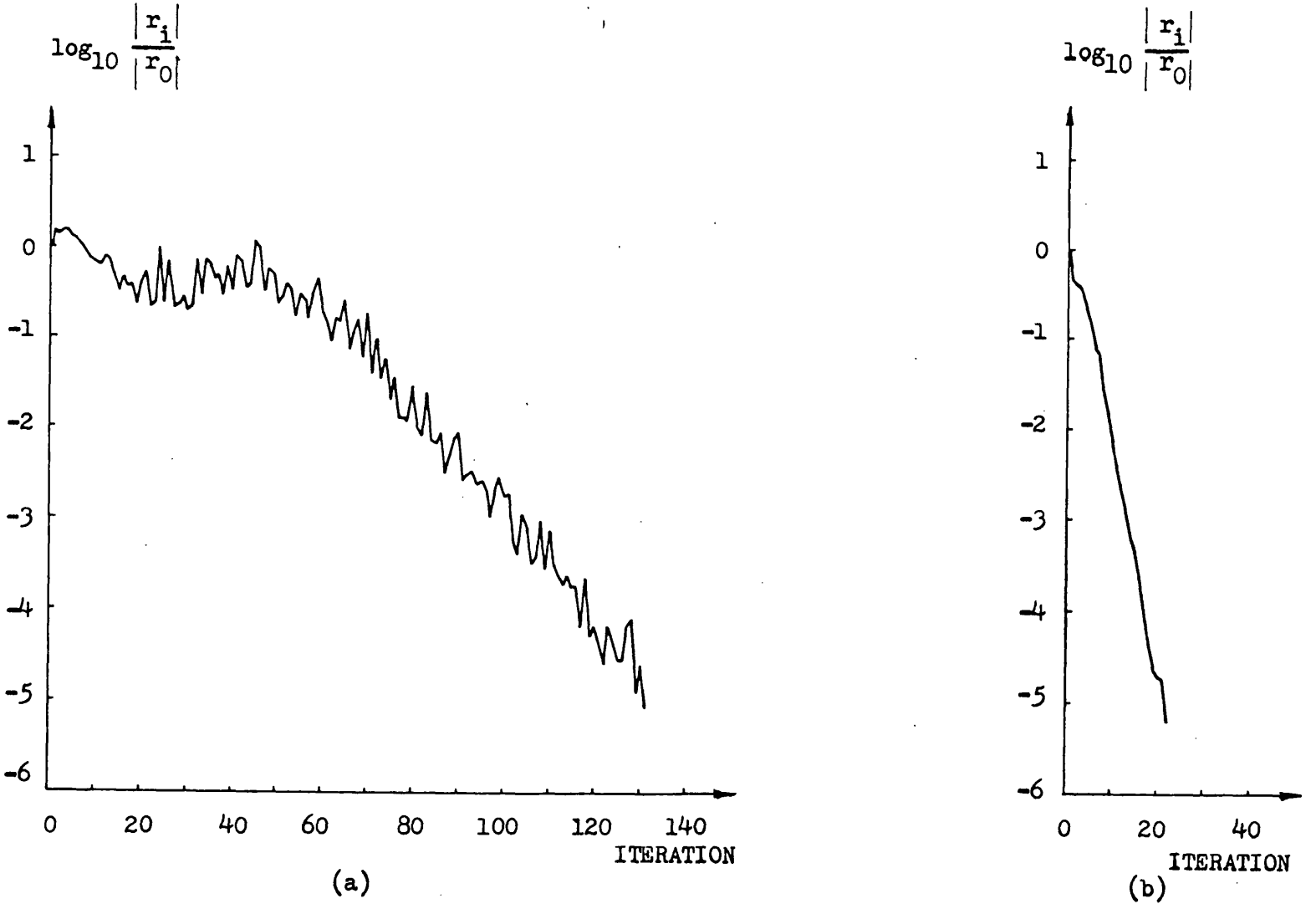

Fig. 3.6 Convergence graphs, using double precision work vectors, for solution of the "small tree" 158 equation problem, (a) without preconditioning (b) with preconditioning

The algorithm is therefore well conditioned with respect to rounding error. This is an important factor which helps convergence to be fast. A comparison of the convergence graphs in Fig. 3.6, with the corresponding results for the regular network model, Fig. 3.3, shows that the improvement in convergence rate as a result of preconditioning is greatest for the small tree network. The use of a small tree network is therefore shown, in this case, to give a substantial improvement in the performance of the preconditioned conjugate gradient algorithm when solving the mesh field equations. This has been found to be true in general, with the degree of improvement in performance depending on the number of tree branches that are small and their relative magnitude.

In the irregular network model, if the branches with the largest reluctance or resistance are tree branches then the coefficient matrix tends to have a weak diagonal. The effect of neglecting fill-in in the approximate decomposition may then become significant. The degree to which this can affect the efficiency of the preconditioning when solving a "large tree" network is demonstrated, again using the test linked network model from the previous sections. For the large tree case the reluctances and resistances of all tree branches in the linked network model are doubled. The eigenvalue spectra of the resultant coefficient matrix without and with preconditioning are given in Fig. 3.7. That for the coefficient matrix of the regular network equations, without preconditioning, is given in Fig. 3.4(a). When this is compared with Fig. 3.7(a), it can be seen that without preconditioning, the equations from the large tree network are only slightly more poorly conditioned than those from the regular mesh. The condition number is increased from 1.22×10^5 to 4.59×10^5. Fig. 3.7(b) shows that the preconditioning for the large tree network has brought the majority of

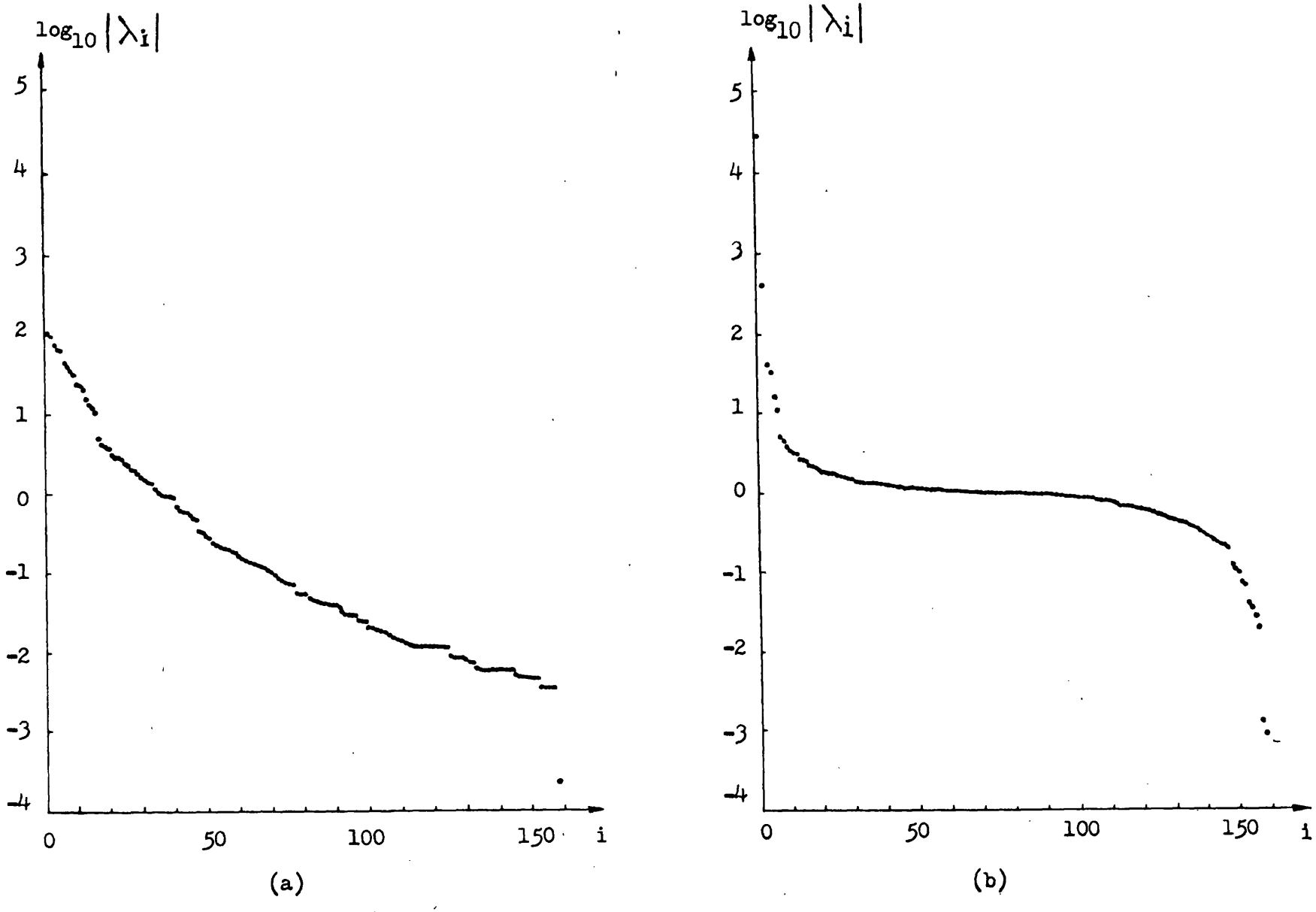

Fig. 3.7 Eigenvalue spectra of the normalized coefficient matrix for the "large tree" 158 equation problem, (a) without preconditioning (b) with preconditioning

the eigenvalues of the coefficient matrix close to unity. These are only slightly further from unity than those of the regular network (Fig. 3.4(b)). The extreme eigenvalues however depart greatly from unity. As a result the overall condition number of the matrix is increased from 4.59×10^5 to 3.22×10^7 by the preconditioning. Nevertheless, the bulk of the eigenvalues are close to unity. In view of Stewart[35] and Kershaw's[34] experience that the conjugate gradient algorithm quickly eliminates the effect of any extreme eigenvalues and then proceeds as if they were not present, it might be expected that the preconditioned algorithm should still perform well.

A solution of the preconditioned large tree equations was attempted with the double precision algorithm. The performance was very poor and the convergence erratic. Violent oscillation of the residual showed that rounding error, due to the overall poor condition of the matrix, was too great for the algorithm to function properly. Quadruple precision was therefore used to reduce rounding error. A comparison of the convergence graphs of $\log_{10} \frac{|r_i|}{|r_0|}$ for solution of the large tree mesh field equations, without and with preconditioning is given in Fig. 3.8. This shows that even with quadruple precision the preconditioned algorithm is still dominated by rounding error and as such it does not converge much faster or more reliably than the algorithm without preconditioning. It is evident that, in this case, the spreading of the extreme eigenvalues of the coefficient matrix by the preconditioning has made the preconditioned algorithm so poorly conditioned with respect to rounding error that it is unable to take advantage of the otherwise near unity eigenvalue spectrum. In view of this fact, the increased work per iteration and the increased storage of the preconditioned algorithm, it is concluded that these large tree equations are better solved without preconditioning.

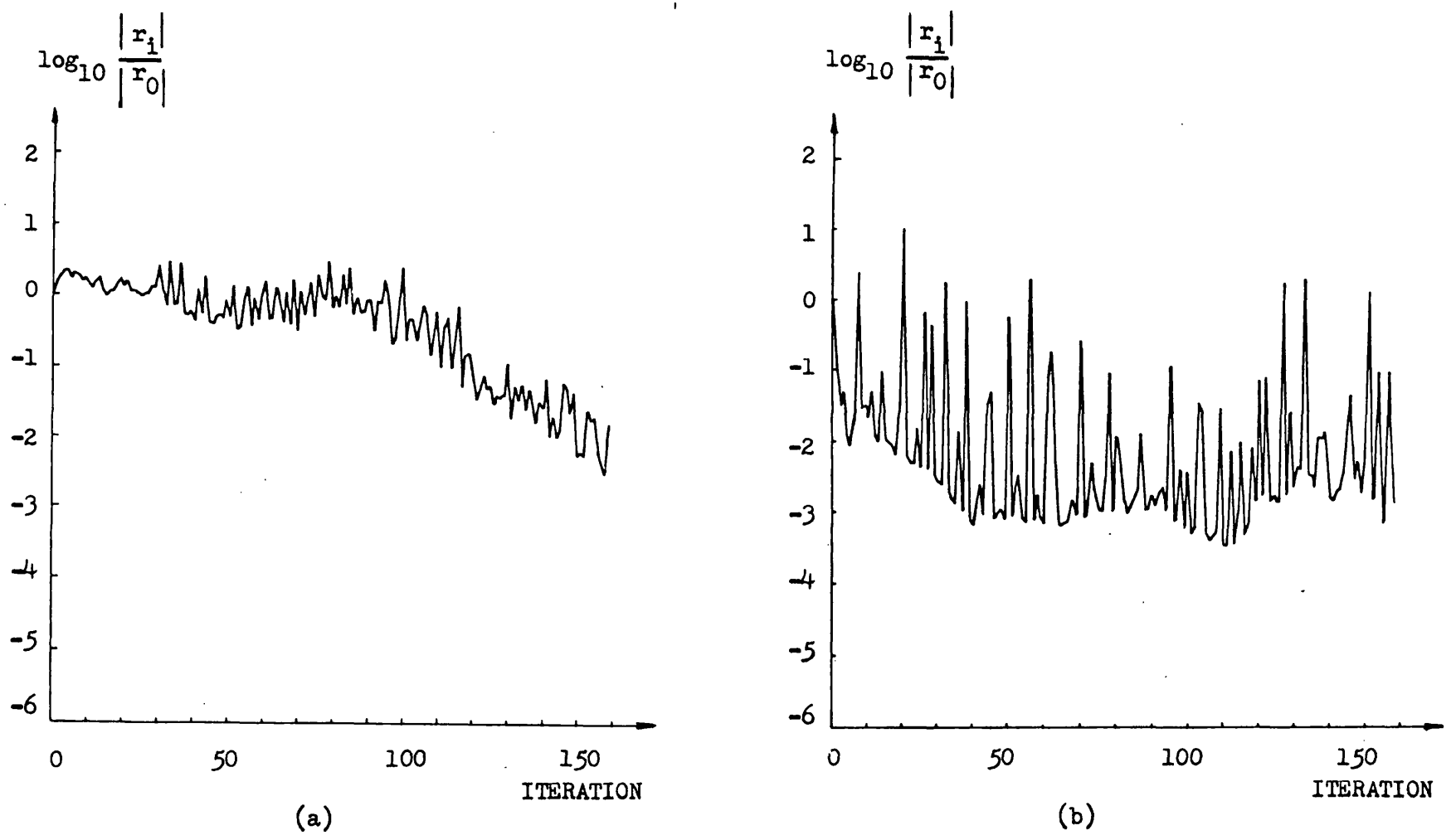

Fig. 3.8 Convergence graphs, using quadruple precision work vectors, for solution of the "large tree" 158 equation problem, (a) without preconditioning (b) with preconditioning

In general, for the mesh field equations of problems in which a few or all the tree branches are large in comparison to the links, the weakening of the diagonal results in a less accurate partial decomposition than if the network were regular. The preconditioned algorithm 3.12 solves the normalized system of equations for which the preconditioned system matrix is $(L^{-1}AL^{-T})^{T}(L^{-1}AL^{-T})$. The eigenvalue spectrum for this matrix is the square of that for the basic preconditioned system matrix $(L^{-1}AL^{-T})$. It has been shown that a severe spreading of the extreme eigenvalues of the normalized system is a possible consequence of preconditioning if the partial decomposition is inaccurate. This effect is obviously accentuated by the eigenvalue squaring in the normalized system. This can make the overall condition of the normalized, preconditioned coefficient matrix very poor. When this is the case, it has been shown that the conjugate gradient algorithm is very susceptible to the build up of round-off error. For this reason the success of incomplete Choleski preconditioning with the normalized system algorithm 3.12 is very dependent on the accuracy of the partial decomposition.

3.4.5 Solution of a larger network

In all field solutions yet attempted by the linked network method the trees of the equivalent circuits have been predominantly "radial", consisting of a number of "limbs" such as that shown in Fig. 3.9.

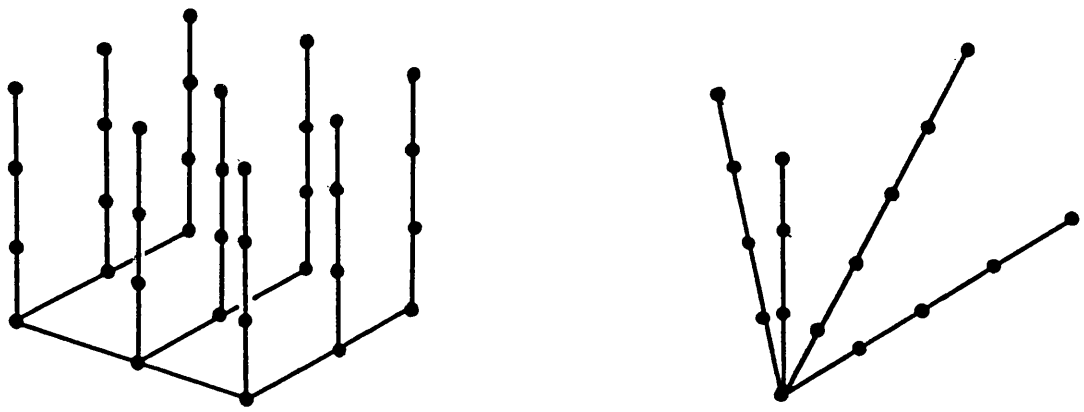

Fig. 3.9 Typical forms of tree used at present in the linked network solution

If this type of tree is used and the network is made larger, for example when solving the same problem with a smaller network interval, the tree has the same form but it may have more limbs and each limb may contain more branches. Obviously, the larger network requires the solution of more equations. When the preconditioned conjugate gradient algorithm is used to solve the larger set of equations it has been found that its performance can be much worse than that for the smaller problem. To demonstrate this effect and the factors believed to cause it, the test problem (Fig. 3.1) solved previously with a 4 x 4 x 4 regular network, is re-solved using a 6 x 6 x 6 regular network. This increases the number of equations from 158 to 569.

It has been found that the coefficient matrix from a larger network generally has more off-diagonal elements per row. The net effect is to weaken the diagonal. As already seen, this can greatly reduce the accuracy of the partial decomposition. In the solution of the equations the coefficient matrix is scaled to have unity diagonal elements. The average value of the sum of the magnitude of the off-diagonal elements increases from 8.13 with the small network to 13.41 with the large network. There is therefore a considerable weakening of the diagonal in this case when the larger network is used.

When the size of the coefficient matrix increases it has also been found that, even though there may be a few more off-diagonal elements per row, the matrix becomes more sparse. This means that there is a lower percentage of non-zero elements and the sparsity coefficient 's' decreases, where

$$s = \frac{\text{Total number of non-zero elements}}{\text{Total number of elements}}$$

There is then the possibility that more fill-in is neglected in the partial decomposition, which is subsequently less accurate. In the test problem the sparsity coefficient decreases from 0.085 for the small matrix to 0.044 for the large matrix.

In addition to the possible decrease in the accuracy of the partial decomposition, the conjugate gradient algorithm itself is more susceptible to the build-up of rounding error when the number of equations being solved is increased.

A rigorous examination of the performance of the conjugate gradient algorithm with larger systems really requires that the eigenvalues of the preconditioned system matrix are calculated as in the previous sections. The NAG routine F02AJF, used to calculate the eigenvalues, requires the complete matrix to be formed totally in core. This was not possible for the large coefficient matrix because the storage required was far greater than that available. The following method was however used to give some indication of the accuracy of the partial decomposition and hence the eigenvalue spectrum of the preconditioned matrix.

The product $I' = L^{-1}AL^{-T}I$, where I is the identity matrix, was formed by columns using forward substitution, sparse matrix multiplication and backward substitution routines. I' is then the preconditioned coefficient matrix of the basic system. The eigenvalues of this matrix are the square root of those for the normalized coefficient matrix with preconditioning. When the decomposition is exact, I' should be equal to I, with unity eigenvalues. When the decomposition is approximate, I' is not exactly equal to a unit matrix. The diagonal elements may differ from unity and the sum of the magnitude of the off-diagonal

elements of each column may not be zero. The error in these factors for each column of the matrix gives some idea of the accuracy of the partial decomposition. If they are generally small, the decomposition is accurate and the majority of the eigenvalues of I' should be close to unity. Conversely, if the errors in the diagonal elements and the off-diagonal sums are large then the decomposition is inaccurate. The eigenvalue spectrum of I' may not then be close to unity. This method does not give a quantitative measure of accuracy, but it can be used to detect any marked improvement or deterioration in the accuracy of the partial decomposition and hence the nature of the eigenvalue spectrum for the preconditioned coefficient matrix.

The error profiles for the diagonal elements and the off-diagonal sums of I' for the "small" coefficient matrix from the 4 x 4 x 4 problem are shown in Fig. 3.10. The length of the bars in the graphs gives the magnitude of the error. The profiles show that the majority of the diagonal elements are close to unity and the majority of the off-diagonal sums are small. This indicates that the partial decomposition is accurate. The majority of the eigenvalues of I' should therefore be close to unity. This is verified by the eigenvalue spectrum, Fig. 3.11, which could be calculated as a check in this case.

The error profiles for the diagonal elements and off-diagonal sums of I' for the "large" 6 x 6 x 6 problem are given in Fig. 3.12. To aid comparison, the same vertical scale has been used as that for the profiles from the small problem. This has only been possible by marking all results larger than 100 in the 6 x 6 x 6 problem as > 100. Some of these values are actually in excess of 10^5. A comparison of these profiles, Fig. 3.12, with those for the small network, Fig. 3.10, shows that the overall error in the diagonal elements and off-diagonal

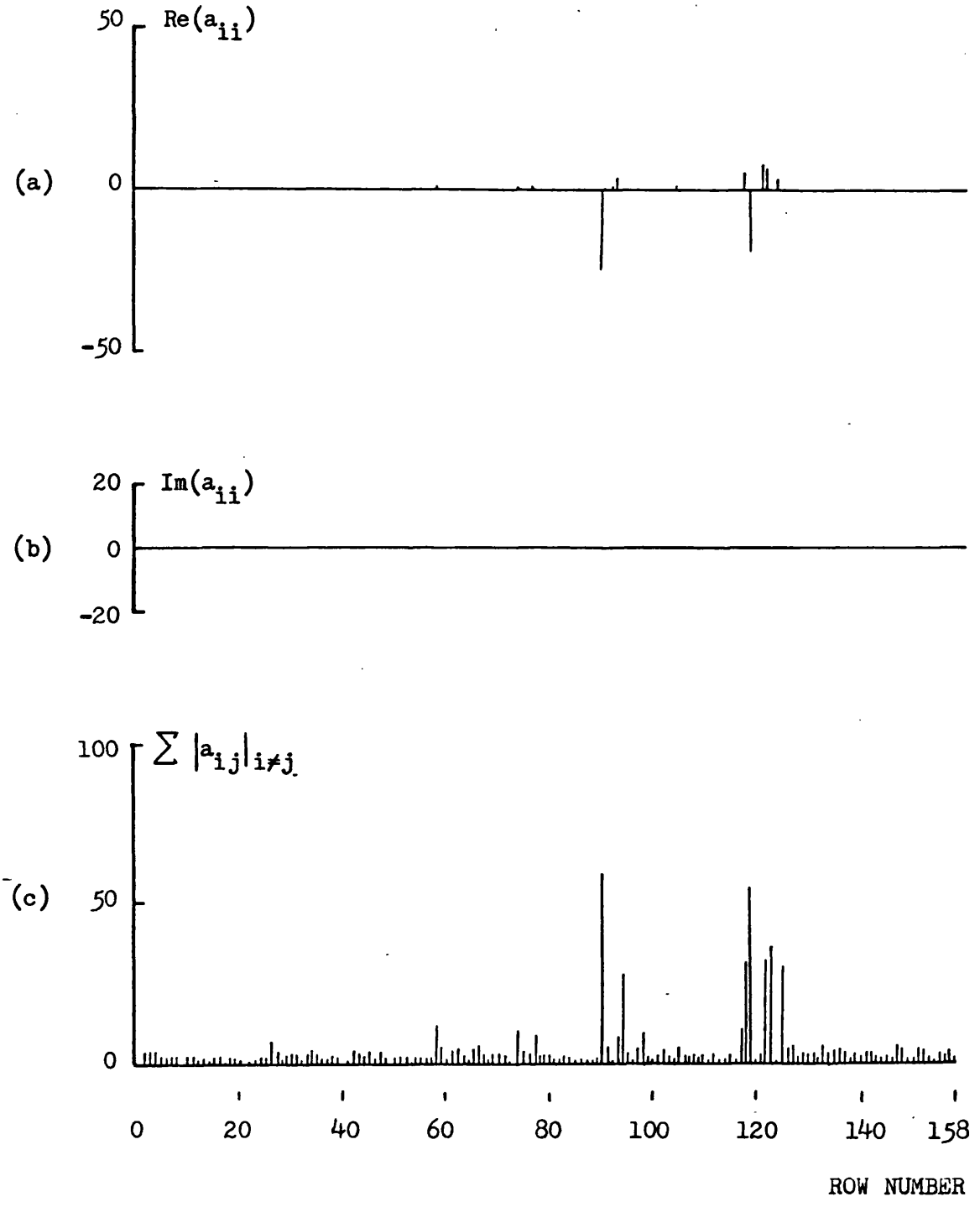

Fig. 3.10 Error profiles of I' for the regular 4x4x4 network problem.
(a) real part of diagonal elements
(b) imaginary part of diagonal elements
(c) sum of magnitude of off-diagonal elements

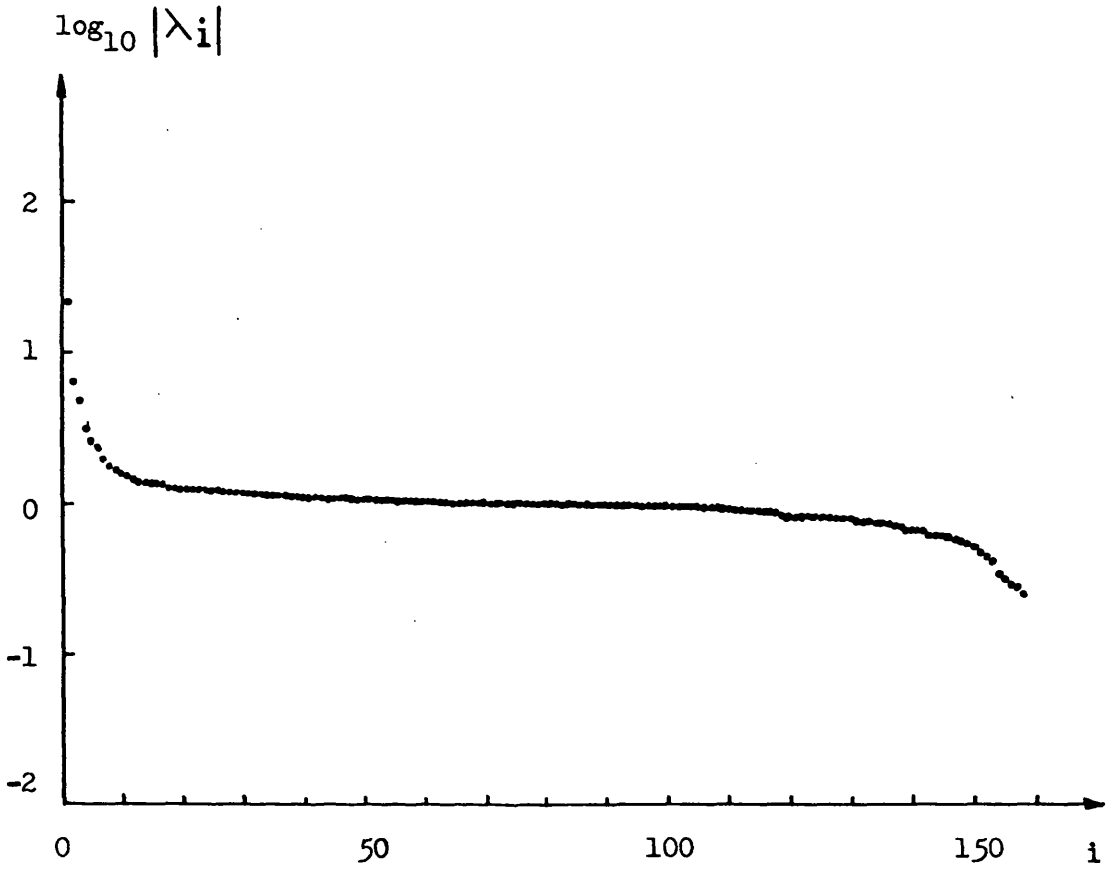

Fig. 3.11 Eigenvalue spectrum of I' for regular 4x4x4 network problem.

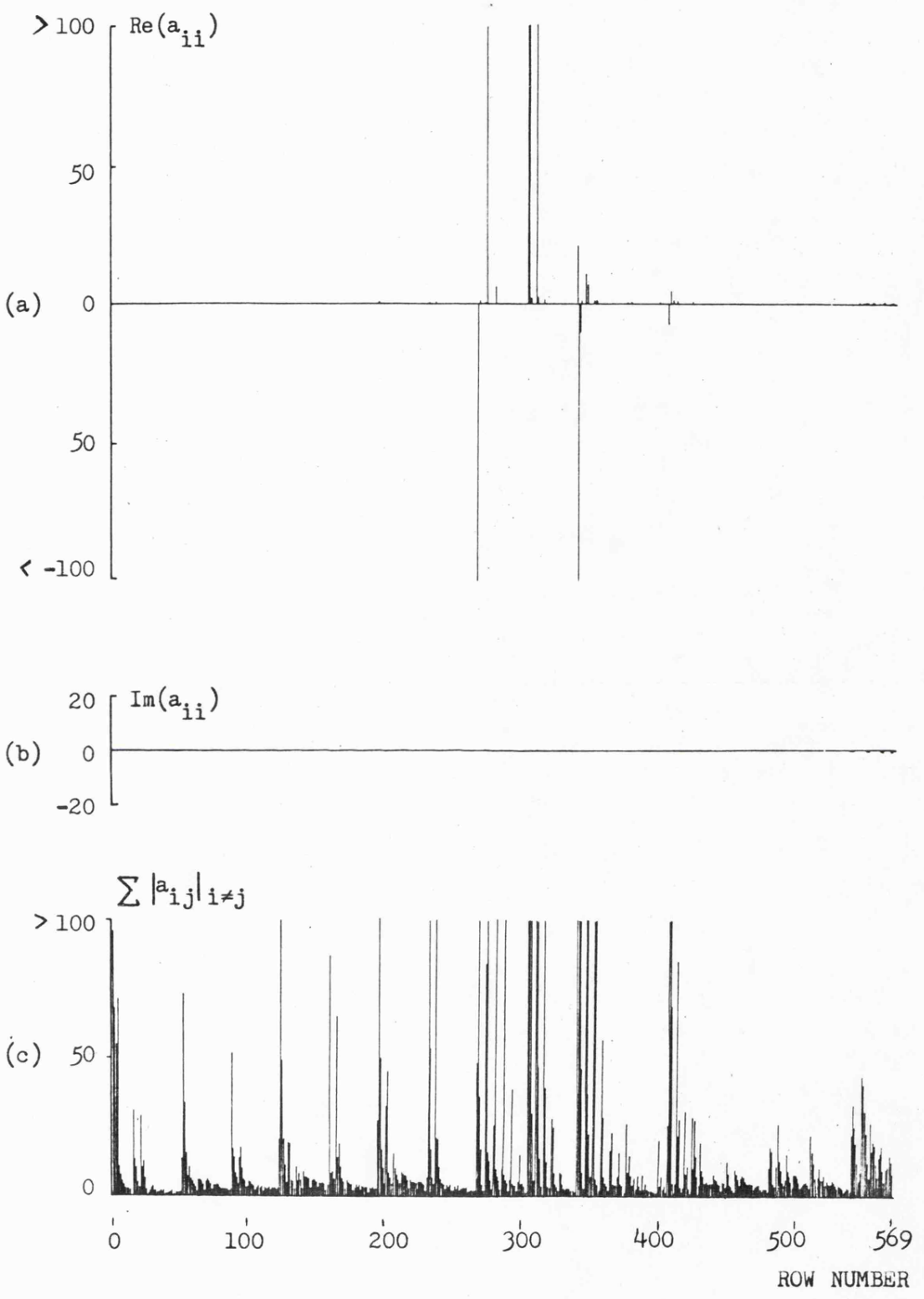

Fig. 3.12 Error profiles of I' for the regular 6x6x6 network problem.
(a) real part of diagonal elements
(b) imaginary part of diagonal elements
(c) sum of magnitude of off-diagonal elements

sums of I' is greatest for the large network. This indicates that the partial decomposition is least accurate with the larger system of equations. The eigenvalue spectrum of I' for the large problem is not therefore expected to be as close to unity as that for the small problem.

The convergence graphs for the solution of the small and large sets of equations by the double precision version of the preconditioned conjugate gradient algorithm are given in Fig. 3.13. The effect of less accurate preconditioning and greater rounding error on the performance of the algorithm in the case of the large problem is clearly shown in this comparison. The residual in the solution of the large problem is highly oscillatory. This indicates the presence of much rounding error. Convergence is erratic and the tolerance of $TOL = 1.0 \times 10^{-5}$ is not reached, even after the theoretical maximum number of iterations $n = 569$. This contrasts with the solution of the small problem which converges to a tolerance of $TOL = 1.0 \times 10^{-5}$ in less than half the theoretical maximum number of iterations $n = 158$. It is therefore concluded that with the large problem the incomplete Choleski preconditioning with no fill-in is not sufficiently accurate to get a satisfactory performance from the conjugate gradient solution.

As already discussed, all solutions of mesh field equations yet attempted have been formulated using a radial type tree. The preconditioned conjugate gradient algorithm has always performed poorly when solving a "large" regular mesh, as shown by the test example. No investigation has yet been made into the use of different shapes of tree. The shape of the tree defines the mesh variable paths and hence the form of the coefficient matrix for the mesh equations. It may

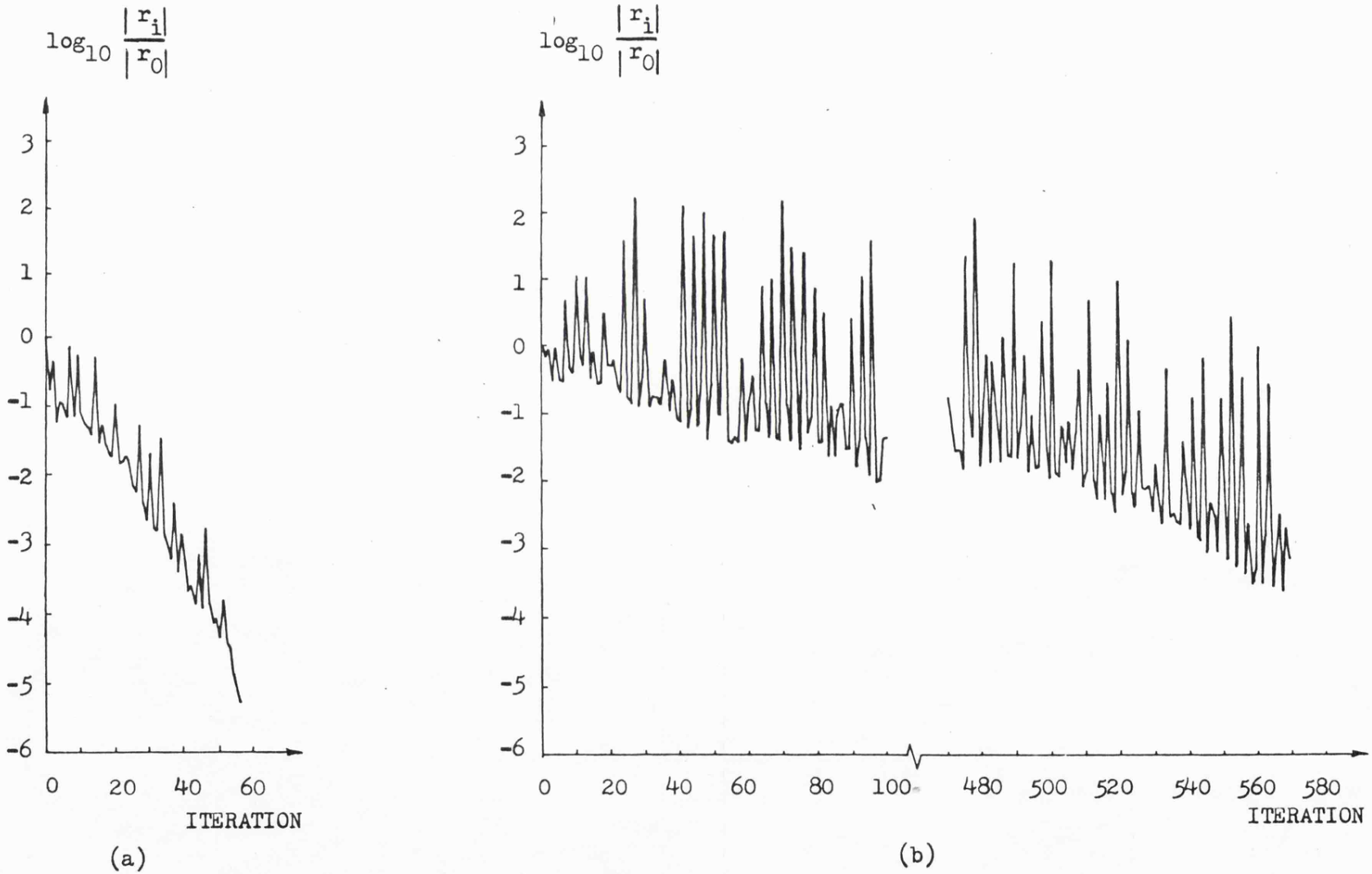

Fig. 3.13 Convergence rates, using double precision work vectors, for solution of the regular 4x4x4 and 6x6x6 problems.

therefore be possible to find a better choice of tree that would not lead to a deterioration in the performance of the preconditioned conjugate gradient algorithm when solving a larger network. The main requirement for such a tree is believed to be that the number of branches in the individual closed paths, defined by the tree, should not increase with the size of the network.

At present, to maintain a good performance in the preconditioned conjugate gradient algorithm when solving large network problems, the network interval in one co-ordinate direction is made slightly less than that in the other two co-ordinate directions. As far as possible, the branches of lowest reluctance and resistance are chosen to be tree branches. If the network is already irregular, through the geometry or material properties of the problem, the branches of lowest reluctance and resistance are always chosen to be trees. This helps to preserve the strength of the diagonal of the coefficient matrix and hence maintain the good performance of the algorithm as described in section 3.4.4. As an example, the regular 6 x 6 x 6 linked network model has been re-solved with the network interval along one co-ordinate direction 30% less than that in the other two co-ordinate directions. The convergence graph for solution by the double precision algorithm is given in Fig. 3.14. A comparison of this figure with the corresponding convergence graph for the regular network (Fig. 3.13(b)) shows that with the branches of lowest reluctance and resistance chosen, as far as possible, to be tree branches, even a small irregularity in the network can greatly improve the performance of the preconditioned conjugate gradient algorithm in solving a large set of mesh field equations.

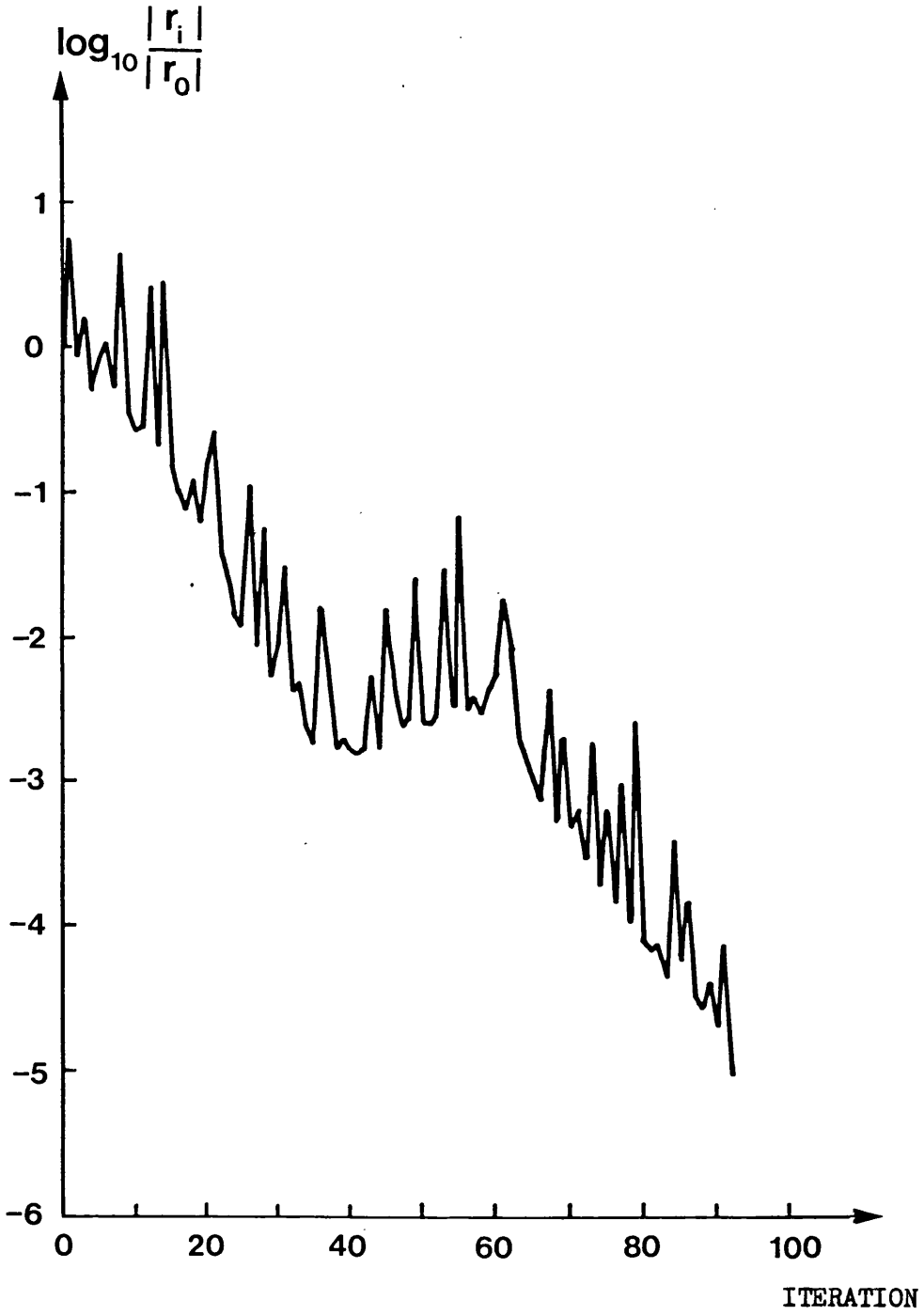

Fig. 3.14 Convergence graph, using double precision work vectors, for solution of the 6x6x6 problem with 30% reduction in the network interval in one co-ordinate direction.

3.5 Conclusions

A preconditioned conjugate gradient algorithm has been described for the solution of large sets of complex linear simultaneous equations in which the coefficient matrix is symmetric but need not have any other special properties. The algorithm solves the normalized system of equations and the preconditioning used is of the incomplete Choleski type with no fill-in. The application of this algorithm to the solution of the mesh field equations has been investigated.

With accurate preconditioning, the solution of the mesh field equations by the conjugate gradient algorithm is fast and efficient, requiring only a fraction of the theoretical maximum number of iterations. The preconditioning has been shown to be most accurate when the diagonal of the coefficient matrix is strong. With a radial type of tree, as used in formulating the mesh field equations, the diagonal of the coefficient matrix is weakened as the number of equations to be solved increases. For the equations from a regular network the preconditioning is sufficiently accurate for "small" systems up to 200-300 equations. In larger systems of equations from a regular network the partial decomposition can become too inaccurate for the preconditioning to be effective. This is due mainly to the weakening of the diagonal in the larger system.

In terms of the mesh field equations, the diagonal of the coefficient matrix is strongest when the tree branches are small in comparison to the links. The performance of the conjugate gradient algorithm in solving large sets of mesh field equations can be greatly improved, if instead of using an exactly regular network, the network interval is made slightly smaller in one co-ordinate direction. The branches in

this direction are then chosen, as far as possible, to be tree branches. Alternatively, if the network is already irregular through the geometry or material of the problem, the branches of smallest reluctance and resistance are chosen to be trees. This strengthens the diagonal of the coefficient matrix. It has been shown that even a small irregularity in the network can be used in this way to produce a significant improvement in the performance of the preconditioned conjugate gradient algorithm.

The algorithm described has been used successfully for the solution of all mesh field equations yet encountered. Its main disadvantage is that it solves the normalized system of equations. This squares the condition number of the coefficient matrix and hence increases rounding error and slows convergence. There exists an algorithm called bi-conjugate gradients[39], which initial studies show to be capable of solving the mesh equations without having to square the condition number of the coefficient matrix. It does, however, require storage for three additional n-dimensional work vectors, where n is the dimension of the system of equations. The algorithm is given in Appendix 2. Provided that the increased storage is acceptable this algorithm should reduce solution times significantly. This is of particular benefit when solving very large systems, where the build up of round-off error has been shown to be a problem with the algorithm for the normalized system.

CHAPTER 4

EXPERIMENTAL VERIFICATION OF THE NETWORK METHOD

4.1 Introduction

The theory developed for the numerical calculation of three-dimensional electromagnetic fields must be verified. One method of verification is to compare the numerical calculations with an analytical solution. Unfortunately it is very difficult to find a problem which can be solved analytically, yet is sufficiently general to fully test the numerical method. Alternatively, the numerical calculations can be compared with experimental measurements. It was found that although many problems have a truly three-dimensional electromagnetic field, no suitable measurements were available against which the calculations could be checked. It was therefore necessary to build a test model from which three-dimensional field measurements could be taken.

In this chapter the test model is described. A comprehensive set of measurements are then given and compared with corresponding calculations from the three-dimensional linked network field model.

4.2 Description of the test model

The test model built to produce the three-dimensional field problem is shown in Plate 1 and diagrammatically in Fig. 4.1. The main magnetic circuit is similar in construction to a three limb transformer. Excitation coils on the two outer limbs drive flux through the centre limb. This limb contains a large gap in which an iron box is placed symmetrically, as shown in Fig. 4.1(a). The centre

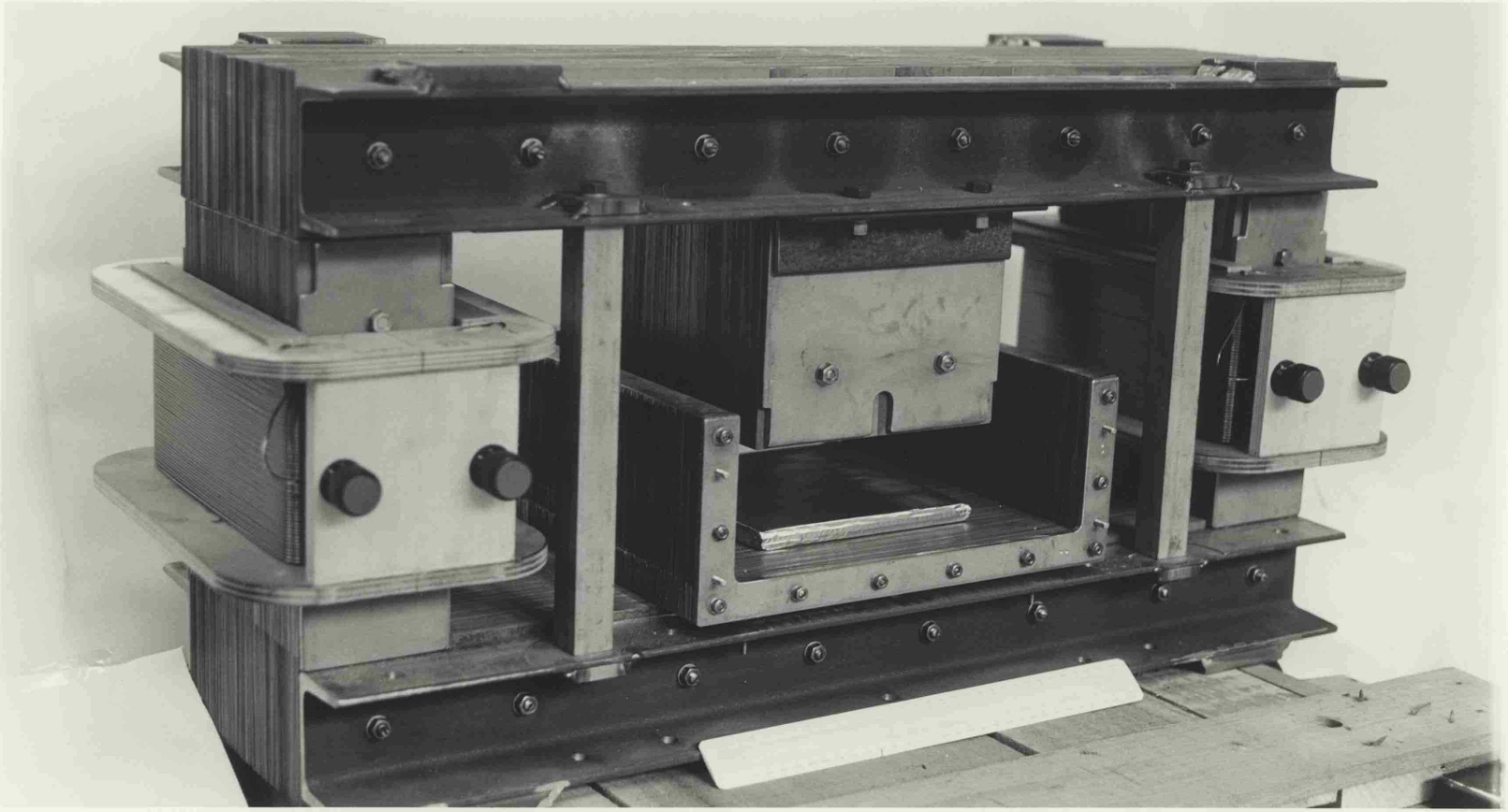

Plate 1 The test model

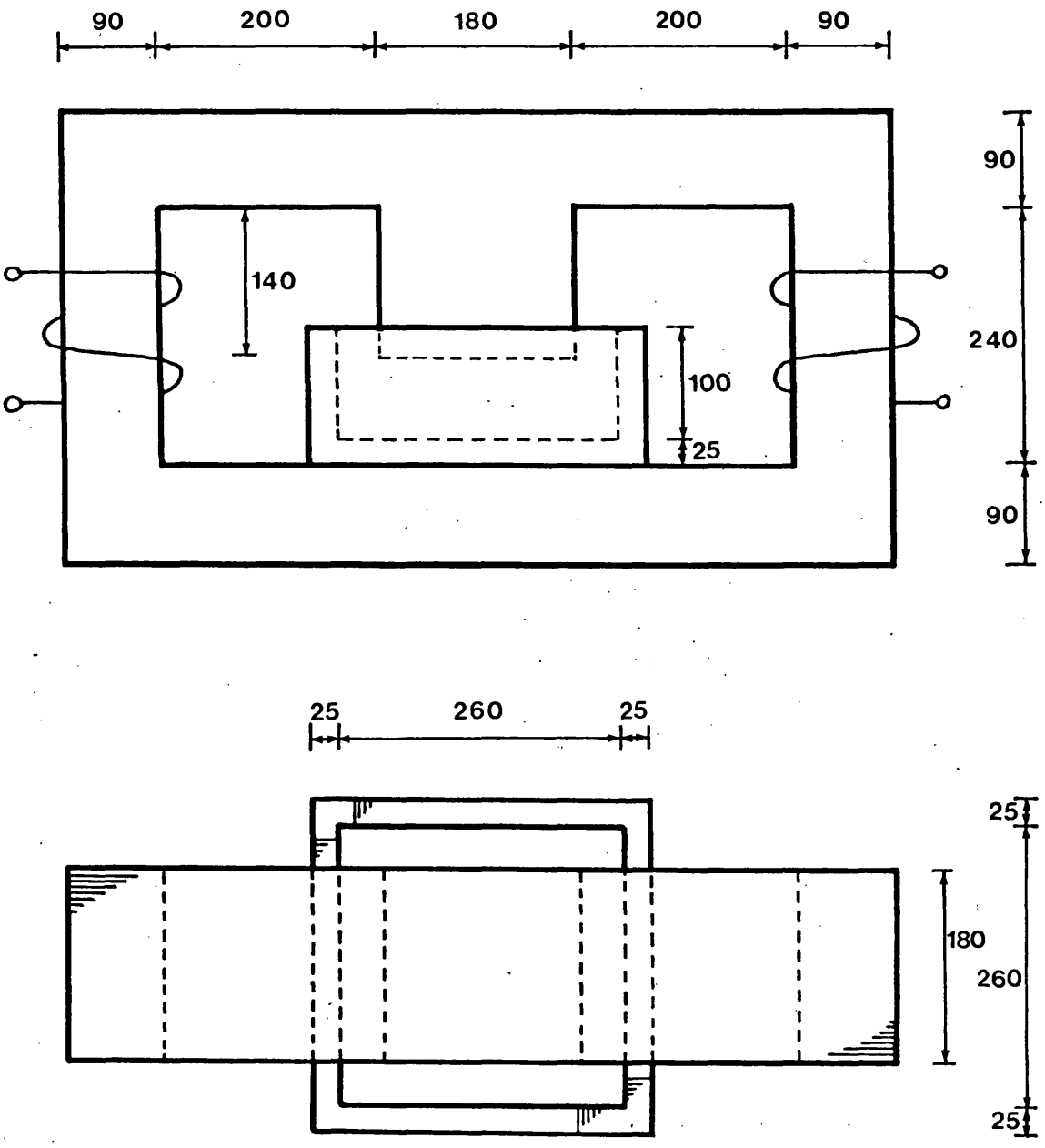

dimensions in millimetres

(a)

Fig. 4.1 Diagram of the experimental apparatus.
(a) the full model
(b) field region to be modelled

(b) over

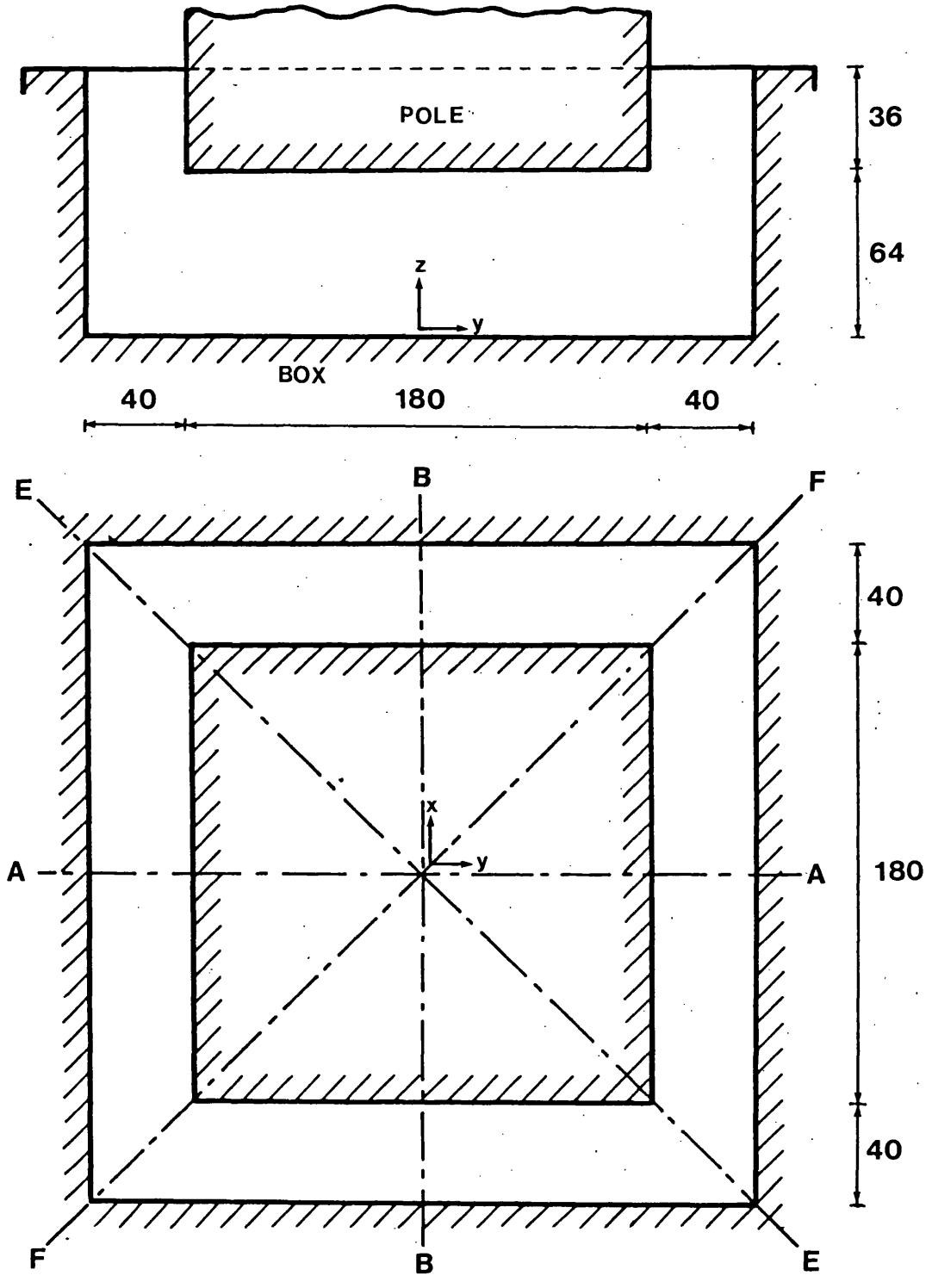
POLE
36
64
z
y
BOX
40
180
40
E
B
F
40
x
y
A
A
180
40
F
B
E
dimensions in millimetres
IRON

(b)

limb then acts as an iron pole protruding into an iron box as shown in Fig. 4.1(b). The pole and iron box, in which samples of solid conductor are placed, is the field region to be modelled. The sinusoidally excited pole drives flux into the box thereby inducing a three-dimensional electromagnetic field in the interior.

The model has been constructed throughout with laminations, directed as shown in Fig. 4.1(a). The main magnetic circuit is in two parts, a T for the top and centre limb and a U for the base and outer limbs. Stainless steel pillars are used to clamp the two parts together. The laminated box is made in a U shape with two separate ends, removable for access. One end is removed in Plate 1.

The excitation of the model, by two coils of 222 turns each, is difficult because of the large air-gap, across which flux must be driven, in the centre limb. As a consequence the flux density levels obtainable in the model are relatively low. For example at 50 Hz with the coils connected in parallel, 150 volts is required to drive a total current of 7 amps. This gives an average flux density of approximately 20 mT in the iron. At this design level there should be no saturation of the iron in the model.

Several planes of symmetry are shown in Fig. 4.1(b) which divide the field region into eight parts. To get all these planes of symmetry exactly, there would have to be four energizing limbs arranged in plan as a cross with the box in a central limb. This would have been much more difficult and expensive to construct than the two limb version. It is also unnecessary in practice because the high permeability of the iron at the low design flux levels ensures that the iron is an approximate equipotential. The two limb model then represents

adequately all planes of symmetry in Fig. 4.1(b).

The excitation for the theoretical model of the field region is the potential between the pole and box. It was not considered sufficiently accurate to assume that all the mmf produced by the coils is applied between the pole and box. A proportion of the coil mmf must be lost across other smaller gaps in the magnetic circuit. The following procedure was used to set the pole/box potential difference. The planes of symmetry marked in Fig. 4.1(b) show that a line in the z-direction from the exact centre of the pole to the exact centre of the box must be a flux line. The flux density along this line is given by $B = \frac{\mu_o M}{g}$ where M is the mmf between the pole and box, and g is the vertical gap across which the flux is driven. The value of B is calculated for the desired mmf and gap. The excitation of the actual model is increased until this value of z-directed flux density is measured at the exact centre of the pole. The coil current is then correct for an mmf M between the pole and box.

4.3 Measurement details

The three-dimensional electromagnetic field produced by the test model consists of a flux distribution throughout the field region and a current distribution in all conductors within the region. To verify the field calculation method, both flux and current distributions should be measured and compared with corresponding calculations.

The most common method used to measure current density in a conductor is the "J probe" technique. This assumes that the current density is constant between two points a known distance apart. Two contacts are made on the conductor at these points and the voltage (V)

measured between them. If the resistivity (ρ) of the conductor is known, the current density (J) between the two points can be found from $J = \frac{V}{\rho L}$. This expression is derived form Ohm's Law, the definition of resistance ($R = \frac{\rho L}{A}$) and the definition of current density ($J = \frac{I}{A}$), where A is an area.

In the test model low resistivity conductor had to be used to permit an eddy current flow large enough to have a significant influence on the flux density. Even with low resistivity conductor the eddy currents are still relatively small in magnitude. The net effect is that the voltages induced in the conductor are very small. The voltage measurement with the "J probes" is then very prone to error. These arise from contact resistance and voltage induced by the changing flux linking the area enclosed by the probes. This made trial measurements of current density difficult and unreliable. For this reason current density measurements have not been made for the model. Flux density only has been measured. Close interlinkage of the current and flux in the electromagnetic field should ensure that a comparison of measured and calculated flux densities only will provide a reliable check for the calculation technique.

All flux density measurements were made in air space. None were made in the interior of the conductors. Flux density was measured in magnitude (peak) and phase. The magnitude measurements were made using an RFL 750A gaussmeter with a Hall probe of active area 2.00 x 4.75 millimetres. This could not be used for phase measurements because the amplified Hall probe signal was not available for comparison with a phase reference. Phase measurements were made using a 50 turn, 3.2 millimetre diameter and 0.5 millimetre thick search coil, the output of which was amplified. All phase measurements are with reference to the supply current.

In a three-dimensional flux distribution there are three cartesian components of flux density at each point. To permit accurate measurement of any one of these components it is essential that the measuring probe is sensitive only in a direction perpendicular to its active area. Careful positioning of the active area perpendicular to the component being measured is also important, particularly when measuring a small flux density along one axis in the presence of large flux densities on any of the other two axes. In this case a small error in positioning the probe can give large errors due to pick-up from the large flux density directions. Accurate positioning of the probe was achieved by mounting it in a perspex chuck which could slide along a perspex rail fixed in the required position. The rail was calibrated in millimetres.

4.4 Comparison of calculated and measured results

4.4.1 Introduction

In all tests the model was energized to give a 50 Hz sinusoidal mmf of 1000 + j0 AT (peak) between the pole and box. This potential was set for a 64 mm gap, using the procedure described in section 4.2.

Flux density measurements were first made with no conducting material in the box, to show the magnetostatic field produced by the model. Conducting material was then introduced. A thin plate conductor gave an easy to visualize two-dimensional eddy current distribution as an initial check for the calculations. Solid conducting blocks allowed the flow of eddy currents in three dimensions. In this section flux density measurements from these cases are presented and compared with corresponding calculations by the linked network method.

4.4.2 Magnetostatic

When no conducting material is present in the box the field should be magnetostatic with all flux in phase with the supply current. Any eddy currents induced in the iron of the model or elsewhere, if significant, will be apparent by a phase shift in the flux. The magnitude and phase of the flux density was measured in the X, Y and Z directions (see Fig. 4.1(b)) at several sections within the box. These sections were chosen mainly because they give a good representation of the magnetostatic flux in each direction. They also give magnetostatic results in equivalent positions to flux density measurements taken when conductors are present. The magnitude measurements are compared with corresponding calculations in Fig. 4.2 to Fig. 4.8. Phase measurements were all within a degree of zero, and have not been shown.

The Z-directed flux density on the base of the box at Z = 2 mm is shown in Fig. 4.2 and Fig. 4.3. This is seen to be almost constant under the pole and decaying in the region outwith the pole, tending to zero at the edge of the box. Measurements could not be obtained exactly at the edge of the box because of the width of the chuck in which the probe was mounted. The X-directed flux density for X = 80 mm, Z = 20 mm, shown in Fig. 4.4, is similarly almost constant in the pole region and decays to zero at the edge of the box. The Y-directed flux density for Y = 80 mm, Z = 20 mm, is given in Fig. 4.5. This is almost identical to the X-directed flux density in Fig. 4.4, thus confirming the symmetry of the model. The X-directed flux density for X = 120 mm, Z = 20 mm in Fig. 4.6 is included for comparison, in section 4.4.6, with results in the same position when eddy currents are present. The Z-directed flux density just under the pole, Fig. 4.7 and Fig. 4.8, shows the edge effect of the pole corner. That is the flux density is highest at the pole edges. At the centre of the pole the

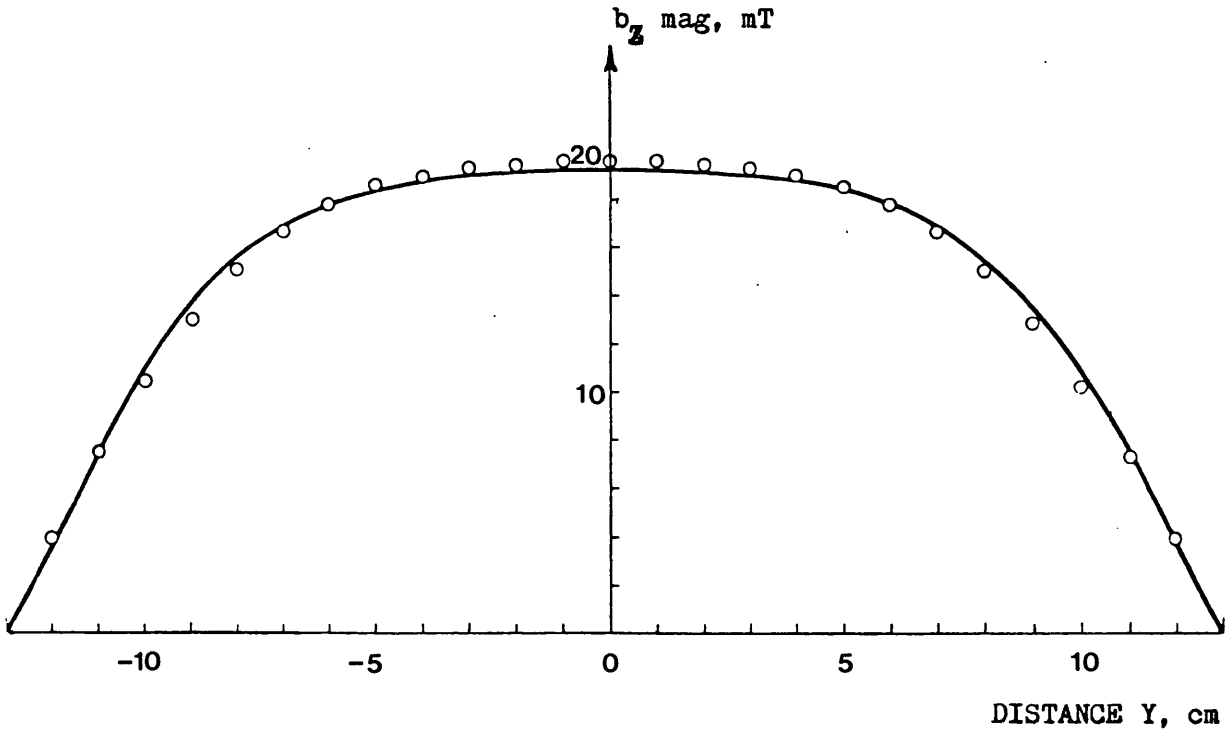

Fig. 4.2 Magnitude of the Z-directed magnetostatic flux density,
X = 0 mm, Z = 2 mm o measured — calculated

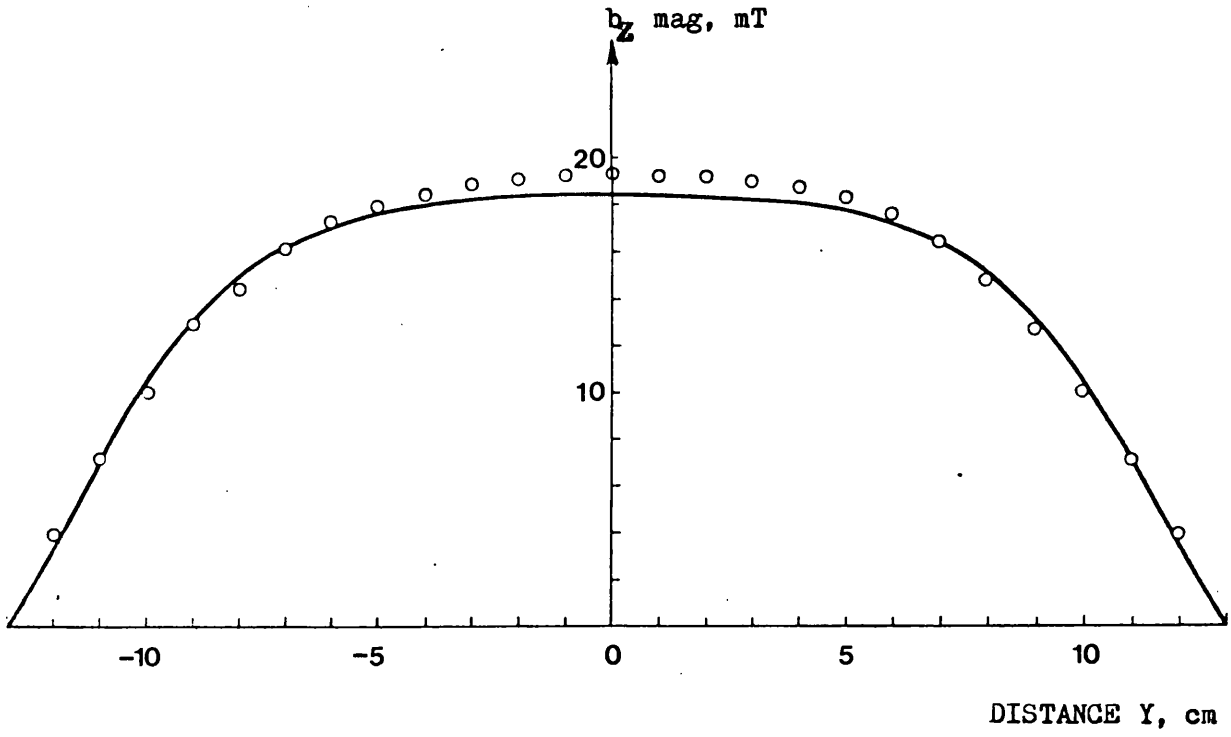

Fig. 4.3 Magnitude of the Z-directed magnetostatic flux density,
X = 50 mm, Z = 2 mm o measured — calculated

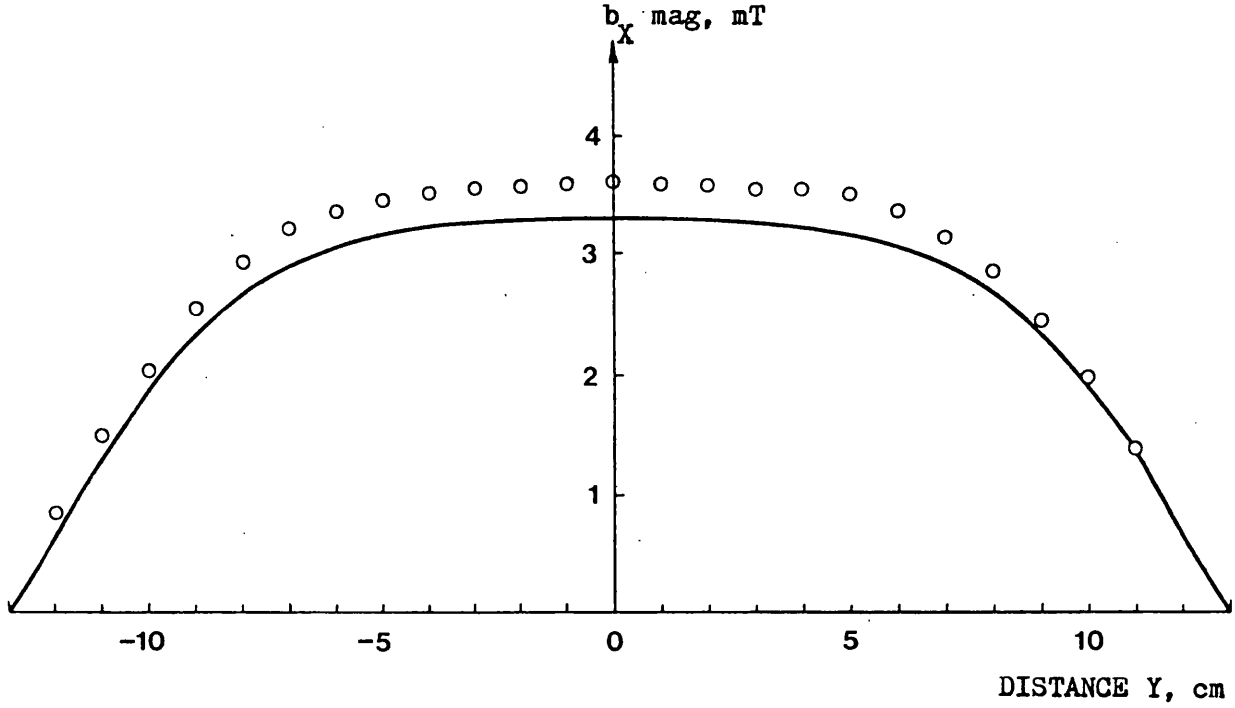

Fig. 4.4 Magnitude of the X-directed magnetostatic flux density,
X = 80 mm, Z = 20 mm o measured — calculated

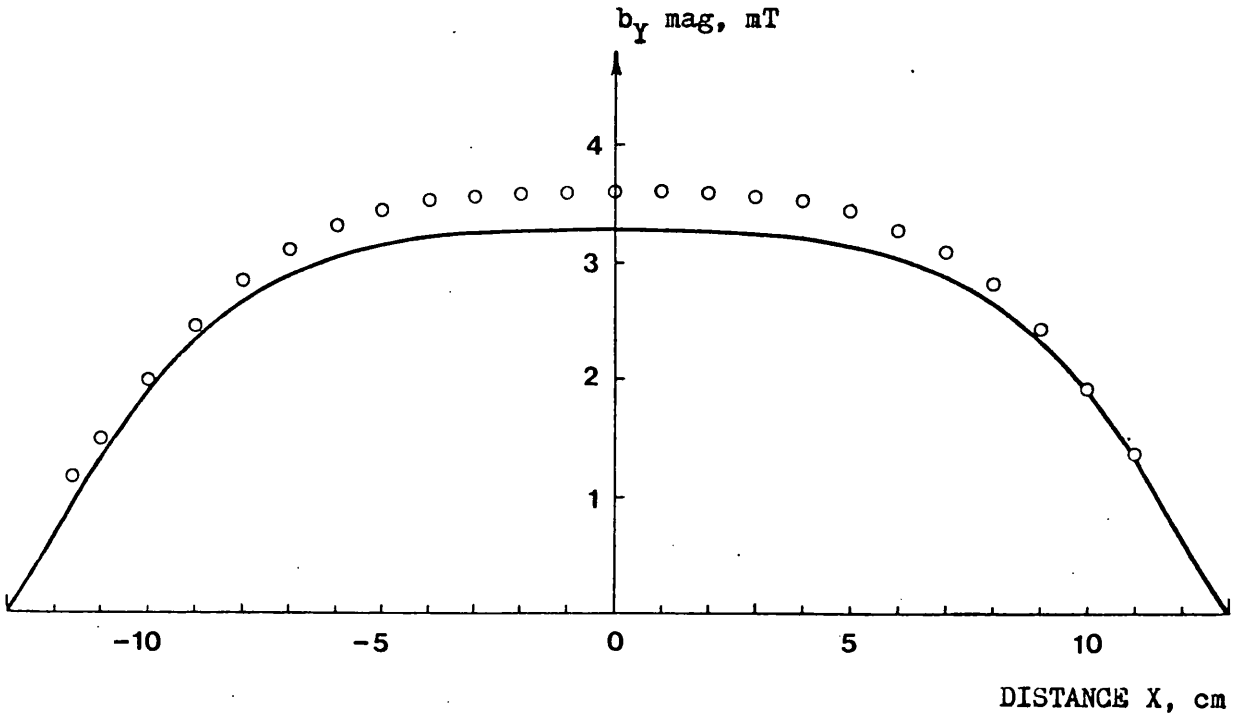

Fig. 4.5 Magnitude of the Y-directed magnetostatic flux density,
Y = 80 mm, Z = 20 mm o measured — calculated

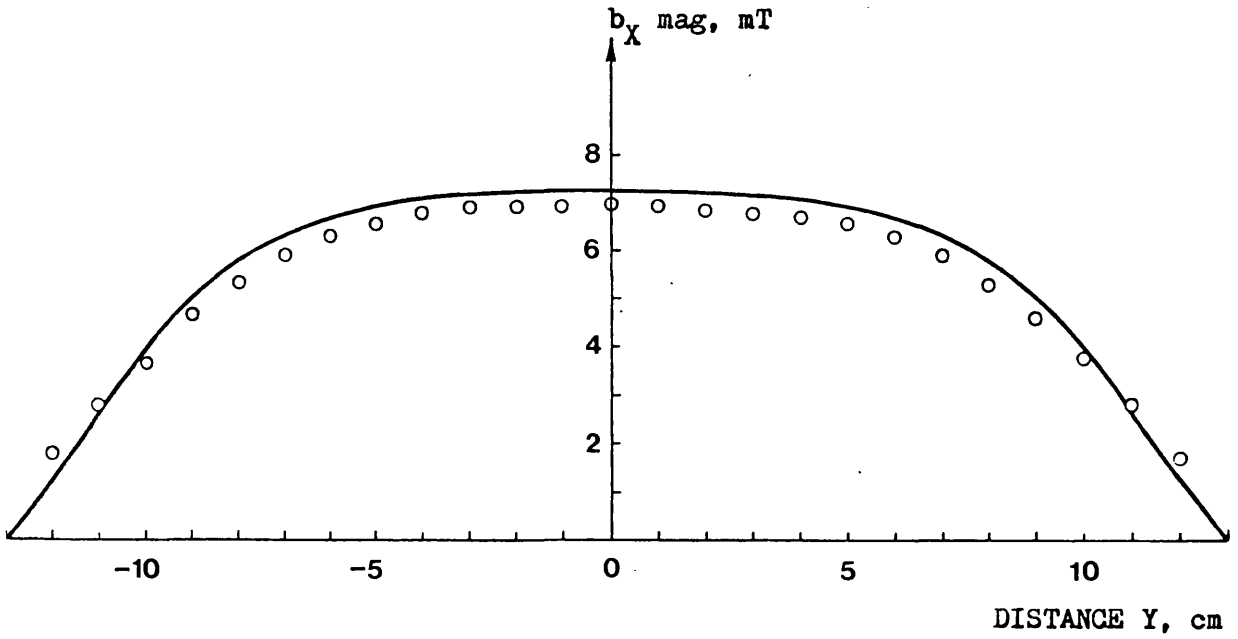

Fig. 4.6 Magnitude of the X-directed magnetostatic flux density, X = 120 mm, Z = 20 mm o measured — calculated

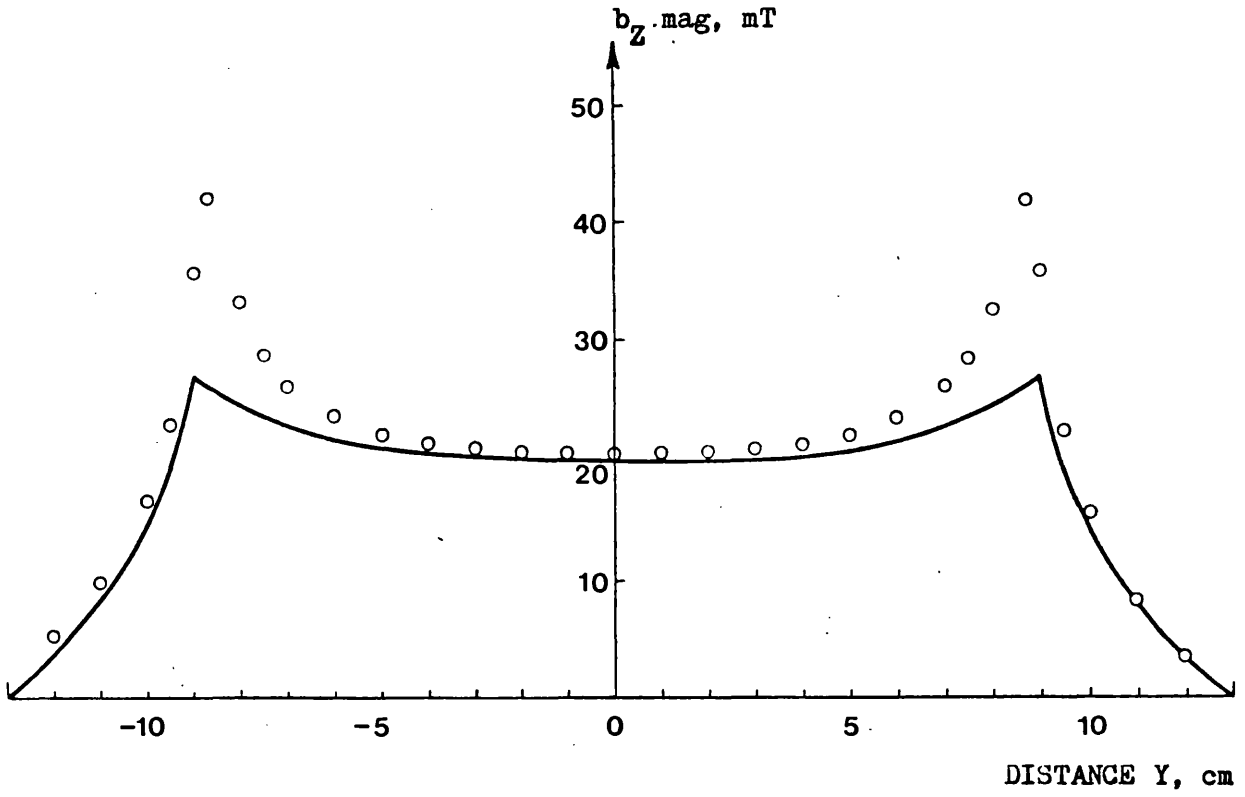

Fig. 4.7 Magnitude of the Z-directed magnetostatic flux density,
X = 0 mm, Z = 61 mm o measured — calculated

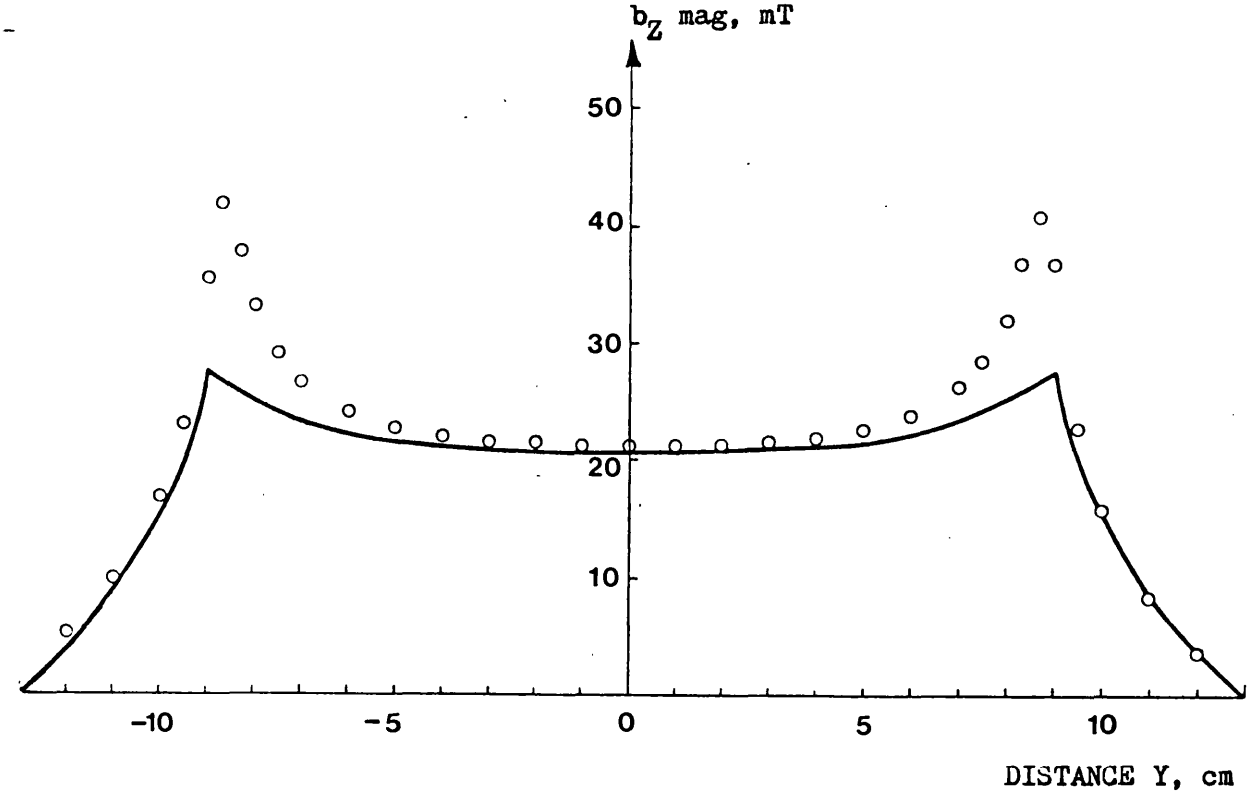

Fig. 4.8 Magnitude of the Z-directed magnetostatic flux density,
X = 50 mm, Z = 61 mm o measured — calculated

magnitude of the Z-directed flux density for Z = 61 mm is seen to be virtually the same as that for Z = 2 mm (Fig. 4.2). This confirms the existence of a z-directed flux line at the centre of the pole and hence validates the method used for setting the potential.

The measured and calculated results are generally in good agreement at most points. For the most accurate comparison between measurement and calculation, the measurements should be made at the mid-point of the branch representing the relevant flux in the theoretical model. This condition was satisfied for all X and Y-directed measurements performed with and without conducting material. When block conductors are present the gap in the Z direction is completely filled, apart from 4 mm. This meant that with the magnetic network used in the calculations, (section 4.5) the Z-directed measurements could not be made at the mid-point of the element when block conductors were present. Measurements could only be made in the 4 mm gap. The Z-directed magnetostatic measurements were also taken in this region so that a direct comparison could be made with the equivalent flux densities when eddy currents were present. In practice, the change in flux density along the length represented by a branch in the model should not be large. The fact that the measurements were not made at the exact centre of the branch will not then greatly affect the accuracy of the comparison between measurement and calculation.

The main discrepancy between measured and calculated results is in the Z-directed flux densities for Z = 61 mm (Fig. 4.7 and Fig. 4.8) and it occurs around the edge of the pole. This is due most probably to the use of an over coarse network in this region (see section 4.5 for the actual network used). The general form of the pole edge effect is represented in the calculated curve but a finer network would be

required in this region to improve the accuracy. The overall discrepancy between measurements and calculations using the original network is only significant over a very small part of the total problem. For this reason the orignal network with no refinement was considered adequate to check the general validity of calculation method.

4.4.3 Thin conducting plate

Eddy current flows were first introduced into the model using a thin conducting plate. The plate of dimension 140 x 140 x 3.17 mm and conductivity $\sigma = 2.3 \times 10^7$ S/m was placed centrally under the pole on the base of the box. The excitation current to the model was the same as that used for the magnetostatic case. This eddy current problem is similar to that solved by Carpenter[10]. The thin plate confines the predominant current flow to two dimensions, giving a familiar eddy current problem as an initial check for the calculation procedure.

The Z-directed flux perpendicular to the plate surface induces the circulation of current in the plate. This current in turn modifies the flux producing it until the steady state is reached. Measured and calculated Z-directed flux density distributions above the plate are given in Fig. 4.9 and Fig. 4.10. Comparing these with the virtually equivalent magnetostatic results in Fig. 4.2 and Fig. 4.3 shows that the flux density above the plate is "damped" by the eddy currents to an almost constant value. The calculated X-directed current density in the plate at X = 0 is given in Fig. 4.11. This shows that the circulation of current in the plate varies almost linearly in magnitude from zero at the centre to a maximum at the plate edge. The phase of the current is also seen to be approximately constant over the width

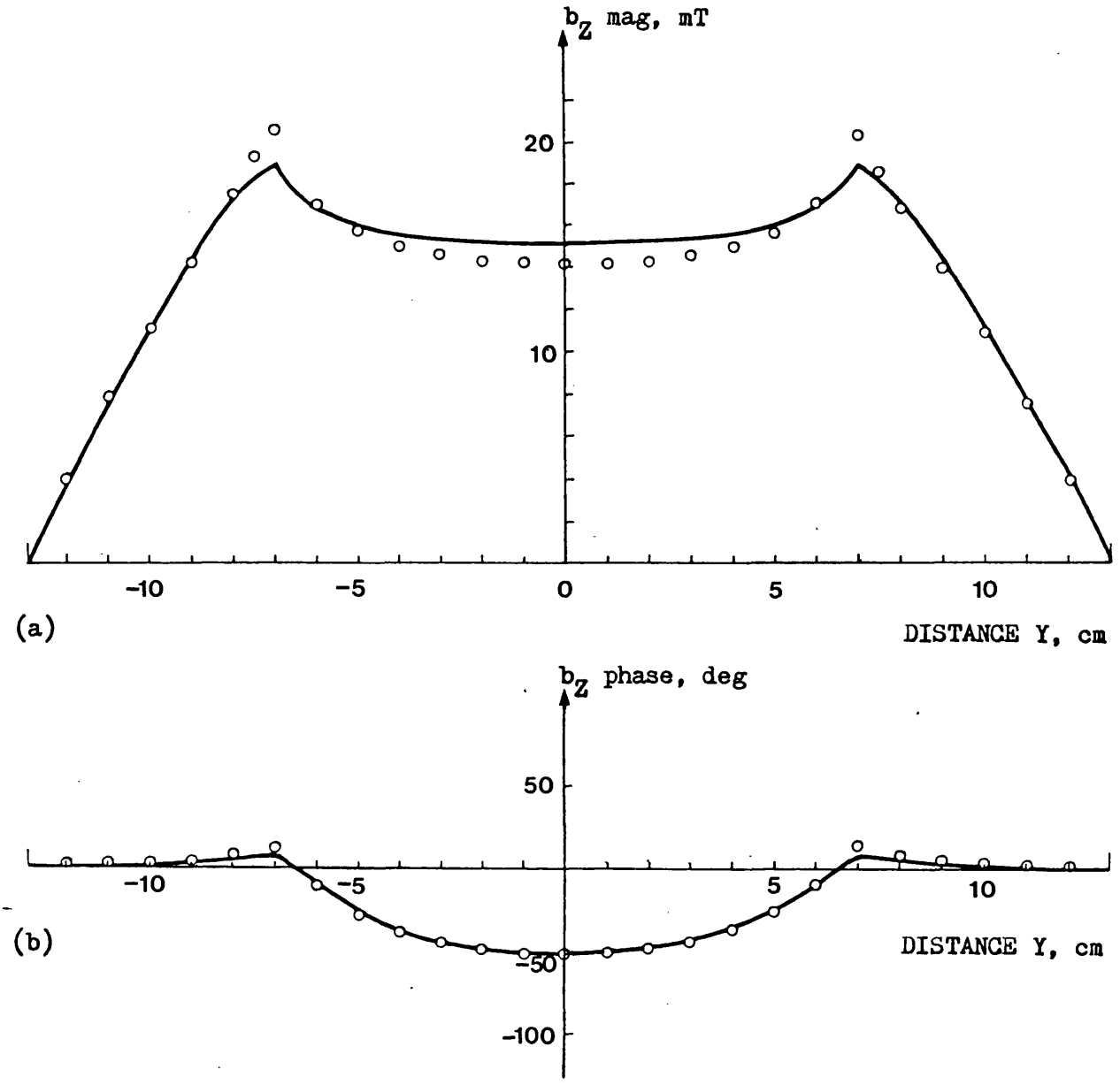

Fig. 4.9 Z-directed flux density for the thin plate,
X = 0 mm, Z = 5 mm o measured — calculated
(a) magnitude (b) phase

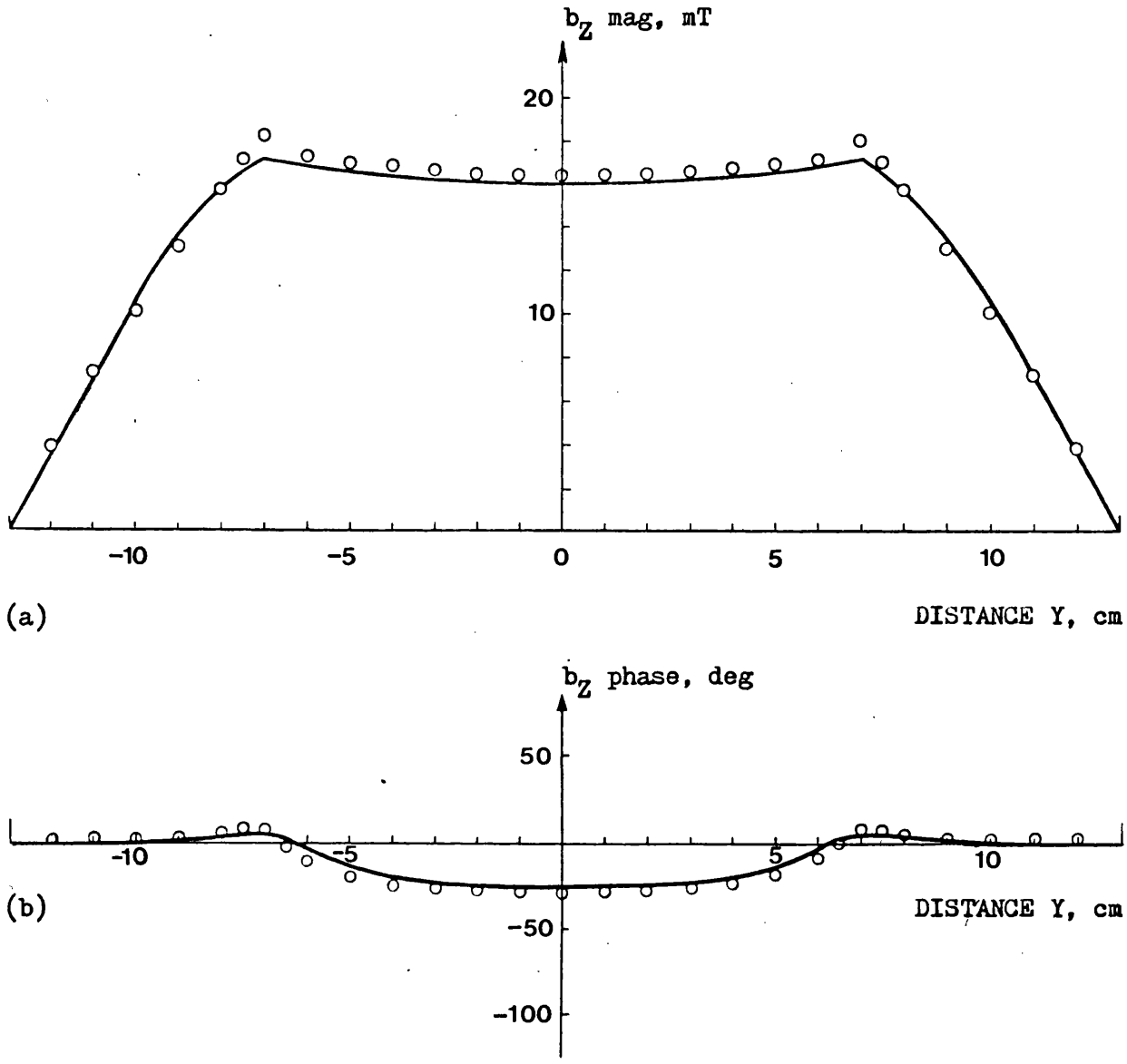

Fig. 4.10 Z-directed flux density for the thin plate,
X = 50 mm, Z = 5 mm o measured − calculated
(a) magnitude (b) phase

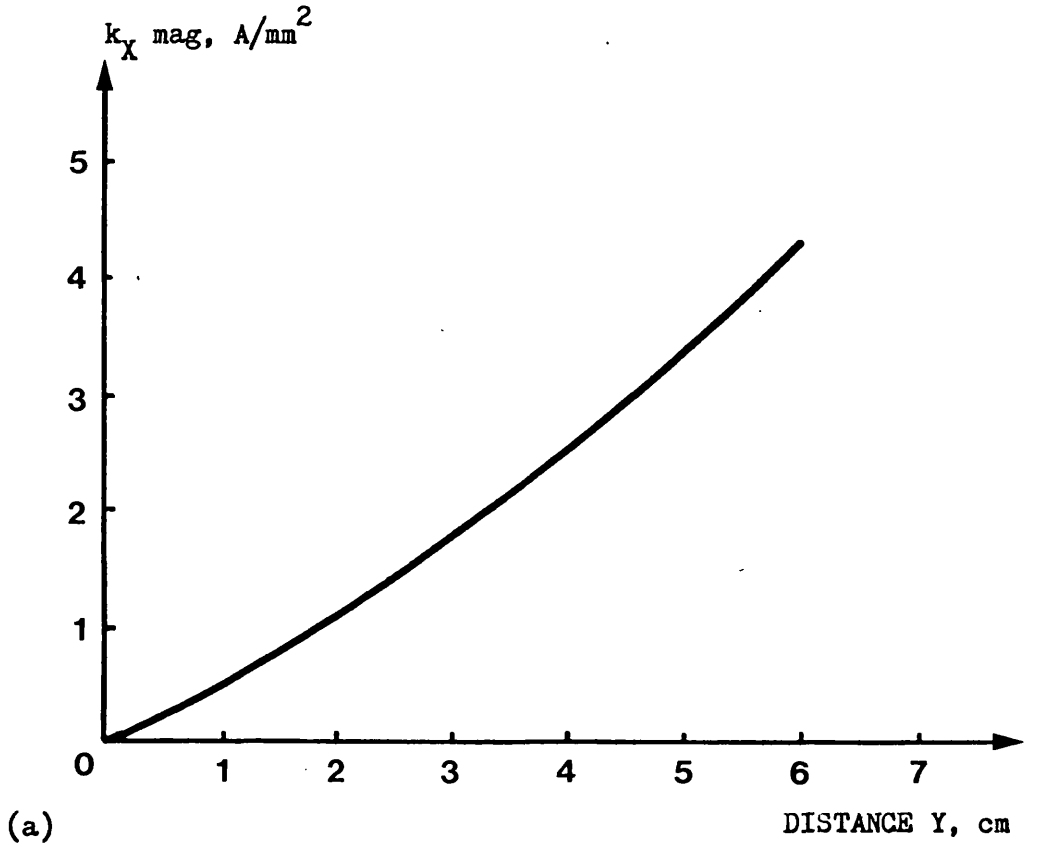

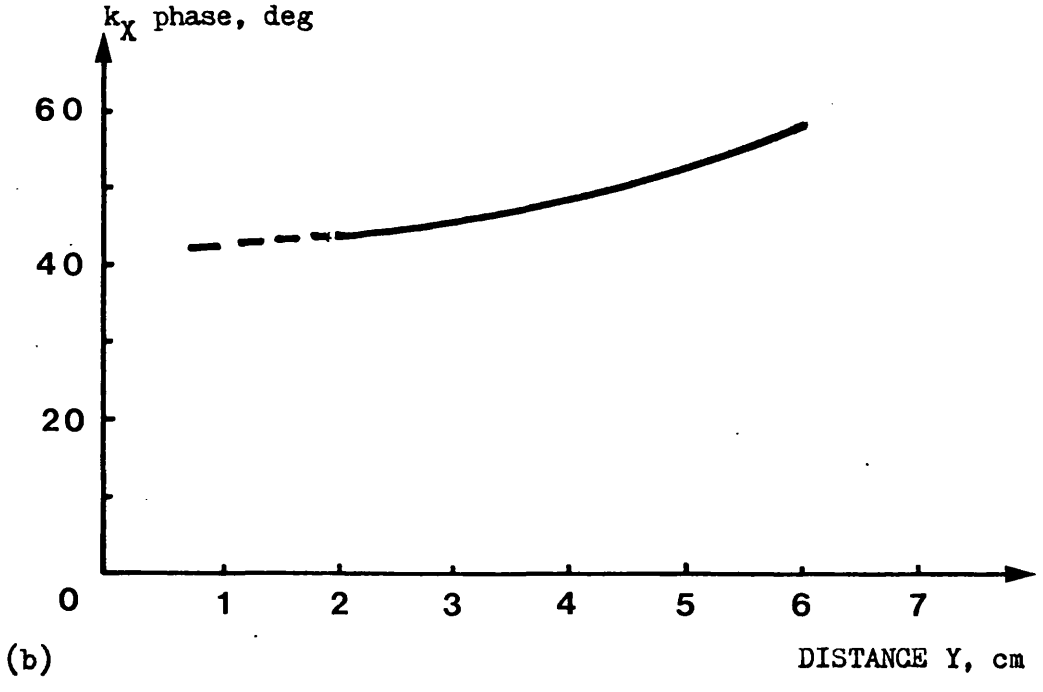

Fig. 4.11 Calculated X-directed current density in the thin plate, X = 0 mm
(a) magnitude (b) phase

of the plate. This distribution is consistent with the eddy current modification to the flux density above the plate.

The agreement between measured and calculated flux densities is generally good for both magnitude and phase. The main difference between measurement and calculation appears where the flux density changes rapidly at the edge of the plate. The discrepancy probably results from the use of an over coarse network at these points (see section 4.5 for the network details). The agreement between the calculations and measurements is however sufficiently good to confirm the validity of the numerical calculation procedure in the case of two-dimensional eddy currents in a three-dimensional magnetic field.

4.4.4 Full conducting block

The thin plate was replaced by a solid conducting block of dimension 140 x 140 x 60 mm and conductivity $\sigma = 2.7 \times 10^7$ S/m. The block was positioned centrally under the pole in the same place as the plate in the previous test. The gap in the Z-direction was then totally filled with conductor apart from 4 mm required for access. The eddy currents were no longer physically restricted to planar flow by the dimensions of the conductor. Current could flow in all three co-ordinate directions, so the model was treated as a full three-dimensional eddy current problem.

Measured and calculated flux density distributions in the Z, X and Y directions are given in Figs. 4.12 to 4.17. The Z-directed distributions show the screening effect of a large circulation of current in the X-Y plane, similar to that seen in the thin plate. In the solid block the screening is more pronounced but as with the plate

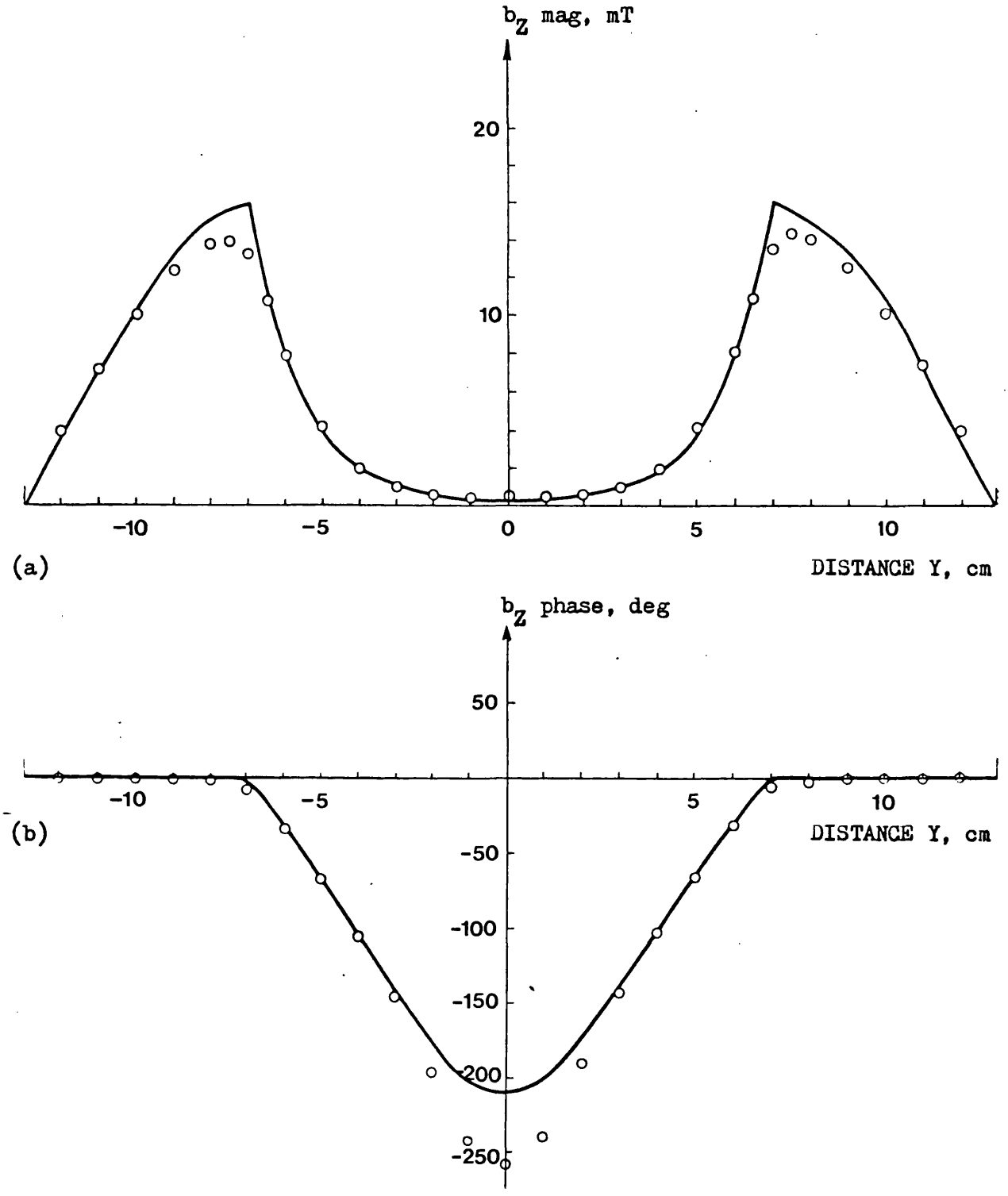

Fig. 4.12 Z-directed flux density for full block,
X = 0 mm, Z = 2 mm o measured — calculated
(a) magnitude (b) phase

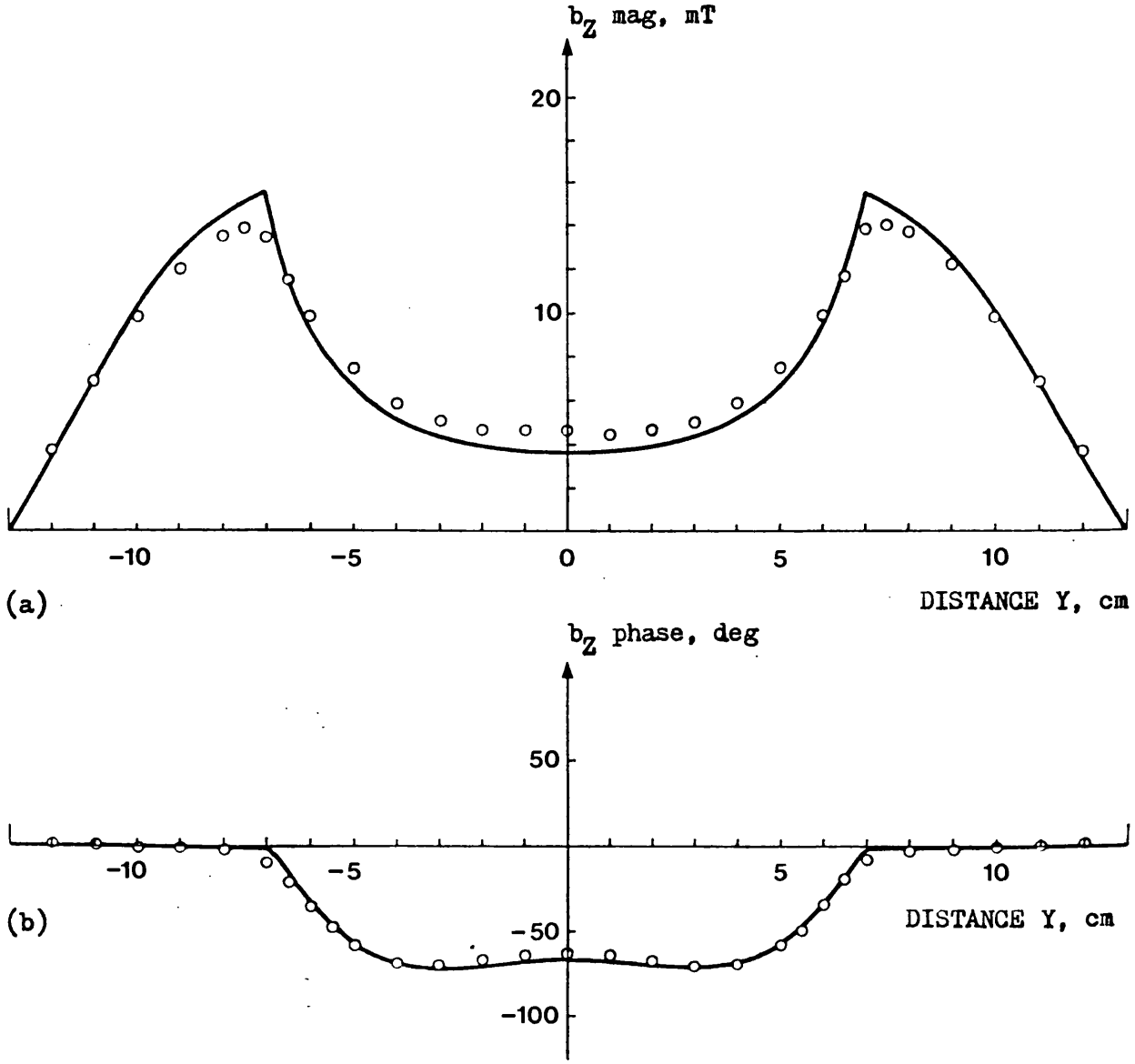

Fig. 4.13 Z-directed flux density for full block,
X = 50 mm, Z = 2 mm o measured – calculated
(a) magnitude (b) phase

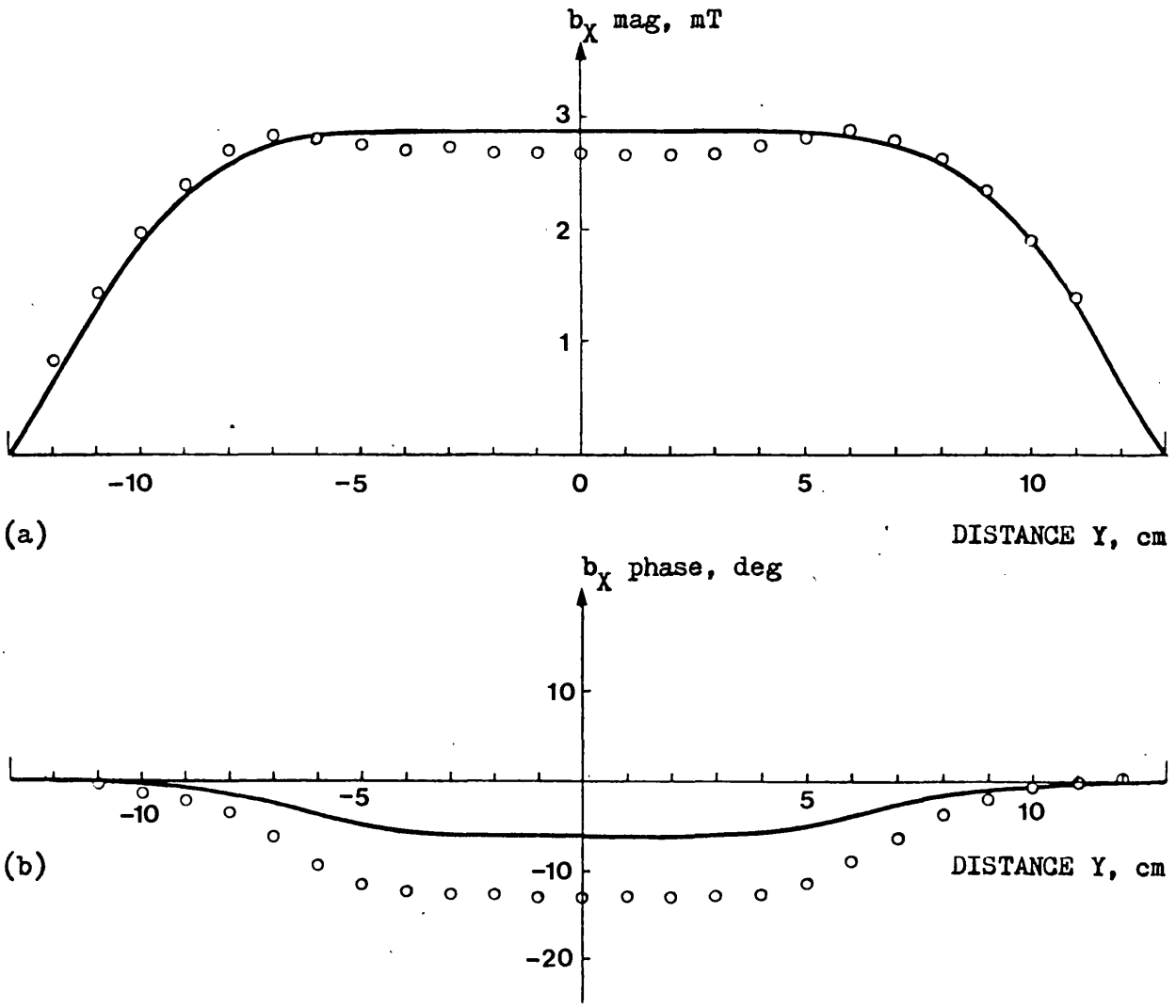

Fig. 4.14 X-directed flux density for full block,
X = 80 mm, Z = 20 mm o measured — calculated
(a) magnitude (b) phase

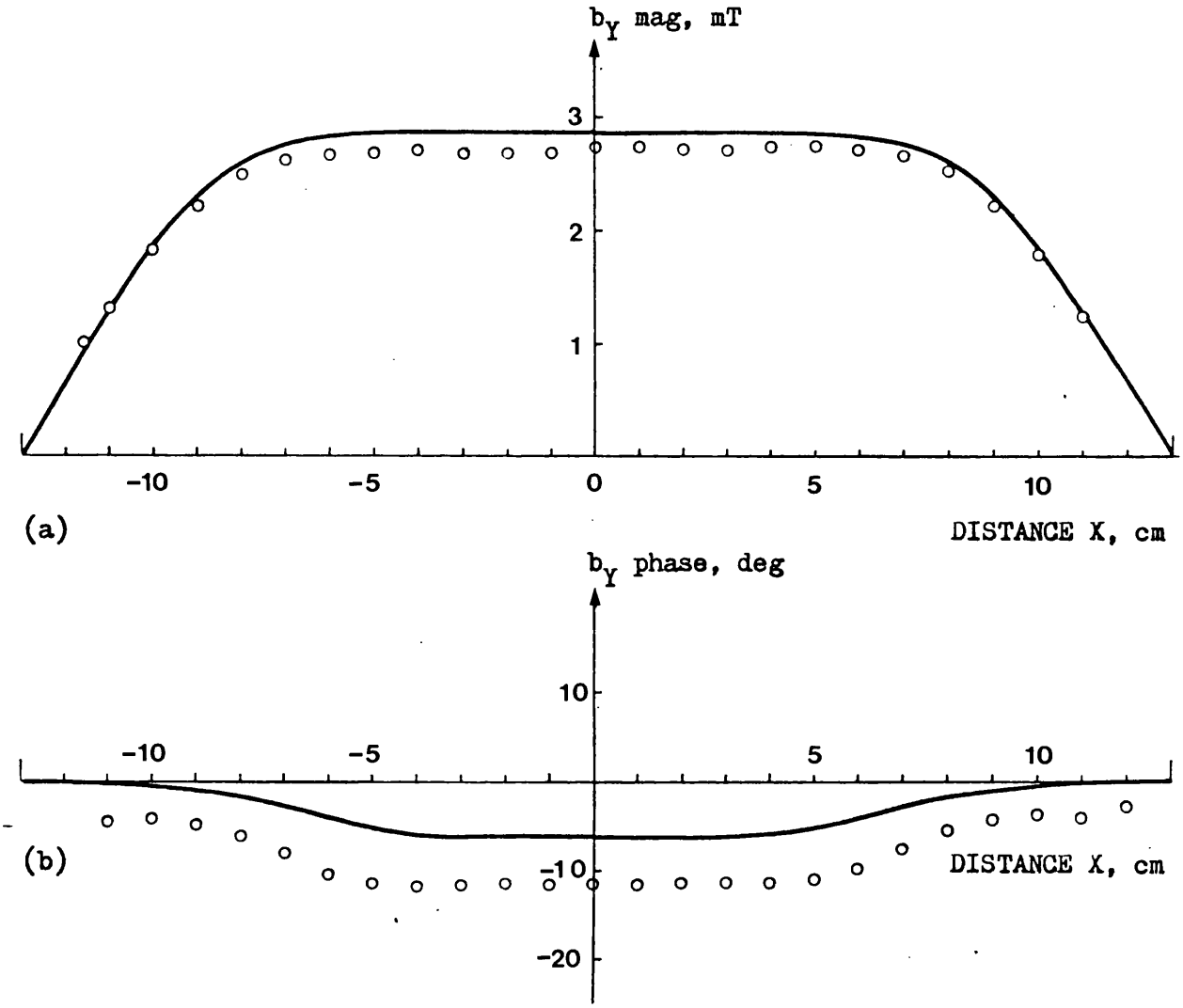

Fig. 4.15 Y-directed flux density for full block,
Y = 80 mm, Z = 20 mm o measured — calculated
(a) magnitude (b) phase

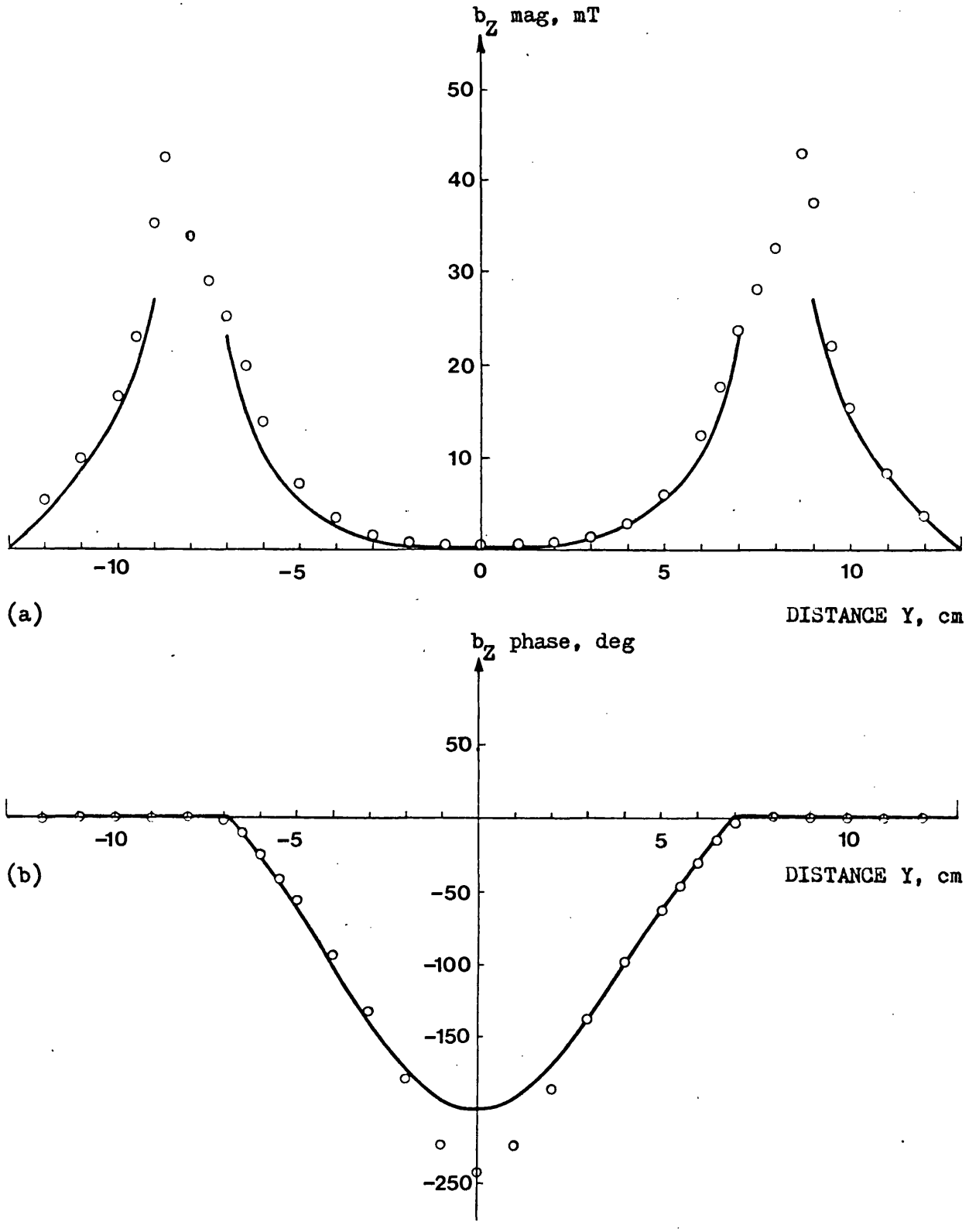

Fig. 4.16 Z-directed flux density for full block,
X = 0 mm, Z = 61 mm o measured — calculated
(a) magnitude (b) phase

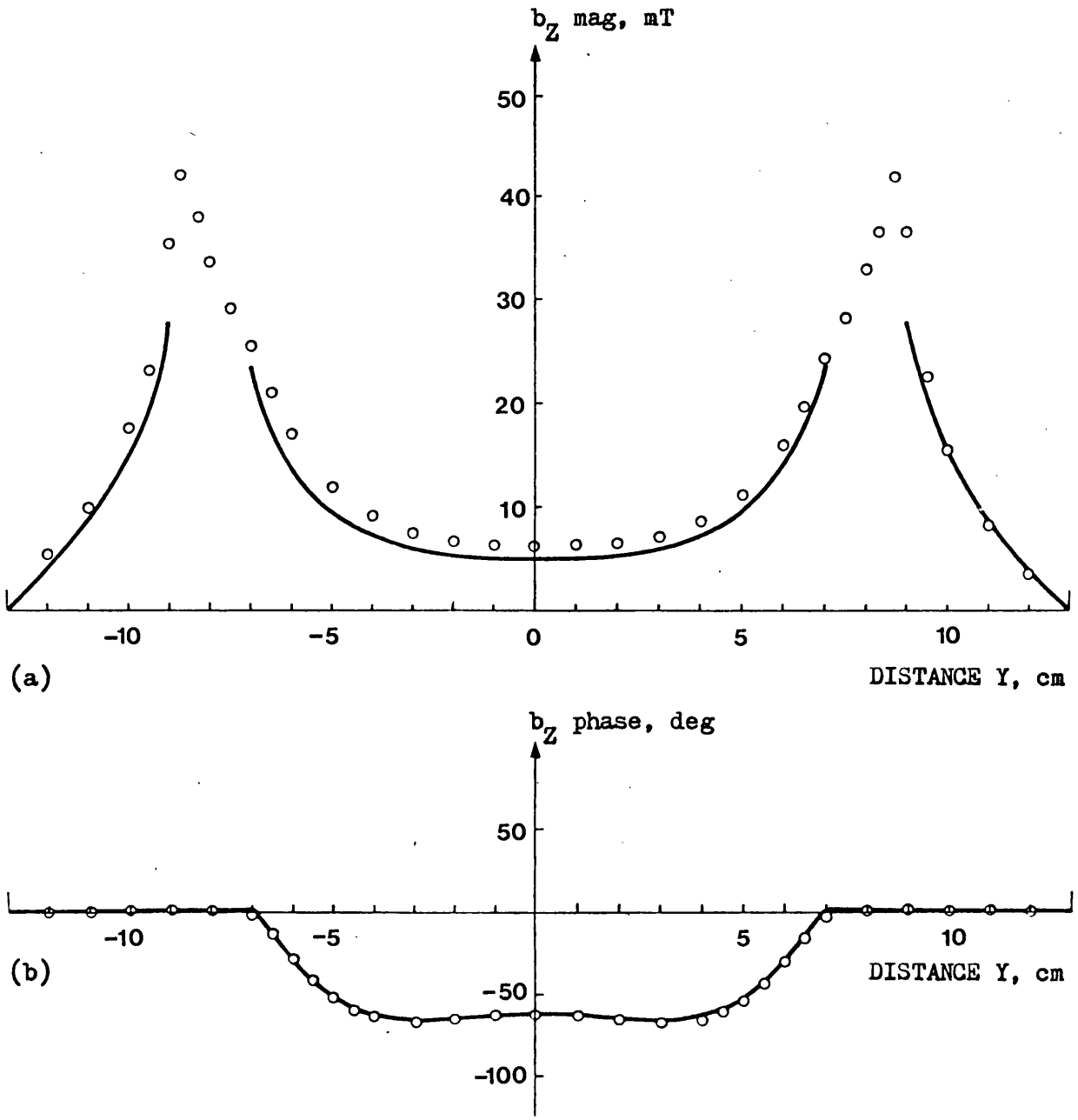

Fig. 4.17 Z-directed flux density for full block,
X = 50 mm, Z = 61 mm o measured — calculated
(a) magnitude (b) phase

the flux outside the block is still virtually unchanged from its magnetostatic value. The X and Y-directed flux densities, Fig. 4.14 and Fig. 4.15, show a slight phase shift and decrease in magnitude from the magnetostatic value, Fig. 4.4 and Fig. 4.5, in the vicinity of the block. This indicates a small flow of current in the Z-direction.

The agreement between calculation and measurement is good at most points. Some of the discrepancies may be due to the use of an over coarse network in certain places. Some measured values may also be slightly in error. For example in Fig. 4.12(a) the difference between measurement and calculation at the peaks will be due, in part, to a low measurement exactly at the peak. This occurs because the Hall probe averages the flux density over its width. The phase measurements around X = 0 in Fig. 4.12(b) may also be slightly in error. The flux density in this region is very small, thereby making any measurement susceptible to error. The measured phase for X and Y results, Fig. 4.14(b) and Fig. 4.15(b), is small. Any pickup from eddy currents in the iron or pickup from fluxes on the other axes will thus result in large percentage errors in these phase measurements. The measurements of the Z-directed flux density above the block, Fig. 4.16 and Fig. 4.17, show a double edge effect caused by the circulation of current and by the edge of the pole. Both edge effects are also seen in the general shape of the calculated curves. That due to the currents is accurately represented but, as explained for the magnetostatic results, there is a discrepancy in the magnitude of the pole edge effect due to the coarseness of the network in this region.

The calculated current density in the X direction for X = 0 mm, Z = 10 mm is given in Fig. 4.18. The Z-directed current density in comparison is very small and has not been shown. The ratio of the maximum magnitude of X or Y-directed current density to the maximum magnitude of Z-directed current density is 70:1. The eddy current flow is therefore still approximately two dimensional with most current circulating in the X-Y plane. However this flow is slightly more complicated than in the thin plate case since it is no longer resistance limited. It is noted also that the skin depth of 13.7 mm for the conductor is predicted almost exactly from the main circulation of current as shown in Fig. 4.18. Finally the general form of the calculated current, as a large inductance limited flow in the X-Y plane and very small Z-directed flow, is consistent with the eddy current effect visible in the flux density results.

4.4.5 Split block

The main circulation of current in the full block was in the X-Y plane. To break up this flow and drive more current in the Z-direction the full block was split into four identical smaller blocks by cutting in the Z direction along the planes X = 0 and Y = 0. The split block was again placed centrally under the pole and the model energised to give a 50 Hz sinusoidal mmf of 1000 + j0 AT between the pole and box.

Measured and calculated flux density distributions for the split block in the Z, X and Y directions are given in Figs. 4.19 to 4.25. The Z-directed results still indicate the presence of a considerable circulation of current in each separate quarter block in the X-Y plane. This current damps the Z-directed flux through the quarter block in the characteristic manner as shown for example in Fig. 4.21.

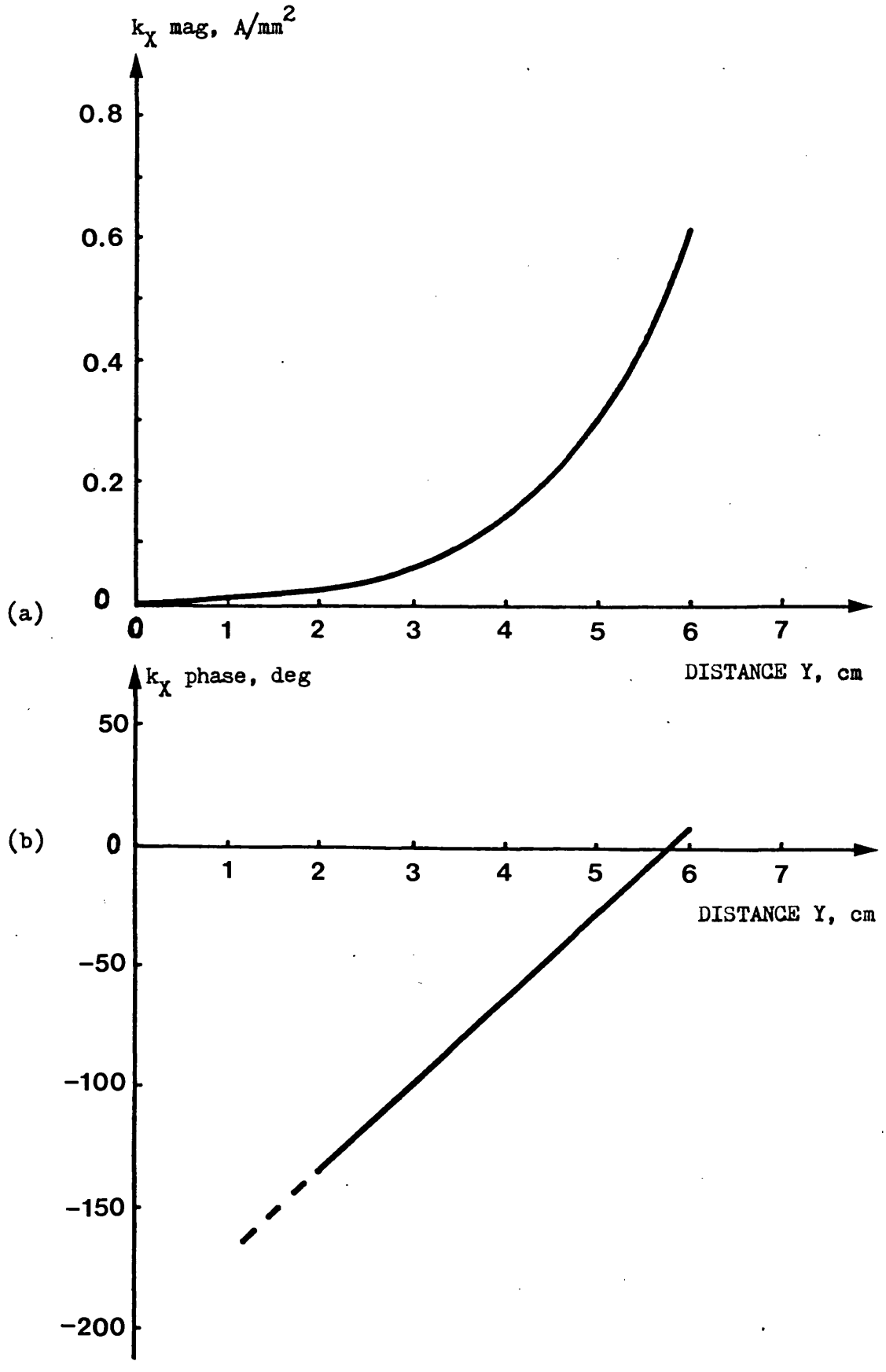

Fig. 4.18 Calculated X-directed current density in the full block, X = 0 mm, Z = 10 mm
(a) magnitude (b) phase

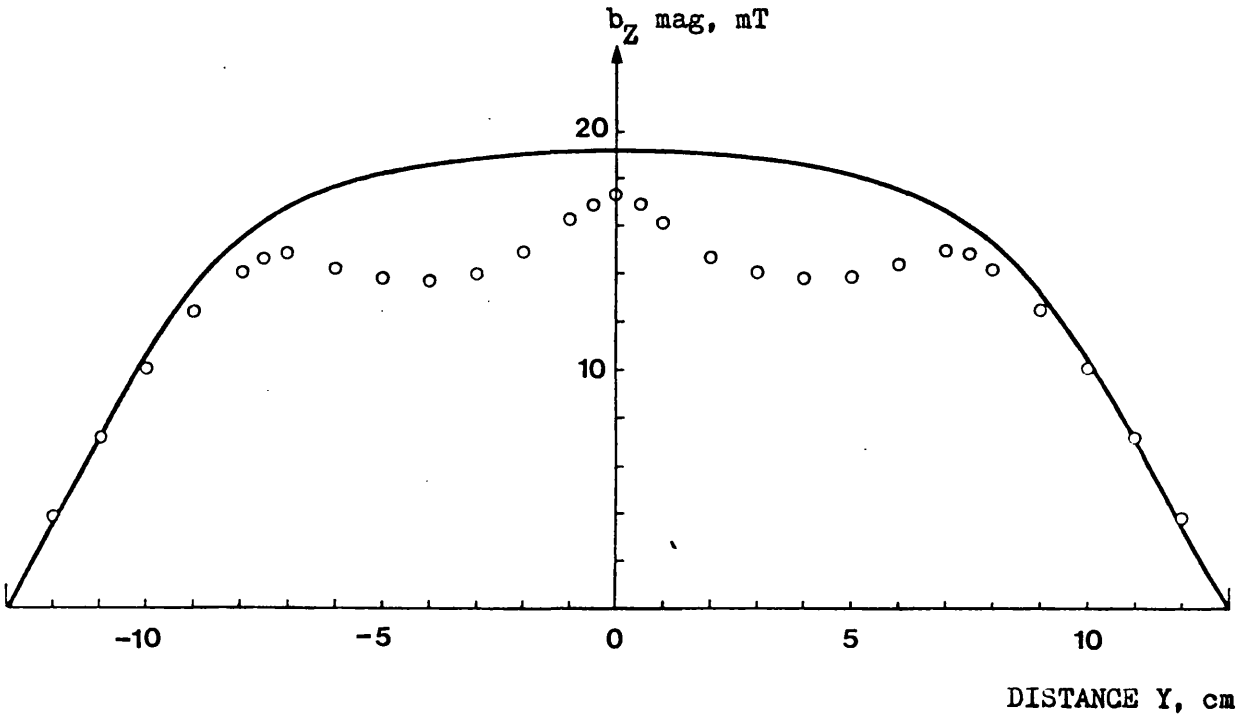

Fig. 4.19 Magnitude of the Z-directed flux density for the split block, X = 0 mm, Z = 2 mm o measured — calculated

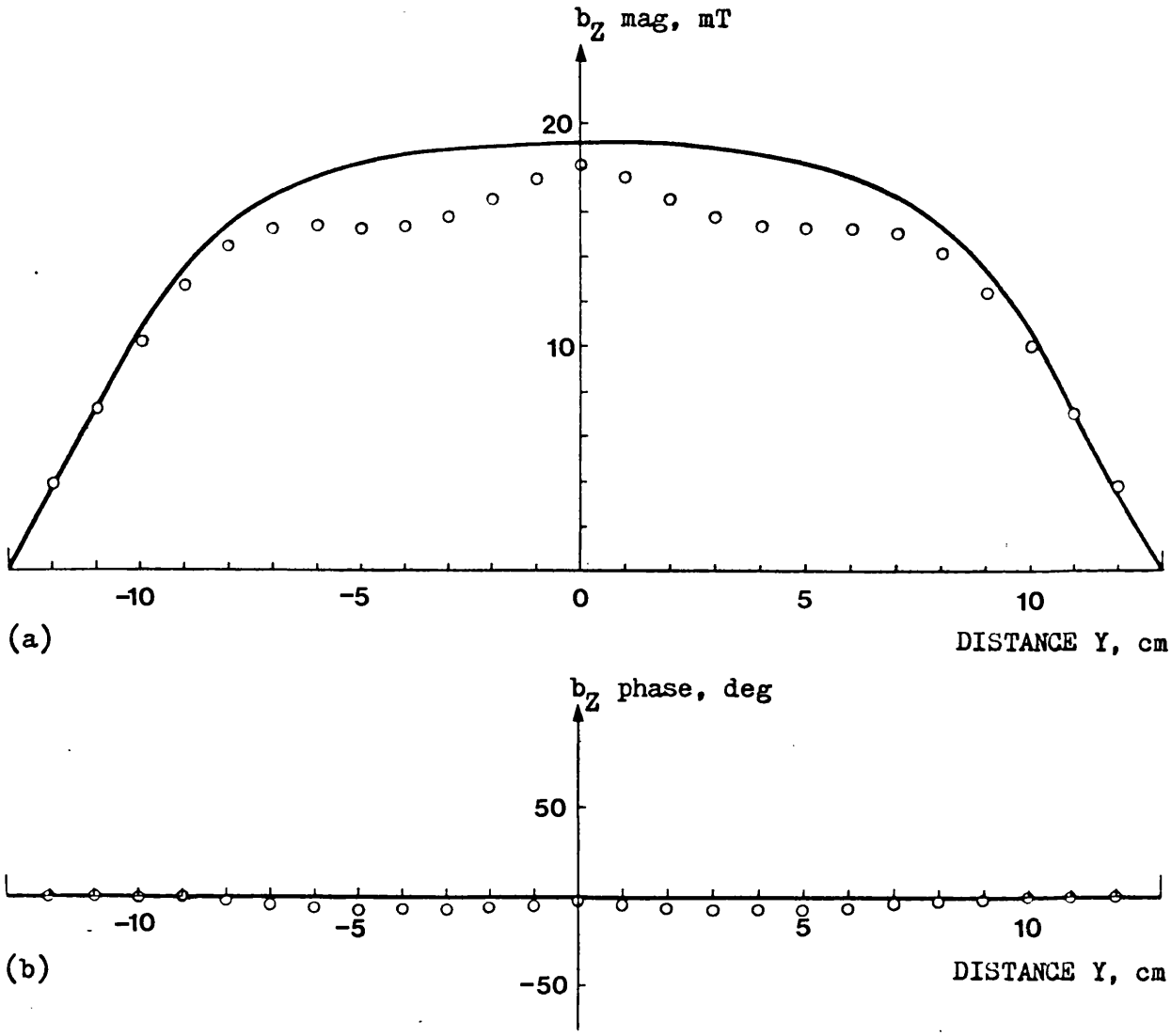

Fig. 4.20 Z-directed flux density for the split block, with 3mm gap between blocks in the case of the measurements, X = 0 mm, Z = 2 mm o measured — calculated
(a) magnitude (b) phase

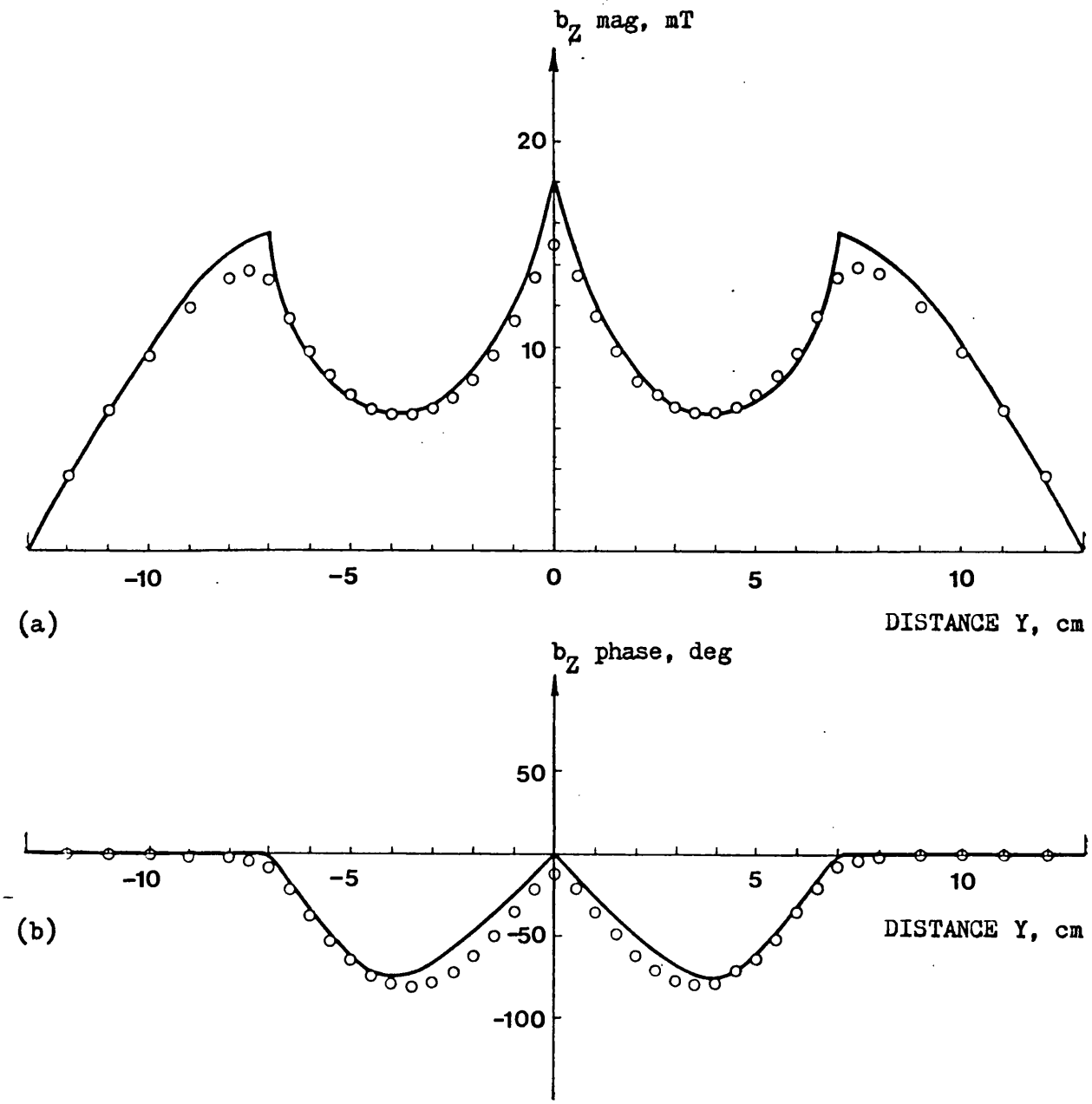

Fig. 4.21 Z-directed flux density for the split block,
X = 50 mm, Z = 2 mm o measured — calculated
(a) magnitude (b) phase

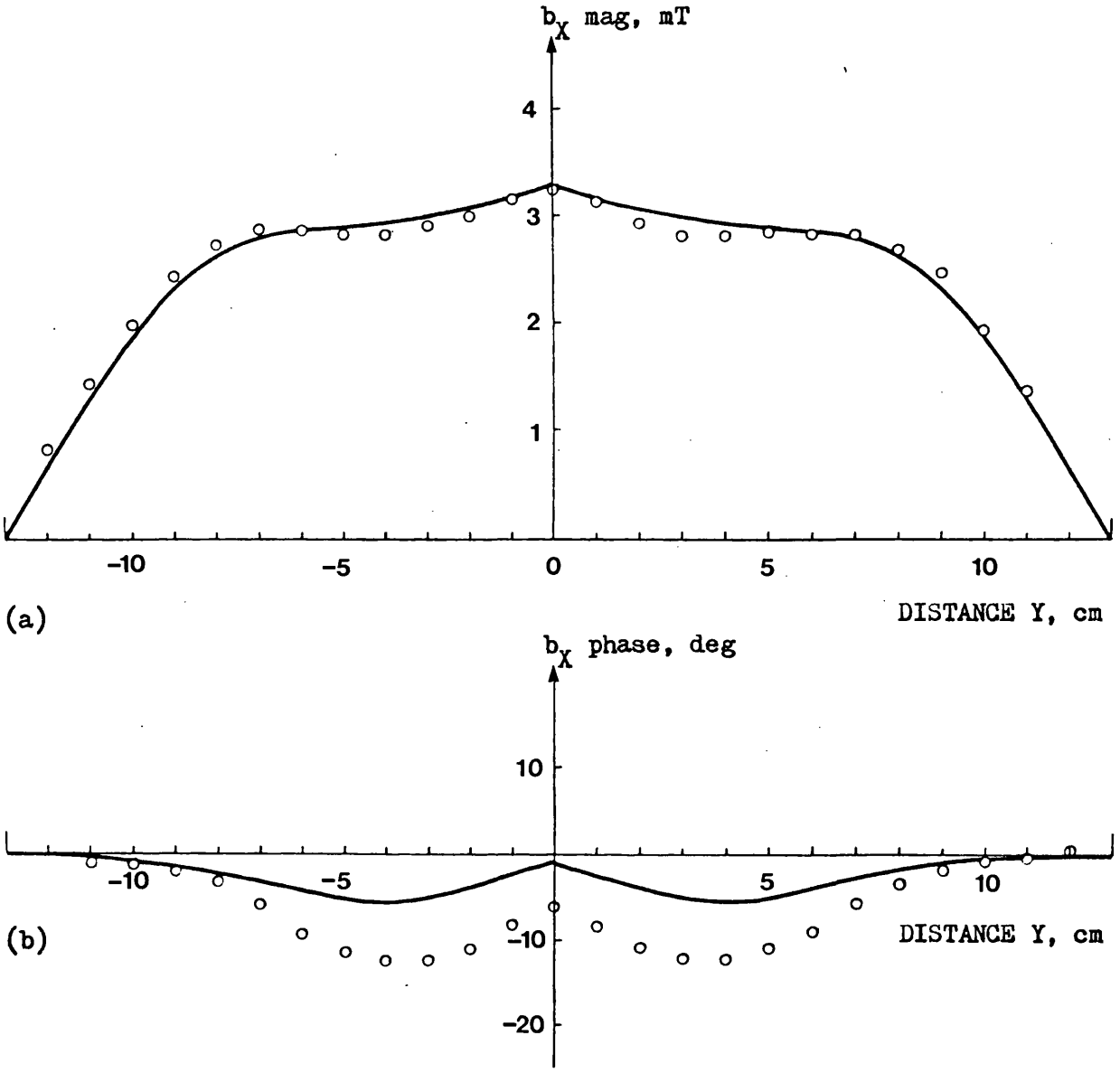

Fig. 4.22 X-directed flux density for the split block,
X = 80 mm, Z = 20 mm o measured — calculated
(a) magnitude (b) phase

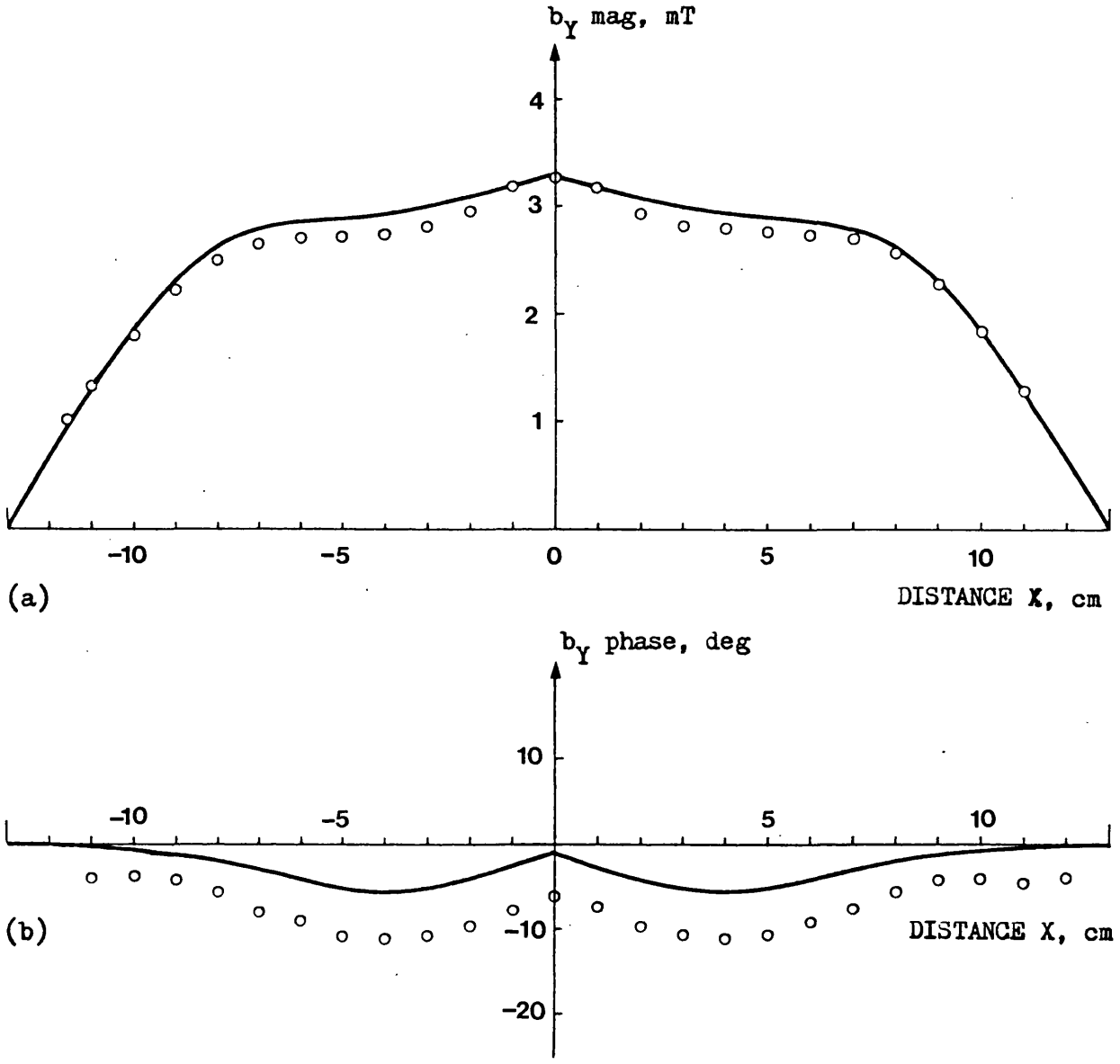

Fig. 4.23 Y-directed flux density for the split block,
Y = 80 mm, Z = 20 mm o measured — calculated
(a) magnitude (b) phase

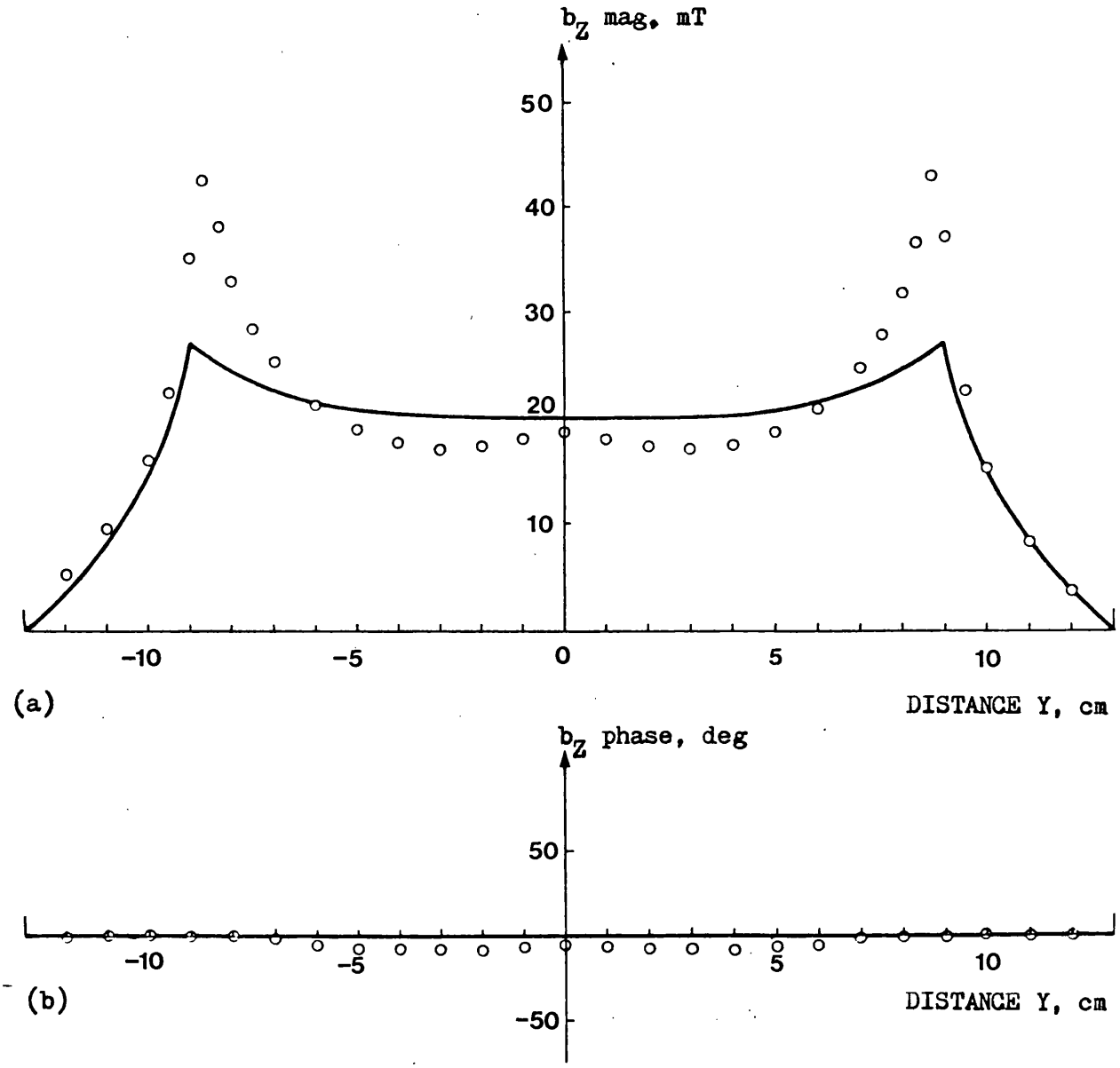

Fig. 4.24 Z-directed flux density for the split block,
X = 0 mm, Z = 61 mm o measured — calculated
(a) magnitude (b) phase

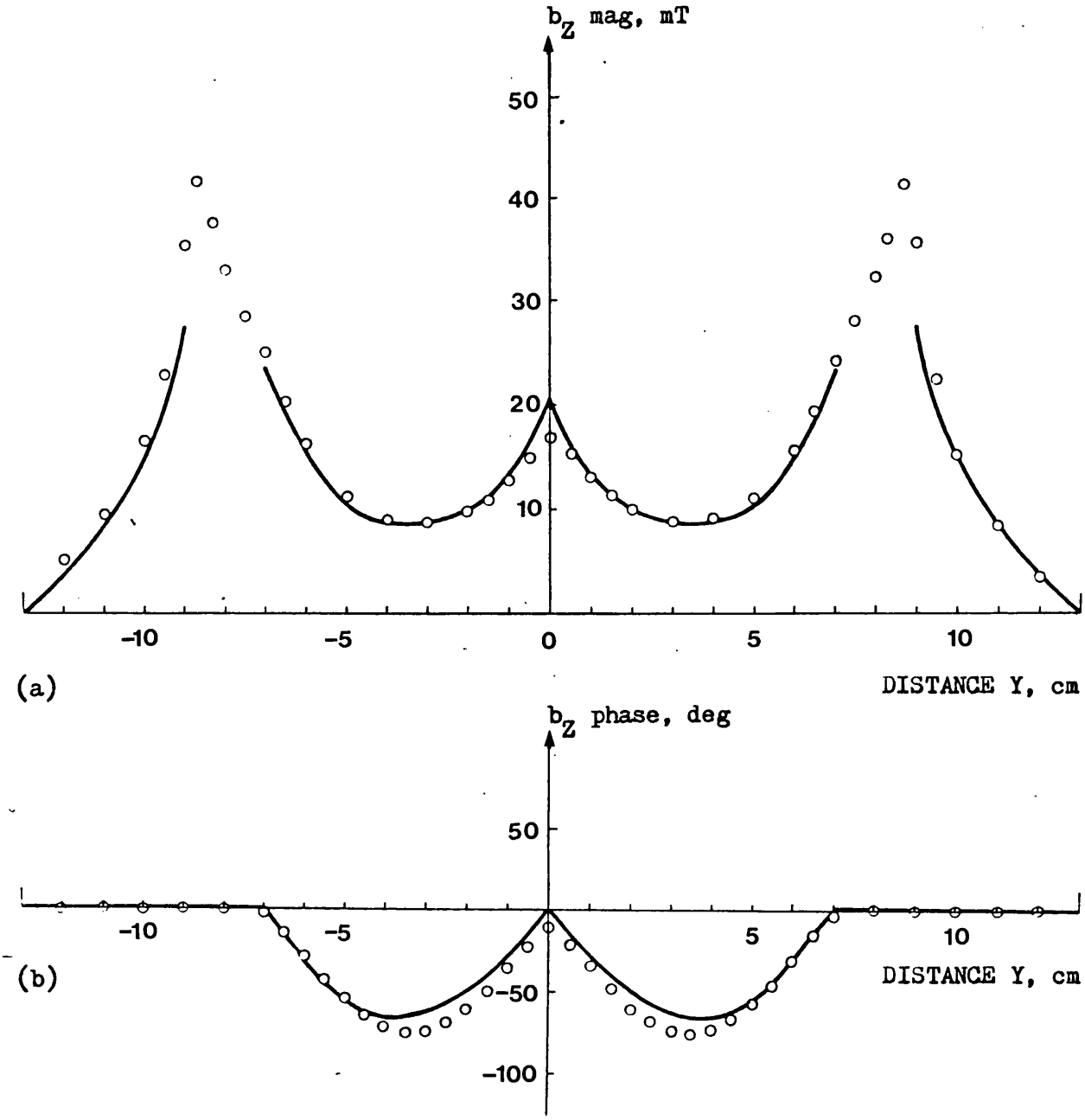

Fig. 4.25 Z-directed flux density for the split block,
X = 50 mm, Z = 61 mm o measured — calculated
(a) magnitude (b) phase

In the ideal case the negative symmetry of the eddy currents about the planes X = 0 and Y = 0 should result in the cancellation of all eddy current effects on these planes. In particular, the flux density will maintain its magnetostatic value. The measured and calculated Z-directed flux densities along the line X = 0 mm, Z = 2 mm are given in Fig. 4.19. The calculated results for this position are seen to be almost identical to those of the corresponding magnetostatic curve shown in Fig. 4.2. The measured results for the split block at X = 0, Z = 2 are however much lower than the calculations in the region of the block. It is felt that the main cause for this discrepancy is a measurement problem. This can be seen from Fig. 4.21. The Z-directed flux density in the region of the cut between the blocks is a "knife edge". Measurement along this edge with a 2 millimetre wide probe will certainly give a low reading because the probe registers the average value of the flux density over its surface. This was verified as a major cause of the discrepancy by separating the blocks with a gap of 3 mm and repeating the Z-directed measurements for X = 0 mm, Z = 2 mm. These are given in Fig. 4.20. The difference between measurement and calculation is much less in these results, although some discrepancy still remains. It is felt that this may still be due to some pickup of the eddy current effect, possibly caused by asymmetry in positioning the blocks or slight inaccuracy in positioning the probe. The Z-directed measurements for X = 0mm, Z = 61 mm were also taken with the 3 mm gap between the blocks. All other measurements were performed with no gap.

The X and Y directed flux density measurements in Fig. 4.22 and Fig. 4.23 do show some effect of Z-directed current flow in each of the quarter blocks. However the effect is not very pronounced,

indicating that again there is only a small component of Z-directed current. Calculated current density distributions in a quarter block are given in Fig. 4.26 and Fig. 4.27. The first of these shows the magnitude of the X-directed current density along the line X = 30 mm, Z = 10 mm. The path of the main circulation of current in the X-Y plane is also shown diagrammatically in this figure. In the second, Fig. 4.27, the magnitude of the Z-directed current density normal to the plane Z = 20 mm is shown together with a diagram of the main flow path for the Z-directed current. These calculated current densities appear to be consistent with the eddy current effect visible in the flux density results for the split block.

The coarseness of the network and the distribution of the current in the split block case has led to current density calculations which appear to be rather inaccurate at certain points. For example, in Fig. 4.26(a) the X-directed current density on the edge of the block (Y = 0) is represented by a point at Y = 20 mm. This means that if measurements were available for the X-directed current density at Y = 0 there would be poor agreement with calculation because of the position difference between the measurement and calculation points. This, possibly large, discrepancy in the current density at the edge of the conductor does not necessarily lead to corresponding errors in the calculated flux density at that point. The flux density predicted for a region by the linked network model depends on the total current linking closed circuits in the magnetic network of the model. In the above example the measured and calculated current density may be in poor agreement at Y = 0, but the current density calculated for the electric circuit branch at Y = 20 mm, when multiplied by the area the branch represents, can give a good approximation to the total current linking that area in the magnetic circuit. A more accurate current

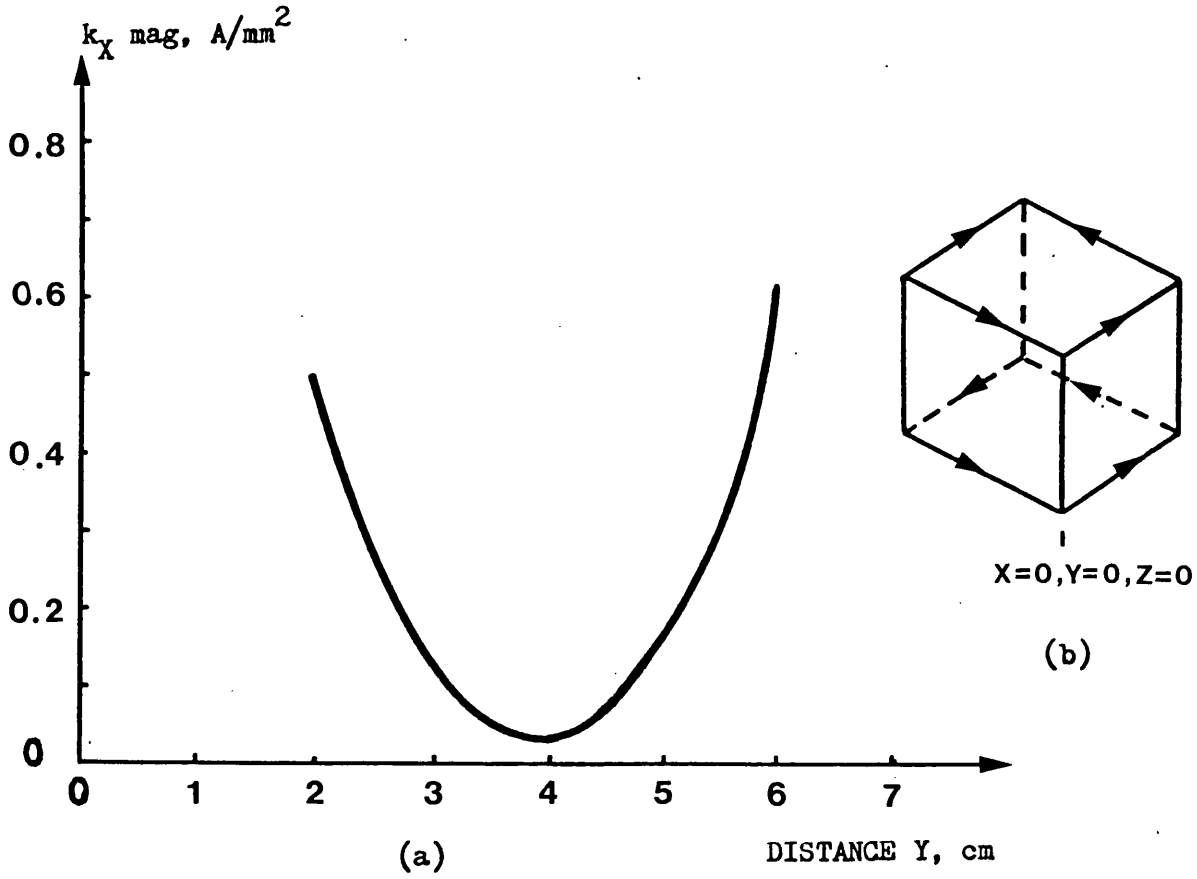

Fig. 4.26 Calculated X-directed current density in one quarter of the split block, X = 30 mm, Z = 10 mm
(a) magnitude
(b) path of main circulation of current in X-Y plane

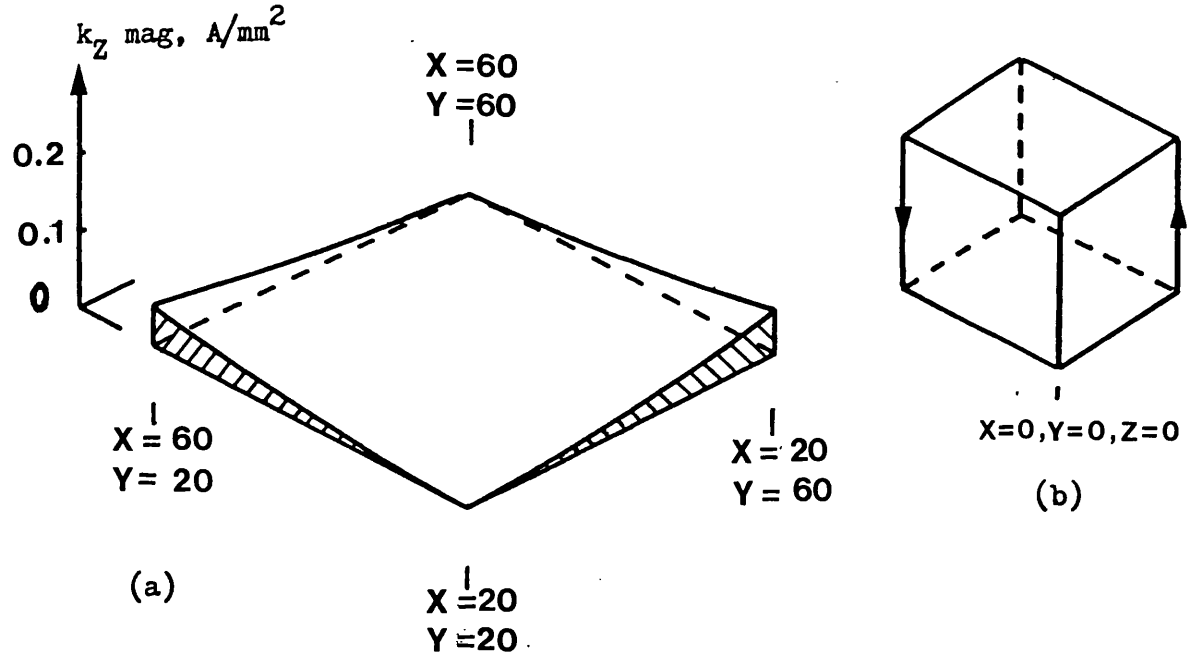

Fig. 4.27 Calculated Z-directed current density in one quarter of the split block, normal to plane Z = 20 mm
(a) magnitude
(b) path of main circulation of current in Z direction

density curve could obviously be obtained using a finer network. At this stage the object of the work is to prove the general validity of the theory. It is felt that this has been achieved for the split block, in view of the accuracy of the comparison between measured and calculated flux density. The eddy currents in the split block are however still predominantly two-dimensional. The ratio of the maximum magnitude of the calculated X or Y directed current density to that in the Z-direction is 15:1. This is more approximately three-dimensional than in the full block but further tests were necessary to check the theory with a truly three-dimensional eddy current distribution.

4.4.6 Split block moved outwards

The four quarters of the split conducting block were moved out symmetrically from under the pole to the position shown in Fig. 4.28. When magnetostatic, the flux directly under the pole is predominantly Z-directed. In the new position of the blocks the X, Y and Z components of the magnetostatic flux density have comparable magnitudes (Fig. 4.2 to Fig. 4.8). This led to a truly three-dimensional eddy current distribution in each of the quarter blocks.

A comparison of measured and calculated flux densities for the case with the blocks moved outwards is given in Figs. 4.29 to 4.31. The flux density along the lines of symmetry between the blocks is again virtually equal to its magnetostatic value. The Z-directed flux density for X = 70 mm, Z = 2 mm in Fig. 4.30 shows the characteristic damping caused by a circulation of current in the X-Y plane of each quarter block. The X-directed flux density (Fig. 4.31) for X = 120 mm, Z = 20 mm now also shows considerable effect due to the flow of current in the Z-direction. Comparison with the equivalent magnetostatic

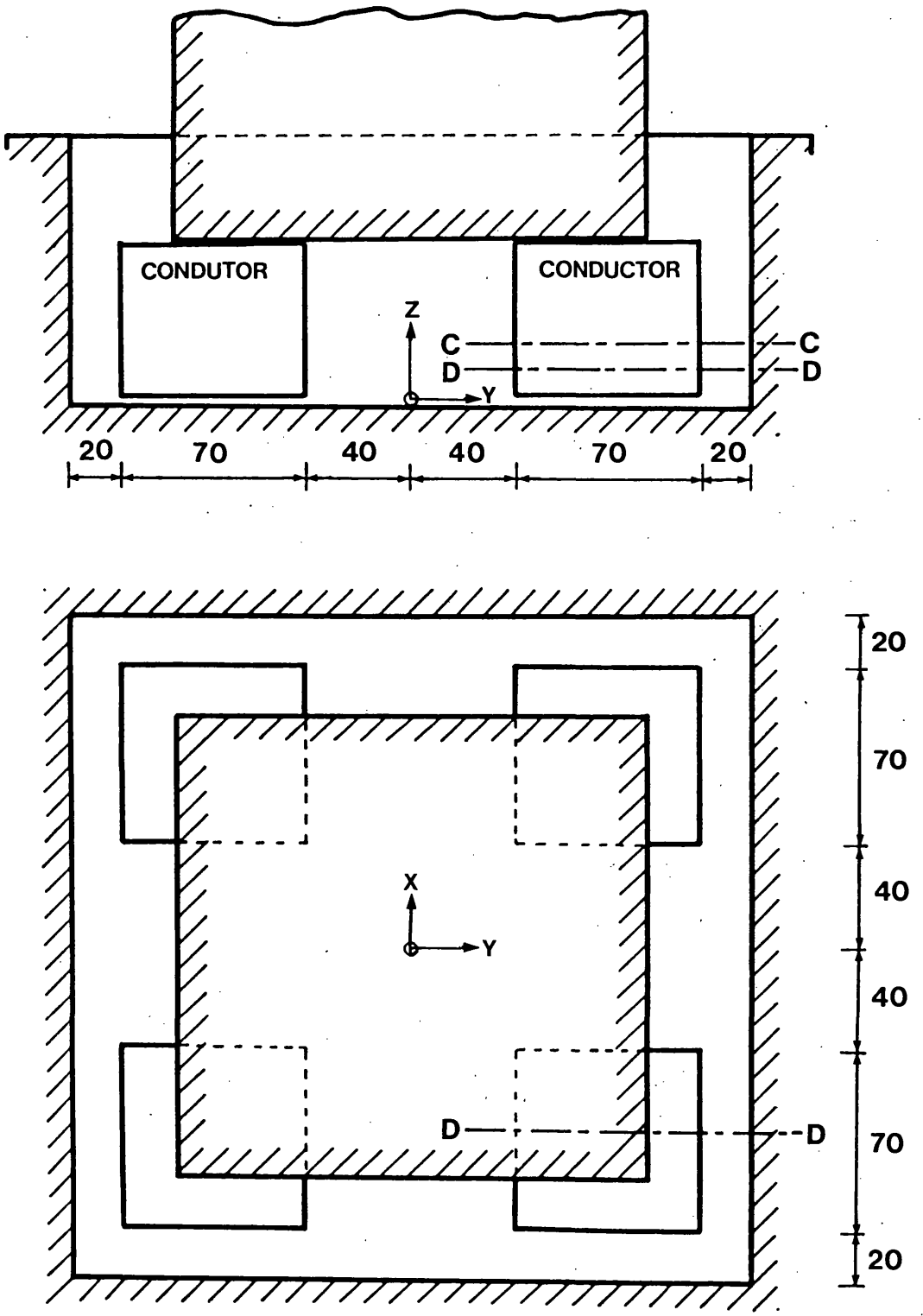

Fig. 4.28 Field region with the four quarters of the split conducting block moved outwards.

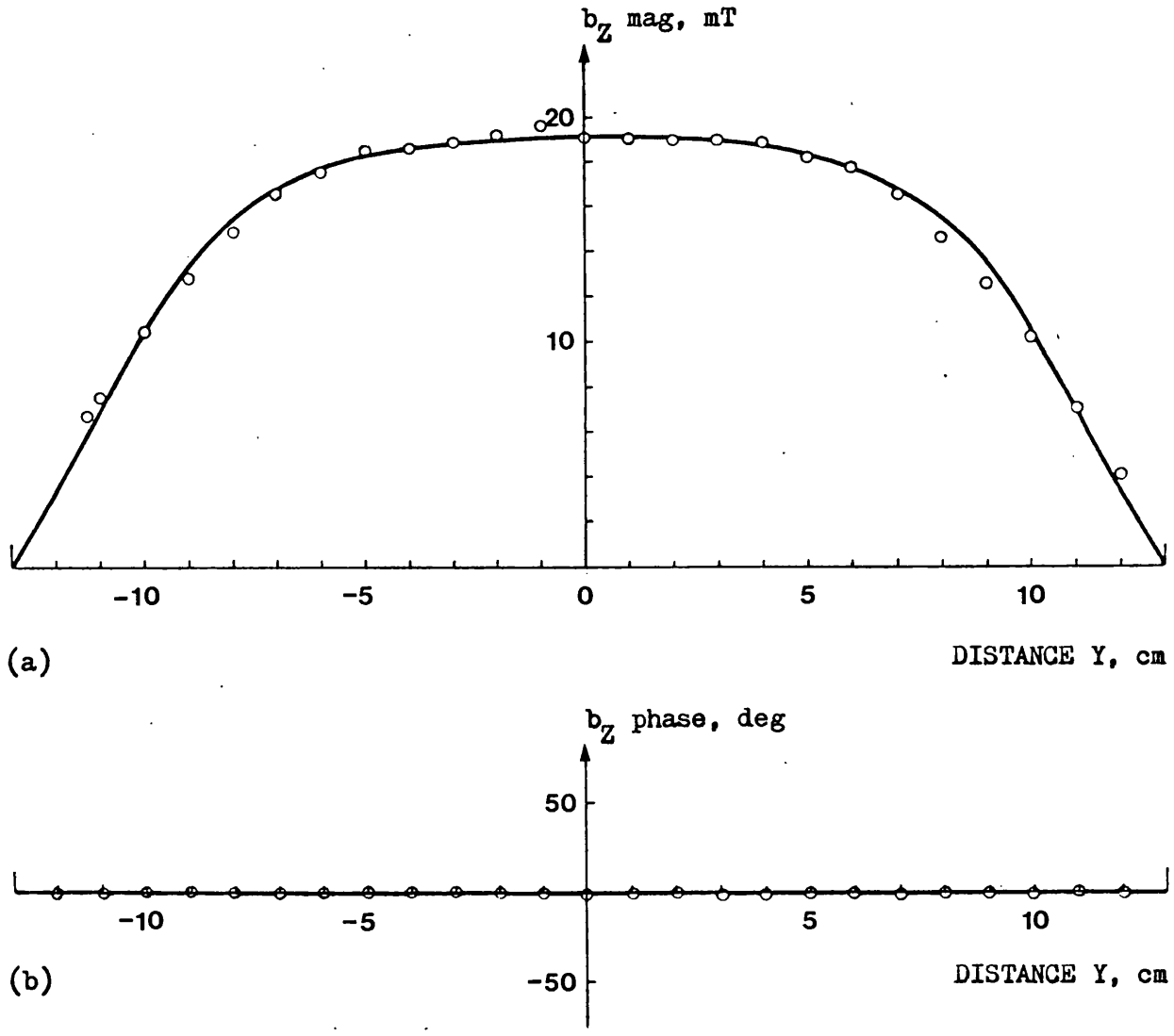

Fig. 4.29 Z-directed flux density for the split block moved outwards, X = 0 mm, Z = 2 mm o measured — calculated
(a) magnitude (b) phase

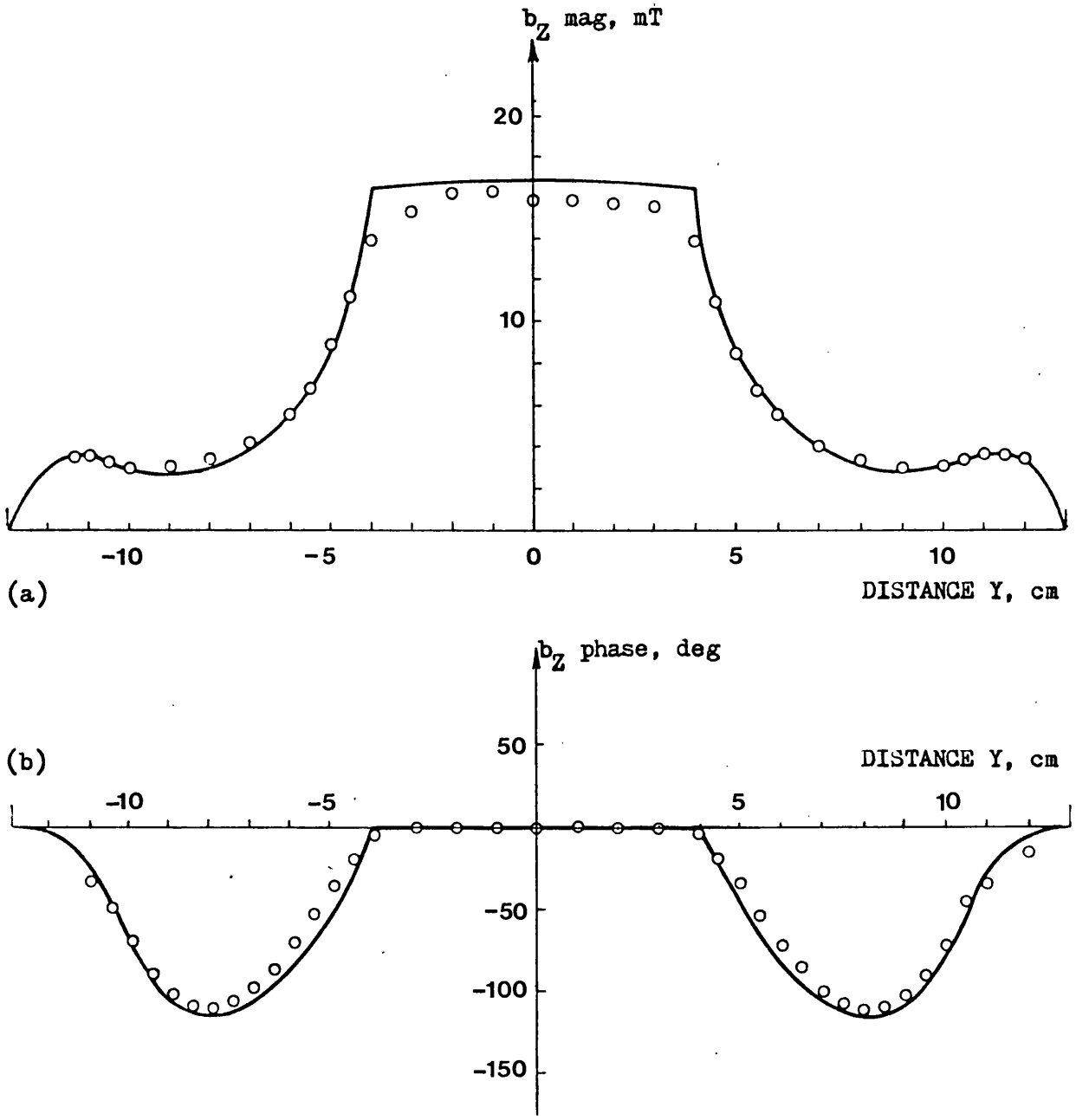

Fig. 4.30 Z-directed flux density for the split block moved outwards, X = 70 mm, Z = 2 mm o measured — calculated
(a) magnitude (b) phase

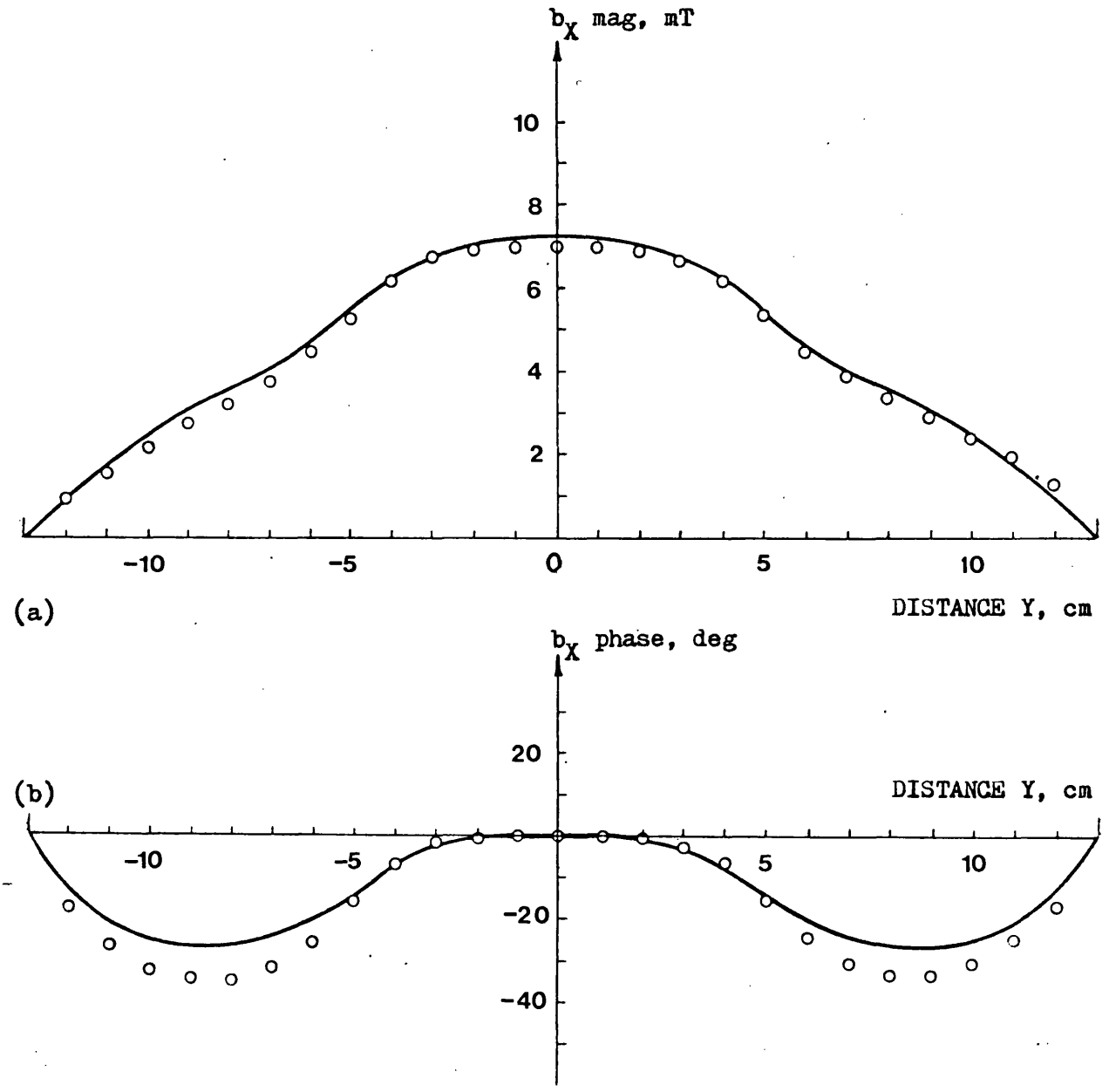

Fig. 4.31 X-directed flux density for the split block moved outwards, X = 120 mm, Z = 20 mm o measured — calculated
(a) magnitude (b) phase

results, Fig. 4.6, shows that the Z-directed current flow has decreased the magnitude of the X-directed flux density at some points in the vicinity of the block to almost half the magnetostatic value and produced a phase shift of over 30 degrees. This is comparable to the effect of the X-Y circulation of current on the Z-directed flux density seen in Fig. 4.30. Current flow in all the three co-ordinate directions must therefore be of the same order of magnitude.

The magnitude of calculated current densities in the quarter blocks in the X direction and the Z direction are given in Fig. 4.32 and Fig. 4.33 respectively. The currents represented by these figures have the same general circulation paths as those shown in Fig. 4.26(b) and Fig. 4.27(b), for the split block completely under the pole. The ratio of the maximum magnitude of the X or Y directed current density to the maximum magnitude of that in the Z direction is now less than 2:1. A truly three-dimensional eddy current problem has therefore been solved. Close agreement between the calculated and measured flux density values in this problem therefore gives confirmation of the validity of the linked network method for the calculation of three-dimensional electromagnetic fields.

4.5 Details of calculations

Calculations were performed over a quarter of the field region, using the planes of symmetry AA and BB, shown in Fig. 4.1(b), as flux plane boundaries. To simplify the remaining boundary conditions all iron was assumed to have infinite permeability and a further flux plane boundary was assumed to exist between the pole and box at (a)(a) shown in Fig. 4.34. These assumptions are not a requirement of the method, but they help to reduce the number of elements required for a solution.

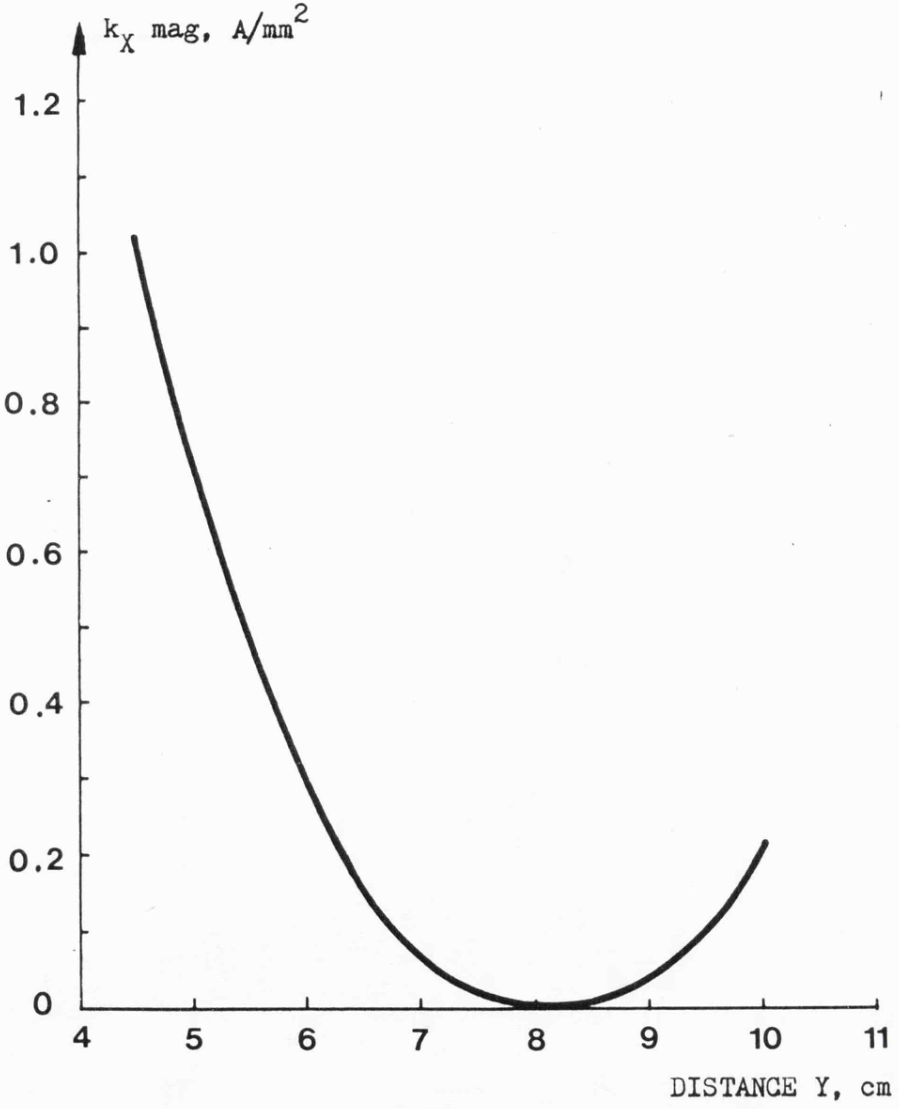

Fig. 4.32 Magnitude of the calculated X-directed current density in a quarter of the split block moved outwards, X = 70mm, Z = 10mm (line DD Fig. 4.28)

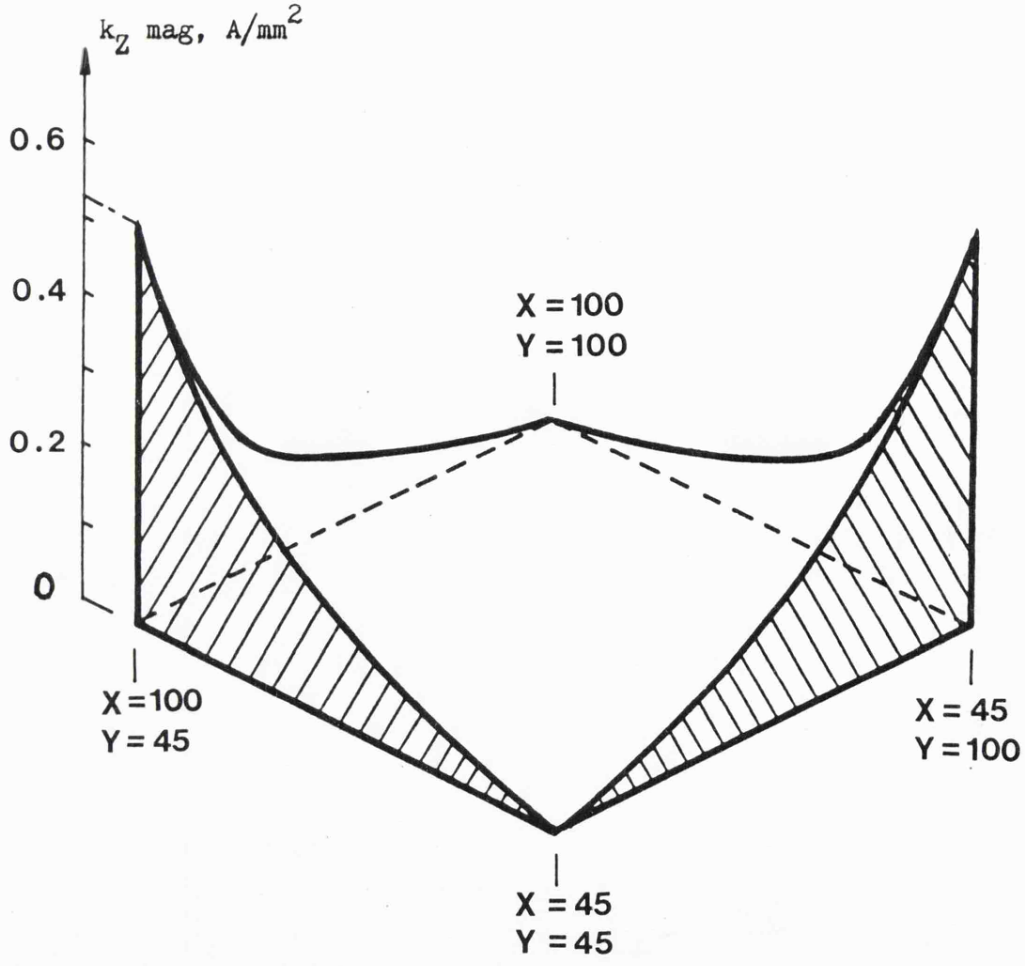

Fig. 4.33 Magnitude of the calculated Z-directed current density in a quarter of the split block moved outwards, normal to plane Z = 20mm (plane CC Fig. 4.28)

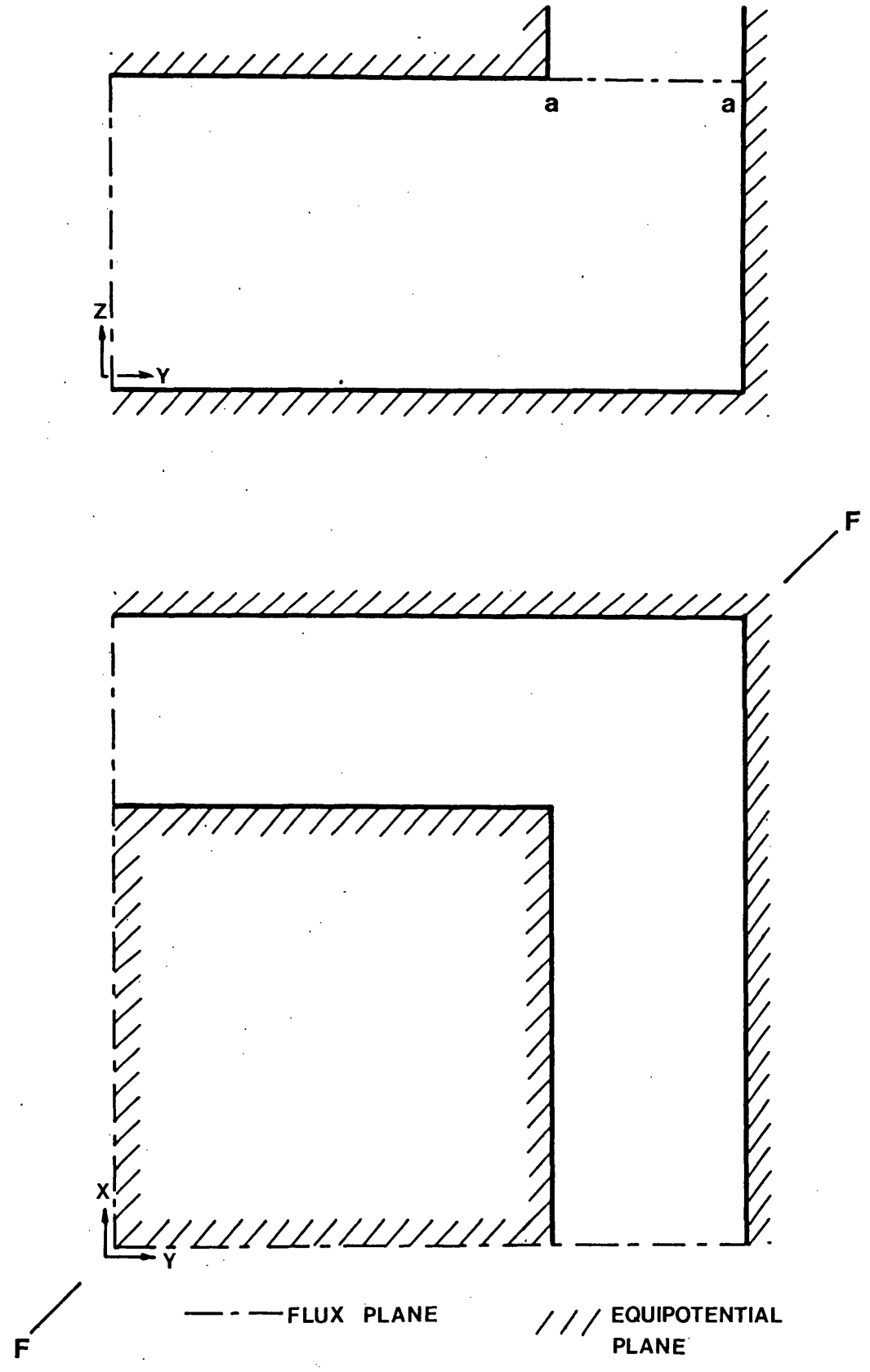

Fig. 4.34 Field region showing boundary conditions for calculations.

The calculation region, shown in Fig. 4.34, is then a block shape with equipotential boundaries on the base and two sides, flux plane boundaries on the remaining two sides and a mixed equipotential/flux plane boundary on the top. A further plane of symmetry exists along FF in the calculation region as shown in Fig. 4.34. This has not been exploited in the calculations because its use as a boundary would require the introduction of tetrahedral blocks[20]. All the present work has been confined to the use of rectangular brick elements. The presence of this plane of symmetry in the model is nevertheless useful as an additional check for the calculations. In all cases this plane of symmetry did appear naturally in the results.

The dimensions of the magnetic network used in the calculations for magnetostatic, thin plate, full block and split block completely under the pole are shown in Fig. 4.35. This network is 6 x 6 x 3 blocks in the X, Y and Z directions respectively. For the magnetostatic and thin plate calculations the longest Z-directed elements were placed at the top of the network as shown in Fig. 4.35. These elements were similarly placed for the full and split block cases when the 4 mm access gap was above the block, but were placed on the bottom of the network when the gap was under the block. This enabled the position of the access gap to be taken into account without having to change the electric circuit. In all cases the excitation mmf was included as an ideal mmf generator of 1000 + j0 AT (peak) in a zero reluctance branch connected between the pole and box. The dimensions of the electric circuits for the thin plate, full block and split block completely under the pole are shown in Fig. 4.36. In the space between the quarters of the split block, when they are in the "moved

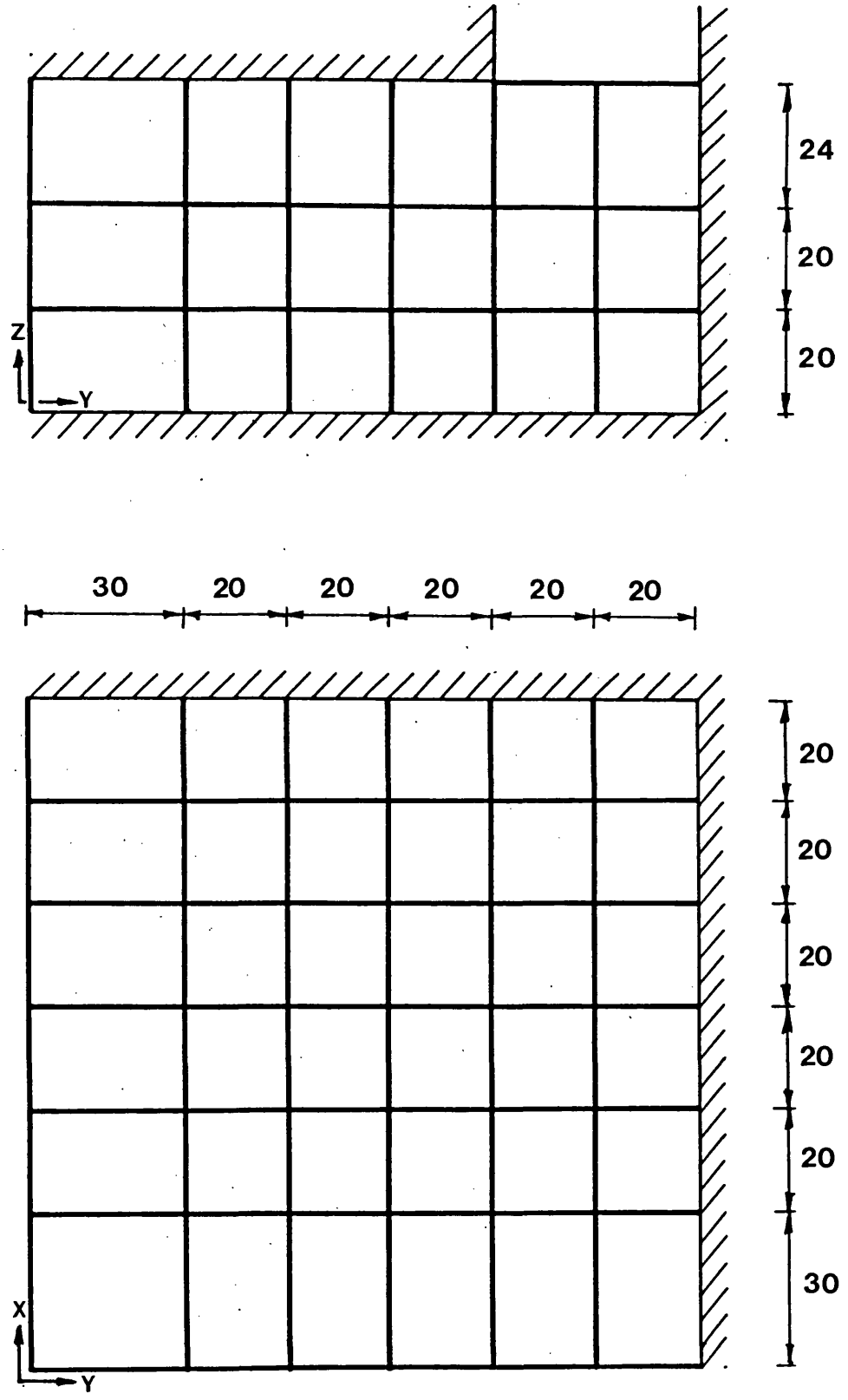

Fig. 4.35 Dimensions of the magnetic network for magnetostatic, thin plate, full block and the split block completely under the pole calculations.

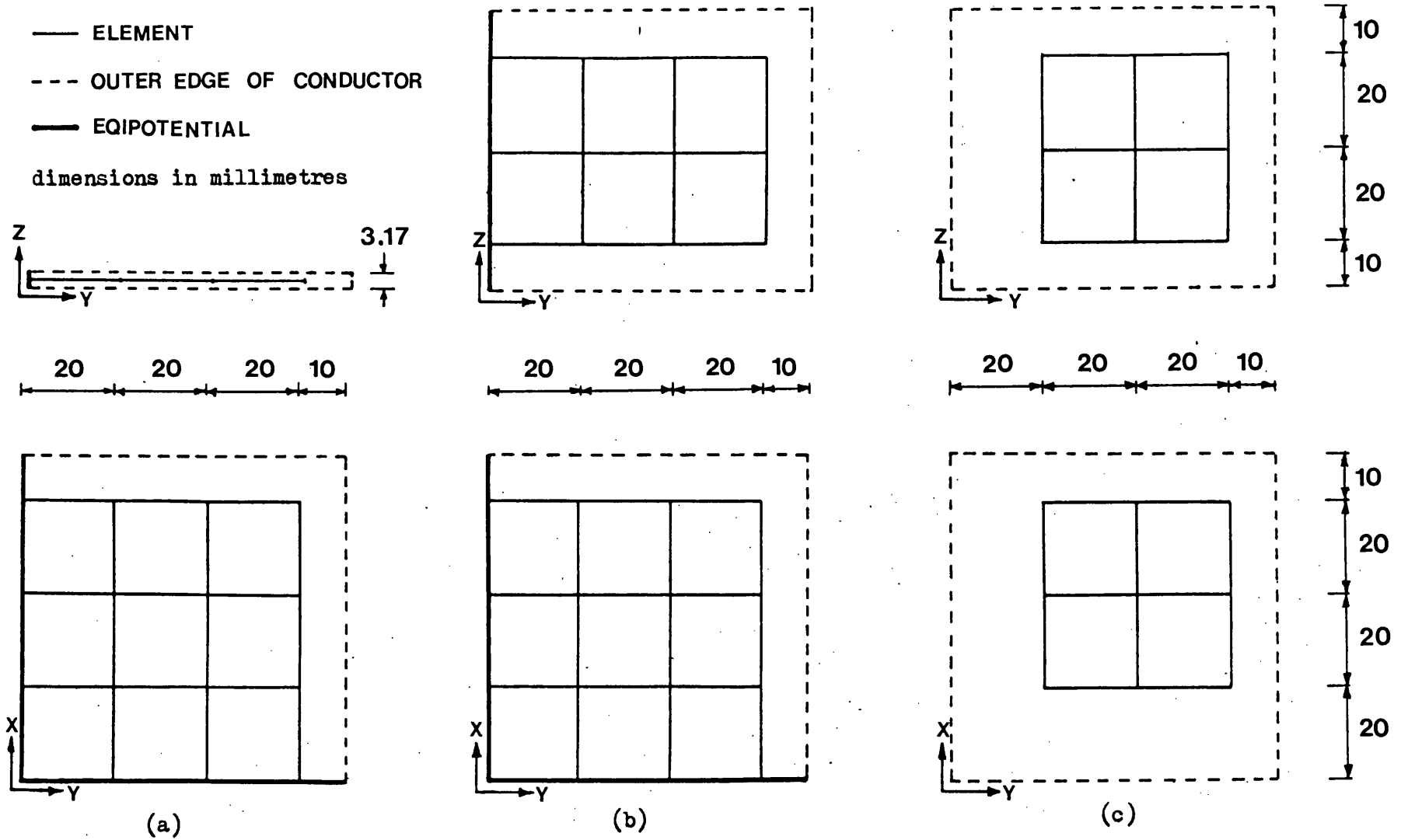

Fig. 4.36 Dimensions of the electric networks for calculations with,
(a) thin plate
(b) full block
(c) split block completely under the pole

out" position, the magnetostatic field is almost constant. For this case the branch dimensions of the magnetic network were therefore changed to that shown in Fig. 4.37. This allowed the use of more elements in the region of the block, where the field is likely to be changing rapidly, without increasing the total number of magnetic circuit elements. The electric circuit used for this case is shown in Fig. 4.38.

Detailed network statistics, storage and computation times are given in Table 4.1 for each of the problems solved. Calculation times are for solutions performed on the SERC IBM 195 computer. The column entitled "variables" gives the dimension of the set of linear simultaneous equations solved. The variables per node quoted are obtained by dividing the total number of variables by the total number of nodes. The variables per block are obtained in a similar manner. As can be seen from Table 4.1 these two quantities are different for each problem. For this reason they are not of great value in describing the number of variables required in the mesh method solution of the linked network problem. The number of variables for the mesh method must be calculated over the whole network model and is equal to the total number of link branches in both magnetic and electric circuits. The variables per node and variables per block have been included, however, as they do give a rough idea of the number of variables required, for the problems solved, in a form used widely for field calculation methods. A comparison is made in Chapter 5, between the number of variables required by the mesh variable linked network method and that required by the T-Ω method to solve identically subdivided field regions for two specific problems.

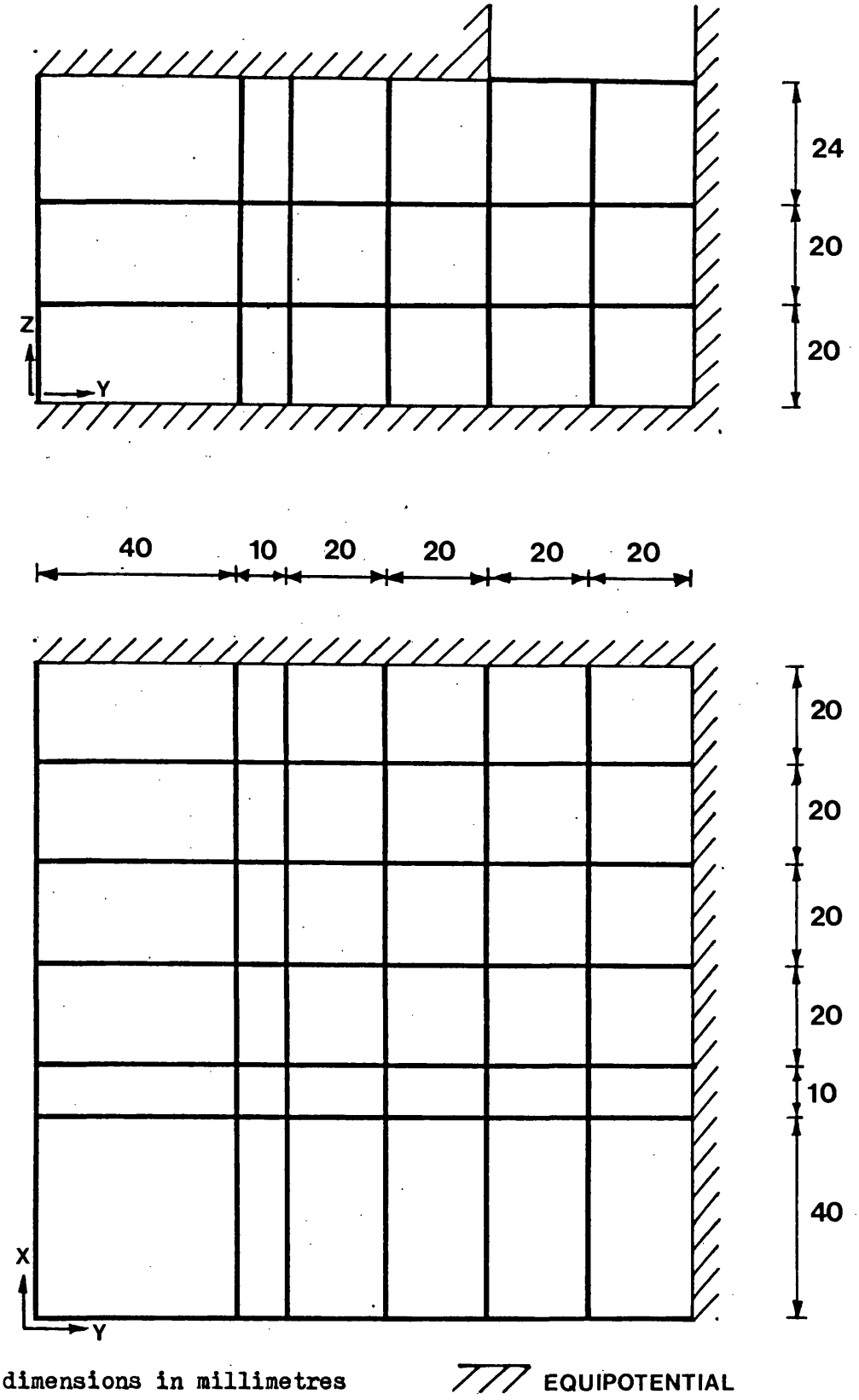

Fig. 4.37 Dimensions of the magnetic network for the calculations with the split block moved outwards.

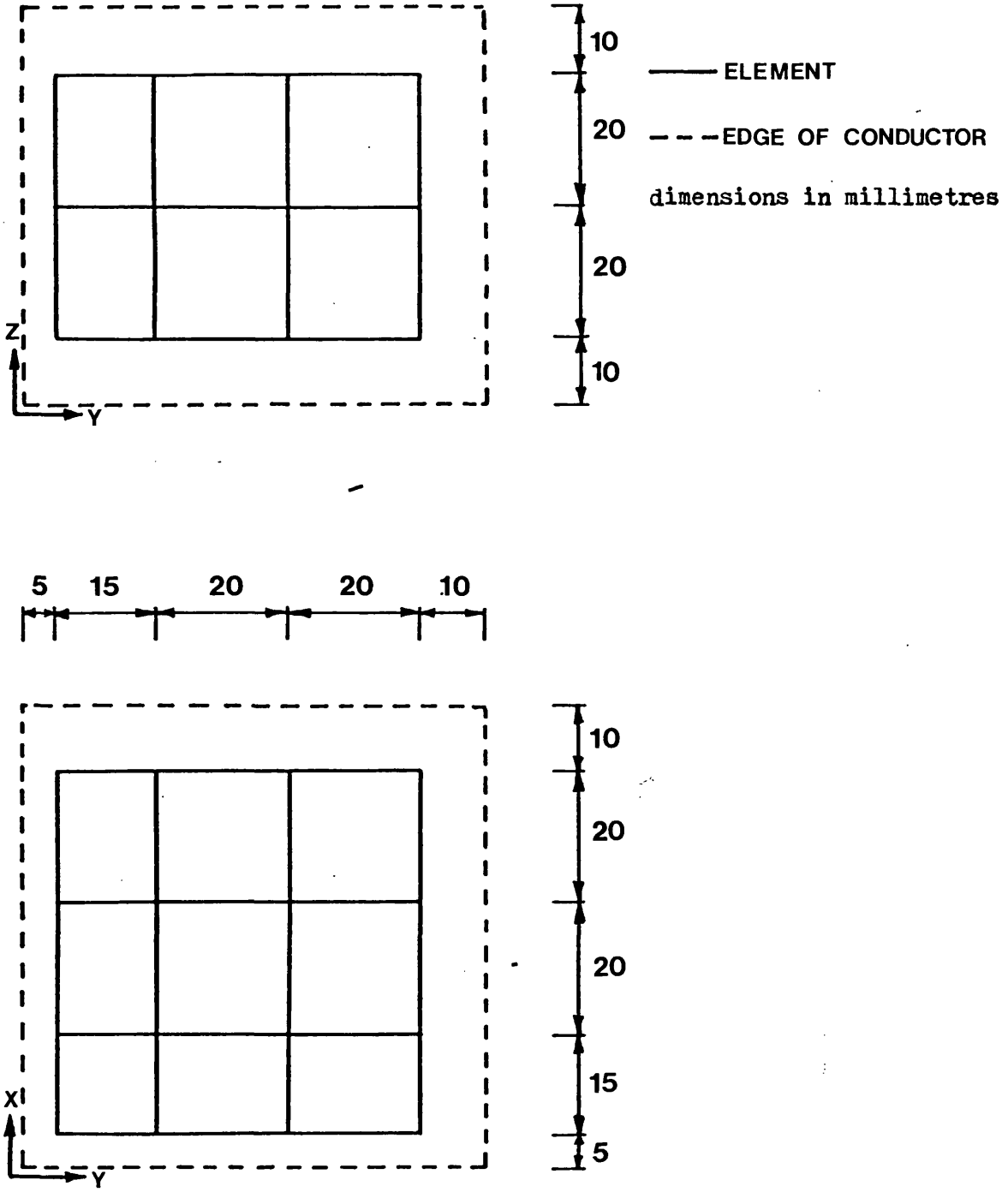

Fig. 4.38 Dimensions of the electric network for the calculations with the split block moved outwards.

		Blocks	Nodes	Branches	Variables	Variables per Node	Variables per Block	Storage (K bytes)	CPU Time (sec)
Magnetostatic	Magnetic	108	85	285	201	2.36	1.86	33	5
	Electric	0	0	0	0				
	Total	108	85	285	201				
Thin Plate	Magnetic	108	85	285	201	2.21	1.79	63	12
	Electric	9	10	18	9				
	Total	117	95	303	210				
Full Block	Magnetic	108	85	285	201	2.18	1.95	79	17
	Electric	18	28	72	45				
	Total	126	113	357	246				
Split Block Under Pole	Magnetic	108	85	285	201	2.04	1.97	69	14
	Electric	8	27	54	28				
	Total	116	112	339	229				
Split Block Moved Outwards	Magnetic	108	85	285	201	1.94	2.05	84	21
	Electric	18	48	104	57				
	Total	126	133	389	258				

Table 4.1 Network statistics, storage requirements and computation times for the calculations

4.6 Discussion and conclusions

A comparison has been made between measured flux density results from a variety of two and three-dimensional eddy current problems and equivalent calculations using the linked network method. The calculations were performed with a relatively coarse network to obtain a solution program that did not require excessive computer storage and run time. Nevertheless, in all cases the general shape of the flux density was predicted in magnitude and phase. The shape of the calculated current density was also consistent with the flux density in the region of the conductors. Furthermore, the agreement between measured and calculated flux density was good at most points. Some discrepancies did exist in certain regions. These were attributed mainly to the coarseness of the network and also to possible slight errors in measurement at certain points. However, the agreement between calculated and measured flux density was sufficiently good to validate the linked network method for the solution of three-dimensional eddy current problems. Regarding the numerical accuracy of the mesh method for the solution of the linked network problem, no evidence has been found to suggest any numerical instability or ill-conditioning in the solution.

The test problem has a relatively simple geometry and in the calculations all boundaries were well defined. These conditions were only imposed to limit the number of elements required in the solution. Any geometry can be solved by the linked network method. The accuracy of the results will of course depend on how well each shape in the region is modelled by the discrete network. At present only rectangular brick shaped elements have been considered. These are obviously more suited to straight boundaries but they can be used to approximate curves in a stepwise manner if required. With regard to the boundaries,

most field problems can be terminated at some point by a far field boundary consisting of a flux plane or equipotential surface. Both these types of boundary were used in the test example.

The conductor in the test problem was assumed to be non-magnetic. This was implemented in the network solution by using unit relative permeability for the magnetic elements in the region of the conductor. A value other than unity could well have been specified. This method can be used to represent non-conducting iron of finite permeability and also as a first approximation for a ferromagnetic conductor, with no conceptual change to the calculation technique. It is therefore concluded that the linked network method presented for the calculation of full three-dimensional electromagnetic fields is applicable to a wide range of field problems encountered in electrical engineering.

CHAPTER 5

COMPARISON OF THE NUMBER OF VARIABLES REQUIRED TO SOLVE AN IDENTICALLY SUBDIVIDED FIELD PROBLEM BY THE LINKED NETWORK METHOD AND THAT REQUIRED BY THE T-Ω METHOD

The T-Ω method is described in references 11 and 13. It uses a single magnetic scalar potential Ω to define the field in non-conducting regions. In conductors, Ω alone is not sufficient to describe the field. It is therefore supplemented by the electric vector potential T, defined by equations 5.1 and 5.2,

$$\text{Curl } T = k \tag{5.1}$$

$$H = T - \text{grad } \Omega \tag{5.2}$$

where k is the solenoidal component of current density and H is the total magnetic field strength.

Equation 5.1 shows that T is a current describing function and equation 5.2 shows that T is the solenoidal component of the magnetic field strength. The vector T is therefore equivalent to h, defined in the linked network field model. Also the scalar potential Ω is equivalent to the node potential in the magnetic network. Hence, both T and Ω are represented in the linked network model. The T-Ω method and the mesh variable linked network method differ, however, in the set of variables for which the field is solved. In the linked network method a set of independent closed loop flow variables are chosen and in the T-Ω method a set of "node potentials" are used. This makes a comparison of the two methods, on the basis of the number of variables required, difficult because, in general, the ratio of the number of

independent closed paths to the number of nodes in a subdivision is not a constant. A comparison of this type has been made, however, for two specific cases. These give a general idea of the ratio of the number of variables required to solve an identically subdivided problem by the mesh variable linked network method, to the number required to solve it by the T-Ω method. The general trend as to which type of problem either method is best suited, on the basis of the number of variables required, is also shown. The comparison does not attempt to show any aspect of the relative accuracies of the two methods.

In the T-Ω method, the Ω variables give rise to one variable at each separate node in the subdivision representing the whole field region. Boundary conditions are imposed in the usual way for magnetic scalar potential. T is a three-dimensional vector, so there are in general three components of T at each node in conducting regions. The vector T is zero in non-conducting regions. In theory, because div T = 0, it should only be necessary to explicitly calculate a maximum of two components of T at each point where T is non-zero. This method has been used[14], but following a discussion with the authors, it is believed that there are numerical difficulties associated with this approach. This being the case, it is preferable to calculate all three components of T explicitly. The T variables in the T-Ω method therefore give rise to three unknowns at each node within conducting regions. On the surface of conductors the boundary condition, that the normal component of current density is zero, is imposed by making all tangential components of T zero for the surface nodes. This makes the total number of unknowns resulting from T slightly less than three times the number of nodes in conducting material. Summing

the number of unknowns resulting from both T and Ω gives the total number of variables for a T-Ω solution.

The example field problems chosen for comparison of the number of variables required by the mesh variable linked network and the T-Ω methods are the thin plate and split block moved outwards problems solved in Chapter 4. The same subdivisions of the field regions are used as before. These are shown in Chapter 4, Fig. 4.35 and Fig. 4.36(a) for the thin plate and Fig. 4.37 and Fig. 4.38 for the split block moved outwards. The number of variables required for a mesh variable linked network solution of these problems have already been given in Chapter 4, Table 4.1. These values are repeated in Table 5.1 below. The corresponding number of variables for a T-Ω solution of the problems, using a subdivision identical to that used for the magnetic circuit in the linked network solutions, are also given in Table 5.1.

	variables for network solution	variables for T-Ω solution	$r = \frac{\text{network variables}}{\text{T-Ω variables}}$
thin plate	210	130	1.61
split block moved out	258	181	1.42

Table 5.1 Variables required to solve identical subdivisions by mesh variable linked network and T-Ω methods

It can be seen from the comparison in Table 5.1 that for the two example problems the ratio (r) of the number of variables required for the network method to that for the T-Ω method is approximately 1.5. This figure is of course problem dependent, but it does give an order

of magnitude for comparing the number of variables required by the two methods in a typical eddy current problem. Of greater importance, however, is the trend shown for the number of variables required. That is, if the field subdivision is predominantly in non-conducting material the ratio r increases, thereby favouring the T-Ω method. If, however, much of the field subdivision is in solid conductor the ratio r decreases and thereby moves to favour the mesh variable linked network method.

The comparison given has only been made on the basis of the number of variables required to solve a given subdivision. This is only one factor affecting the suitability of a particular method. Other factors such as computer storage, ease of solution and numerical accuracy must be considered before making a recommendation on the suitability of either method. In particular, the mesh method has the important advantage that the coefficient matrix of the field equations is symmetric, whereas that for a T-Ω solution is asymmetric. This means that only half the coefficient matrix need be stored in the mesh method solution.

CHAPTER 6

CONCLUSIONS AND SUGGESTIONS FOR FUTURE WORK

A numerical method has been developed for the calculation of three-dimensional electromagnetic fields. The validity of the method has been confirmed by comparing calculated results with equivalent measurements for a full three-dimensional power frequency eddy current problem.

The field model used represents the continuous electromagnetic field in terms of two separate networks, one to represent the magnetic part and the other to represent the electric part of the field. Linkage between the two networks has been specified so as to produce a complete field model in which the role of all field variables is clearly defined. Interface conditions are represented in the field model merely by assigning appropriate branch reluctance or resistance values in either part of the network. This is straightforward to perform and does not complicate the numerical solution procedure. The field model is therefore simple yet concise and because it is expressed in circuit terms it should be easy to use by electrical engineers in general.

A field model expressed in network terms has the further advantage that conventional circuit analysis programs, that are normally readily available to the electrical engineer, can be used to solve the model. At present the commercial programs do not have extensive use in this respect for three-dimensional networks, because they are too limited in the number of degrees of freedom that can be solved.

The use of network analysis programs for field solution is, however, a useful facility that should prove increasingly important as more powerful commercial programs are developed.

The network method has been developed using only rectangular brick elements to subdivide the field. Such elements are believed to be the most convenient subdivision to visualize and set up in three-dimensional problems. Curved boundaries can be represented in a stepwise manner by these rectangular elements, but some form of tetrahedral block would obviously be more efficient in terms of the number of elements required. The initial development of a tetrahedral element for the network method has been performed and is published in reference 20. Further investigation into the use of tetrahedral elements would form a useful area for future work.

In the work presented the linked network field model has been solved by the mesh current technique. The number of independent variables required to solve a network by this method is equal to the number of link branches in the network. In general, more independent variables are required to solve a three-dimensional network by mesh variables than by node potentials. For the network field model, in which linkage between two separate parts of the network is through mesh quantities, solution exclusively in terms of node potential has not yet been achieved. However, the use of mesh variables does have the advantage that when flux or current is the desired field quantity, as is often the case, these are solved for directly. If the linked network was solved for node potential, the solution would have to be differentiated numerically to obtain flux and current. When high permeability or high conductivity materials are present, this leads to a requirement for higher accuracy in a node potential than in a mesh variable solution. There is obviously a need for future work in this

area to investigate possible alternative methods for solving the network and to compare their performance with the mesh variable solution. In addition to a complete node potential solution, a mixed node and mesh variable formulation or a solution including solenoidal branch sources as independent variables might be considered.

The solution of the complex simultaneous equations resulting from the mesh variable formulation of the linked network problem has been investigated. The coefficient matrix of the field equations is very sparse but does not have any recognisable structure that limits the creation of non-zero elements during an elimination process. For large sets of equations, this can make the solution by a direct method costly in terms of storage and computation time. The coefficient matrix is also symmetric, but it is not positive definite. The symmetry of the matrix is a great advantage because it means that only approximately half the matrix need be stored during a solution. However, the general form of the coefficient matrix makes the solution of the field equations by many of the most common iterative methods impracticable. A preconditioned conjugate gradient algorithm, applied to the normalized system of equations, was therefore proposed as a method for solving the mesh field equations. The preconditioning used was an incomplete Choleski decomposition with no non-zero elements generated, and the sparsity pattern of the original matrix imposed on the decomposition. It was shown that this algorithm gives efficient solution of the mesh equations in many fewer iterations than the theoretical maximum, provided that the preconditioning is accurate.

The effectiveness of the incomplete Choleski preconditioning for the mesh equations was shown to depend greatly on the choice of the tree and link branches in both parts of the linked network

model. If the tree branches in the linked networks are chosen, as far as possible, to be the branches of smallest reluctance or resistance, then the most accurate preconditioning is achieved. With the choice of a radial type of network tree, as used throughout, it was further shown that the accuracy of the incomplete Choleski preconditioning is reduced as the size of the network increases. Future work would therefore include an investigation into an alternative choice of tree form, with a view to avoiding this problem. The bi-conjugate gradient method should also be investigated because an algorithm of this type can solve the basic, symmetric, non-positive definite system without using the normalized equations. This should give a reduction in solution times but would increase storage.

Flux density distributions from a three-dimensional eddy current field solution using the mesh variable linked network method have been compared with equivalent measurements from a test problem. A relatively coarse network was used for the calculations, but nevertheless these were shown to be in good agreement with measurements. The fact that a relatively coarse network appears to give a good representation of the field is important in three-dimensional problems, because in this case the number of independent variables increases rapidly as the network is refined. Further tests are really required with the test problem solved using an increasingly fine mesh before any quantitative measure of accuracy can be estimated for the method. It is hoped that this can be included in future work.

A comparison has been made between the number of variables required by the mesh variable linked network method and that required by the T-Ω method to solve identically subdivided problems. This showed that the mesh method is likely to use more variables than T-Ω to solve a

given subdivision, particularly when much of the field region is in non-conducting material. The comparison was made solely on the number of variables required for a given subdivision. Other factors such as computer storage, ease of solution and accuracy are also important in the field solution method. The mesh method has the significant advantage that the coefficient matrix of the mesh field equations is symmetric, whereas that for T-Ω is asymmetric. Thus, only half the coefficient matrix need be stored in the mesh method solution.

A feature which is common to all numerical three-dimensional field calculation techniques is the rapid increase in the number of elements required when the subdivision is extended in all three dimensions. For three-dimensional problems that are periodic in one co-ordinate direction, the number of elements required is greatly reduced by the use of a quasi-three-dimensional (quasi-3D) form of the field problem. In this model the field in a periodic direction is represented by a Fourier series. A network model for the quasi-3D field has been developed, in Annex 1, from the general model. Its validity has been confirmed by comparison of calculated flux density, normal and thrust force characteristics with equivalent measurements from an axial flux linear induction motor. For problems that are periodic in one co-ordinate direction the quasi-3D model gives a full three-dimensional field solution at low cost in terms of both storage and computation time.

ANNEX 1

SOLUTION OF QUASI-THREE-DIMENSIONAL ELECTROMAGNETIC FIELDS BY THE LINKED NETWORK METHOD

A 1.1 Introduction

The calculation of full three-dimensional electromagnetic fields requires a great deal of computer time and storage. In situations where the field is periodic in one or more co-ordinate directions a great simplification of the field solution is possible. The field in this case is said to be quasi-three-dimensional (quasi-3D).

The technique of quasi-3D field solution is well known[40,11]. A quasi-3D form of the full three-dimensional linked network model described in Chapter 2 is now developed. It is applicable to three-dimensional field problems that can be considered periodic along one cartesian co-ordinate direction.

With certain simplifying assumptions the magnetic field of a linear induction motor (LIM) can be regarded as a quasi-3D field problem. To demonstrate the validity of the quasi-3D form of the linked network field model, it is used to calculate the electromagnetic field in the analysis of a LIM. The calculated flux density is compared with measured values at standstill. Subsequent field calculations are then used to obtain normal and thrust force characteristics that are again compared with measurements from the test machine.

A1.2 Derivation of the quasi-3D linked network model

A1.2.1 The quasi-3D field equations

The quasi-3D field model is derived for a cartesian co-ordinate system x, y, z in which the field varies sinusoidally in the y direction. The following assumptions are made regarding the field.

1) All geometrical sections in the x/z plane are the same.

2) All field components vary in the y-direction with either $\sin(ay + \alpha)$ or $\cos(ay + \alpha)$ where a and α are constants.

3) Permeability (μ) and conductivity (σ) are constants within individual elements of a subdivided field region.

4) The time rate of change of the field is such that the displacement current is negligible.

The electromagnetic field is governed, as usual, by Maxwell's equations and the constitutive relations,

$$\begin{aligned} \text{curl } h &= k & \text{curl } H &= 0 \\ \text{curl } f &= -\frac{\partial b}{\partial t} & \text{curl } F &= 0 \\ \text{div } b &= 0 & & \\ \text{div } k &= 0 & \text{div } K &= -\frac{\partial \rho}{\partial t} \\ (K + k) &= \sigma(F + f) & & \\ b &= \mu(H + h) & & \end{aligned} \qquad \text{(A1.1)}$$

where lower and upper case symbols represent the solenoidal and lamellar components of the field respectively. Let the excitation to the field be such that the components of the flux density vector, b, are of the form,

$$b_x = \hat{b}_x \cos ay$$

$$b_y = \hat{b}_y \sin ay \qquad \text{(A1.2)}$$

$$b_z = \hat{b}_z \cos ay$$

where variables covered by '^' are the peak values of the corresponding y distribution. These may be a function of time. The constant 'a' is also equal to $\frac{\pi}{\tau_p}$, where τ_p is the pole pitch of the y distribution. For consistency of the field equations A1.1 the form of the components of the remaining field variables are:

$$h_x = \hat{h}_x \cos ay \qquad H_x = \hat{H}_x \cos ay$$

$$h_y = \hat{h}_y \sin ay \qquad \text{A1.3} \qquad H_y = \hat{H}_y \sin ay \qquad \text{A1.4}$$

$$h_z = \hat{h}_z \cos ay \qquad H_z = \hat{H}_z \cos ay$$

$$k_x = \hat{k}_x \sin ay \qquad f_x = \hat{f}_x \sin ay$$

$$k_y = \hat{k}_y \cos ay \qquad \text{A1.5} \qquad f_y = \hat{f}_y \cos ay \qquad \text{A1.6}$$

$$k_z = \hat{k}_z \sin ay \qquad f_z = \hat{f}_z \sin ay$$

$$F_x = \hat{F}_x \sin ay$$

$$F_y = \hat{F}_y \cos ay \qquad \text{A1.7}$$

$$F_z = \hat{F}_z \sin ay$$

Equations A1.2 to A1.7 express the y-distribution of all field components in terms of their peak values. When these conditions are incorporated in the linked network model for the full three-dimensional electromagnetic field, equivalent circuits are obtained for the quasi-3D field problem.

A1.2.2 Equivalent circuit for the magnetic part of the quasi-3D field

The conditions imposed by equations A1.2 to A1.7 on the full network model of the magnetic field derived in Chapter 2 are found by recalculating the branch relations. This is performed for the full network model of the magnetic field, shown in outline in Fig. A1.1. A semi-regular network has been used in which the network separation in each of the x, y and z directions is a constant and is given by Δx, Δy and Δz respectively. This type of network has been used to simplify the algebra in the derivation of the quasi-3D model. The model for a general irregular network follows immediately from that of the semi-regular case. Let the region between planes P and Q in Fig. A1.1 represent one pole of the y co-ordinate distribution in the quasi-3D field. Planes P and Q are equipotential surfaces, because for $y = \pm \frac{\tau_p}{2}$ there is only y-directed flux (equation A1.2). The potential of these two planes must be the same, but the actual value is arbitrary. They have therefore been assigned a potential of zero.

The magnetic potential or magnetomotive force (mmf) relations between node 0 in Fig. A1.1 and the surrounding nodes 1-6 are first found. The mmf is defined by the line integral of the magnetic field strength. In the full three-dimensional network model derived in Chapter 2, the lamellar and solenoidal components of mmf were given the symbols M and m respectively. The mmf relation between nodes 0 and 1 (Fig. A1.1) of a quasi-3D field obeying equations A1.2-A1.7 is therefore given by,

$$0\text{-}1 \text{ (at } y = 0) \qquad (M + m)_{01} = \int_0^1 (\hat{H}_x + \hat{h}_x)_{01}\, dx$$

This simplifies to,

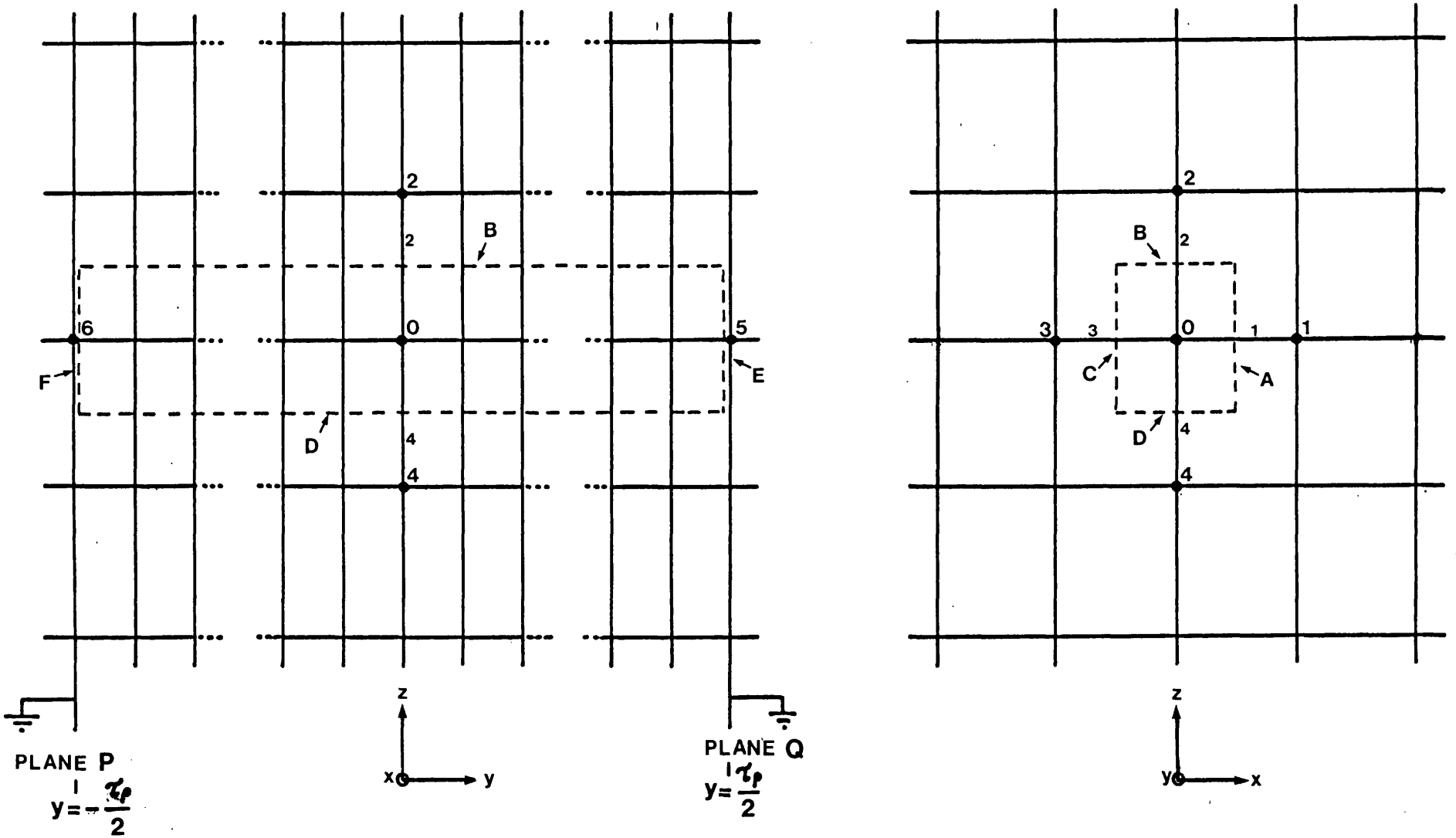

Fig. A1.1 Outline of a full three dimensional network model to represent a magnetic field that is periodic in the y direction.

$$(M + m)_{01} = (\hat{H}_x + \hat{h}_x)_{01} \Delta x \qquad \text{A1.8}$$

where Δx is the distance between nodes 0 and 1 in Fig. A1.1. The mmf relations for the following node pairs are obtained in a similar manner.

3–0 $$(M + m)_{30} = (\hat{H}_x + \hat{h}_x)_{30} \Delta x \qquad \text{A1.9}$$

0–2 $$(M + m)_{02} = (\hat{H}_z + \hat{h}_z)_{02} \Delta z \qquad \text{A1.10}$$

4–0 $$(M + m)_{40} = (\hat{H}_z + \hat{h}_z)_{40} \Delta z \qquad \text{A1.11}$$

However between nodes 0 and 5 the mmf relation is

0–5 $$(M + m)_{05} = \int_0^{\tau_p/2} (\hat{H}_y + \hat{h}_y)_{05} \sin ay \, dy$$

This simplifies to

$$(M + m)_{05} = \frac{1}{a} (\hat{H}_y + \hat{h}_y)_{05} \qquad \text{A1.12}$$

Similarly between nodes 6 and 0

6–0 $$(M + m)_{60} = \frac{-1}{a} (\hat{H}_y + \hat{h}_y)_{60} \qquad \text{A1.13}$$

The flux relationships between node 0 and the surrounding nodes 1 to 6 (Fig. A1.1) of a quasi-3D field obeying equations A1.2–A1.7 are found as follows. Referring again to Fig. A1.1, a dotted volume surrounding node 0 is formed by areas A → F shown. The sides A→D of this volume are defined by the double subdivision of a region as used in the derivation of the full three-dimensional model (Chapter 2, section 2.2). The sides E and F are defined by the equipotential planes P and Q. Let ϕ_{01} be the total flux through area A. This area is perpendicular to branch 1 and hence,

$$\phi_{01} = \int_{-\tau_p/2}^{\tau_p/2} \Delta z \, (\hat{b}_x)_{01} \cos ay \, dy$$

$$\therefore \quad \phi_{01} = \frac{2\Delta z}{a} (\hat{b}_x)_{01} \qquad \text{A1.14}$$

Similar expressions are obtained for the total flux through areas B, C and D, perpendicular to branches 2, 3 and 4 respectively.

$$\text{i.e.} \quad \phi_{02} = \frac{2\Delta x}{a} (\hat{b}_z)_{02} \qquad \text{A1.15}$$

$$\phi_{30} = \frac{2\Delta z}{a} (\hat{b}_x)_{30} \qquad \text{A1.16}$$

$$\phi_{40} = \frac{2\Delta x}{a} (\hat{b}_z)_{40} \qquad \text{A1.17}$$

Let ϕ_{05} be the flux through area E at $y = \frac{\tau_p}{2}$. This area is perpendicular to the line of branches between nodes 0 and 5. Hence from equation A1.2

$$\phi_{05} = (\hat{b}_y)_{05} \Delta x \, \Delta z \qquad \text{A1.18}$$

Similarly for area F at $y = -\frac{\tau_p}{2}$

$$\phi_{60} = (\hat{b}_y)_{60} \Delta x \, \Delta z \qquad \text{A1.19}$$

The branch relations for the equivalent circuit to represent the quasi-3D field follow when the constitutive relation $b = \mu(H + h)$, for the magnetic field, is enforced. For the x-directed branches

$$\hat{b}_x = \mu(\hat{H}_x + \hat{h}_x) \qquad \text{A1.20}$$

Using this equation to combine the mmf and flux relations, equations A1.8 and A1.14 respectively, gives the branch relation between nodes 0 and 1,

$$\phi_{01} = \frac{2\mu\Delta z}{a\Delta x} (M + m)_{01} \qquad \text{A1.21}$$

Similarly the branch relation between nodes 3 and 0 is,

$$\phi_{30} = \frac{2\mu\Delta z}{a\Delta x} (M + m)_{30} \qquad \text{A1.22}$$

For the z-directed branches,

$$\hat{b}_z = \mu(\hat{H}_z + \hat{h}_z) \qquad \text{A1.23}$$

Combining the appropriate mmf and flux equations with this expression gives the branch relation between nodes 0 and 2,

$$\phi_{02} = \frac{2\mu\Delta x}{a\Delta z}(M + m)_{02} \qquad \text{A1.24}$$

and between nodes 4 and 0,

$$\phi_{40} = \frac{2\mu\Delta x}{a\Delta z}(M + m)_{40} \qquad \text{A1.25}$$

For the y-directed branches

$$\hat{b}_y = \mu(\hat{H}_y + \hat{h}_y) \qquad \text{A1.26}$$

This similarly gives the branch relations between the node pairs 0-5 and 6-0 as

$$\phi_{05} = \mu a\, \Delta x\, \Delta z\, (M + m)_{05} \qquad \text{A1.27}$$

$$\phi_{60} = \mu a\, \Delta x\, \Delta z\, (M + m)_{60} \qquad \text{A1.28}$$

Applying all the branch relations given by equations A1.21, A1.22, A1.24, A1.25, A1.27 and A1.28 for the node pairs 0-1, 3-0, 0-2, 4-0, 0-5 and 6-0 respectively leads to the equivalent circuit shown in Fig. A1.2. The reluctances Rx, Ry and Rz are given by equations A1.29-A1.31 below.

$$Rx = \frac{a\Delta x}{2\mu\Delta z} \qquad \text{A1.29}$$

$$Ry = \frac{1}{a\mu\ \Delta x\ \Delta z} \qquad \text{A1.30}$$

$$Rz = \frac{a\Delta z}{2\mu\Delta x} \qquad \text{A1.31}$$

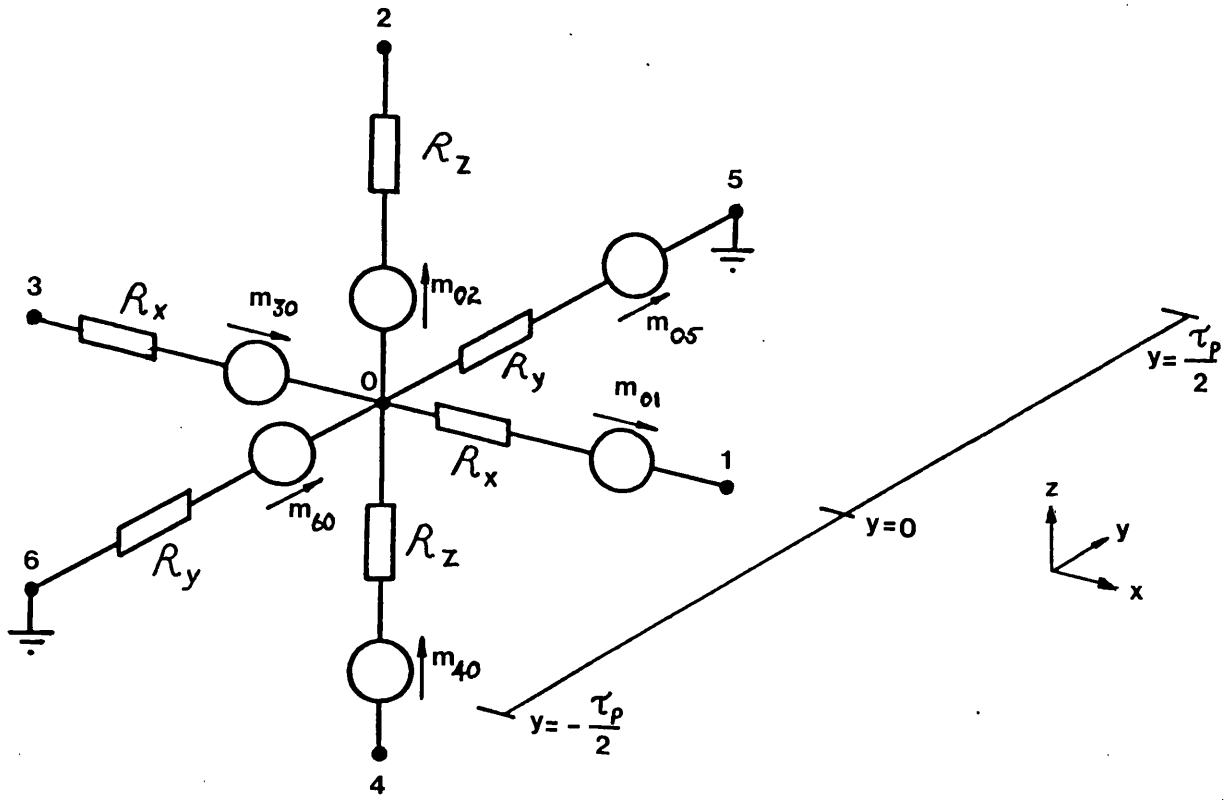

Fig. A1.2 Basic unit of the magnetic equivalent circuit representing one pole of the quasi-3D field.

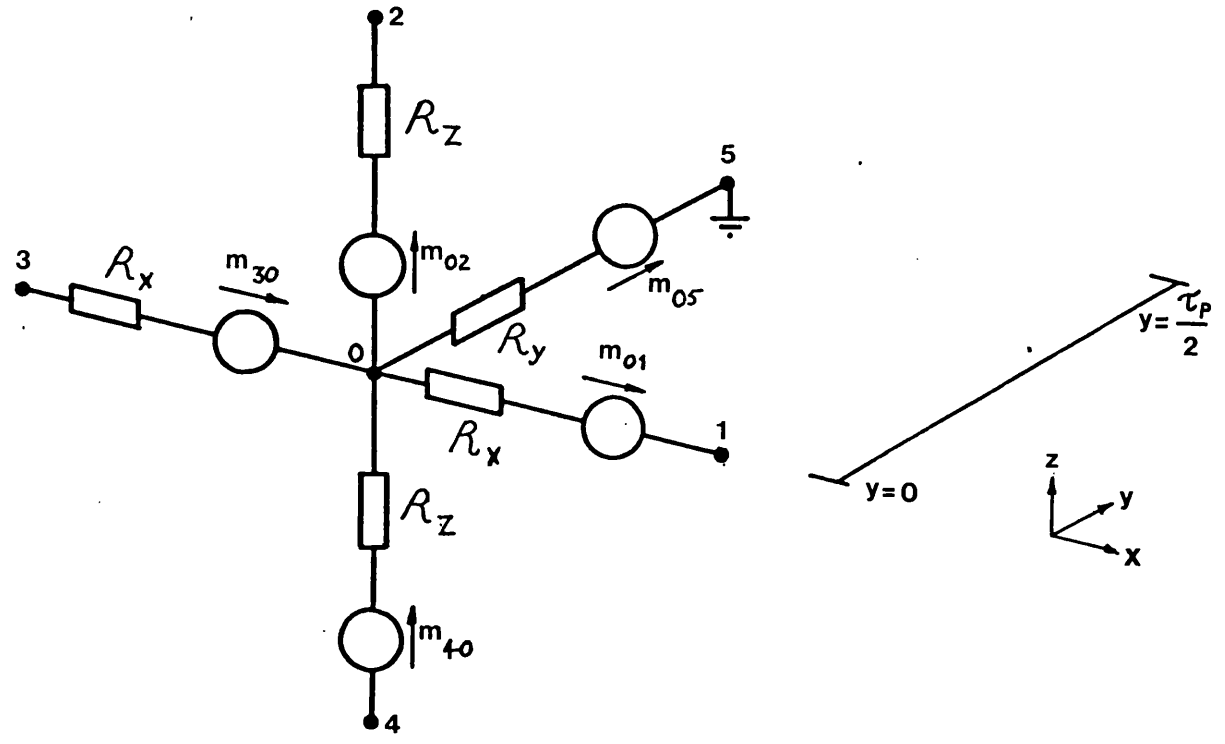

Fig. A1.3 Basic unit of the magnetic equivalent circuit representing half a pole of the quasi-3D field.

The equivalent circuit of Fig. A1.2 can be simplified to that shown in Fig. A1.3 because the x-z plane at y = 0 is a plane of positive symmetry. Rx, Ry and Rz are now defined by equations A1.32-A1.34 where Ry is unchanged.

$$Rx = \frac{a\Delta x}{\mu \Delta z} \qquad \text{A1.32}$$

$$Ry = \frac{1}{a\mu\ \Delta x\ \Delta z} \qquad \text{A1.33}$$

$$Rz = \frac{a\Delta z}{\mu \Delta x} \qquad \text{A1.34}$$

Similar circuits exist for each node of the subdivision on the x-z plane at y = 0. These circuits are interconnected on the x-z plane, as shown in outline in Fig. A1.4, to form the complete equivalent circuit for the magnetic part of the quasi-3D field. This is seen to be a two-dimensional network of branches in the x-z plane at y = 0 with y-directed branches from each node to the ground plane at $y = \tau_p/2$.

A comparison of the branch reluctance expressions, A1.32-A1.34, with the standard reluctance formula $R = \ell/\mu A$, shows that, in terms of branch reluctances, the equivalent circuit for the quasi-3D magnetic field can be considered to be a normal network with interval Δx, $1/a$, and Δz in the x, y and z directions respectively. That is the x, y and z-directed branches have lengths Δx, $1/a$, Δz and areas $\Delta z/a$, $\Delta x \Delta z$, $\Delta x/a$ respectively. These branch lengths and areas were derived for a constant network interval in each of the x, y and z directions. In the general case, the quasi-3D network model does not necessarily have a constant interval in each of the x and z directions. However, the y-directed branches for the general case always have equivalent lengths of $1/a$ and the areas for x and z-directed branches are always of length $1/a$ in the y direction. The remaining dimensions for the

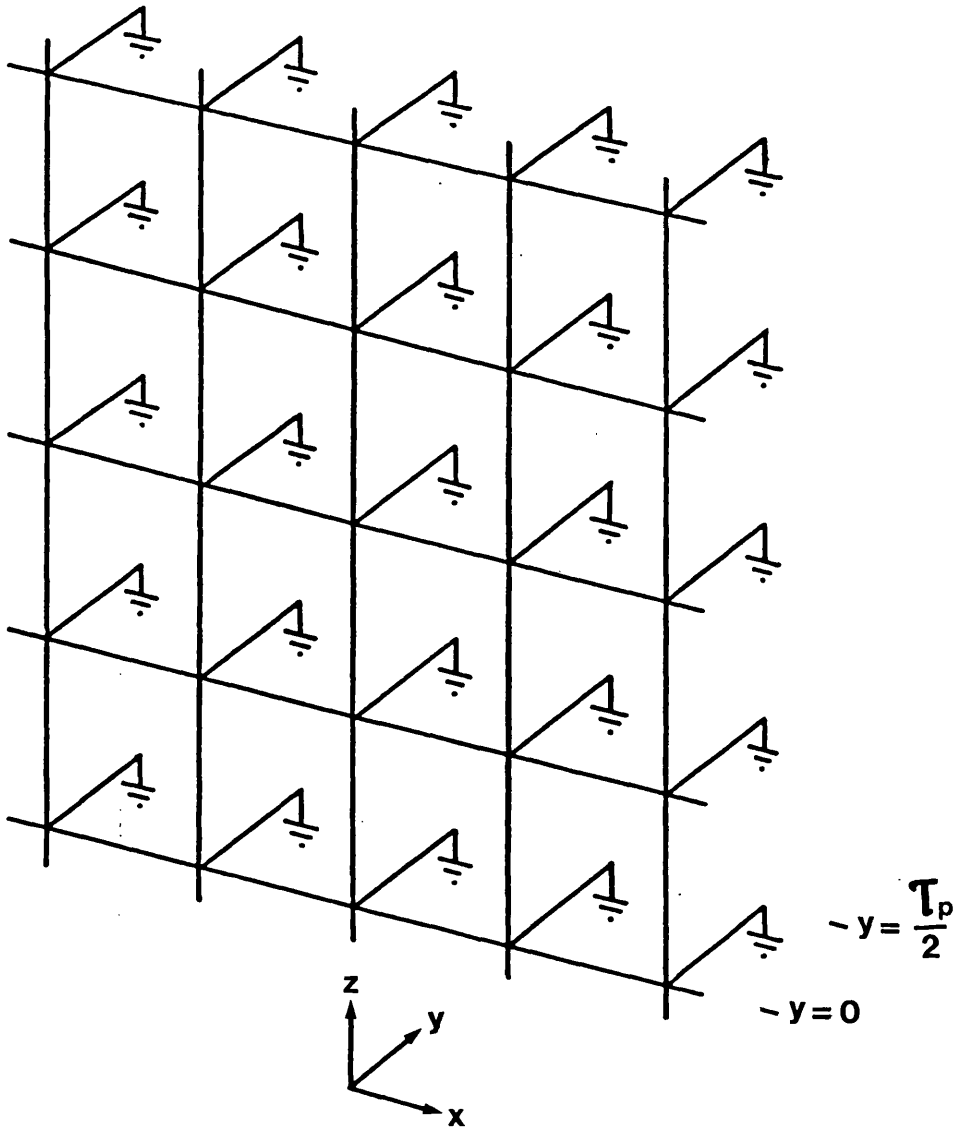

Fig. A1.4 Outline of the complete magnetic equivalent circuit representing half a pole of the quasi-3D field.

areas are defined in the normal way by the double subdivision technique. Branch reluctance values then follow from the standard reluctance formula $R = \ell/\mu A$.

The subdivision of the region on the x-z plane of the quasi-3D model is made in exactly the same way as that for a similarly positioned plane in the full three-dimensional model. All x, y and z directed branches then obey exactly the same rules as those given for the full three-dimensional model, such as the assigning of branch permeabilities and positioning of the network to represent boundary conditions. The difference in the quasi-3D case is that all branches represent the field over a half pole length of the y distribution in that direction, as confirmed by the reluctance expressions, equations A1.32-A1.34. This means that, as shown in the derivation of the quasi-3D model, the x and z directed branches carry the total flux in the appropriate position over the half pole of the y distribution represented. The y-directed branches, however, carry the peak flux of the y-directed flux distribution, in the appropriate position. Regarding the branch mmf sources shown in the quasi-3D magnetic equivalent circuit, these represent the distribution of solenoidal mmf within the half pole represented. These sources may also be formed partly of an independent source term m_s, as in the full three-dimensional model.

A1.2.3 Equivalent circuit for the electric part of the quasi-3D field

The derivation, from the electric circuit of the full three-dimensional model, of the equivalent circuit to represent the electric part of the quasi-3D field follows exactly the same procedure as that used for the magnetic circuit. The only difference is that the y-distributions in the electric field are displaced in space by 90^{o} from

the corresponding distributions in the mangetic field. This is seen for example by comparing equations A1.3 and A1.6 in section A1.2.1. A plane of positive symmetry also exists in the electric part of the quasi-3D field. Due to the space phase difference between magnetic and electric distributions, this symmetry plane is situated, for example, at $y = \tau_p/2$. The resulting equivalent circuit for a node on the plane of symmetry is shown in Fig. A1.5. Similar circuits exist for each node on the plane of symmetry, thus giving the complete equivalent circuit for the electric part of the quasi-3D field. The resistance values for x, y and z directed branches in this circuit are given by equations A1.35, A1.36 and A1.37 respectively.

$$Rx = \frac{a\Delta x}{\sigma \Delta z} \qquad \text{A1.35}$$

$$Ry = \frac{1}{\sigma a\ \Delta x\ \Delta z} \qquad \text{A1.36}$$

$$Rz = \frac{a\Delta z}{\sigma \Delta x} \qquad \text{A1.37}$$

These expressions correspond to the case where the network interval in each of the x, y and z directions is constant and is equal to Δx, $1/a$ and Δz respectively. As in the magnetic equivalent circuit the network interval in the x and z directions is not necessarily constant. This case is dealt with in an exactly analogous manner to that used in the magnetic network, but with the general resistance values calculated from the standard formula $R = \ell/\sigma A$.

The equivalent circuit for the electric part of the quasi-3D field represents the field over a half pole region of the y-distribution in exactly the same way as the magnetic equivalent circuit (Fig. A1.3) represents the magnetic part of the field over a half-pole region. The x and z directed branches carry the total current flowing in the

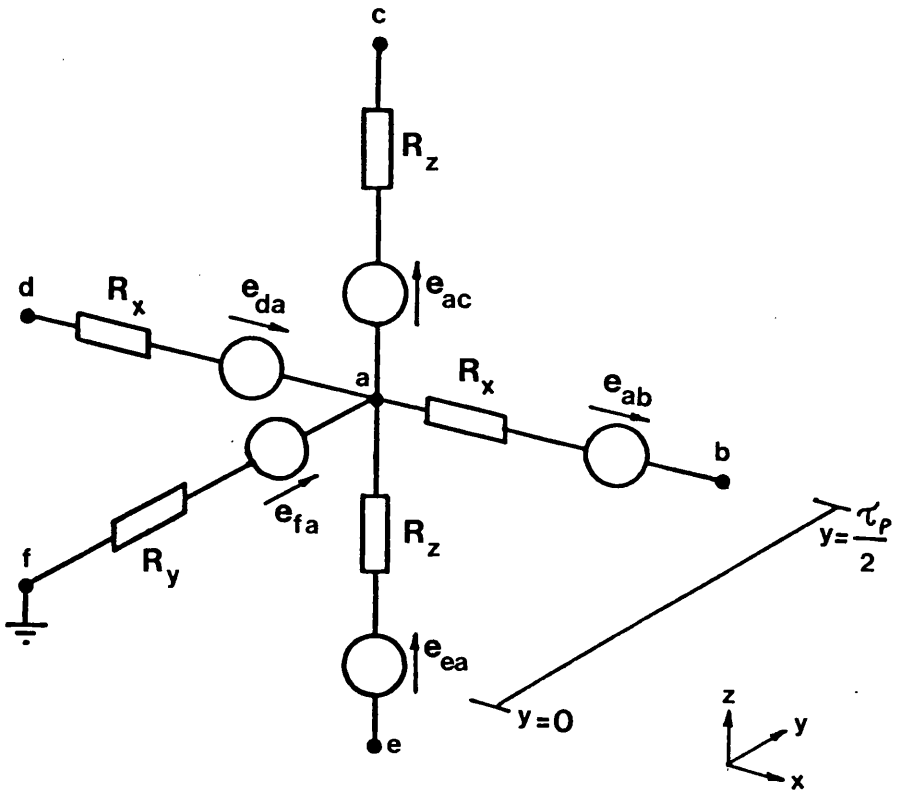

Fig. A1.5 Basic unit of the electric equivalent circuit representing half a pole of the quasi-3D field.

appropriate position over the whole length of the half pole and the y branches carry the peak current of the y-directed distribution in the appropriate position. Again, as in the full three-dimensional model, the solenoidal sources may be formed partly of an independent source, e_s in this case.

A1.2.4 The complete equivalent circuit for the quasi-3D electromagnetic field

The complete field model may consist of both magnetic and electric circuits. The magnetic circuit is normally required to represent the whole of the field region of interest and the electric circuit exists only in conducting regions. In regions where both circuits exist they interlink as shown in Fig. A1.6. That is each basic mesh on the x-z plane of the magnetic circuit in this region encircles a branch to ground in the electric circuit and vice versa.

A1.2.5 Solution of the quasi-3D field model

The complete circuit model for the quasi-3D field, as represented in Fig. A1.6, is a linked circuit problem similar to that solved in the full three-dimensional field model. Linkage between the two physically separate parts of the circuit is again through mesh variables. Currents flowing in the branches of the electric circuit inject mmf into the meshes they link in the magnetic circuit. Changing flux in the magnetic circuit branches similarly induce voltage in the meshes linked in the electric circuit.

The linked circuit problem is solved in exactly the same way as in the full three-dimensional case. The mesh method is used, giving an independent set of variables equal to the link fluxes and currents

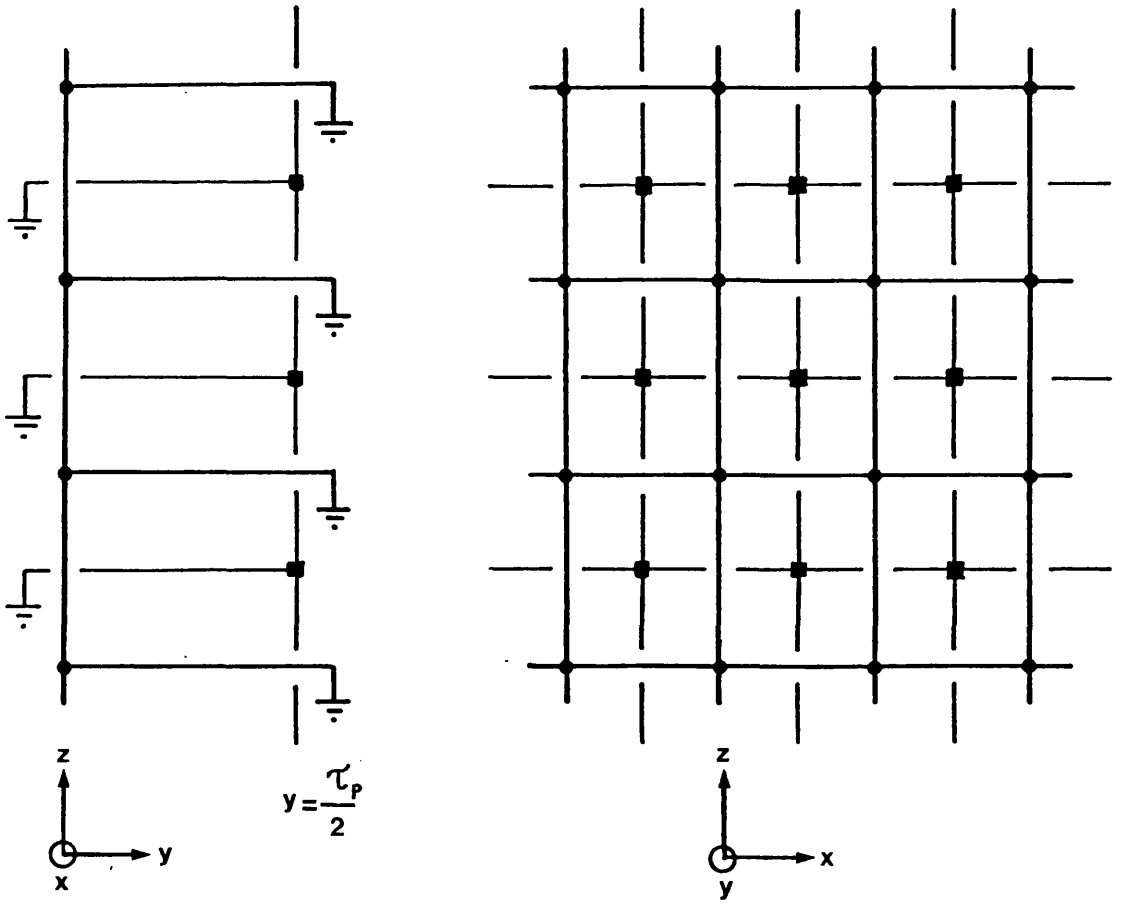

Fig. A1.6 Interlinkage of the magnetic and electric networks of the complete equivalent circuit for the quasi-3D model.

in the two parts of the equivalent circuit. The field equations for the quasi-3D model therefore have exactly the same form as those, equation 2.24 of Chapter 2, for the full three-dimensional model. The procedure to set up and solve these field equations is also identical to that for the full three-dimensional case.

A1.2.6 Solution of a travelling wave field using the quasi-3D model

In many field problems that are periodic along one axis, the field is not stationary in space but appears to move at some velocity along the periodic axis. This is the familiar travelling wave problem encountered in electrical machines.

In the quasi-3D model just described the sinusoidal y-distribution can vary in amplitude but it is stationary in space. Any sinusoidal travelling wave can always be expressed as the sum of two such stationary waves that differ in time and space phase by 90°. Hence, the travelling field $\hat{b} \cos(\omega t - ay + \alpha)$, where ω is the angular frequency in radians and α is an arbitrary phase angle, can be written,

$$\hat{b} \cos(\omega t - ay + \alpha) = \hat{b} \cos(\omega t + \alpha) \cos ay + \hat{b} \sin(\omega t + \alpha) \sin ay \qquad \text{A1.38}$$

The travelling wave field problem is therefore solved by using the quasi-3D method just described to find the amplitude of either stationary part. The amplitude is the same for both stationary parts so the travelling field can be constructed using equation A1.38.

A1.3 Analysis of a linear induction motor, based on a field solution using the quasi-3D linked network model

A1.3.1 Quasi-3D linked network model for the field of a linear induction motor (LIM) at standstill

The basic single sided linear motor consists of a three phase wound primary which runs over an iron backed conducting track (secondary) as shown in Fig. A1.7. The primary currents produce a travelling field that induces currents in the secondary. The airgap field from the primary and secondary interact to give normal and tangential forces that lift and propel the primary along the track.

For the purpose of the analysis the LIM is assumed to be as shown in the region L of Fig. A1.8. In this model the primary iron extends beyond the end of the winding in the y-direction. A simplification of this type may seem unjustified in view of the familiar end effect in linear motors. This effect is due however to both the ends of the primary excitation, that are to be represented in the model, and to the ends of the primary iron, that are not to be represented directly. By ignoring the discontinuities in the primary iron, the calculated flux density in front and behind the machine will obviously be higher than that in the real machine. The entry edge flux density is usually very low, so the assumption of continuous iron in front of the machine should have little effect on the performance calculations. At high speeds the flux density at the exit end can be considerable. Performance calculations based on the field results from the model of Fig. A1.8 should however be valid if an allowance is made in these for the effect of the exit iron end.

In the model shown in Fig. A1.8 the section L has been repeated in the y direction to plus and minus infinity, to form a series of

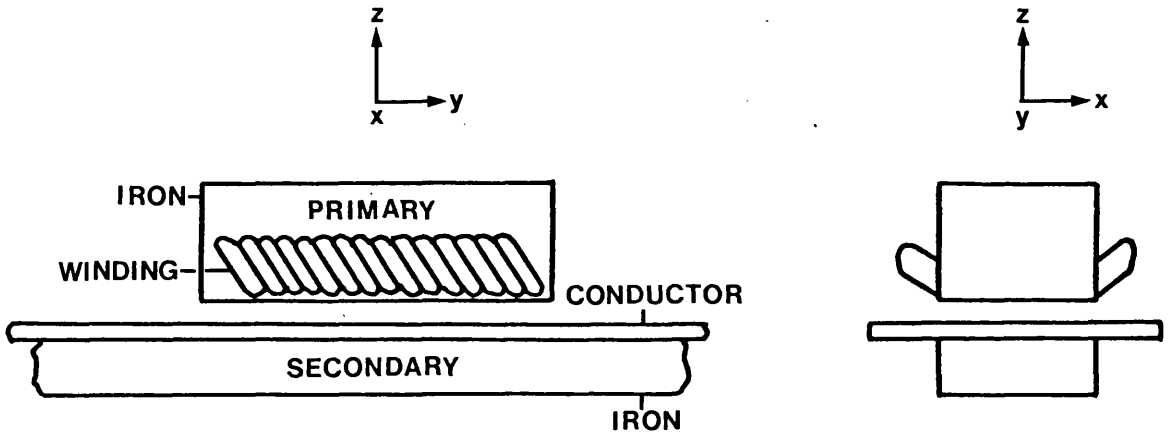

Fig. A1.7 Axial flux linear induction motor.

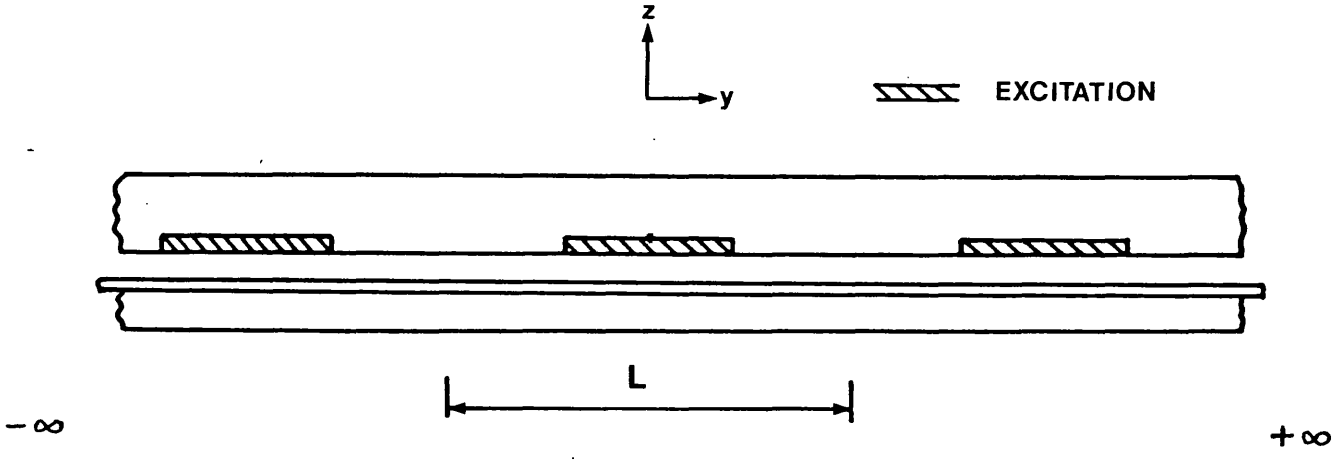

Fig. A1.8 Representation of the linear induction motor for the quasi-3D field calculations.

excited primaries on the same track. The primary excitation is now periodic, of period L, and can be represented by a Fourier series. This Fourier series represents the excitation of a single machine on the track provided that the distance between excited patches is large enough to allow the gap flux to decay virtually to zero before it enters the next excited patch.

For each component of the excitation Fourier series the flux density produced in the machine is sinusoidal. At standstill the velocity of the primary is zero. The field produced by each component of the excitation Fourier series can therefore be found using the quasi-3D method for the travelling field exactly as described in the previous section. In theory there are an infinite number of harmonics in the Fourier series that represents the excitation mmf. A typical frequency spectrum is shown in Fig. A1.9, in which the vertical lines represent the frequency components present. In practice it is normally only necessary to consider those in the main lobe of the spectrum because all other frequency components have a low and always decreasing amplitude. The total magnetic field is then found by summing the fields produced by all individual frequency components considered, taking into account their different pole pitches.

In a practical machine the mmf produced by the winding is not perfectly sinusoidal and has to be represented by a Fourier series consisting of a fundamental and a number of winding harmonics. For general performance calculations in most machines it is normally only necessary to consider the fundamental and possibly one or two of the lower winding harmonics. The fundamental and each winding harmonic considered give rise to a patch of excitation of the appropriate pole

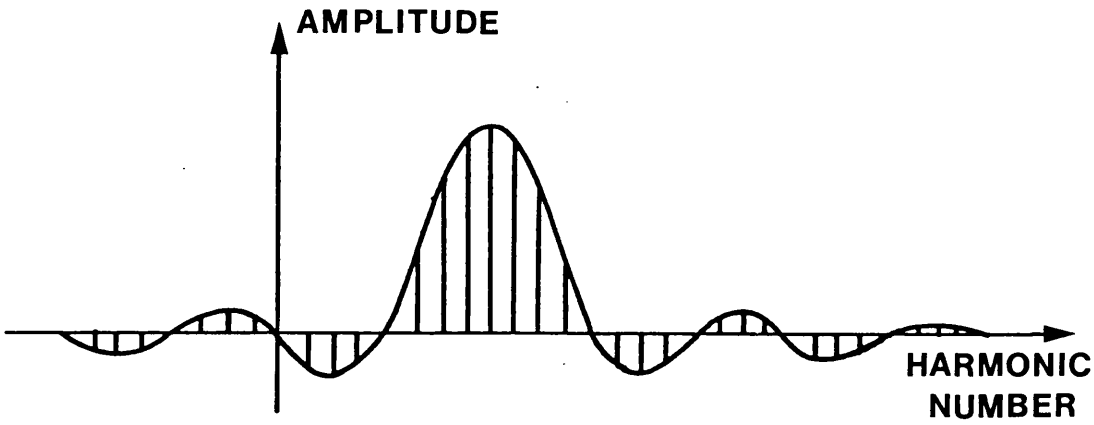

Fig. A1.9 Typical frequency spectrum of a Fourier series representing a patch of sinusoidal excitation mmf in the linear induction motor model.

pitch in the region L as shown in Fig. A1.8. Each patch of excitation is represented by a Fourier series and the field calculated using the quasi-3D method as described previously. Finally, the total field is found by summing the fields due to the fundamental and all winding harmonics considered.

A1.3.2 Quasi-3D field model for a LIM, including motion of the machine

In section A1.2.6 the solution of the quasi-3D travelling field was described for a magnetic field of the form given below.

$$b = \hat{b} \cos(\omega t - ay + \alpha) \qquad (a = \pi/\tau_p)$$

This field travels at velocity ω/a m/s with respect to the electric circuit in the quasi-3D model. In the LIM, when there is relative motion between the primary and secondary, the primary magnetic field travels at velocity $s\omega/a$ m/s with respect to the secondary, where s is the fractional slip. In this case the relative velocity of the magnetic field with respect to the electric circuit in the quasi-3D model is therefore

$$b = \hat{b} \cos(s\omega t - ay' + \alpha) = \hat{b} \cos(s\omega t + \alpha) \cos ay' + \hat{b} \sin(s\omega t + \alpha) \sin ay' \qquad \text{A1.39}$$

where y' is the y co-ordinate relative to the secondary.

The solution procedure for the field using two stationary models differing only in space and time phase by 90^o is identical, but the field equations must be modified by substituting $s\omega$ for ω. These now become,

$$\begin{bmatrix} C_M^T R C_M & -N \\ -N^T & -C_E^T \frac{R}{js\omega} C_E \end{bmatrix} \begin{bmatrix} \phi_I \\ i_I \end{bmatrix} = \begin{bmatrix} C_M^T m_s \\ C_E^T \frac{e_s}{js\omega} \end{bmatrix} \qquad \text{A1.40}$$

Equation A1.40 shows that in the quasi-3D model for the LIM, motion is accounted for by a simple resistance change in the electric network. The resistance of branches are given by R/s, where R is the equivalent resistance derived in section A1.2.3 and s is the fractional slip. This is consistent with the standstill resistance where s = 1.

Finally, in the case of the LIM the only excitation is normally from the primary winding. This is represented in the model by the known mmf sources m_s. The sources e_s in the electric circuit are then zero.

A1.3.3 Calculation of thrust force from the quasi-3D field results

In the standard phase equivalent circuit, shown in Fig. A1.10, for a round induction motor, the power dissipation in the resistance R_2'/s represents the electromagnetic power input to the rotor per phase. R_2' is the rotor phase resistance referred to the primary and s is the fractional slip. The instantaneous power per phase, P_i, into the rotor is therefore given by equation A1.41

$$P_i = i_2^2 \frac{R_2}{s} \qquad \text{A1.41}$$

where R_2 is the rotor phase resistance and i_2 is the instantaneous rotor current. By analogy, for a linear induction motor, the

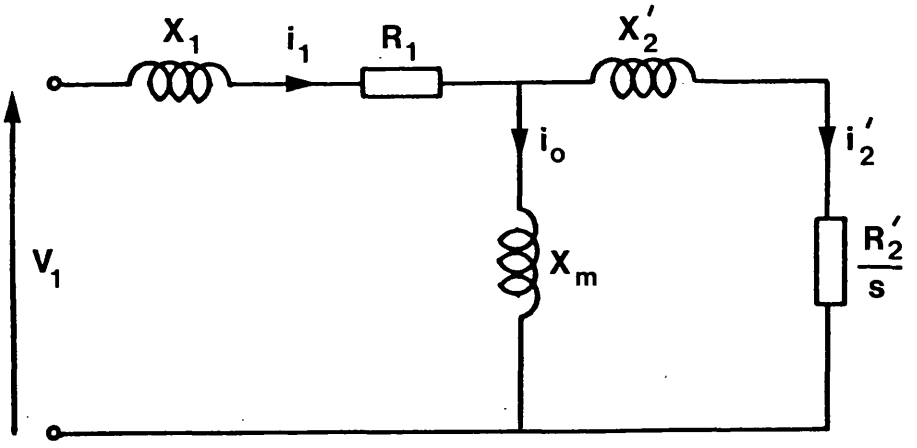

Fig. A1.10 Phase equivalent circuit for a round induction motor.

instantaneous power input to a small element of track of resistance R_2, carrying a sinusoidal current i_2, is again given by equation A1.41. The instantaneous electromagnetic power into the same track element is also given by equation A1.42,

$$P_i = \Delta T_i v_s \qquad \text{A1.42}$$

where ΔT_i is the instantaneous component of thrust force for the track element and v_s is the synchronous speed, in m/s, of the travelling airgap field. Combining equations A1.41 and A1.42 gives an expression for the instantaneous thrust force ΔT_i due to the current flowing in the element of track considered. That is,

$$\Delta T_i = \frac{1}{v_s} i_2^2 \frac{R_2}{s} \qquad \text{A1.43}$$

In the LIM model the track current is not sinusoidal but is represented by a Fourier series. Equation A1.43 can therefore be used to find the thrust force produced by each frequency component of the series. A summation over all frequency components then gives the total thrust force for the element. In the quasi-3D field model the space distribution of track current is expressed in terms of x, y and z components of current in a resistance network model. When all frequency components and the whole space distribution of track current is conisdered an expression, equation A1.44, is obtained for the total average thrust force, T, produced by the LIM,

$$T = L \sum_{p=1}^{m} \left(\sum_{q=1}^{nx} \frac{a_p}{v_{sp}} I^*_{xpq} I_{xpq} \frac{R_{xpq}}{s_p} + \sum_{q=1}^{ny} \frac{a_p}{v_{sp}} I^*_{ypq} I_{ypq} \frac{R_{ypq}}{s_p} + \sum_{q=1}^{nz} \frac{a_p}{v_{sp}} I^*_{zpq} I_{zpq} \frac{R_{zpq}}{s_p} \right) \qquad \text{A1.44}$$

Equation A1.44, derived in Appendix 3, gives the total, average thrust force in terms of the actual branch resistances and rms currents flowing in the electric network part of the quasi-3D field model. The variables in equation A1.44 have the following definitions,

p = harmonic number

m = number of frequency components considered

q = branch number

n_x, n_y, n_z = number of x, y and z-directed electric circuit branches respectively

R_{xpq} = resistance of the q^{th} x-directed branch for the p^{th} harmonic. R_{ypq}, R_{zpq} have similar definitions for y and z branches respectively

I_{xpq} = p^{th} harmonic rms current flowing in the q^{th} branch. I_{ypq} and I_{zpq} have similar definitions

L = period of the track current distribution

v_{sp} = synchronous speed of the p^{th} harmonic

s_p = fractional slip for the p^{th} harmonic

a_p = π/τ_p where τ_p is the pole pitch of the p^{th} harmonic

$*$ denotes complex conjugate

Equation A1.44 gives the total average thrust force assuming the primary iron to be continuous. In a real machine having a finite length of primary iron the field at the exit edge produces a retarding force. It is possible to estimate this force and subtract it from that predicted with equation A1.44 as follows.

Induction machines normally have a small airgap so it can be assumed that most of the flux crosses the gap normally. In this case the magnetic energy stored in the gap can be approximated by,

$$E = \frac{b^2}{2\mu_o} \quad J/m^3 \qquad \text{A1.45}$$

where b is the rms magnitude of the flux density across the gap. With a continuous iron primary the removal of energy by the rotor at the exit end of the gap field distribution results in a steady power loss of,

$$P_1 = \frac{b_{ex}^2}{2\mu_o} w\, g\, v_r \quad \text{(Watts)} \qquad \text{A1.46}$$

where b_{ex} = rms flux density across the gap at the exit end

w = width of the machine

g = gap length

v_r = velocity of primary relative to track

The loss defined by equation A1.46 is supplied by the electrical input to the machine. In a real machine the primary iron has a finite length. This modifies the "gap flux" beyond the exit edge. When the primary iron is removed the effective airgap for a flux distribution of pole pitch τ_p is τ_p/π[41]. If it is assumed that the effective pole pitch of the exit flux is equal to that of the fundamental, then the power loss P_2 at the machine exit when the effect of the primary iron end is considered is given by equation A1.47,

$$P_2 = \frac{b_{ex}^2}{2\mu_o} w\, v_r \frac{\tau}{\pi} \qquad \text{A1.47}$$

where τ is the pole pitch for the fundamental. The increase in loss predicted by equation A1.47 over that calculated from equation A1.46, on the assumption of continuous primary iron, must be supplied from the track. This results in a retarding force F_{ret} given by equation A1.48,

$$F_{ret} = \frac{b_{ex}^2 \, w \, v_r}{2\mu_o} \left(\frac{\tau}{\pi} - g\right) \qquad \text{A1.48}$$

To approximate the retarding effect of the end of the primary iron at the machine exit, F_{ret} is subtracted from the thrust force calculated using equation A1.44. This is only an approximate correction but it is felt that it is justified in view of its success in practice[42].

A1.3.4 Calculation of normal force from the quasi-3D field results

The normal force produced by the LIM was calculated using the method of Maxwell's stress[43]. To calculate the force on a body using this method a closed surface must first be defined round the body. The only limitations on the surface are that,

a) it must totally enclose the body of interest

b) it must be closed

c) it must not cut any iron regions

It is also necessary to know the flux density over the whole surface. The resultant force on the body enclosed is then found by integrating the following force densities over the whole closed surface.

Average normal force density $F_n = \frac{\mu_o}{2} (b_n^* b_n - b_t^* b_t)$ N/m^2 A1.49

Average tangential force density $F_t = \mu_o b_n b_t$ N/m^2 A1.50

The variables b_n and b_t are the rms flux densities normal and tangential to the surface respectively. The symbol * denotes complex conjugate and μ_o is the permeability of free space.

The surface chosen for calculating the normal force produced by the LIM is a plane situated at the mid point of the airgap. The

plane is parallel to the primary surface and it extends to infinity in all directions. The surface therefore closes at infinity. The normal force produced by the machine is then equal to the integral of the normal force density, equation A1.49, over the whole plane.

For the field calculation it has been assumed that the flux density is zero outside the region subdivided in the field model. For the normal force calculation it has also been assumed that the flux density is zero in front and behind the machine. In a real machine the finite length of primary iron quickly attenuates the flux in these positions. For the purpose of calculating the normal force, which is proportional to the flux density squared, this was thought to be a more accurate approximation to the true field beyond the ends than that calculated assuming a continuous iron primary. These assumptions limit the Maxwell's stress surface to a finite plane over which the flux density can be calculated.

The integration of the normal force density over the chosen surface, as described above, was performed numerically. The quasi-3D field results were used to obtain the total normal and tangential components of flux density, due to all frequency components considered, at each point in a rectangular array of points covering the complete Maxwell's stress surface. In this problem the z-directed flux is normal to the Maxwell's surface and the x and y-directed flux is tangential to it. Integration along the length of the machine was performed by Simpson's rule and integration in the transverse direction by the Trapezoidal rule. This was found to be adequate because no appreciable increase in accuracy was achieved by using higher order integration routines.

A1.4 Experimental justification of the quasi-3D field calculation method

A1.4.1 Details of the test problem

The problem chosen on which to test the quasi-3D field calculation method was a transverse flux linear induction motor. Details of the machine are given below and further dimensions in Fig. A1.11.

number of poles	4
length of primary	914.4 mm
slot width	12.7 mm
tooth width	6.35 mm
conductors per slot	28
angle of coil short pitch	120^{o}
resistivity of secondary conductor	0.305×10^{-7} Ωm
supply frequency	50 Hz

A1.4.2 Comparison of calculated and experimental results

Flux density magnitude measurements were made of the z-directed (see Fig. A1.11) flux with the machine at standstill, star connected and energized with 5A rms per phase. The measurements were made using a 19 x 2 mm search coil, the output of which was amplified and calibrated. The coil was made 19 mm long, that is equal in length to a tooth pitch, in order to average the longitudinal "tufting" of the gap flux caused by the teeth on the primary. The winding harmonic content in the machine results in a gap flux that is not constant in magnitude along the machine. Flux density measurements were therefore made over a transverse section at both maximum and minimum points of the gap flux distribution along the machine. The measurement

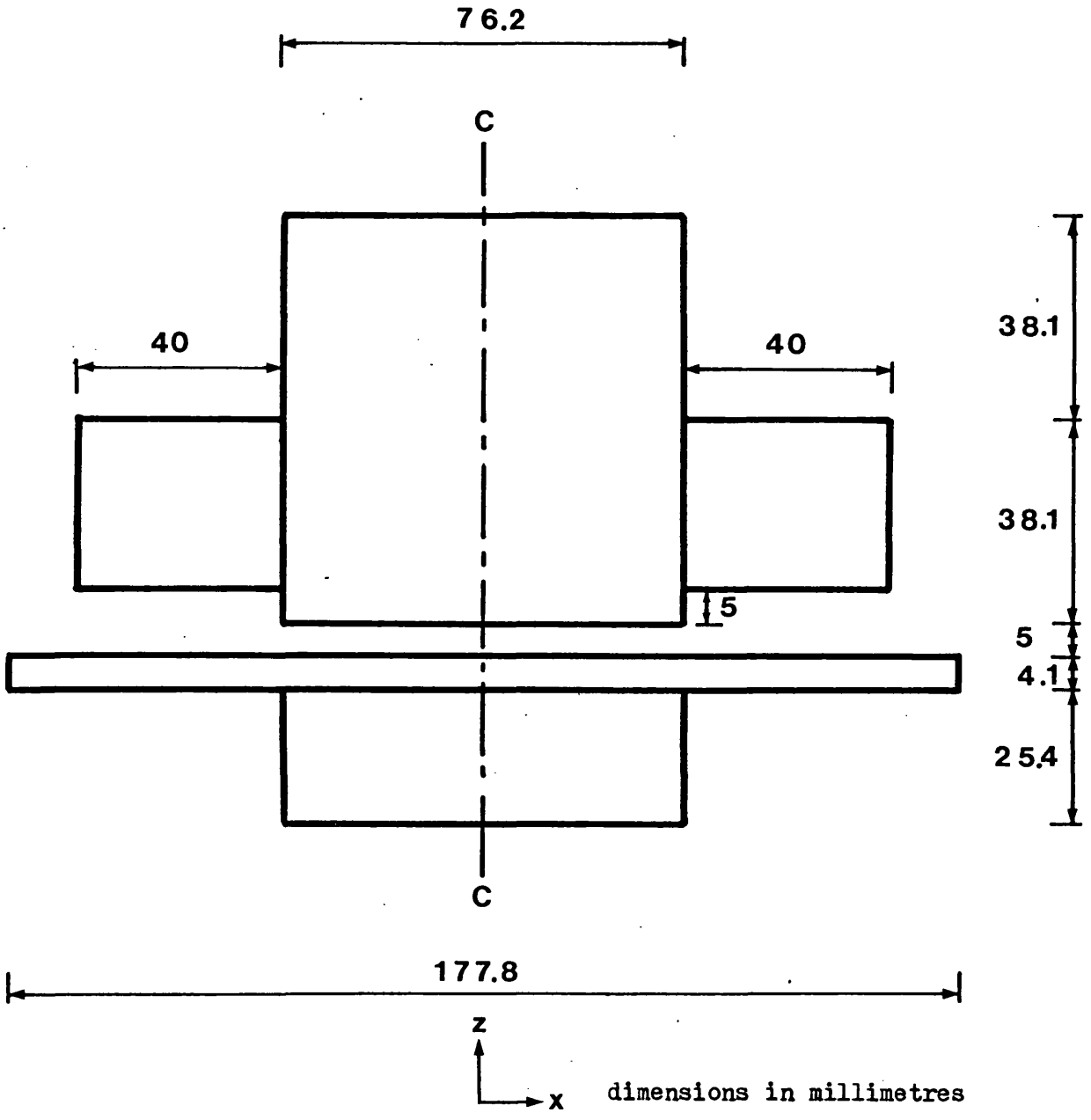

Fig. A1.11 Dimensions of the test problem.

position along the length of the machine was also chosen to be as far from the primary ends as possible. These measurements are compared in Fig. A1.12 with corresponding quasi-3D field calculations in which only the fundamental, fifth and seventh winding harmonics were used. Details of all the field calculations are described in full in the following section.

In the flux density distributions given in Fig. A1.12, both the edge effect of the primary iron at x = 38 mm and that of the secondary current flow at x = 89 mm are clearly visible. The calculations are therefore shown to predict the general shape of the flux density and agreement with experiment is satisfactory for the degree of subdivision used. The accuracy of the flux density calculations at standstill give initial verification of the validity of the basic quasi-3D field model.

The ultimate aim of field calculation in machine problems is normally to predict the output characteristics of the machine. The quasi-3D field calculations were therefore used to find the thrust and normal force characteristics for the test LIM over a range of slips from unity to zero, with an excitation of 32 A rms per phase. These characteristics are compared with corresponding measured curves in Fig. A1.13 and Fig. A1.14. Reasonable agreement is shown to be obtained between calculation and experiment for both thrust and normal force characteristics.

In view of the fact that the force characteristics are effectively found from the square of the calculated field quantities, the quasi-3D field model has given a relatively accurate representation of the complex field conditions within the LIM. Considering the agreement

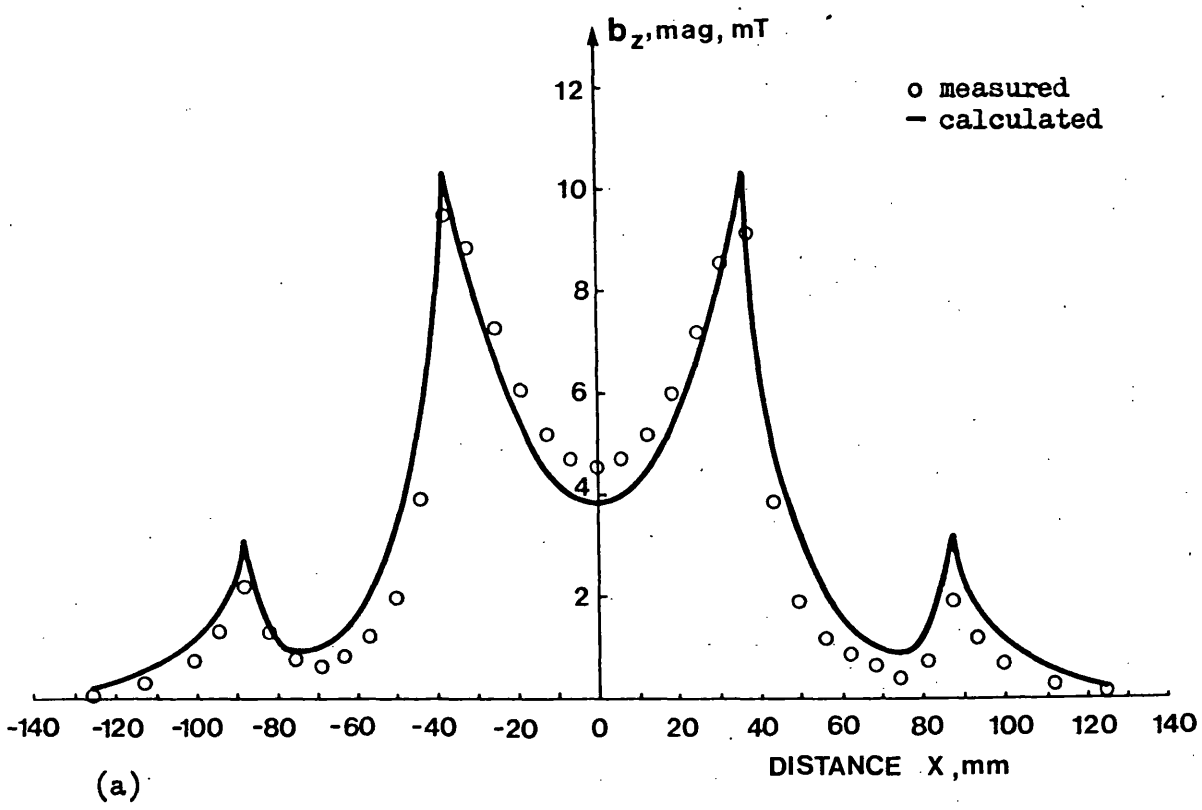

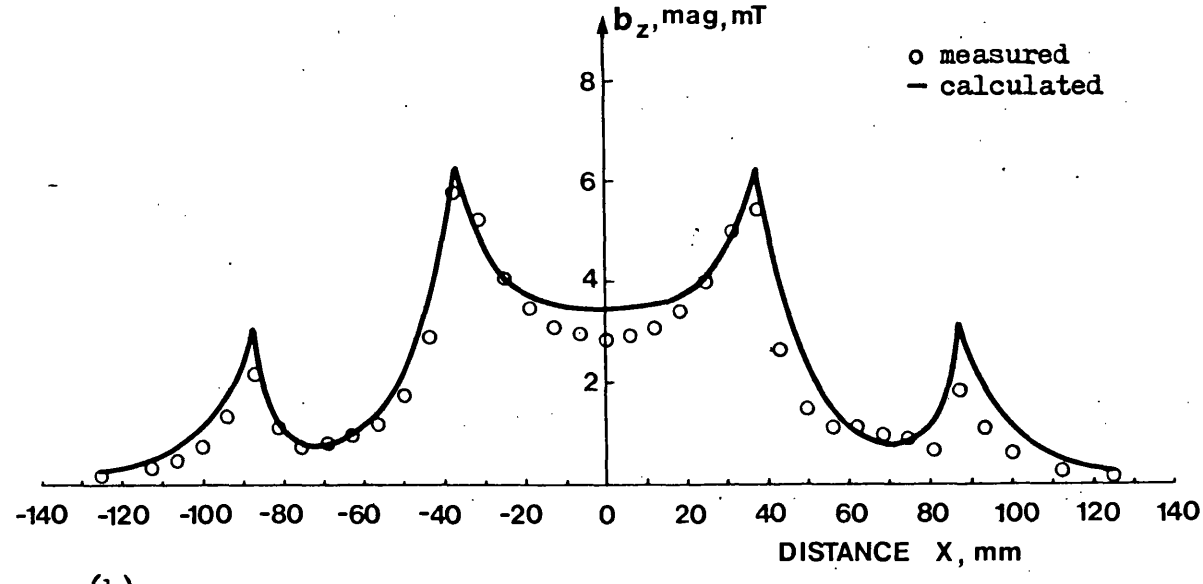

Fig. A1.12 Magnitude of the z-directed flux density, at standstill, for an excitation current of 5A rms per phase.
(a) maximum (b) minimum

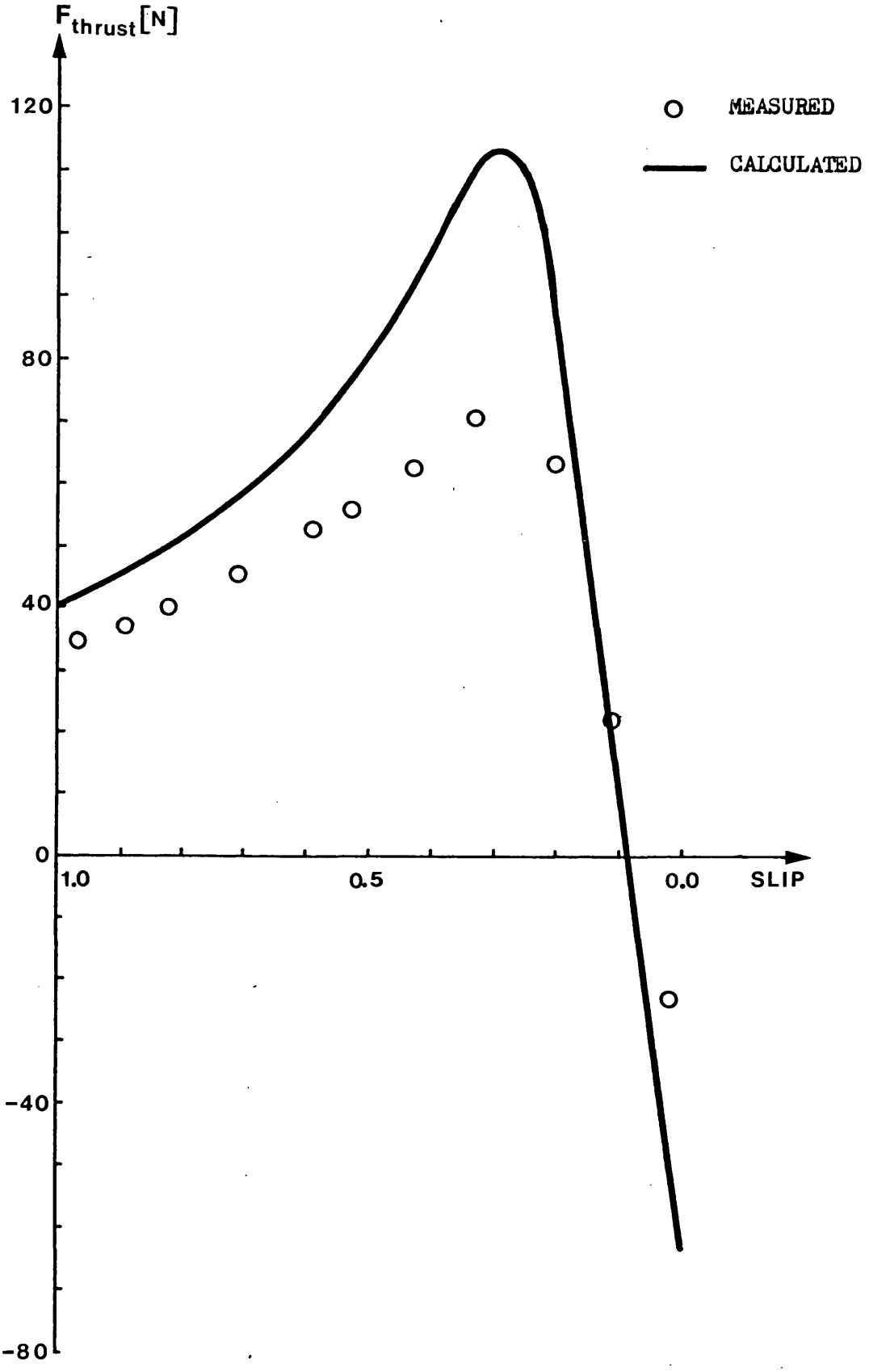

Fig. A1.13 Thrust force characteristic of the test LIM with an excitation current of 32A rms per phase.

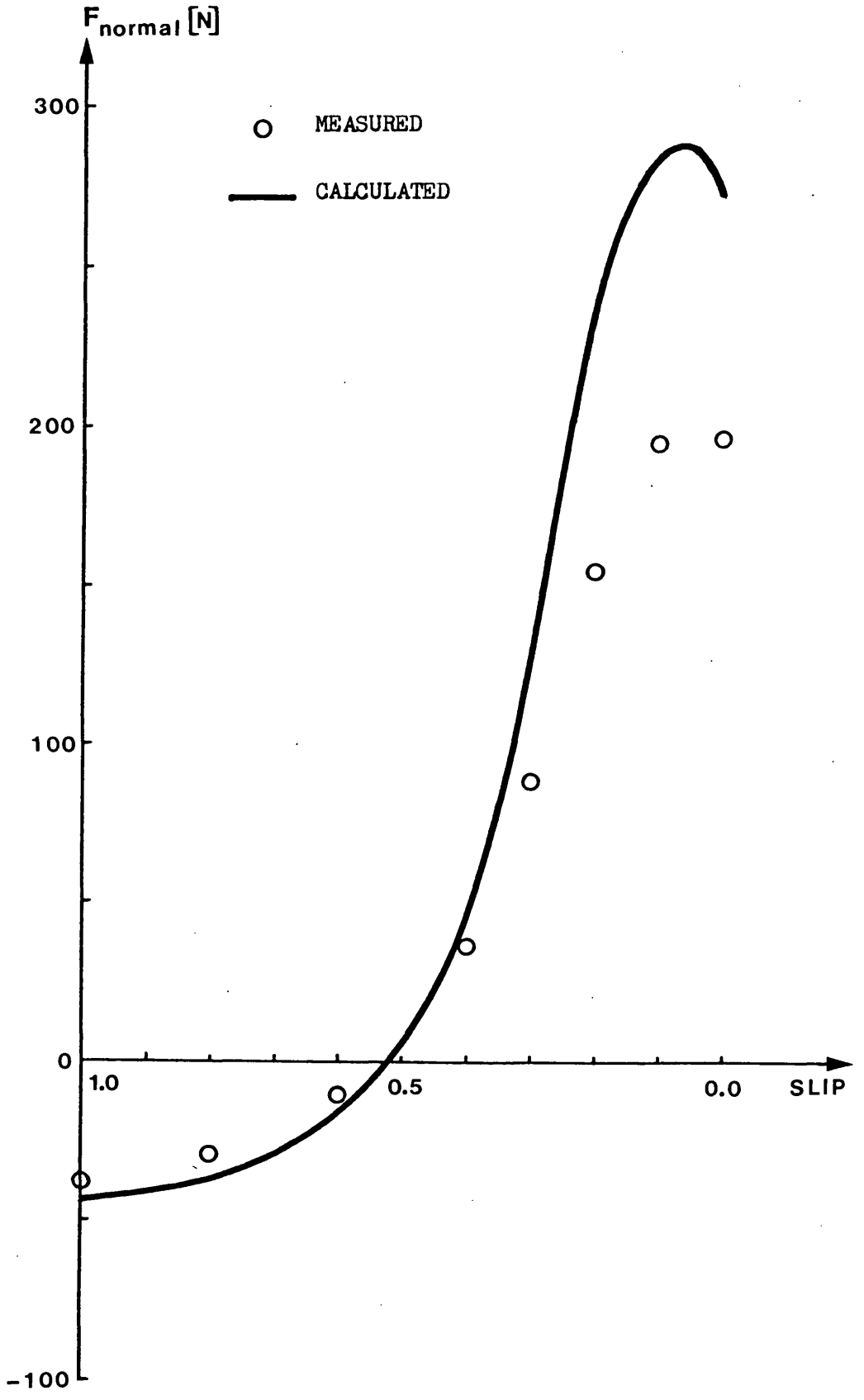

Fig. A1.14 Normal force characteristic of the test LIM with an excitation current of 32A rms per phase.

with experiment of both the calculated standstill flux density and the calculated force characteristics for the test LIM, it is felt that the validity of the quasi-3D linked network field model has been confirmed.

A1.4.3 Details of calculations

In addition to the assumptions made in the derivation of the quasi-3D linked network model for the LIM, the following assumptions were made for the calculations

a) All iron had infinite permeability and infinite resistivity
b) Current flow in the secondary was confined to the x-y plane
c) Only the fundamental, fifth and seventh winding harmonics were significant in the field calculation

The excitation to the field model was the mmf produced by the primary winding for a specified current. This was represented as known branch mmf sources in the magnetic part of the model. The triangular shape of the coil end-windings were modelled by assuming that the mmf produced by the coil dropped sinusoidally to zero at the full overhang. Slotting on the primary was represented by the use of Carters coefficient[44]. This increased the total gap length, between the primary and secondary iron surfaces, from its actual value of 9.1 mm to an effective value of 10.56 mm.

The test machine was assumed to be symmetrical, at all times, about the plane CC shown in Fig. A1.11. By treating plane CC as a flux plane, only half the machine had to be modelled in the field

solution. The resulting magnetic and electric networks of the quasi-3D linked network field model are shown in Fig. A1.15. As described in section A1.2.5 the solution of the quasi-3D linked network model is performed in exactly the same way as that used in the full three-dimensional case. The same computer program was therefore used to solve the quasi-3D model, with only slight modification to include the slip term and to perform repeated solutions for all the required frequency components. Apart from the amplitude of the excitation mmf, the field network models for individual frequency components differ only in the pole pitch of the y-distribution. The pole pitch is specified by the value of $a_p = \pi/\tau_p$ used in the calculation of the branch reluctances and resistances. This meant that the field equations for individual frequency components could be set up very easily by scaling the reluctances and resistances of a fundamental model for the appropriate value of a_p.

The mesh solution of the linked network model shown in Fig. A1.15 required the use of 200 variables for the magnetic circuit and 7 for the electric circuit. This gave a total of 207 simultaneous equations to be solved. The solution was performed on the SERC IBM 195 computer. The storage requirement was approximately 33 Kbytes. The computation time for the solution of the field equations by the conjugate gradient method is dependent on the harmonic number of the frequency component and the slip. As a guide to the computation times involved, an average value of approximately 10 seconds was required per solution of the field equations for an individual frequency component.

For the calculation of the flux density shown in Fig. A1.12, with the machine at standstill, it was assumed that the mmf on the

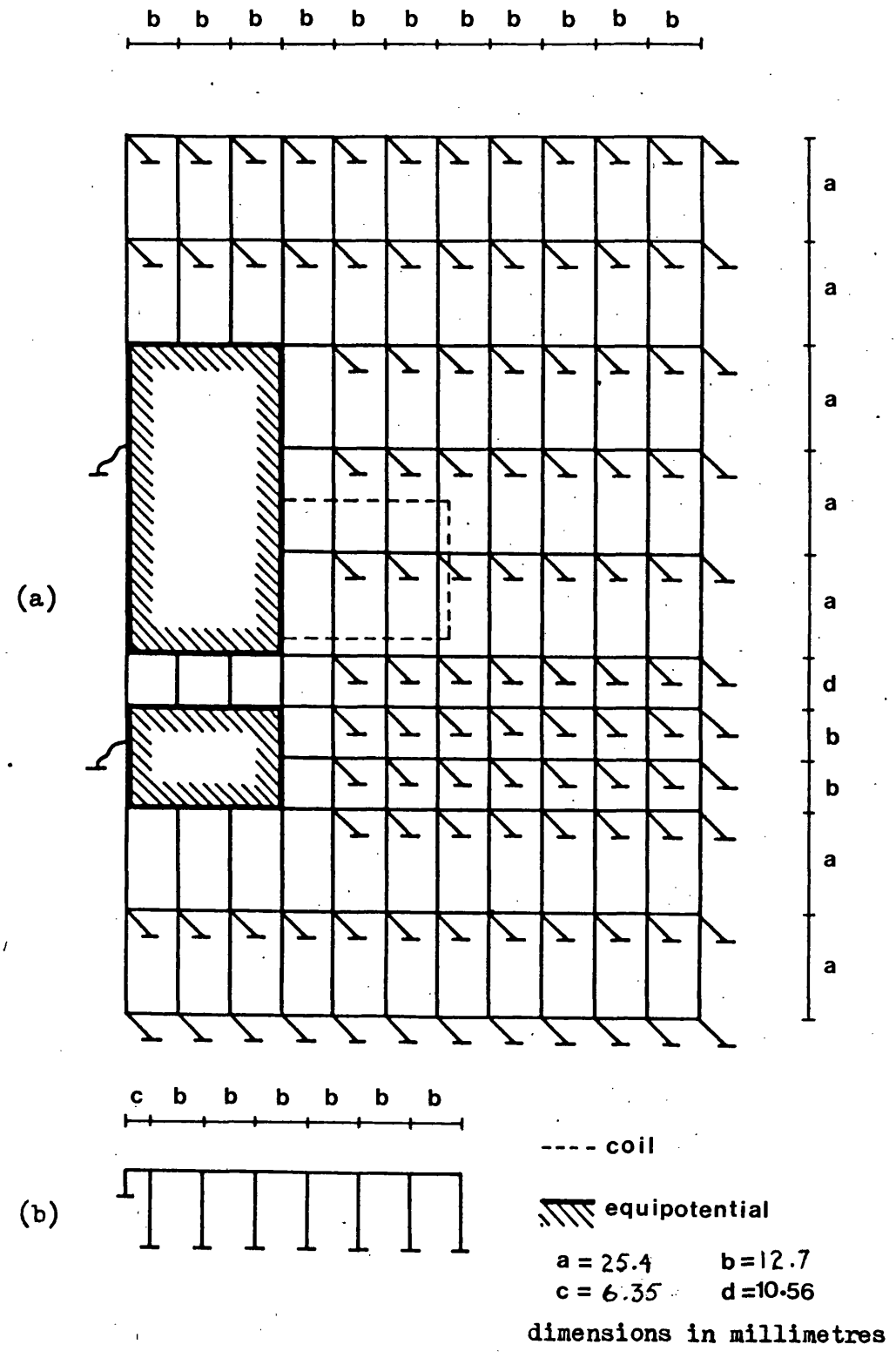

Fig. A1.15 Magnetic and electric networks of the quasi-3D linked network model for the test LIM problem. (a) magnetic (b) electric

primary was continuous in the y-direction. That is, the effect of the ends of the machine were not considered. It is felt that this is justified because the ends should have little effect on the stand-still flux density in the central length of the machine, where the measurements were made.

The thrust and normal forces were calculated by the procedures described in sections A1.3.3 and A1.3.4 respectively. In the calculation of these forces it was found that the fifth and seventh winding harmonics contributed very little to the total force. Only the fundamental component of the primary winding mmf was therefore used in the calculation of the thrust and normal force characteristics given in Fig. A1.14 and Fig. A1.15. The ends of the primary excitation were however included in the field calculations, as described in section A1.3.1. The distance between the excited patches of the stator in this representation was chosen to be three times the length of the actual machine. This was found to be adequate to allow the track current to decay sufficiently before entering the next excited patch. Only components in the main lobe of the frequency spectrum of the Fourier series representation for the fundamental patch of primary excitation were considered in the force calculations. Other harmonics were found to contribute little to the total force. The main lobe of the spectrum contained seven components, thus requiring seven quasi-3D field solutions per slip value on the force curves.

A1.5 Discussion and Conclusions

A form of the general linked network model for the calculation of three dimensional electromagnetic fields has been developed for use in problems where the field is periodic in one direction. The validity of this quasi-3D model has been confirmed by comparison of calculations with equivalent experimental results for a linear induction motor.

The quasi-3D network model is similar, in terms of network dimension, to a single layer of the equivalent full three-dimensional network model. It is solved as a linked network problem in exactly the same manner as the full three-dimensional model. For three-dimensional problems that are periodic in one co-ordinate direction the use of the quasi-3D model therefore reduces greatly the number of independent variables required for the field solution. The fact that the periodic distribution may have to be represented by a Fourier series requiring the solution for many harmonics, as in the LIM example, might appear to cancel the advantage of solving for fewer variables. In practice, however, the solution time for the smaller sets of equations from the quasi-3D model can be several orders of magnitude less than that for an equivalent large set from the full three-dimensional model. The quasi-3D model has the additional important advantage of a much lower storage requirement.

In conclusion, the quasi-3D linked network model is seen as a very useful development from the full three-dimensional linked network model. At present the solution of three-dimensional electromagnetic field problems by the full model is limited by the size of computer time and storage requirements that soon result as the

subdivision is extended in all three dimensions. For problems that are periodic in one co-ordinate direction the quasi-3D model gives an equivalent full three-dimensional field solution with greatly reduced computer time and storage.

APPENDIX 1

PROOF OF THE EQUIVALENCE OF THE TRUE AND RECURSIVE RESIDUALS IN THE CONJUGATE GRADIENT ALGORITHM

The equivalence of the true residual $\bar{r}_n = b - Ax_n$ and the recursive residual $r_n = r_{n-1} - \alpha_{n-1}Ap_{n-1}$, used in the basic conjugate gradient algorithm given below as equation a1.1, is now proved.

$$
\begin{aligned}
p_o &= r_o = b - Ax_o \\
\alpha_i &= \frac{|r_i|^2}{(p_i, Ap_i)} \\
x_{i+1} &= x_i + \alpha_i p_i \\
r_{i+1} &= r_i - \alpha_i Ap_i \\
\beta_i &= \frac{|r_{i+1}|^2}{|r_i|^2} \\
p_{i+1} &= r_{i+1} + \beta_i p_i
\end{aligned}
\qquad \text{a1.1}
$$

The equivalence of the two forms of the nth residual is proved using the following three formulae from the conjugate gradient algorithm a1.1,

$$r_o = b - Ax_o \qquad \text{a1.2}$$

$$x_{i+1} = x_i + \alpha_i p_i \qquad \text{a1.3}$$

$$r_{i+1} = r_i - \alpha_i Ap_i \qquad \text{a1.4}$$

Equation a1.3 may be expanded to express the estimate of x at the nth iteration as,

$$x_n = x_o + \alpha_o p_o + \alpha_1 p_1 + \alpha_2 p_2 + \ldots + \alpha_{n-2} p_{n-2} + \alpha_{n-1} p_{n-1} \qquad \text{a1.5}$$

Equations a1.2 and a1.4 can be used to express the recursive residual

at the nth iteration as,

$$r_n = b - Ax_o - \alpha_o Ap_o - \alpha_1 Ap_1 - \alpha_2 Ap_2 + \ldots + \alpha_{n-2} Ap_{n-2} - \alpha_{n-1} Ap_{n-1} \qquad a1.6$$

All values of α are scalars so r_n can be expressed as

$$r_n = b - A(x_o + \alpha_o p_o + \alpha_1 p_1 + \alpha_2 p_2 + \ldots + \alpha_{n-2} p_{n-2} + \alpha_{n-1} p_{n-1}) \qquad a1.7$$

From equation a1.5 the quantity in brackets in a1.7 is equal to x_n so the equivalence of the true and recursive residuals is proved.

$$r_n = b - Ax_n = \bar{r} \qquad a1.8$$

This relation only holds of course when exact arithmetic is used throughout. Reid[36] has shown however that when exact arithmetic is not used the recursive residual only departs very slowly from the true residual provided that the algorithm is not working close to the machine accuracy. He recommends the use of the recursive residual in this instance because of its slightly better behaviour during the main part of the iteration and the fact that its use involves substantially less work per iteration.

APPENDIX 2

PRECONDITIONED BI-CONJUGATE GRADIENT ALGORITHM FOR THE SOLUTION OF GENERAL SETS OF SIMULTANEOUS EQUATIONS IN WHICH THE COEFFICIENT MATRIX IS SYMMETRIC AND NON-SINGULAR

A description of the basic bi-conjugate gradient technique is given by Fletcher[39]. The advantage of bi-conjugate gradients is that a non-positive definite system can be solved without having to use the normalised equations. This should mean that a bi-conjugate gradient algorithm converges faster than the ordinary conjugate gradient algorithm applied to the normalized system. The main disadvantages of a bi-conjugate gradient algorithm are that more computer storage and more work per iteration is required, than for ordinary conjugate gradients applied to the normalized system.

The following bi-conjugate gradient algorithm, including incomplete Choleski preconditioning, can be used for the solution of a general, complex set of linear simultaneous equations, $Ax = b$, where A is symmetric and non-singular.

$$A = LL^T + E \qquad (E = \text{error matrix})$$

$$\begin{aligned}
x_o &= (LL^T)^{-1}b \\
r_o &= b - Ax_o \\
\bar{r}_o &= r_o^* \\
p_o &= (LL^T)^{-1}r_o \\
\bar{p}_o &= ((LL^T)^*)^{-1}\bar{r}_o \\
\alpha_i &= \frac{(\bar{r}_i, (LL^T)^{-1}r_i)}{(A^*\bar{p}_i, p_i)}
\end{aligned} \qquad \text{a2.1}$$

$$x_{i+1} = x_i + \alpha_i p_i$$

$$r_{i+1} = r_i - \alpha_i A p_i$$

$$\bar{r}_{i+1} = \bar{r}_i - \alpha_i^* A^* \bar{p}_i$$

$$\beta_i = - \frac{(A^* \bar{p}_i, (LL^T)^{-1} r_{i+1})}{(A^* \bar{p}_i, p_i)}$$

a2.1 (cont.)

$$p_{i+1} = (LL^T)^{-1} r_{i+1} + \beta_i p_i$$

$$\bar{p}_{i+1} = ((LL^T)^*)^{-1} \bar{r}_{i+1} + \beta_i^* \bar{p}_i$$

In the algorithm a2.1, * denotes the complex conjugate and all inner products are evaluated using the complex conjugate transpose.

APPENDIX 3

DERIVATION, FROM THE QUASI-3D LINKED NETWORK FIELD MODEL, OF A FORMULA FOR THE THRUST FORCE PRODUCED BY A LINEAR INDUCTION MOTOR

By analogy with the simple equivalent circuit model for a round induction motor , the instantaneous thrust force, T_i, produced by a sinusoidal current i flowing in a small section of track of resistance R in a linear induction motor is given by,

$$T_i = \frac{1}{v_s} i^2 \frac{R}{s} \qquad a3.1$$

The variable v_s is the synchronous speed of the gap flux and s is the fractional slip. In the quasi-3D field model for a linear induction motor (LIM), described in Annex 1, the current is not sinusoidal but is represented by a Fourier series. The total instantaneous thrust force for the element is then found by summing the contributions due to all the sinusoidal currents in the series for i.

In the quasi-3D linked network field model for the LIM the space distribution of the actual track current is expressed in terms of x, y and z components of two stationary distributions differing in time and space phase by 90^o. The x, y and z components of one stationary distribution are represented by respective branch currents in the electric circuit of the quasi-3D linked network model. The total average thrust force produced by the machine is derived in terms of the actual branch resistances and currents flowing the network model. This is achieved by calculating the contributions from the x, y and z-directed currents as follows.

A section of track is shown in Fig. a3.1. It is of dimension Δx and Δz in the x and z directions respectively and length L in the y direction. L is equal to the period of the track current distribution, represented by a Fourier series. Let the section of track shown in Fig. a3.1 be appropriate for the x-directed current flow that is represented by the current in the q^{th} x-directed branch of the electric circuit for the quasi-3D model. That is the current i'_{xpq} in the q^{th} x-directed electric circuit branch due to the p^{th} harmonic of gap flux, is given by,

$$i'_{xpq} = \int_0^{\tau_p/2} k'_{xpq}(y)\, \Delta z\, \Delta y \qquad a3.2$$

where τ_p is the pole pitch for the p^{th} harmonic and Δy and Δz are as defined in Fig. a3.1. The value $k'_{xpq}(y)$, defined by equation a3.3, is the x-directed current density in the plate element of Fig. a3.1 for a single stationary p^{th} harmonic current distribution as used in the quasi-3D network model of Annex 1.

$$k'_{xpq}(y) = \hat{k}_{xpq} \sin s_p \omega t \sin a_p y \qquad a3.3$$

$$(a_p = \pi/\tau_p)$$

In equation a3.3 the harmonic slip s_p is included in the time frequency term to account for relative motion between the primary and secondary.

After substituting in equation a3.2 for $k'_{xpq}(y)$ from equation a3.3 and integrating,

$$i'_{xpq} = \frac{\Delta z}{a_p} \hat{k}_{xpq} \sin s_p \omega t \qquad a3.4$$

The thrust force produced by the p^{th} harmonic of the actual x-directed current flowing in the track element of Fig. a3.1 is expressed in terms of the branch current i'_{xpq}, defined by equation a3.4. This is

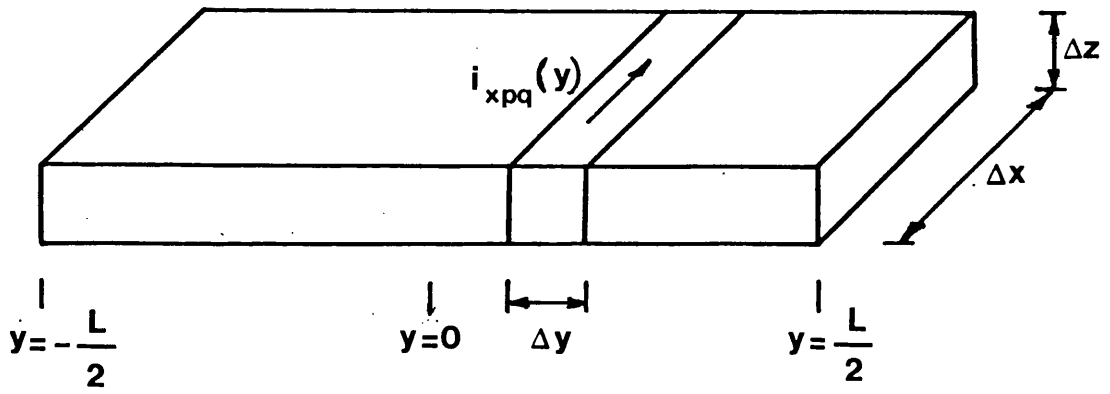

Fig. a3.1 A section of track conductor from the LIM.

performed using equation a3.1. The instantaneous thrust force, ΔT_{xpq}, from the p^{th} harmonic of the actual x-directed current, $i_{xpq}(y)$, flowing in the track element of Fig. a3.1 is given by

$$\Delta T_{xpq} = \int_{-L/2}^{L/2} \frac{1}{v_{sp}} i_{xpq}^2(y) \frac{\Delta R}{s_p} \qquad a3.5$$

where $\Delta R = \frac{\Delta x}{\sigma \Delta z \Delta y}$ a3.6

with Δx, Δy and Δz as defined in Fig. a3.1 and σ equal to the conductivity of the track. The current $i_{xpq}(y)$ is found from the travelling distribution of current density $k_{xpq}(y)$ in the actual track. Expressed as the sum of two stationary distributions, differing in time and space phase by 90°, $k_{xpq}(y)$ is defined in equation a3.7,

$$k_{xpq}(y) = \hat{k}_{xpq} \cos s_p \omega t \cos a_p y + \hat{k}_{xpq} \sin s_p \omega t \sin a_p y \qquad a3.7$$

Let $\alpha_{xpq} = \hat{k}_{xpq} \cos s_p \omega t$ a3.8

and $\beta_{xpq} = \hat{k}_{xpq} \sin s_p \omega t$ a3.9

giving $k_{xpq}(y) = \alpha_{xpq} \cos a_p y + \beta_{xpq} \sin a_p y$ a3.10

Hence, α_{xpq} and β_{xpq} can be regarded as the coefficients of a Fourier series representing the current density $k_{xpq}(y)$. The current $i_{xpq}(y)$, in the part of the element $\Delta x \Delta y \Delta z$ shown in Fig. a3.1, is therefore given by

$$i_{xpq}(y) = \Delta y \Delta z \, k_{xpq}(y) \qquad a3.11$$

Substituting in equation a3.5 for $i_{xpq}(y)$ using equations a3.10 and a3.11 and also substituting for ΔR using equation a3.6 gives,

$$\Delta T_{xpq} = \frac{1}{\sigma v_{sp} s_p} \int_{-L/2}^{L/2} (\alpha_{xpq} k_{xpq}(y) \cos a_p y + \beta_{xpq} k_{xpq}(y) \sin a_p y) \Delta x \Delta y \Delta z \qquad a3.12$$

However α_{xpq} and β_{xpq} are the coefficients of the Fourier series for $k_{xpq}(y)$, as described earlier and are therefore defined as,

$$\alpha_{xpq} = \frac{2}{L} \int_{-L/2}^{L/2} k_{xpq}(y) \cos a_p y \, dy \qquad a3.13$$

$$\beta_{xpq} = \frac{2}{L} \int_{-L/2}^{L/2} k_{xpq}(y) \sin a_p y \, dy \qquad a3.14$$

with $a_p = \frac{\pi}{\tau_p} = \frac{2p\pi}{L}$

Equation a3.12 therefore simplifies to,

$$\Delta T_{xpq} = \frac{L}{2\sigma v_{sp} s_p} (\alpha^2_{xpq} + \beta^2_{xpq}) \Delta x \Delta z \qquad a3.15$$

Re-substituting for α_{xpq} and β_{xpq} from equations a3.8 and a3.9 respectively gives,

$$\Delta T_{xpq} = \frac{L}{2\sigma v_{sp} s_p} \hat{k}^2_{xpq} (\cos^2 s_p \omega t + \sin^2 s_p \omega t) \Delta x \Delta z \qquad a3.16$$

This simplifies to,

$$\Delta T_{xpq} = \frac{L}{2\sigma v_{sp} s_p} \hat{k}^2_{xpq} \Delta x \Delta z \qquad a3.17$$

In terms of the amplitude $\hat{i}'_{xpq}$ of the branch current i'_{xpq}, defined by equation a3.4, in the q^{th} x-directed branch of the network model for the p^{th} harmonic, equation a3.17 becomes,

$$\Delta T_{xpq} = \frac{L}{v_{sp} s_p} \frac{\hat{i}'^2_{xpq}}{2} \frac{a_p^2 \Delta x}{\sigma \Delta z} \qquad a3.18$$

The resistance of an x-directed branch is defined in Annex 1, equation A1.35, as $R_x = \frac{a\Delta x}{\sigma \Delta z}$. Let R_{xpq} be the resistance of the q^{th} x-directed branch for the p^{th} harmonic and let I_{xpq} be the rms value

of the branch current i'_{xpq}. The thrust force ΔT_{xpq} can then be written,

$$\Delta T_{xpq} = \frac{L}{v_{sp}} a_p I^*_{xpq} I_{xpq} \frac{R_{xpq}}{s_p} \qquad a3.19$$

where the * denotes the complex conjugate. The force ΔT_{xpq} is the thrust force produced over the length of track L, by the p^{th} harmonic x-directed current flow that is defined by the q^{th} x-directed branch current in the electric circuit of the quasi-3D model. It is noted that the force ΔT_{xpq} is not a function of time. The total thrust force T_x due to all m frequency components and all x-directed current flow, represented by the nx x-directed branches, is found by a double summation as follows.

$$T_x = L \sum_{p=1}^{m} \sum_{q=1}^{nx} \frac{a_p}{v_{sp}} I^*_{xpq} I_{xpq} \frac{R_{xpq}}{s_p} \qquad a3.20$$

A similar procedure is followed for the y and z-directed current flows. This gives corresponding thrust force expressions in terms of the appropriate rms branch currents and branch resistances in the actual quasi-3D model. The total thrust force T_y for all m frequency components and all y-directed branch current flow is given by equation a3.21, where ny is the total number of y branches in the electric part of the quasi-3D model.

$$T_y = L \sum_{p=1}^{m} \sum_{q=1}^{ny} \frac{a_p}{v_{sp}} I^*_{ypq} I_{ypq} \frac{R_{ypq}}{s_p} \qquad a3.21$$

Similarly, the thrust force T_z for all z-directed current flow, with nz equal to the total number of z-directed electric circuit branches in the quasi-3D model, is given by,

$$T_z = L \sum_{p=1}^{m} \sum_{q=1}^{nz} \frac{a_p}{v_{sp}} I^*_{zpq} I_{zpq} \frac{R_{zpq}}{s_p} \qquad a3.22$$

The total thrust force, T, produced by the machine is then found by summing the x, y and z contributions to give finally,

$$T = L \sum_{p=1}^{m} \left(\sum_{q=1}^{nx} \frac{a_p}{v_{sp}} I^*_{xpq} I_{xpq} \frac{R_{xpq}}{s_p} + \sum_{q=1}^{ny} \frac{a_p}{v_{sp}} I^*_{ypq} I_{ypq} \frac{R_{ypq}}{s_p} + \sum_{q=1}^{nz} \frac{a_p}{v_{sp}} I^*_{zpq} I_{zpq} \frac{R_{zpq}}{s_p} \right) \qquad a3.23$$

REFERENCES

1. EASTHAM, J.F.: "Iron-cored linear synchronous machines", IEE Electronics and Power, March, 1977, pp.239-242.

2. POPOVIĆ, B.D.: "Introductory Engineering Electromagnetics", (Addison-Wesley, 1973).

3. LAWRENSON, P.J. and RALPH, M.C.: "General three-dimensional solution of eddy current and Laplacian fields in cylindrical structures", Proc. IEE, Feb. 1970, Vol.117, No.2, pp.467-472.

4. TROWBRIDGE, C.W.: "Application of integral equation methods for the numerical solution of magnetostatic and eddy current problems", Rutherford Laboratory, June 1976, RL-76-071.

5. NEWMAN, M.J., TROWBRIDGE, C.W. and TURNER, L.R.: "GFUN: An interactive program as an aid to magnet design", Proc. 4th International Conference on Magnet Technology, Brookhaven, 1972.

6. ARMSTRONG, A.G., COLLIE, C.J., SIMKIN, J., TROWBRIDGE, C.W. "The solution of 3D magnetostatic problems using scalar potentials", Proceedings of COMPUMAG Conference, Grenoble, Sept. 1978, Paper 1.2.

7. McWHIRTER, J.H. and ORAVEC, J.J.: "Three-dimensional electrostatic field solutions in a rod gap by a Fredholm integral equation", Proceedings, International Symposium on High Voltage Engineering, Milan, August 28-31 1979.

8. SIMKIN, J. and TROWBRIDGE, C.W.: "On the use of the total scalar potential in the numerical solution of field problems in electromagnetics", International Journal for Numerical Methods in Engineering, Vol.14, pp.423-440.

9. SILVESTER, P. and CHARI, M.V.K.: "Finite element solution of saturable magnetic field problems", IEEE Trans., P.A.S., Sept/Oct, 1970, Vol.80, No.7, pp.1642-1651.

10. CARPENTER, C.J. and DJUROVIC, M.: "Three-dimensional numerical solution of eddy currents in thin plates", Proc. IEE, June 1975, Vol. 122, No.6, pp.681-688.

11. CARPENTER, C.J. and WYATT, E.A.: "Efficiency of numerical techniques for computing eddy currents in two and three dimensions", Proceedings COMPUMAG, 1976, pp.242-250.

12. CARPENTER, C.J.: "Comparison of alternative formulations of 3-dimensional magnetic-field and eddy-current problems at power frequencies", Proc. IEE, Nov. 1977, Vol. 124, No.11, pp.1026-1034.

13. PRESTON, T.W. and REECE, A.B.J.: "Finite element solution of 3-dimensional eddy current problems in electrical machines", Proceedings COMPUMAG Conference, Grenoble 1978, Paper 7.4.

14. PRESTON, T.W. and REECE, A.B.J.: "Solution of three dimensional eddy current problems: the T-Ω method", IEE Colloquium on "Computer Solution of Three-dimensional Electromagnetic Fields: the State of the Art", November 1980, paper 2.

15. KRON, G: "Equivalent circuit for the field equations of Maxwell-I", Proc. IRE, 1944, Vol.32, pp.289-299.

16. ROBERTS, J.: " Analogue treatment of eddy-current problems involving two-dimensional fields", Proc.IEE, 1960, Vol.107C, pp.11-18.

17. CARPENTER, C.J.: "Numerical solution of magnetic fields in the vicinity of current carrying conductors", Proc.IEE, Nov. 1967, Vol.114, No.11, pp.1793-1800.

18. GUILLEMAN, E.A.: "Introductory Circuit Theory", (Wiley-Toppan, 1953).

19. WEEKS, W.T., JIMENEZ, A.J., MAHONEY, G.W., MEHTA, D., QASSEMZADEH, H. and SCOTT, J.R.: "Algorithms for ASTAP - A network analysis program", IEEE Trans. C.T., Nov.1973, Vol.20, No.6, pp.628-634.

20. BALCHIN, M.J. and DAVIDSON, J.A.M.: "Numerical method for calculating magnetic flux and eddy current distributions in three dimensions", Proc. IEE, Jan. 1980, Vol.127, Pt.A, No.1, pp.46-53.

21. DAVIDSON, J.A.M. and BALCHIN, M.J.: "Experimental verification of network method for calculating flux and eddy-current distributions in three dimensions", Proc. IEE, Oct. 1981, Vol.128, Pt.A, No.7, pp.492-496.

22. BRANIN Jr., F.H.: "D-C and transient analysis of networks using a digital computer", IRE International Convention Record, Pt.2, March 1962, pp.236-256.

23. BRANIN Jr., F.H.: "The relation between Kron's method and the classical methods of network analysis", IRE WESCON Convention Record, Part 2, 1959, pp.3-28.

24. JENNINGS, A.: "Matrix Computation for Engineers and Scientists", (Wiley and Sons, 1977).

25. GIBBS, N.E., POOLE Jr., W.G. and STOCKMEYER, P.K.: "An algorithm for reducing the bandwidth and profile of a sparse matrix", SIAM Journal of Numerical Analysis, April 1976, Vol.13, No.2, pp.236-250.

26. IRONS, B.M.: "A frontal solution program for finite element analysis", International Journal of Numerical Methods in Engineering Science, 1970, Vol.2, pp.5-32.

27. CURTIS, A.R. and REID, J.K.: "The solution of large sparse unsymmetric systems of linear equations", Journal of the Institute of Mathematics and its Applications, 1971, Vol.8, pp.344-353.

28. GEORGE, J.A.: "Nested dissection of a regular finite element mesh", SIAM Journal of Numerical Analysis, 1973, Vol.10, pp.345-363.

29. PEACEMAN, D.W. and RACHFORD Jr., H.H.: "The numerical solution of parabolic and elliptic differential equations", Journal of Society of Industrial Applications of Mathematics, March 1955, Vol.3, No.1, pp.28-41.

30. STONE, H.L.: "Iterative solution of implicit approximations of multi-dimensional partial differential equations", SIAM Journal of Numerical Analysis, 1968, Vol.5, pp.530-558.

31. STOLL, R.L.: "Solution of linear steady state eddy current problems by complex successive overrelaxation", Proc. IEE, 1970, Vol.117, pp.1317-1323.

32. HESTENES, M.R. and STIEFEL, E.: "Methods of conjugate gradients for solving linear systems", Journal of Research of National Bureau of Standards, Dec. 1952, Vol.49, pp.409-436.

33. MEIJERINK, J.A. and VAN DER VORST, H.A.: "An iterative solution method for linear systems of which the coefficient matrix is a symmetric M-matrix", Mathematics of Computation, Jan. 1977, Vol.31, No.137, pp.148-162.

34. KERSHAW, D.S.: "The incomplete Cholesky-conjugate gradient method for the iterative solution of systems of linear equations", Journal of Computational Physics, 1978, Vol.26, pp.43-65.

35. STEWART, G.W.: "The convergence of the method of conjugate gradients at isolated extreme points of the spectrum", Numerical Mathematics, 1975, Vol.24, pp.85-93.

36. REID, J.K.: "On the Method of Conjugate Gradients for the Solution of Large Sparse Systems of Linear Equations", (Academic Press, New York, 1971).

37. WILKINSON, J.H. and REINSCH, C: "Handbook for Automatic Computation", Vol.II, Linear Algebra, pp.339-358 and 396-403, (Springer-Verlag, 1971).

38. BRAMELLER, A., ALLAN, R.N. and HAMAM, Y.M.: "Sparsity, its practical application to systems analysis", (Pitman, London, 1976).

39. FLETCHER, R.: "Conjugate gradient methods for indefinite systems", Lecture Notes in Mathematics (506), Proceedings of the Dundee Conference on Numerical Analysis, 1975, pp.73-89.

40. PRESTON, T.W. and REECE, A.B.J.: "Transverse edge effects in linear induction motors", Proc. IEE, June 1969, Vol.116, No.6, pp.973-979.

41. LAITHWAITE, E.R.: "Induction Machines for Special Purposes", (Newnes, 1966).

42. BALCHIN, M.J.: "The analysis and design of some windings for linear induction machines", Ph.D. Thesis, Imperial College, 1975.

43. CARPENTER, C.J.: "Surface-integral methods of calculating forces on magnetized iron parts", Proc. IEE, 1960, Vol.107, Part C, pp.19-28.

44. CARTER, F.W.: "The magnetic field of the dynamo-electric machine", Journal of IEE, 1926, Vol.64, pp.1115-1138.

SCIENCE

Numerical method for calculating magnetic-flux and eddy-current distributions in three dimensions

M.J. Balchin, B.Sc.(Eng.), Ph.D., D.I.C., and J.A.M. Davidson, B.Sc.(Eng.)

Indexing terms: *Electromagnetics, Numerical methods, Eddy currents*

Abstract: A practical technique is presented for the numerical solution of general three-dimensional electrodynamic field problems. Circuit models are derived separately for the electric and magnetic parts of the field. Conventional network-analysis techniques are then developed to isolate the independent closed paths that link the models. This avoids the difficulty, inherent in the usual differential equation approach, of describing the field interactions. Network techniques are again employed to formulate a straightforward solution. Sample calculations are performed for three power-frequency steady-state a.c. problems to demonstrate the application of the method.

List of principal symbols

A = area
b = magnetic flux density
C = capacitance
C_E, C_M, N = connection matrices
E, e = voltage
F, f = electric field strength
G = conductance
I, i = current
K, k = current density
M, m = magnetomotive force (m.m.f.)
n = unit outward normal vector
P = permeance
p = time derivative, d/dt
ϵ = permittivity
σ = conductivity
ϕ = magnetic flux

1 Introduction

A significant proportion of the development cost of an item of electrical apparatus is associated with the construction of prototypes. It is possible to avoid some of this expense if the performance of trial designs can be reliably predicted. The operation of many electrical devices is dependent on, or is influenced by, spatial distributions of magnetic flux and electric current. Performance predictions for these devices will therefore involve the calculation of electromagnetic field quantities.

Analytical solutions of the electromagnetic field equations are possible in cases where boundaries and interfaces are suitably simple. In devices for which the boundary surfaces cannot be sufficiently simplified, the field equations must be solved using a numerical method. This paper is concerned with the techniques associated with the discrete representation of differential equations.

Although much effort is required in the preparation of computer programs, solution techniques are now well established for all electrostatic, magnetostatic and one- and two-dimensional electrodynamic problems. Three-dimensional electrodynamic problems have also been solved,[1] but an exhaustive search of the current literature has shown that practical techniques exist only for the case in which either the magnetic flux or the electric current is confined to two-dimensional surfaces.[2] Recent activity in the field of advanced ground transport has revealed a need for accurate performance predictions for linear induction machines, vehicle lift magnets and new types of linear synchronous machine.[3] Examples of other problems currently receiving attention are waveguide junctions, turbogenerator end regions and transformer leakage. The configuration of all these devices is such that their geometry is complex. As a result, the distribution of both electric and magnetic fields in three dimensions must be considered. The purpose of this paper is to present what is believed to be the first practical numerical method of calculating general three-dimensional electrodynamic field distributions.

In Reference 1 the interaction between a two-dimensional electric, and a three-dimensional magnetic field is considered. The electric and magnetic fields are treated separately with finite-difference network models being obtained for each. These discretised fields include all boundary and interface conditions, and the disposition of the elements is such that a number of rectangular surfaces of the electric model are intersected by branches of the magnetic model. Since the electric field quantities are restricted to two dimensions, the corresponding network model is planar. In a planar network each closed path can be considered to support an independent circulating current.[4] Thus, each rectangular surface of the electric field model is responsible for the injection of m.m.f. into its intersecting magnetic branch. The circulating electric current is driven by an e.m.f. that is equal to the time rate of change of flux in the intersecting magnetic branch. The limitation of this method lies in the requirement for one of the circuit models to be planar. This has to be so in order to be able to isolate independent paths for the application of both Faraday's and Ampere's Laws. In this paper conventional network techniques are used to define the independent paths such that the planar restriction is removed. Three-dimensional electrodynamic field solutions are then shown to be possible.

2 Discrete field model

2.1 *Derivation of one network element for the electric field*

When constructing electromagnetic field models, it is usual

Paper 488 A, first received 30th March 1979 and in revised form 6th August 1979

Dr. Balchin and Mr. Davidson are with the Department of Electrical Engineering, University of Bath, Claverton Down, Bath BA2 7AY England

0143-702X/80/010046 + 08 $01.50/0

to begin by obtaining a partial differential equation for one field quantity at one point in space. The partial differential equation is then represented in finite-difference or finite-element form, and the network analogue follows. Finite-difference techniques usually lead to network models with a rectangular mesh structure. This is not a restriction because any polygonal shape can be used,[5] including irregular triangles[6] which are usually associated with finite element techniques.[7] The procedure for deriving network models is satisfactory for both electrostatic and magnetostatic field problems in three dimensions. This is because scalar potentials can be used, and there is only a minimum number of variables. The method is also appropriate for certain electromagnetic problems in two or three dimensions in which a restricted set of vectors can be treated as scalar quantities.[2] For general electromagnetic problems in three dimensions a vector partial differential equation, which may also include scalars, must be discretised. Unfortunately the elimination process used in deriving the equation obscures the interaction between the variables and so complicates the solution process. The numerical method described in this paper employs separate network models for the electric and magnetic parts of the electromagnetic field. An advantage of this approach is that each of the field vectors, scalars and interface conditions are readily identifiable in the model. Furthermore the complete circuit can be solved using conventional network-analysis techniques which implies the use of a minimum, independent set of vector components. This is in contrast to the more obvious methods. These require, at the very least, the solution of equations for three components of both electric and magnetic field strength at each nodal point.

The derivation of the network model is based on the method described in Reference 5. It will be illustrated by means of the tetrahedral region shown in Fig. 1, although the same process can be employed for any volume shape. The complete field is divided into regions such as 1-2-3-4 of Fig. 1. Each region supports a uniform current density and the material of which it is formed is assumed to be isotropic. Anisotropy can be included as is shown in Reference 8. Components of the current density within the volume are assigned to each of its edges. In order to divide the current, the concept of geometric duality in three dimensions is employed. For example, in Fig. 1, the point O is the dual of volume 1-2-3-4. The line O-A is the dual of surface 1-2-3 which it intersects normally. Area A is part of the polygonal surface that is the dual of line 1-2.

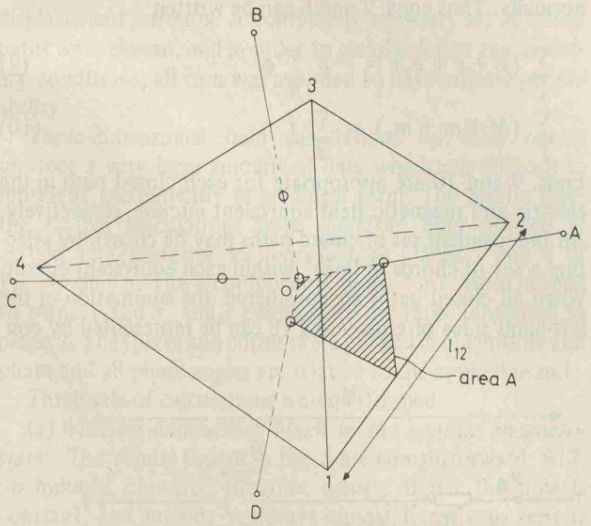

Fig. 1 *Region of subdivided field*

Within an isotropic electrically conducting medium the constitutive relation is

$$K + k = (\sigma + \epsilon p)(F + f)$$

In this expression the vector quantities are represented as the sum of solenoidal and lamellar components. The solenoidal parts are represented by lower-case symbols and the lamellar parts by upper case.

Resolving the current density and electric field strength in a direction parallel to line 1-2 gives

$$(K + k)\cos\alpha = (\sigma + \epsilon p)(F + f)\cos\alpha \quad (1)$$

where α is the angle between the vectors and line 1-2.

The components of current within the region that are associated with edge 1-2 are those flowing through area A, i.e.

$$\left.\begin{aligned} I_{12} &= AK\cos\alpha \\ i_{12} &= Ak\cos\alpha \end{aligned}\right\} \quad (2)$$

The potential differences existing between points 1 and 2 are given by

$$\int_1^2 F\cos\alpha dl = E_{12}$$

$$\int_1^2 f\cos\alpha dl = e_{12}$$

where dl is parallel to line 1-2.

Evaluating the integrals for a constant field strength gives

$$\left.\begin{aligned} Fl_{12}\cos\alpha &= E_{12} \\ fl_{12}\cos\alpha &= e_{12} \end{aligned}\right\} \quad (3)$$

Substituting eqns. 3 and 2 into eqn. 1 gives

$$I_{12} + i_{12} = (\sigma + \epsilon p)\frac{A}{l_{12}}(E_{12} + e_{12}) \quad (4)$$

In eqn. 4 the quantities $\sigma A/l_{12}$ and $\epsilon A/l_{12}$ represent the conductance and capacitance that admit the flow of current through area A in Fig. 1. It is therefore convenient to represent the equation by means of an equivalent circuit, one possible combination of elements being shown in Fig. 2. The fact that certain of the variables are represented by means of sources and others by means of branch quantities

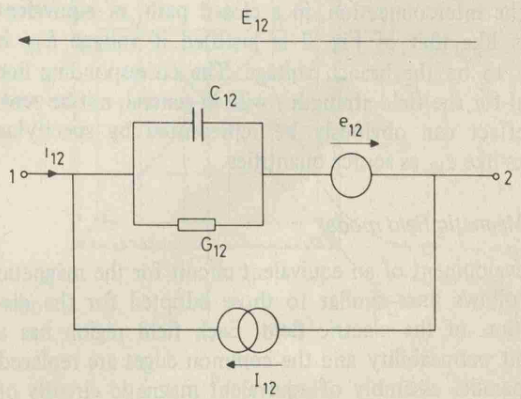

Fig. 2 *Element of electric field model*

is explained in the following Section. The procedure described in this Section is repeated at each of the region edges. This results in a circuit, similar to that of Fig. 2, replacing each edge of the region.

2.2 Complete electric field model

In order to model the complete electric field, the space in which it exists is first subdivided into a number of regions. As volumes associated with the region edge are replaced by equivalent electric circuits, there will be a number of these elements connected in parallel along each region edge. This means that the conductivity and permittivity of the material contained within each volume need not necessarily be the same. Interface or boundary conditions can therefore be imposed at the surface of any region.

The distribution of current density in an electric field is described by means of a surface integral relationship. In Fig. 1 the dual of each vertex is a closed surface S. The surface is formed of a number of areas such as A across which a uniform and normal current density exists. For the complete closed surface,

$$\int_S kn\,dS = 0$$

applies.

Because of the way in which the total current has been subdivided, this expression can be written

$$\sum_S i = 0$$

Thus the interconnection, at a vertex, of circuits like that of Fig. 2 is justified if current i_{12} is chosen to be the branch current. The corresponding surface integral for the current density K is equal to the time rate of change of charge contained within S. This accumulation of charge can be obtained by specifying that currents like I_{12} be represented by means of independent source quantities.

The distribution of field strength in an electric field is described by means of a line-integral relationship. Within the complete field model a closed path l can be traced by following region edges. Along each region edge the field strength is uniform so that the expression

$$\int_l Fdl = 0$$

can be interpreted as

$$\sum_l E = 0$$

Thus the interconnection, in a closed path, of equivalent circuits like that of Fig. 2 is justified if voltage E_{12} is chosen to be the branch voltage. The corresponding line integral for the field strength f will, in general, not be zero. This effect can obviously be represented by specifying voltages like e_{12} as source quantities.

2.3 Magnetic field model

The development of an equivalent circuit for the magnetic field follows lines similar to those adopted for the discretisation of the electric field. Each field region has a constant permeability and the common edges are replaced by a parallel assembly of equivalent magnetic circuits of the type shown in Fig. 3. Branch variables are again chosen following a consideration of the line and surface integrals of field strength and flux density. In this case however the integral of the lamellar component of flux density does not exist since there are no free magnetic poles. This means that sources of magnetic flux, analogous to I_{12} in Fig. 2, do not appear in the equivalent circuit.

2.4 Complete electromagnetic field model

Both the electric and magnetic field regions are subdivided into discrete volumes using the methods explained in Sections 2.1 to 2.3. The subdivision is arranged so that the surfaces of each magnetic volume are intersected normally by edges of the electric volumes and vice versa. The reason for this will become apparent when the interaction between the electric and magnetic circuits is considered in Section 3.

3 Derivation and solution of field equations

The way in which the field model has been derived has led to there being only one type of source quantity. This source is the current generator I_{12} shown in Fig. 2. It is often found, however, that excitation of the field system can be considered to be due to applied potentials. In order to represent this, independent potential sources are introduced. An assembly of equivalent circuits of the type shown in Figs. 1 and 2 will therefore be represented by the following matrix equations:

$$E + e + e_s = (G + pC)^{-1} i \tag{5}$$

$$M + m + m_s = P^{-1}\phi \tag{6}$$

in which e_s and m_s are independent potential sources.

Eqns. 5 and 6 are solved by the use of a discrete form of Faraday's and Ampere's Laws. For one closed path l in the electric model surrounding a surface S

$$\int_l (F + f)\,dl = -p \int_S bn\,d^S \tag{7}$$

A similar expression holds for the magnetic model, i.e.

$$\int_l (H + h)\,dl = \int_S kn\,dS \tag{8}$$

The manner in which the fields are subdivided is such that each closed path is formed with segments of uniform field strength parallel to the path. Furthermore each closed path surrounds a surface through which flux or current passes normally. Thus eqns. 7 and 8 can be written

$$\sum_l (E + e + e_s) = -p \sum_S \phi \tag{9}$$

$$\sum_l (M + m + m_s) = \sum_S i \tag{10}$$

Eqns. 9 and 10 are appropriate for each closed path in the electric and magnetic field equivalent circuits, respectively. An independent set of closed paths may be chosen by selecting a set of chords or links[4] within each equivalent circuit. When all closed paths are considered, the summation of the left-hand sides of eqns 9 and 10 can be represented by con-

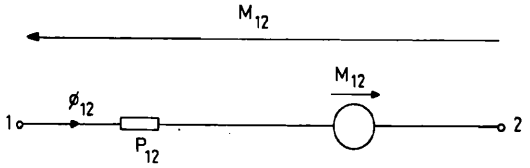

Fig. 3 *Element of magnetic field model*

nection matrices.[9] The right-hand sides of eqns. 9 and 10 can similarly be represented by a connection matrix that indicates which of the closed path fluxes links a closed path in the electric model and vice versa. Thus eqns. 9 and 10 become

$$C_E^T (E + e + e_s) = -pN^T \phi_I \tag{11}$$

$$C_M^T (M + m + m_s) = Ni_I \tag{12}$$

where ϕ_I and i_I are the closed-path fluxes and currents. These quantities are the minimum independent set of variables that are required to solve the field problem.

It is shown in Reference 9 that

$$i = C_E i_I \tag{13}$$

and it follows that

$$\phi = C_M \phi_I \tag{14}$$

The set of eqns. 5, 6 and 11–14 can be solved to give the magnetic fluxes and electric currents, i.e.

$$\begin{aligned}\phi = {} & C_M\{[C_M^T \boldsymbol{P}^{-1} C_M] \\ & + pN[C_E^T(G + pC)^{-1}C_E]^{-1}N^T\}^{-1}\{C_M^T m_s \\ & + N[C_E^T(G + pC)^{-1}C_E^T e_s\}\end{aligned} \tag{15}$$

$$\begin{aligned}i = {} & C_E\{[C_E^T(G + pC)^{-1}C_E] \\ & + pN^T[C_M^T P^{-1} C_m]^{-1}N\}^{-1}\{C_E^T e_s \\ & - pN^T[C_M^T P^{-1}\, C_m]^{-1}C_M^T m_s\}\end{aligned} \tag{16}$$

4 Sample calculations and discussion of results

In order to demonstrate the method, the electric and magnetic fields were calculated within the region shown in Fig. 4. Each field was subdivided into rectangular regions, the whole being energised by a constant m.m.f. of $100 + 0j$A/m. Several planes of symmetry, AA, BB, CC and DD exist in the region as shown, so that only one-eighth of the volume need be considered. In fact the calculations were performed over a quarter of the region using only the symmetry properties of planes AA and BB, the symmetry along CC and DD being sought in the results. Steady-state a.c. conditions were assumed using a frequency of 50 Hz. To represent these conditions p was replaced by $j\omega$ in eqns. 15 and 16, and C was set to infinity, thereby neglecting displacement currents. A completely arbitrary set of closed paths were chosen, and in order to clearly define the boundary conditions, all iron was assumed to have infinite permeability.

Three-dimensional field calculations by their nature produce a very large amount of data which are difficult to represent conveniently in graphical form. The results from the sample calculations were therefore only plotted at certain representative sections such as planes 1 and 2 of Fig. 4*a* and *b*. The z-components plotted are those normal to plane 1 and x- and y-components are those tangential to plane 2. The fluxes and currents are plotted in magnitude and phase and all phase angles are relative to the applied m.m.f.

Three sets of calculations were performed:

(*a*) *With no conducting block in the gap; i.e. magnetostatic:* The results shown in Fig. 5 are straightforward. With no induced currents, the flux density under the pole is constant, and outside it decays almost linearly to zero at the iron boundary. The phase angles for all fluxes are equal to 180°, and so have not been plotted.

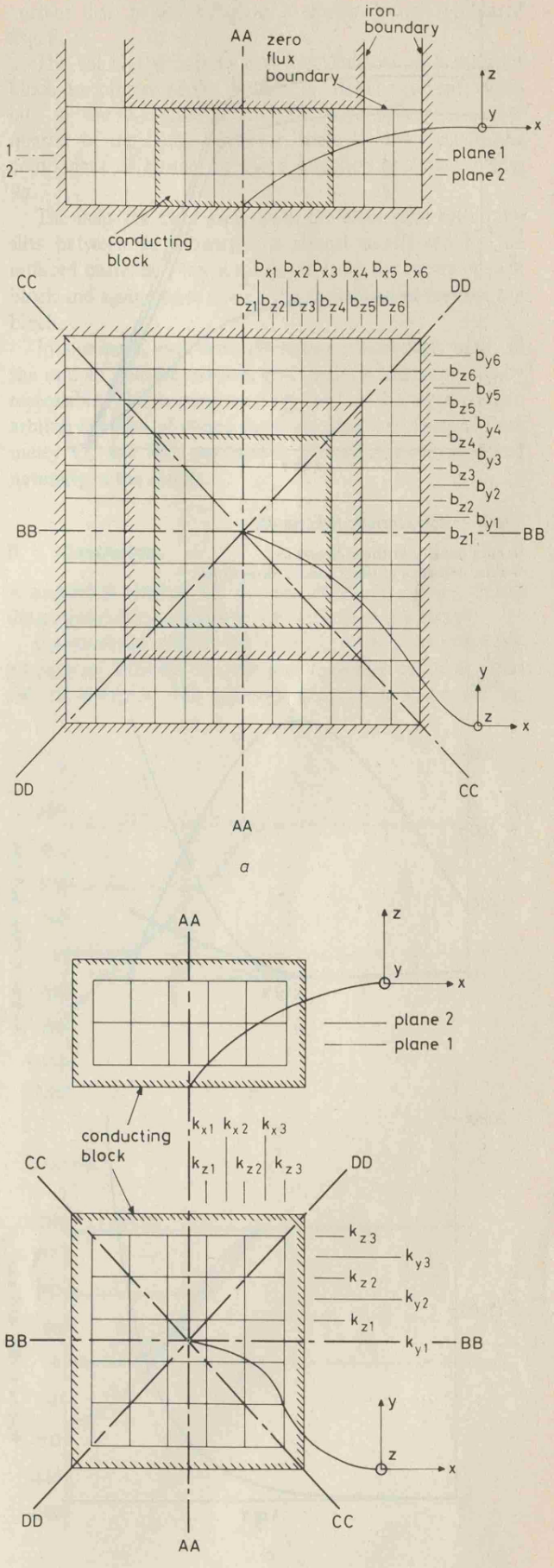

Fig. 4 *Model for sample calculations*

a The magnetic circuit
b The electric circuit

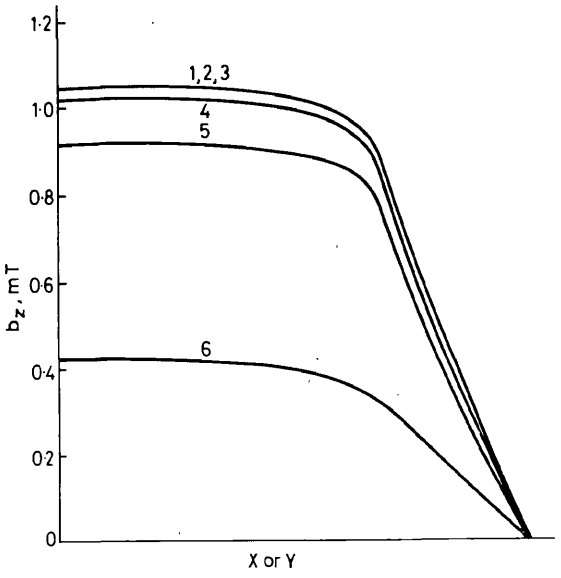

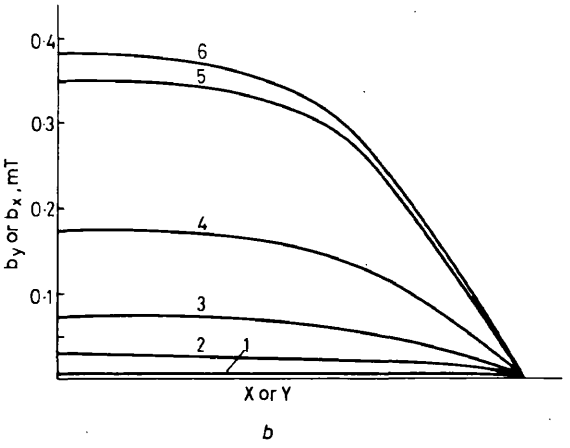

Fig. 5 *Magnetostatic field results*

a Flux density in the *z*-direction
b Flux densities in the *X*- and *Y*-directions

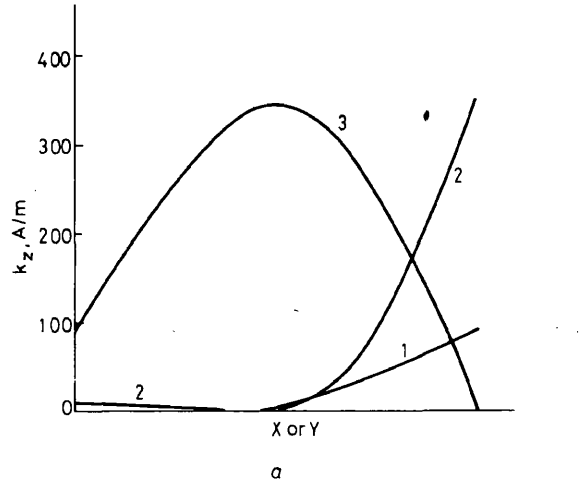

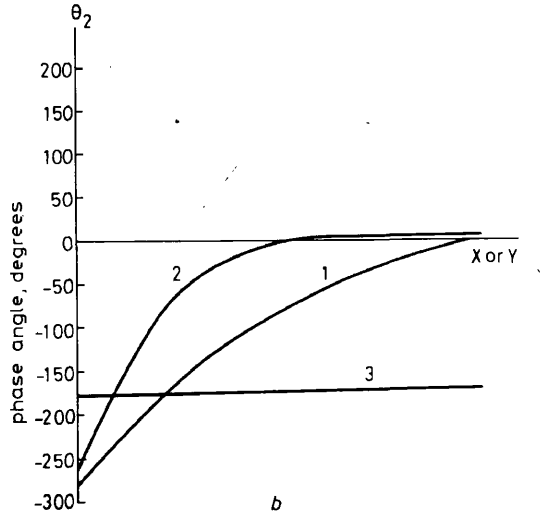

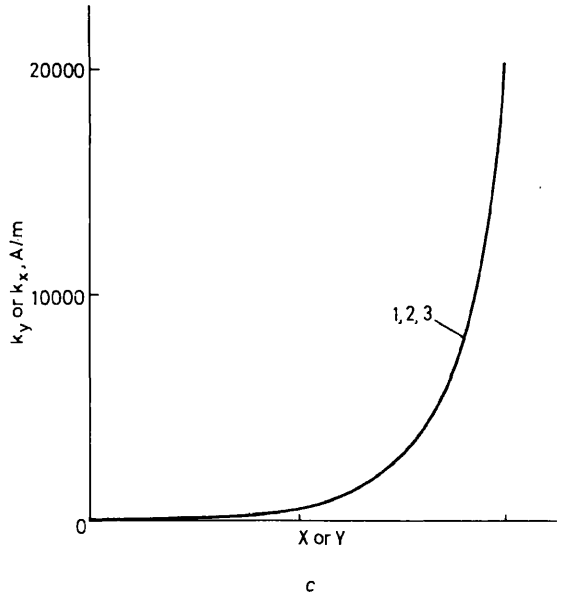

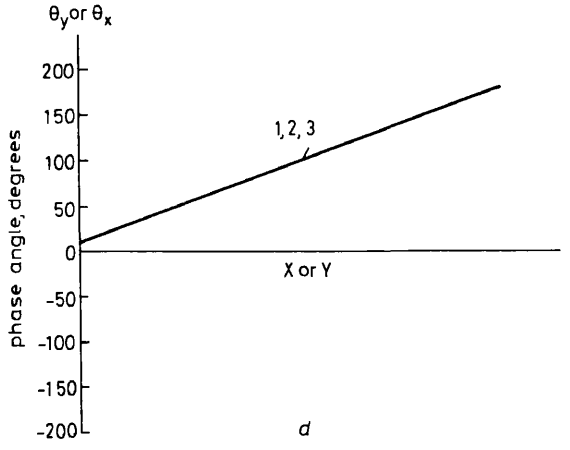

Fig. 6 *Electric field results with conducting block*

a Magnitude of current density in *z*-direction
b Phase of current density in *z*-direction
c Magnitude of current densities in *X*- and *Y*-directions
d Phase of current densitites in *X*- and *Y*-directions

(*b*) *With a single conducting block placed centrally under the pole, as in Fig. 4:* The calculated current and flux densities for this case are plotted in Fig. 6 and Fig. 7, respectively. These show currents circulating mainly in the *XY*-planes. The distribution exhibits deep bar effect in that the current density is greatest near the sides of the block. There is only a very small component of current flowing in the *z*-direction.

The flux density calculations show that away from the block the magnetic field is virtually unaffected by the induced currents. Flux has been displaced from the centre of the block and passes around the vertical outer surfaces giving an increase in flux-density in this region over that observed in the magnetostatic case.

(*c*) *With a conducting block as in (b), but with slits introduced along planes AA and BB;* Figs. 6 and 7 show that the current flow in the single conducting block is practically two-dimensional. To obtain a more three-dimensional flow slits were introduced into the block along the symmetry planes AA and BB. The effect of the slits on current flow in the *XY*-plane is shown in the sketches of Fig. 8.

The calculated current and flux densities with the split block are plotted in Fig. 9 and Fig. 10. The currents circulate in the *XY*-plane around the edge of each separate quarter of the block. However, there is now a significant component of current in the *z* direction as shown in Fig. 9*a*.

The magnetic field away from the block, and within the slits between each quarter, is almost unaffected by the induced currents. Flux is displayed from the centre of each block and again passes around the vertical outer faces of the block.

In summary, even with the rather coarse mesh used, all the sample field calculations give results which appear to be reasonable. This is reinforced by the fact that even with an arbitrary choice of closed paths the diagonal planes of symmetry CC and DD, not used in the calculations, appeared naturally in the results.

5 Conclusions

A numerical method for the calculation of general three-dimensional electromagnetic fields has been presented.

Conventional differential equation techniques make the interaction between electric and magnetic variables difficult to interpret. The approach adopted in this work has

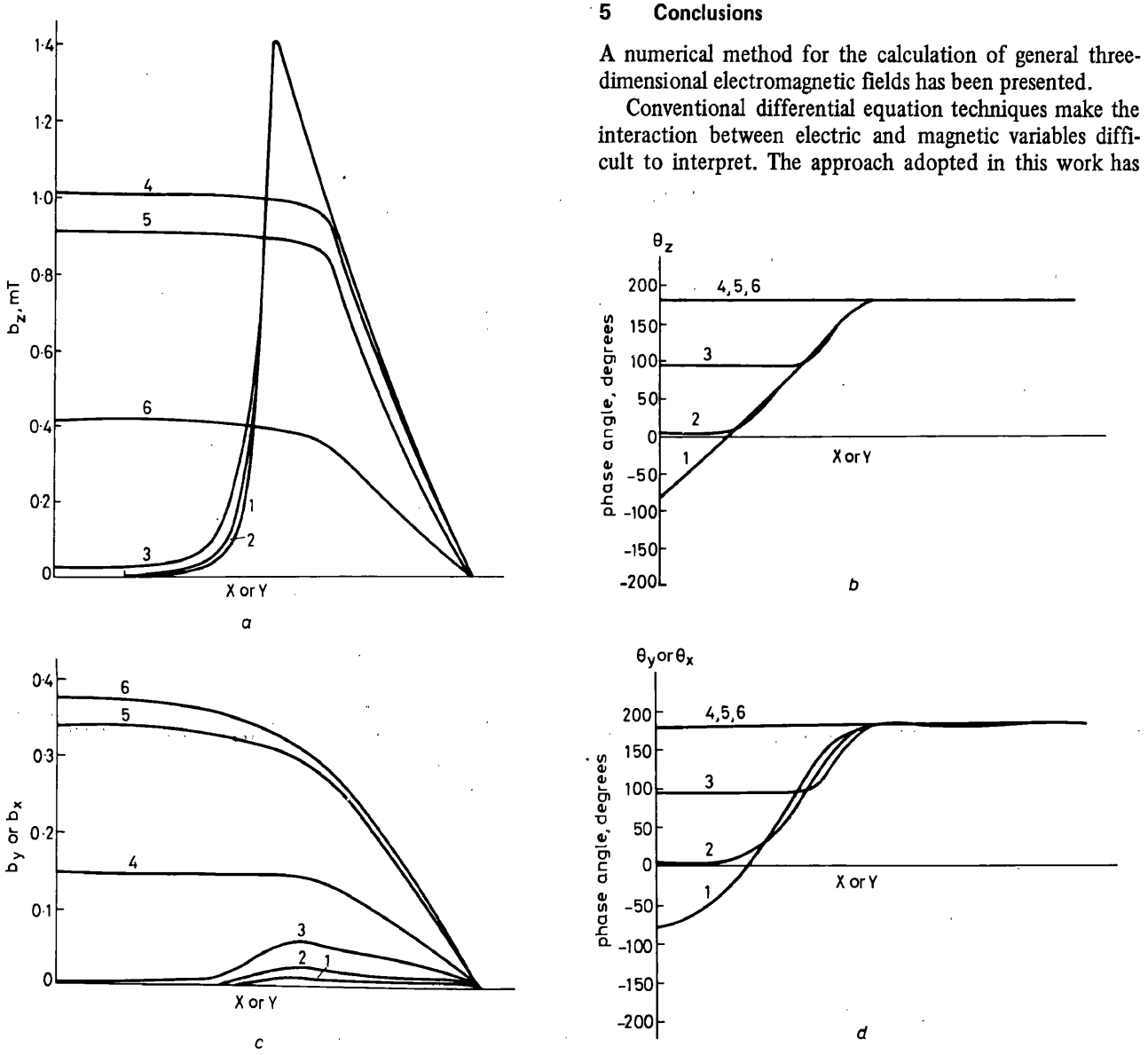

Fig. 7 *Magnetic field results with conducting block*

a Magnitude of flux density in *z*-direction
b Phase of flux density in *z*-direction
c Magnitude of flux densities in *X*- and *Y*-directions
d Phase of flux densities in *X*- and *Y*-directions

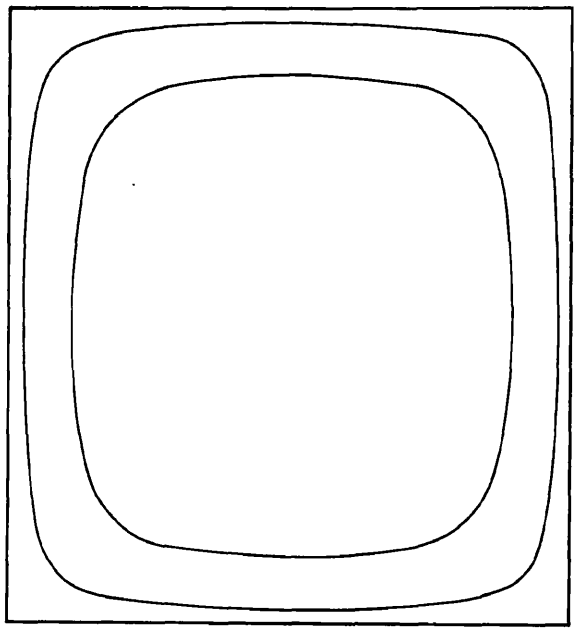

a

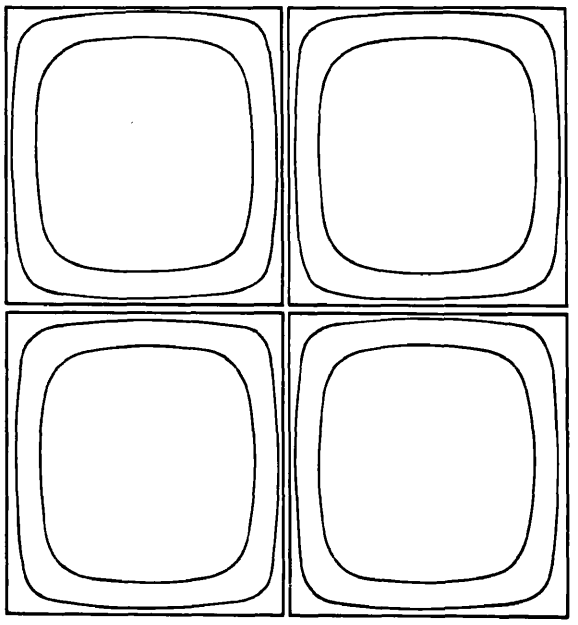

b

Fig. 8 *Sketch of current-flow paths in the XY-plane*

a Solid conducting block
b Split conducting block

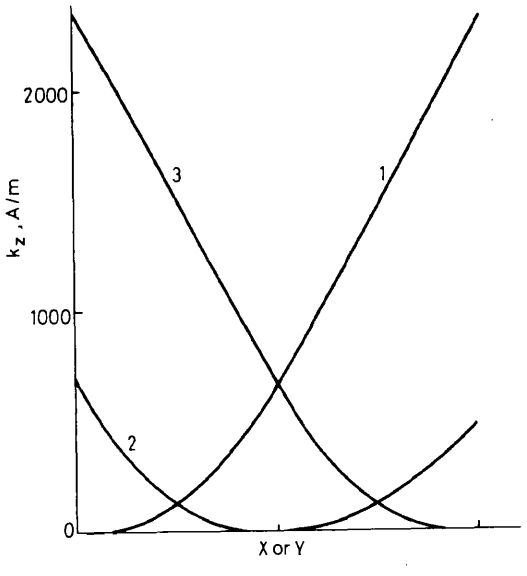

a

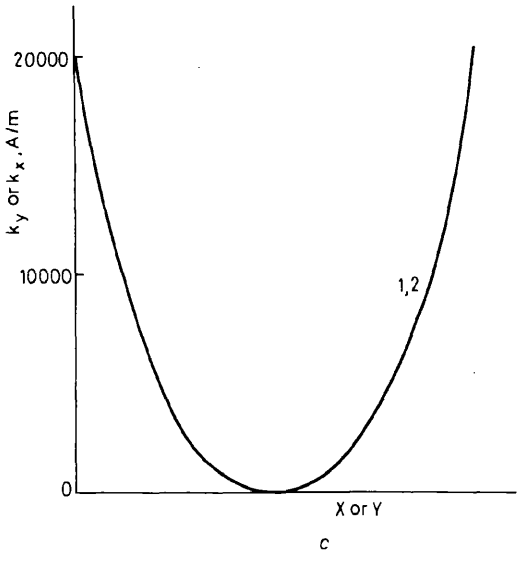

c

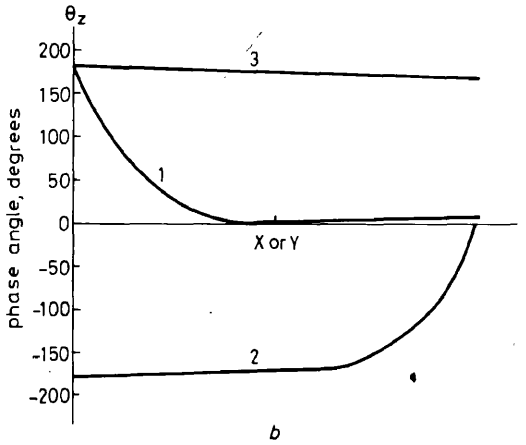

b

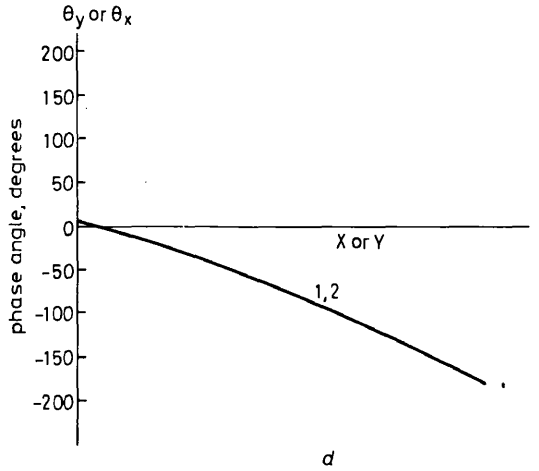

d

Fig. 9 *Electric field results with split conducting block*

a Magnitude of current density in *z*-direction
b Phase of current density in *x*-direction
c Magnitude of current densities in *X*- and *Y*-directions
d Phase of current densities in *X*- and *Y*-directions

been to derive separate network models for both the electric and magnetic fields. Using conventional network analysis techniques, the interaction between the models can then be clearly defined. The solution of the network also follows conventional techniques and therefore represents a practical method for analysing complex three-dimensional field problems. Furthermore, the method is not limited to power frequencies since displacement currents have been included.

Sample calculations were performed for steady-state a.c. conditions at a frequency of 50 Hz. These calculations showed that even with the rather coarse mesh used, the method gives plausible results.

6 References

1 CARPENTER, C.J., and DJUROVIC, M.: 'Three-dimensional numerical solution of eddy currents in thin plates', *Proc. IEE*, 1975, **122**, (6), pp. 681–688

2 CARPENTER, C.J.: 'Comparison of alternative formulations of 3-dimensional magnetic-field and eddy-current problems at power frequencies', *ibid.*, 1977, **124**, (11) pp. 1026–1034

3 EASTHAM, J.E.: 'Iron-cored linear synchronous machines', *Electron & Power.*, 1977, **23**, pp. 239–242

4 GUILLEMAN, E.A.: 'Introductory circuit theory' (Wiley-Toppan, 1953)

5 MACNEAL, R.H.: 'An asymmetrical finite difference network', *Q. Appl. Math.*, 1953, **11**, pp. 295–310

6 TASNY-TSCHIASSNY, L.: 'The triangulation of a two-dimensional continuum for the purpose of the approximate solution of second-order partial differential equations', *J. Appl. Phys.*, 1949, **20**, pp. 419–424

7 CARPENTER, C.J.: 'Finite-element network models and their application to eddy-current problems', *Proc. IEE*, 1975, **122**, pp. 455–462

8 TASNY-TSCHIASSNY, L.: 'Assymetrical finite difference network for tensor conductivities', *Q. Appl. Math.*, 1954, **12**, pp. 417–420

9 KRON, G.: 'Tensor analysis of networks' (Wiley, New York, 1939)

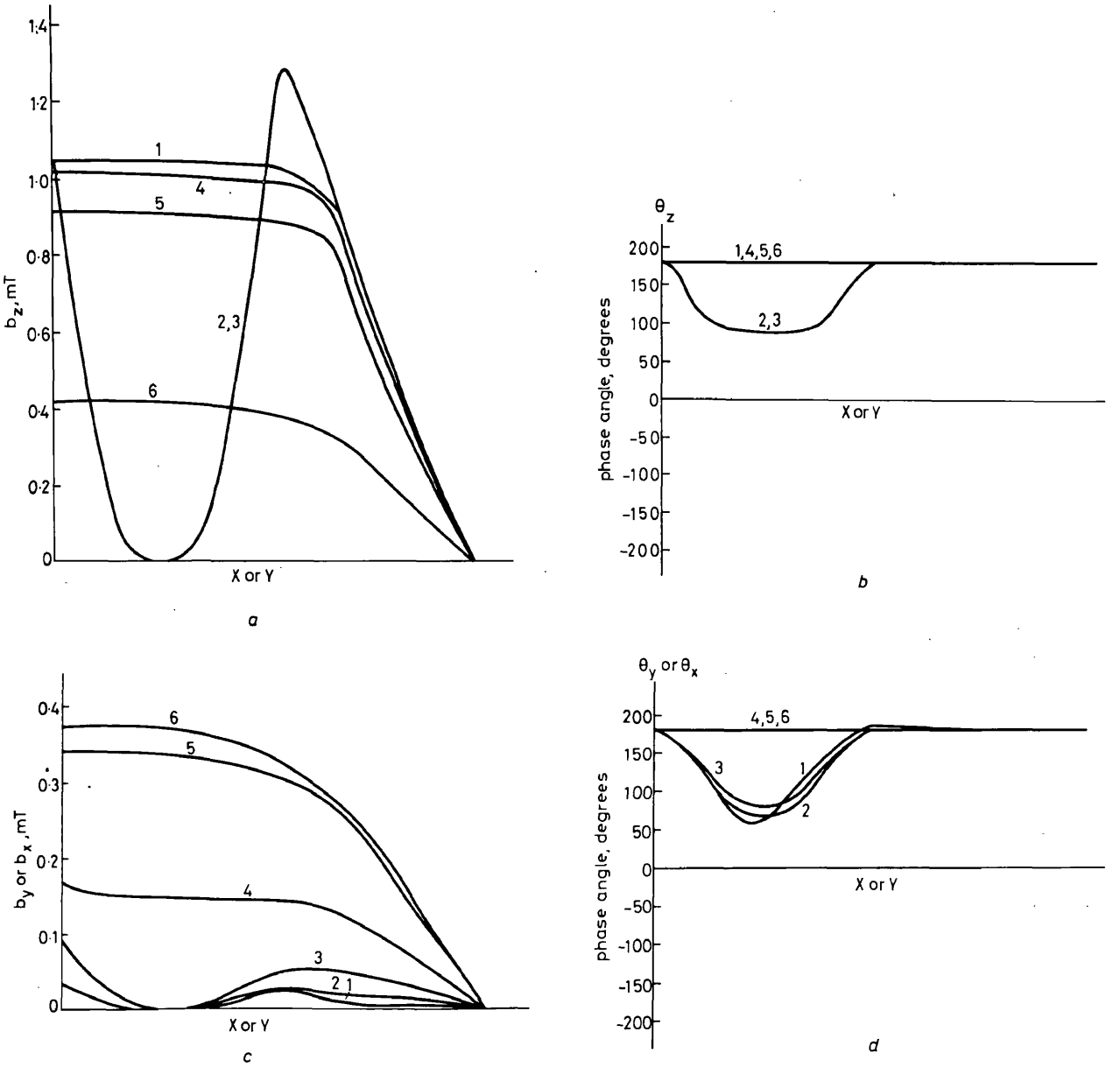

Fig. 10 *Magnetic field results with split conducting block*

a Magnitude of flux density in *z*-direction
b Phase of flux density in *z*-direction
c Magnitude of flux densities in *X*- and *Y*-directions
d Phase of flux densities in *X*- and *Y*-directions

Experimental verification of network method for calculating flux and eddy-current distributions in three dimensions

J.A.M. Davidson, B.Sc (Eng), and M.J. Balchin, B.Sc. (Eng), Ph.D., D.I.C., A.G.C.I.

Indexing terms: *Electromagnetics, Networks*

Abstract: A network method for the solution of general electromagnetic field problems has been introduced in a previous publication. The method was shown to give plausible results but no experimental evidence was given. The present paper describes the methods used for the solution of the circuit equations and a comprehensive set of measurements are presented which demonstrate the validity of the method. Some advantages and drawbacks of the method are also discussed.

List of principal symbols

b = magnetic flux density
C = capacitance
C_E, C_M, N = connection matrices
E, e = voltage
F, f = lamellar and solenoidal components of electric field strength
G = conductance
H, h = lamellar and solenoidal components of magnetic field strength
I, i = lamellar and solenoidal components of current
K, k = lamellar and solenoidal components of current density
M, m = magnetomotive force (MMF)
n = unit outward normal vector
P = permeance
p = time derivative d/dt
V = electric scalar potential
ϵ = permittivity
μ = permeability
σ = conductivity
ϕ = magnetic flux
Ω = magnetic scalar potential

1 Introduction

When developing a new theoretical method, particularly if numerical in nature, very often the only method for checking the calculations is to compare them with equivalent experimental results. A recent publication by the authors [1] has introduced and described the theory of a numerical method for computing three-dimensional electromagnetic fields. It was found that although many problems had truly three-dimensional field distributions there was a dearth of actual measurements against which these calculations could be checked. It is the purpose of this paper to present a set of measurements to demonstrate the validity of the method and to make these measurements available to other workers involved in the calculation of three-dimensional electromagnetic fields.

The technique presented in Reference 1 represents an extension of the network approach to field calculations adopted by Carpenter [2] for problems involving two-dimensional eddy currents in a three-dimensional magnetic field. At present the method is capable of calculating three-dimensional current and flux distributions due to time sinusoidal excitation in a stationary linear medium.

Paper 1568A, first received 20th January and in revised form 10th June 1981

The authors are with the Department of Electrical Engineering, University of Bath, Claverton Down, Bath BA2 7AY, England

2 Equivalent circuit model

The region of interest is subdivided into two sets of rectangular prisms. As far as is possible the edges of one set of prisms are arranged to intersect the surfaces of the other set normally and vice versa. Each set of subdivisions supports a conventional finite-difference or finite-element representation (including boundary conditions) of one of the equations

$$\begin{aligned} \text{div}\,(\sigma + p\epsilon)\,\text{grad}\,V &= \text{div}\,\{(\sigma + p\epsilon)f - K\} \\ \text{div}\,\mu\,\text{grad}\,\Omega &= \text{div}\,\mu h \end{aligned} \tag{1}$$

In these equations V and Ω are electric and magnetic scalar potentials, $p = d/dt$ and f and h are the solenoidal (zero divergence) components of the field strength vectors. K is a lamellar (zero curl) current density representing space charge effects.

The discrete forms of eqns. 1 are interpreted in terms of equivalent circuits (Fig. 1) in which the potential sources are associated with the solenoidal components of field strengths and the flow quantities with the solenoidal components of current and flux density. The two circuits are physically separate, but there is electromagnetic coupling between them. The relations for all branches of the type shown in Fig. 1 are given by the matrix equations

$$E + e + e_s = (G + pC)^{-1} i \tag{2}$$

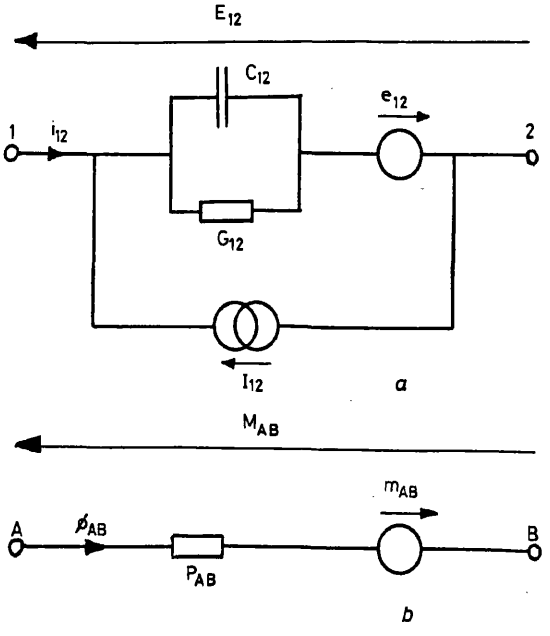

Fig. 1 *Two equivalent circuits*
a Element of electric field model
b Element of magnetic field model

$$M + m + m_s = P^{-1}\phi \tag{3}$$

where e_s and m_s are known source quantities.

3 Solution of complete field equivalent circuit

To solve the linked-circuit problem it is necessary to formally define the linkage between the two parts of the equivalent circuit. This is done using a discrete form of Faraday's and Ampere's laws. For one closed path L in the electric model surrounding a surface S

$$\int_L (F + f)\,dl = -p \int_S bn\,dS \tag{4}$$

A similar expression holds for the magnetic model, i.e.

$$\int_L (H + h)\,dl = \int_S kn\,dS \tag{5}$$

The manner in which the fields are subdivided is such that each closed path is formed with segments of uniform field strength parallel to the path. Furthermore each closed path surrounds a surface through which flux or current passes normally. Thus eqns. 4 and 5 can be written

$$\sum_L (E + e) = -p \sum_S \phi \tag{6}$$

$$\sum_L (M + m) = \sum_S i \tag{7}$$

The complete linked-circuit model is solved using the 'mesh-current' technique [3]. This gives all branch fluxes and currents in terms of an independent set of fluxes and currents that flow in closed paths. The minimum number of such closed paths required to solve the networks by the mesh method is equal to the total number of 'link' or 'co-tree' branches in both networks. This is represented formally by the expressions [3]

$$i = C_E i_I \tag{8}$$

$$\phi = C_M \phi_I \tag{9}$$

where C_E and C_M are connection matrices and i_I and ϕ_I are the vectors of closed path currents and fluxes. When eqns. 6 and 7 are applied to the closed paths defined in eqns. 8 and 9, the following matrix equations are obtained:

$$C_E^T (E + e) = -pN^T \phi_I \tag{10}$$

$$C_M^T (M + m) = N i_I \tag{11}$$

where N is a connection matrix that indicates which of the closed path fluxes links a closed path in the electrical model and vice versa.

The set of eqns. 2, 3 and 8–11 reduce to the following set of linear simultaneous equations in the variables ϕ_I and i_I

$$\begin{bmatrix} C_M^T P^{-1} C_M & -N \\ -N^T & -C_E^T (G/P + C)^{-1} C_E \end{bmatrix} \begin{bmatrix} \phi_I \\ i_I \end{bmatrix} = \begin{bmatrix} C_M^T m_s \\ -C_E^T e_s/P \end{bmatrix} \tag{12}$$

Following a solution to eqn. 12 it is possible to obtain all fluxes and currents in the equivalent circuit by using exprs. 8 and 9.

The field problem has been reduced to the solution of a complex set of linear simultaneous equations. The type of method to be used for the solution of the equations is largely determined by the form of the coefficient matrix. The coefficient matrix for the mesh method is symmetric, but in general for most eddy current problems it is not positive definite. It is complex, very sparse and the elements are scattered, having none of the recognisable structures which limit the number of elements that can become nonzero during a direct solution procedure. The zero elements are not normally stored in a practical solution, and so the 'fill-in' of elements, that were previously zero, increases the storage requirement. This can cause storage problems in the direct solution of even a moderately large system. Iterative methods are attractive because the problem of fill-in does not arise, but the form of the present coefficient matrix will not in general guarantee convergence for most methods. A semi-iterative method was therefore used of the preconditioned conjugate gradient type [4] to solve the normalised system of equations. This method does not suffer from 'fill-in' and it at least gives a theoretical guarantee of convergence.

The conjugate gradient algorithm for the normalised system of equations was programmed to operate with complex arithmetic and also to exploit the sparseness and symmetry of the coefficient matrix. For the problems solved in this paper, very good results have been obtained using this programme, with convergence on a fraction of the theoretical number of iterations. This success is attributed to the fact that the incomplete factorisation step with no 'fill-in' gives a good approximation to the actual inverse, and so the conditioned system matrix is close to the identity matrix. Also, care was taken to minimise rounding error when programming. For example all accumulations were performed in double precision, and products such as a complex number and its conjugate were explicitly stored as real numbers. In cases where the approximate inverse is poor convergence has been found to be slow, requiring up to or more than the theoretical number of iterations. As an iterative method a great amount of arithmetic is performed in each iteration, and so with large systems it is important that the approximate inverse is accurate, otherwise the run time for a solution may become prohibitive.

The program does however give an economical solution to many problems which are difficult to solve by any other means.

4 Experimental verification

4.1 Comparison between measured and calculated results

An experimental model (Fig. 2) has been designed and built to verify the three-dimensional field calculations. The field region modelled consists of a laminated iron pole placed centrally over a laminated iron box. Specimens of solid conductor were placed in the box and the model was energised to give a constant sinusodial MMF of $1000 + j0$ AT between the pole and box.

Flux-density magnitude measurements were obtained using a Hall probe (active area 0.078 x 0.187 ins) and phase measurements with a search coil (0.125 ins diameter), the signal of which was amplified. All phase measurements are with reference to the supply current. It has not been possible to measure flux density inside the solid conductor, and so measurements were limited to the air region. Current-density measurements have not been performed because the currents only produce a very small voltage in the conductor, thereby making current-probe-type measurements very difficult and unreliable.

The first comparison made between experimental and calculated results is similar to a case solved by Carpenter [2] with a three-dimensional magnetic field and two-dimensional current flow. A thin plate, of dimension 140 x 140 x 3.17 mm and conductivity 2.325×10^7 S/m, was placed centrally under

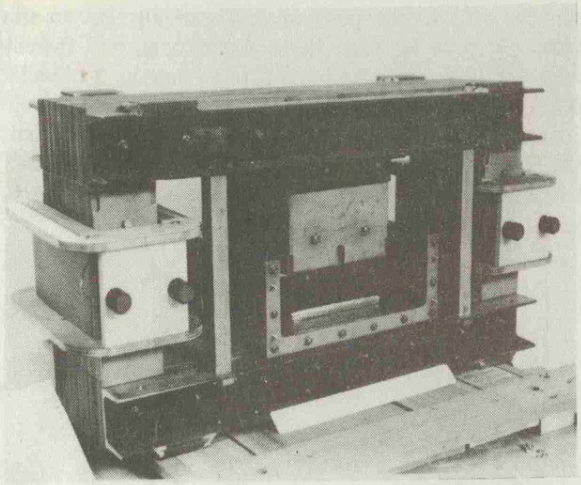

Fig. 2A *Experimental apparatus with laminated box front removed*

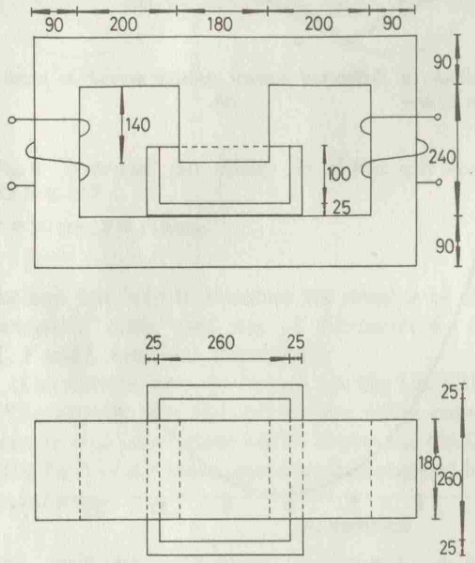

Fig. 2B *Diagram of experimental apparatus*

Dimensions in millimetres

the pole on the bottom of the box. Fig. 3 shows the flux density normal to the surface of the plate at $X = 0$. The currents flowing in the X-Y plane are damping the Z-directed flux which induces the current. The calculated and measured results are generally in good agreement. The calculated peaks at the edge of the plate, $X = \pm 70$ mm in Fig. 3, where the flux density changes rapidly, are slightly low. This factor is due most probably to the coarseness of the mesh, (see Section 4.2). A finer mesh around these points would no doubt improve the accuracy of the calculations.

The accuracy of the thin plate calculations gave confidence in the computer program. The plate was then replaced with a thick block of dimension 140 x 140 x 60 mm and conductivity 2.703×10^7 S/m, placed centrally under the pole. The conducting block totally filled the vertical gap apart from 4 mm required for access. The current was no longer constrained to planar flow and current density calculations confirmed that a Z-directed component of current was in fact present in the block. The ratio of the maximum calculated magnitude of X- or Y-directed to Z-directed current density is approximately 70:1. The current flow pattern was therefore still predominantly two-dimensional with the main current circulating round the block in the X-Y plane and only a very small proportion in the Z direction.

The experimental and calculated Z-directed flux density values under the block at $X = 0$ are given in Fig. 4. These have the same form as the corresponding thin plate results but show a greater screening effect due to the increased flow of current in the X-Y plane. The X- and Y-directed flux densities outside the block were also measured, but the effect of the Z-directed current flow was barely evident.

The agreement between calculation and experiment in Fig. 4 is good at most points. The slight discrepancy in the magnitude of the flux density at the edge of the block, $X =$

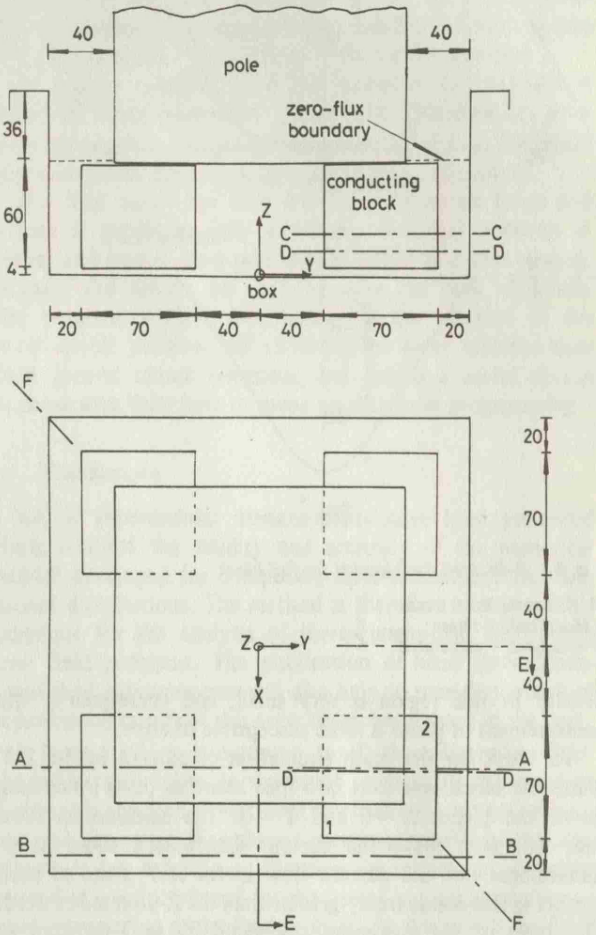

Fig. 2C *Schematic diagram of field region in experimental apparatus*

Dimensions in millimetres

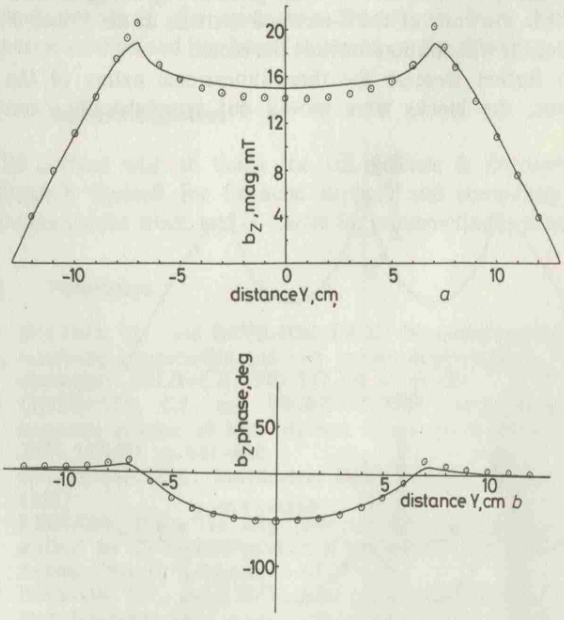

Fig. 3 *Z-directed flux density for thin plate*

$Z = 4$mm, $X = 0$mm
a Magnitude *b* Phase
o measured — calculated

± 70 mm, may again be due partly to the coarseness of the mesh at these points. The measured values exactly at the peak will also be slightly low because of the averaging caused by the width of the probe. The discrepancy in the phase near $X = 0$ may be due in part to errors in the measured points. The flux

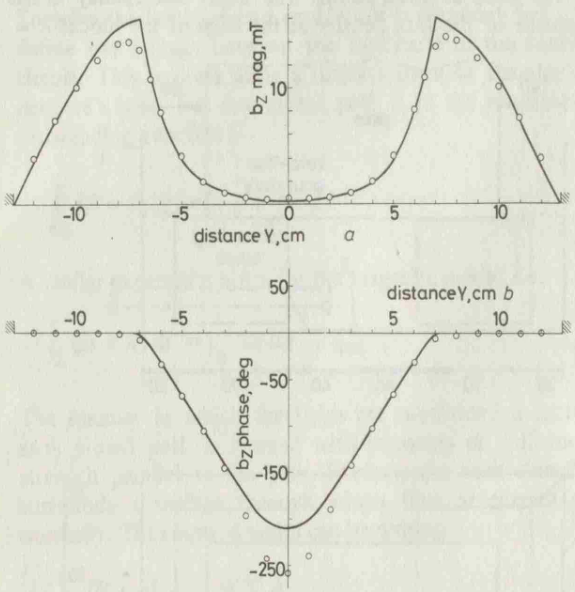

Fig. 4 *Z-directed flux density for full block*

$Z = 2$ mm, $X = 0$ mm
a Magnitude *b* Phase
○ measured — calculated

density in this region is very small, and consequently the measurement of phase is more susceptible to error.

To break up the main circulation of current in the X-Y plane the block was split into four identical parts by cutting down the planes $X = 0$ and $Y = 0$. The calculations show that this does make the current distribution more three-dimensional but the current flow in the X-Y plane of each quarter is still considerably greater than the Z-directed current. The ratio of the maximum calculated X- or Y-directed to Z-directed current density is now 15:1.

The measured and calculated Z-directed flux density values under the split block at $X = 50$ are given in Fig. 5. Again there was little evidence of the Z-directed currents in the X and Y flux density distributions outside the block.

To further increase the three-dimensional nature of the currents, the blocks were moved out symmetrically from

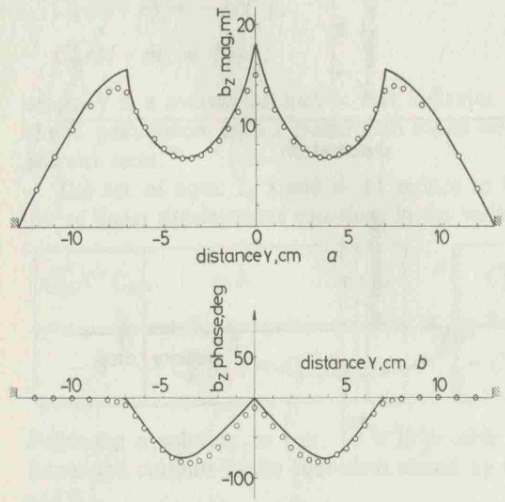

Fig. 5 *Z-directed flux density for split block*

$Z = 2$ mm, $X = 50$ mm ○ measured — calculated
a Magnitude *b* Phase

under the pole to the position shown in Fig. 2C. In this position the flux is more three dimensional, and thereby excites a truly three-dimensional current flow in the blocks. This is confirmed by the calculations which predict the ratio of the maximum X- or Y-directed to Z-directed current density to be less than 2:1. Typical calculated current-density distributions for the Z and X or Y directions are given Fig. 6.

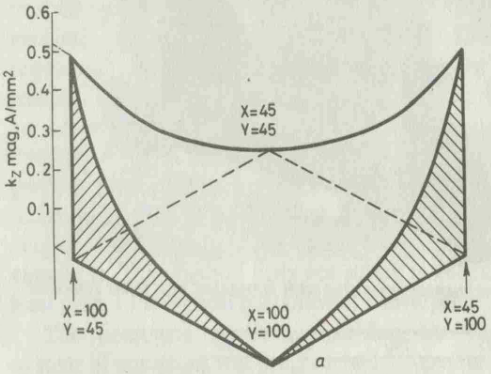

Fig. 6A *Magnitude of Z-directed current density normal to plane CC (Fig. 2C) Z = 20 mm*

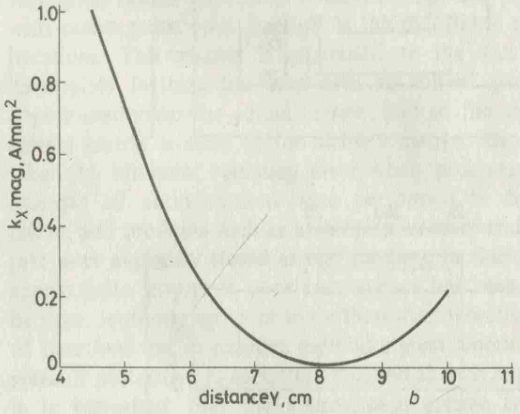

Fig. 6B *Magnitude of X-directed current density along line DD (Fig. 2C) Z = 10 mm, X = 70 mm*

These show the familiar circulation of X or Y current round the edge of each block and also that most Z-directed current flows either up or down edges 1 and 2 (Fig. 2C) of the block.

The comparison between measured and calculated flux-density distributions in both Z and X directions are given in Fig. 7 and 8. These confirm the validity and accuracy of the method presented for the calculation of three-dimensional electromagnetic fields.

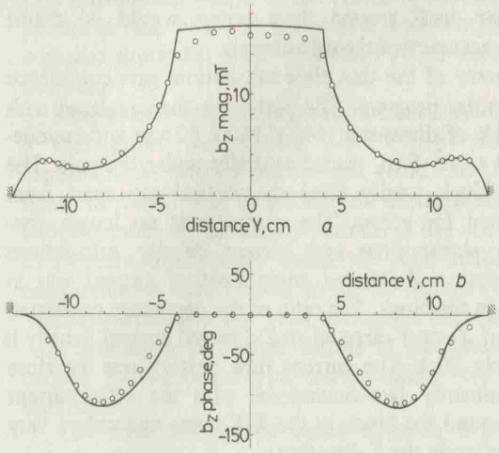

Fig. 7 *Z-directed flux density for shifted split blocks along line AA (Fig. 2C)*

$Z = 2$ mm, $X = 70$ mm
a Magnitude *b* Phase ○ measured — calculated

4.2 Details of calculations

The symmetry of the model enabled calculations to be performed over the quarter section EE (Fig. 2C). To clearly define the boundary conditions all iron was assumed to have infinite permeability and a horizontal zero flux boundary was assumed to exist between the pole and the box as shown in Fig. 2C. These assumptions are not a requirement of the

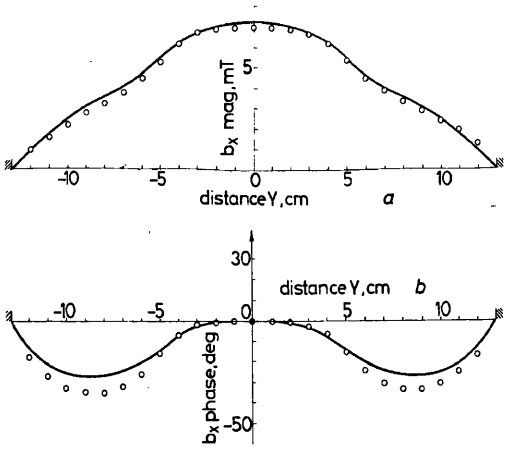

Fig. 8 *X-directed flux density for shifted split blocks along line BB (Fig. 2C)*

$Z = 20$ mm, $X = 120$ mm

method but help to minimise the number of elements. The 'magnetic' mesh used was of dimension 6 x 6 x 3 in the X, Y and Z directions, respectively.

Calculations were performed on the UK SERC IBM 360 195 computer. For the split blocks moved outwards the run time storage requirement was 85 kbytes and the CPU time was 20 s. Each of the other cases described required both less time and storage.

5 Discussion

The validity of the field calculation method has been confirmed by comparison of the calculations with experimental results. Some advantages and drawbacks of the calculation method are now discussed.

The continuous electromagnetic field has been represented in discrete form in terms of two separate networks, one to represent the magnetic part and the other to represent the electric part of the field. Linkage between the two circuits has been specified to produce a complete field model in which the role of all field variables is clearly defined. The representation of interface conditions in the field model is simple, straightforward and does not complicate the numerical solution procedure. In particular no additional potential functions are required to model the interfaces in three dimensions.

The field equivalent circuit has been solved by the mesh current technique. More equations are required to solve a three-dimensional field problem by a mesh-variable method than by a node-variable method in terms of magnetic and electric scalar potential. A node potential solution of this type has not yet been developed. A solution procedure which approaches this ideal is the T/Ω method [5, 6], in that the magnetic field is described by a node potential and the electric field by a vector which can normally be limited to two components only. This method does have the disadvantage that the coefficient matrix of the simultaneous equations is asymmetric. The mesh method has the advantage that it results in a coefficient matrix which is symmetric so that only about half the matrix elements need to be stored during the solution. Furthermore the solution is given directly in terms of flux and current densities, thereby avoiding cancellation problems that can occur when these have to be obtained from a node potential solution.

If direct methods are preferred for the solution of the field equations the mesh method has the disadvantage that although the coefficient matrix is sparse, it does not have any of the recnisable structures that limit 'fill-in'. This does not affect iterative methods, and in particular the complex preconditioned conjugate gradient program has been found to give very good results for the solution of the mesh equations.

At present subdivision of the region of the problem is performed using rectangular prisms only. This does not seem to be too great a limitation because it is felt that this is the most convenient element to visualise in three dimensions.

The field model has been developed in circuit terms and as such it should be easy to use by electrical engineers in general and one of the many readily available circuit analysis program can always be used to solve the field equations. The program written specifically for the solution of the linked-circuit problem will obviously be more efficient than these general circuit programs, but this is a useful option for those with little time to spend on computer programming.

6 Conclusions

A set of experimental measurements have been presented which confirm the validity and accuracy of the numerical method developed for computing three-dimensional flux and current distributions. The method is therefore seen as a viable technique for the analysis of three-dimensional electromagnetic field problems. The publication of some three-dimensional field measurements will also help to remedy the lack of experimental results of this type which has existed in the past.

A feature which is common to all three-dimension field calculation techniques is the rapid increase in the number of elements required when the discretisation is extended into the third dimension. For three-dimensional problems that are periodic in one co-ordinate direction the number of elements required is greatly reduced by the use of a quasi-three-dimensional formulation of the field problem. In this model the field in the periodic direction is represented by a Fourier series. The subdivision of the region is then limited to a plane in the other two co-ordinate directions. Work is in progress to finalise the development of the quasi-three-dimensional form of the general method and it is hoped to report on this shortly.

7 Acknowledgments

The authors wish to thank the UK Science & Engineering Research Council for financial support and computing resources for the work, and G. Carter for constructing apparatus.

8 References

1 BALCHIN, M.J., and DAVIDSON, J.A.M.: 'Numerical method for calculating magnetic-flux and eddy current distributions in three-dimensions', *IEE Proc. A*, 1980, 127, (1), pp. 46–53
2 CARPENTER, C.J., and DJUROVIC, M.: 'Three-dimensional numerical solution of eddy currents in thin plates', *Proc. IEE*, 1975, 122, (6), pp. 681–688
3 GUILLEMAN, E.A.: 'Introductory circuit theory' (Wiley-Toppan, 1953)
4 KERSHAW, D.S.: 'The incomplete Cholesky conjugate gradient method for the iterative solution of systems of linear equations', *J.Comp, Phys*, 1978, 26, pp. 43–65
5 PRESTON, T.W., and REECE, A.B.J.: 'Finite element solution of three-dimensioal eddy current probelms in electrical machines'. Proceedings of Compumag, 1978, pp. 213–220
6 CARPENTER, C.J., and WYATT, E.A.: 'Efficiency of numerical techniques for computing eddy currents in two and three dimensions'. *Ibid.*, 1978, pp. 242–250